THE SPATIAL RESOLUTION OF THE SCANNING AUGER MICROSCOPE

by

Mohamed Mochtar El Gomati

Thesis submitted to the University of York

for the degree of Doctor of Philosophy

Department of Physics

University of York

March 1983

IN THE NAME OF ALLAH, THE BENEFICIENT,

THE MERCIFUL

I DEDICATE THIS WORK TO MY PARENTS

TABLE OF CONTENTS

ACKNOWLEDGEMENTS

With the completion of this thesis, it is my pleasure to acknowledge the help I have received from several people without whom this thesis may not have been presented in this form.

I am particularly indebted to my supervisor, Professor M. Prutton, who first stimulated my interest in Scanning Auger Microscopy. It was his encouragement and interest in the project that made possible the successful completion of this work.

It is my pleasure also to acknowledge the help and encouragement I have received from Dr. R. Browning, with whom I shared the glory of obtaining the first SAM picture in York. Thanks are also due to Dr. J.A.D. Matthew, Mr. D. Peacock and other members of the surface Physics group for several useful discussions: Mr. S. Tear for reading parts of the manuscript: Dr. J. Venables and Dr. A. Janssen for the data used in Chapter 5: Dr. P. Duncumb of TI Research Laboratories for making available a copy of the TI 303 report, which describes the Monte Carlo model used, and Dr. E. Munro, formerly of Cambridge University, for a copy of report CUED/B-Elect. TR 45 used in the calculation of the electron optics: Dr. K. Smith for discussion concerning the design of the second instrument and Professor L. Swanson for discussion on the use of the Zr/W(100) emitters.

The craftsmanship and cooperation of laboratory staff in the Department of Physics is also acknowledged. Messrs. L. Crosby, R. Eason, P. Durkin and L. Jarvis for the construction of the field emission column and Messrs. J. Dee and M. Peters for assistance in the laboratory: Mr. R. Hide for constant repair of the electron column power supply: Mr. A. Gebbie for the preparation of the manuscript and Mrs. M. Pirozek for typing it.

I am also grateful for the financial support and leave from the Physics Department, Faculty of Science, Tripoli, Libya during this Project.

Last, but by no means least, I would like to offer my sincere thanks and appreciation for the support I have received from my family and, in particular, my wife.

PUBLICATION

The work reported in this thesis is the original contribution of the author except where references or acknowledgements are made in the text. Portions of it have been previously published in the following articles:

i) R. Browning, P. Bassett, M.M. El Gomati and M. Prutton, Proc. Roy. Soc., A357, (1977) 213-230.

ii) R. Browning, M.M. El Gomati and M. Prutton, Surf. Sci., 68 (1977).

iii) M.M. El Gomati and M. Prutton, Surf. Sci., 72, (1978) 485-494.

iv) M.M. El Gomati, A.P. Janssen, M. Prutton and J. Venables, Surf. Sci., 85, (1979) 309-316.

v) M.M. El Gomati and M. Prutton, EMAG (79), Sussex, U.K., (1979) 361-4.

vi) J.A.D. Matthew and M.M. El Gomati, Surf. and Interface Analysis, 1 (4), (1979) 135-7.

vii) L.A. Larson, M. Prutton, M.M. El Gomati and L.H. Veneklasen, 28th Inter. F.E. Symposium, Oregon, U.S.A. (1981).

viii) M.M. El Gomati, D. Peacock and M. Prutton, EMAG (81), Cambridge, U.K., (1981) 439-442.

ix) M.M. El Gomati, R. Browning and M. Prutton, EMAG (81) Cambridge, U.K., (1981) 45-6.

x) M. Prutton, R. Browning, M.M. El Gomati and D. Peacock, Vacuum, 32 (6), (1982) 351-57.

ABSTRACT

A study of the effects of backscattered electrons on the resolution of the scanning Auger microscope (SAM) is presented. Monte Carlo methods successfully used in EMPA and SEM are used in the investigation. It is found that the resolution limits in SAM are controlled mainly by the profile of the incident electron beam. Backscattered electrons yield only a low, slowly varying background that should be eliminated with simple discrimination techniques in existing SAM designs. However, the orientation of the chemical edge with respect to the scan direction is shown to have a strong effect upon the resolution. A theory/experiment comparison of this effect is presented with good agreement. In addition the effects of the electron energy, angle of incidence and substrate material on the resolution are also presented.

The experimental investigation was carried out in an all electrostatic digital, high spatial and high energy resolution SAM. The design of two such instruments is presented with results showing two dimensional mapping of different chemicals on solid surfaces (128 x 128 pixel images) with scan times of the order of 6 - 8 minutes. This presents the shortest frame scans in reported SAM designs. Further the second instrument compares better with other reported instruments by featuring quantitative spectroscopy and RHEED facilities while maintaining high spatial resolution and short frame scan times. Particular emphasis is laid on the design of the electron optical column. This consists of a two element electrostatic lens and an 8 pole stigmator/deflector. The electron spot ranges in diameter between 40 - 130 nm for a beam current in excess of 5×10^{-9} A.

A preliminary study on the use of field emission cathodes for probe currents in the range of 1 - 100 nA, and diameter less than 150 nm is

presented. Cold and thermally assisted field emission from two different wire orientations W(310), Zr/O/W(100) is assessed in terms of operational conditions and stability. A high degree of emission stability of the order of 2 - 3%/hr for operating times of the order of many hours is achieved from Zr/W(100).

INTRODUCTION

Auger electron spectroscopy (AES) has become a standard tool in surface physics and chemistry for over a decade. The continued interest in the technique stems from its surface sensitivity (of the order of few atomic monolayers and concentration levels of few hundred parts per million). The successful demonstration by McDonald and co-workers (80) of the combination of AES with the scanning electron microscope (SEM) to map the spatial distribution of a selected chemical on solid surfaces (in much the same way as the electron microprobe analyser EMPA) has started an extensive development of this technique which is called scanning Auger electron microscopy (SAM). This technique has made it possible to obtain chemically specific information about inhomogeneous surface processes in surface science and microanalysis with a lateral resolution of less than 100 nm. Particularly in microanalysis, SAM has shown a reduction in the analysis volume by a factor of the order of 10^5 in comparison with EMPA.

One feature of the present technique is high spatial resolution as compared to EMPA. In the latter, the resolution limits are determined by the extent of the backscattered radius of the diffuse primary electrons that give rise to the detected x-rays. This limits the resolution in EMPA to about 1 μm (85). In the early SAM designs, the nature of the development (of an ad-hoc type) and the requirement for high electron beam currents for the production of Auger electrons (1 in 10^5 - 10^4) have produced SAMs of probe diameter of the order of few microns. But the successful use of the high brightness field electron emitters as cathodes for small probe diameter SEM, has directed developments in SAM towards small probe diameters.

Christou (82) compared different electron sources, including field emitters, used in SAM and has concluded that the limit of spatial resolution is ten times the probe diameter. He attributed this result to the

effects of energetic backscattered electrons. This was both controversial and disappointing for a high spatial resolution technique. On the one hand, Christou's measurement was not quantitative in characterising the chemical edge and probe diameter while on the other hand indications of high resolution SAM were emerging due to efforts directed towards it by several groups (59, 62, 68).

At this stage of development of the technique it is interesting to assess its development and to compare it with the well established technique of x-ray analysis, EMPA. However, SAM should not be considered a rival technique to EMPA but rather a complementary one due to the nature of the information obtained using each technique being surface and bulk respectively.

The present thesis is part of a programme to develop a high energy and spatial resolution digital SAM. The emphasis here is on the effects of backscattered electrons on the resolution. The latter is investigated using Monte Carlo techniques successully used in EMPA and SEM. Experimental verification of the theoretical results obtained is also presented.

The work consists of three inter-related parts and is presented in the ensuing chapters in the following way. Chapter 1 is a brief introduction to the nature of AES. Its purpose is to acquaint the reader with the terminology used and the parameters contributing to AES. It is not however intended as a review of the subject where the reader is referred to more comprehensive papers (189 - 191). Chapter 2 is a feasibility study for a SAM, and is used to shed some light on the difficulties of combining AES with SEM. A review of some techniques currently in use to obtain meaningful imaging in SAM (i.e. separating topographical effects, beam current fluctuations in field emission probes, backscattering contributions and chemical diffusiness) is also given. The chapter is con-

cluded with the characteristics of the first SAM instrument designed and built in York. The design and performance of this instrument is reported in Chapter 3. It was based on the first commercial field emission SEM in Europe (HB 200 by V.G. microscopes Ltd.) and served to demonstrate the possibility of mapping the spatial distribution of a chemical species in the top few atomic monolayers of a solid. Experimental results from a Ti polycrystalline wire are presented with digital Auger maps of 128 x 128 pixel in frame scan times of the order of 28 minutes. The electron energy analyser is of the concentric hemispherical type accessed by electron lenses. However, the engineering compromises involved in the design and construction of this instrument were not resolved (and perhaps still are not for a SAM) to the point where there is a consensus about the most suitable combination of system components.

The second part is an investigation of the effects of the back-scattered electrons on the spatial resolution of the technique and consists of two chapters. Chapter 4 is a description of the Monte Carlo model used and the reasons for its choice with respect to other models. The effects of backscattering on the resolution of a sharp chemical edge in the cases of Aℓ , Cu , and Au are given. A theory/experiment comparison for an Ag edge on a W substrate is reported in Chapter 5. In addition, the complexity of interpreting the results in a SAM due to the geomtrical arrangement is explained with comments on the best arrangement to be used. Experimental verification of this point is also presented.

The third part is concerned with the design, construction and performance of the second instrument using the experience gained with the first and consists of four chapters. This instrument is a computer controlled high energy and spatial resolution SAM, but only the design and construction of the field emission column will be reported in detail, which represents the author's contribution. The computer control is a

separate topic and will be treated elsewhere (192). Chapter 6 is an investigation of the use of field electron emitters in high current (1 - 100 nA) probes. Operational conditions for the emitters and the lens electrodes are discussed. Two W emitters of different orientations (W(310), Zr/W(100)) and modes of operation (cold and thermally assisted) have been used. This chapter is followed by a theoretical investigation of electrostatic lenses used in field emission probes in the energy range 0.1 - 30 keV. Modelling of the electron trajectories and calculation of the lens aberrations have been obtained by using a library of computer programs provided by E. Munro (158). Chapter 8 is concerned with the construction of the electron optical column based on a two element lens and an 8 pole electrostatic stigmator/deflector (160). The chapter contains also a review of the criteria for choosing the different materials used in the construction. Chapter 9 is an assessment of the performance of the second instrument with an emphasis on the electron probe. It is concluded with representative results in the Auger mode to obtain point analysis, line scanning, and two dimensional mapping. The instrument is compared with other reported SAM designs. The last chapter is a conclusion and suggestions for further work.

CHAPTER 1

AUGER ELECTRON SPECTROSCOPY (AES)

1.1 INTRODUCTION

In 1925, Pierre Auger was the first to observe and correctly explain the origin of what became known as Auger electrons (1-3). P. Auger found, while studying particle tracks in a cloud chamber, that electrons of constant energy irrespective of the bombarding x-ray excitation energy used, were ejected from the bombarded atoms. He described these electrons as "compound photoelectrons". Electrons, x-rays, ions and protons are some of the methods to generate Auger electrons.

Scientists have detected these electrons over the years but with no comment on their application until 1953 when Lander (4) suggested their use for surface chemical analysis. He further pointed out that the technique may provide a complement to soft x-ray emission to determine energy band densities of states.

Lander's suggestion was based on two important properties of the Auger electrons. The first is their well defined energies, which makes them characteristic of the analysed atoms. The second is that electrons with kinetic energies below 1000 eV have a short inelastic mean free path (of the order of few atomic monolayers), thus giving the technique its high surface sensitivity.

There were two reasons that initially prevented Lander's suggestions being pursued. The first is the difficulty of detecting the Auger electrons which appear as small bumps on the background of the secondary electron energy distribution. The second was the lack of ultra high vacuum (UHV) technology at the time and hence contaminants on the surface

prevent the Auger electrons from escaping.

The recent advance of Auger Electron Spectroscopy (AES) as an experimental technique in surface physics is in major part due to the realisation by Harris (5) in 1968 that electronic differentiation of the secondary electron energy distribution can be used to discriminate between structure due to processes such as Auger emission, and the much stronger but relatively unstructured background. In the same year, Webber and Peria (6) showed that existing Low Energy Electron Diffraction (LEED) systems can be used with little modifications for the detection of Auger electrons. Today AES forms a routine analytical technique in most surface science laboratories with a steady increase in its use to study physical and chemical processes in gases and solids.

A brief review of the various aspects and parameters which contribute to AES will be given below. The purpose of this review is to familiarise the reader with AES and to serve as the basis for some of the assumptions used in the design of this instrument. Comprehensive reviewsof the subject can be found elsewhere (1-3,181,189-191).

1.2 THE ELECTRON ENERGY DISTRIBUTION

In an Auger electron spectroscopy experiment, the electron energy distribution is the quantity that concerns scientists most, both qualitatively and quantitatively. Figure (1.1) shows a typical secondary electron energy spectrum produced by irradiating a solid with electrons of primary energy Ep. The curve can be classified into three regions:

(i) The first region at Ep is the elastic peak, containing the elastically reflected electrons.

(ii) The second is a broad peak near E = o representing the secondary electrons. Electrons in this peak are called "true

secondaries" and are produced in a cascade process within the solids. Electrons with energies up to 50 eV are called true secondaries.

(iii) The region between the above two mentioned peaks is relatively flat and is termed the region of re-diffused primary electrons. It contains inelastically scattered primary electrons and the more energetic secondary electrons.

Superimposed on this background are the Auger peaks which appear as small bumps. These peaks have positions independent of the primary energy used.

Figure (1.1b) shows the effect of differentiating the energy distribution of Figure (1.1a) with respect to E where the small Auger peaks appear now as large double peaks because of higher slope of Auger peak with respect to slope of background. Figure (1.1) shows also the loss peaks. These are small peaks close to the elastic peak produced by electrons that have suffered well defined energy losses (7). If the primary energy is changed by an amount ΔEp , all the loss peaks will also move by ΔEp , while the Auger peaks will stay at the same energy. Electron losses are beyond the scope of this work and will not be treated further.

1.3 THE AUGER PROCESS

An ionised atom may relax to a state of lower energy via two routes, X-ray or Auger electron emission. The latter is a radiationless transition where the ionised atom relaxes to a state of lower energy by ejecting an electron to carry off the energy difference (Figure 1.2). This is illustrated as follows. Consider an atom that has an electron missing from one of its filled levels, say level A at binding energy E_A

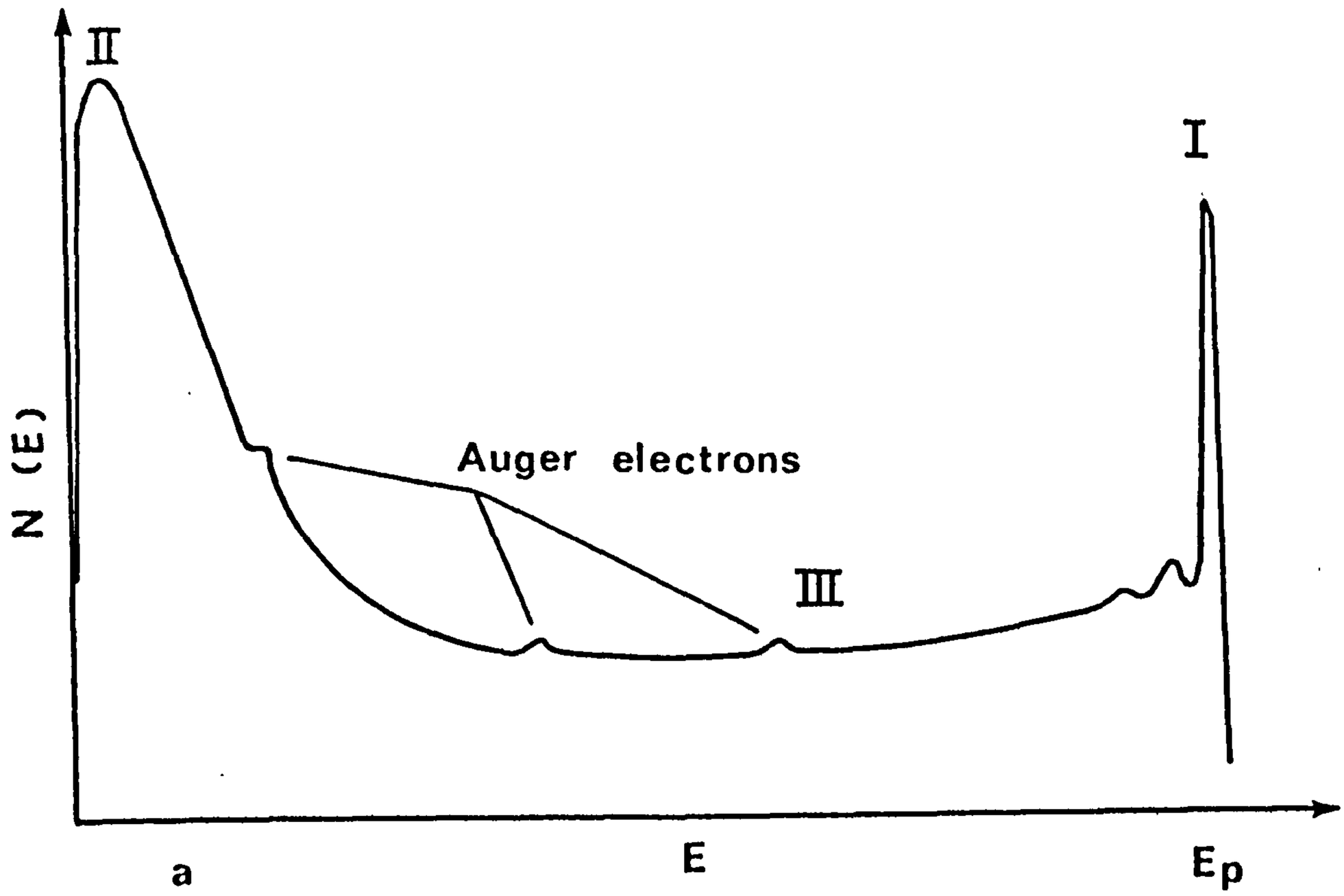

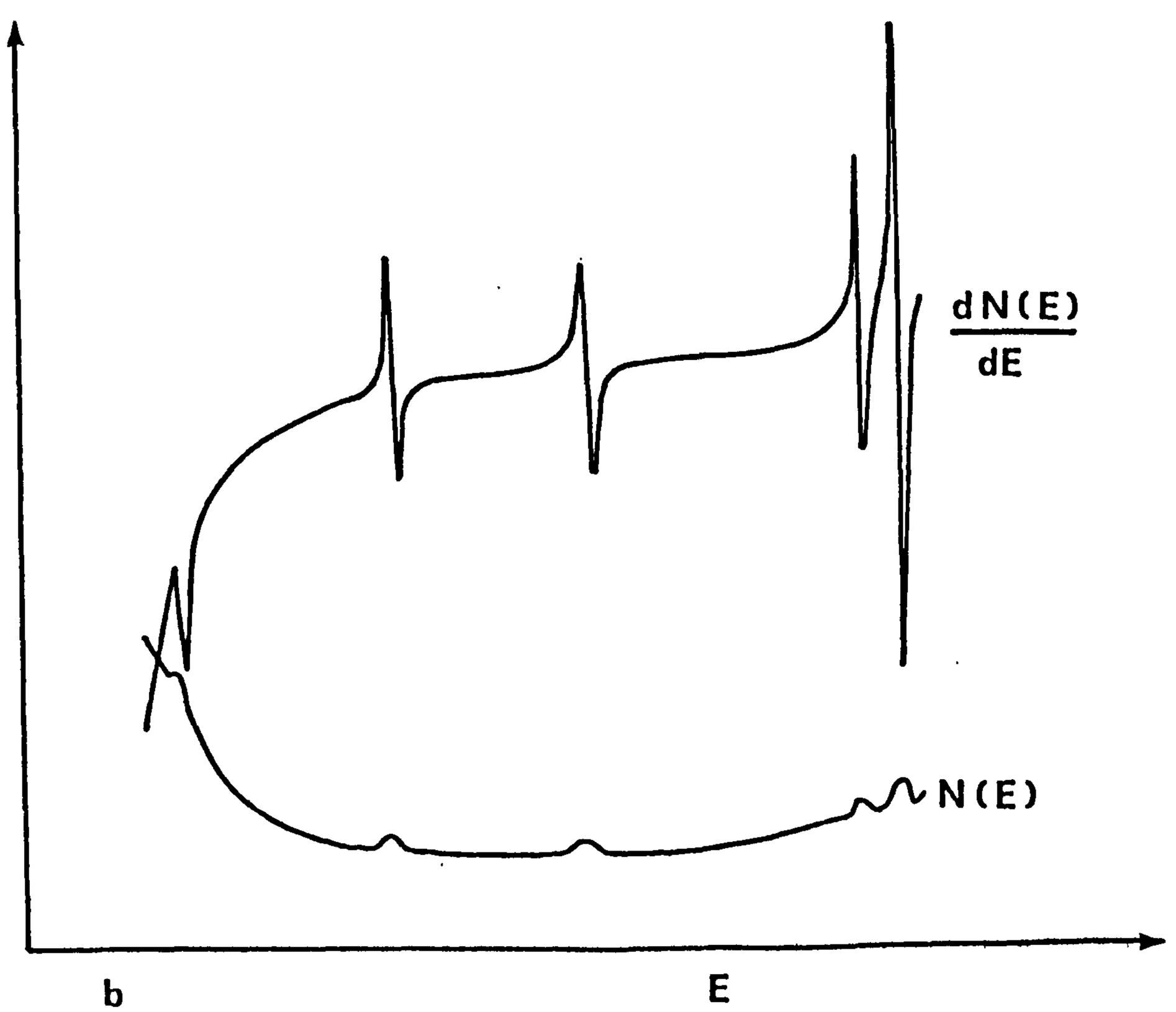

Fig. 1.1 (a) The secondary electron spectrum.
(b) The effect of differentiation.

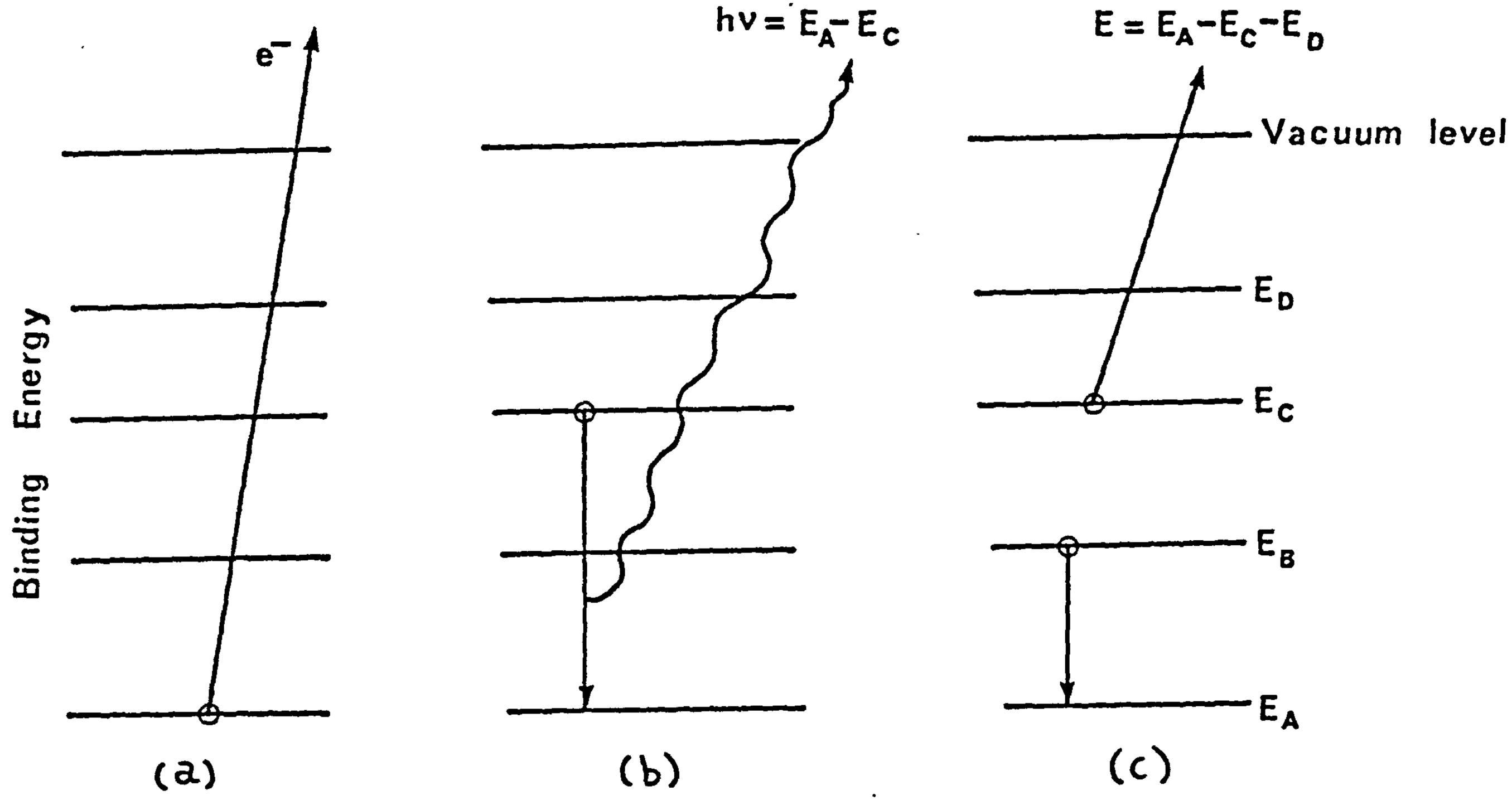

Fig. 1.2 The Auger process

(Figure 1.2a). An electron from level C with binding energy E_C can drop to fill the vacancy at level A. As a result of this process, an energy $(E_A - E_C)$ would be liberated. This can be emitted as an X-ray (Figure 1.2b), or can be transferred to an electron in another level, e.g. level D, which could be emitted as an Auger electron. The energy of this electron will be approximately

$$E_{ACD} = E_A - E_C - E_D \qquad (1.1)$$

relative to the vacuum level, with E_X being the binding energy of the level X. The electron can escape from the atom only if the energy $(E_A - E_C - E_D) > 0$ and is called an ACD Auger electron, with A having the greatest binding energy.

The use of the X-ray terms K, L, M, N, ... is an accepted nomenclature for labelling the different levels. In solids if one or both of the final state holes are in the conduction band, then it is conventional to use the notation V for labelling these holes e.g. KVV.

1.4 THE AUGER ELECTRON ENERGIES AND LINE SHAPES

In the previous section a first order approximation for the energy of an emitted Auger electron (eqn. 1.1) was given. Such an estimate is inaccurate because the energy required to produce a two-hole final configuration is greater than the sum of the energies required to generate the holes singly. In this case, once the hole has been created in the C shell, the D shell becomes more tightly bound owing to the absence of the repulsion of the removed electron. Based on a suggestion by Burhop (2), Chung and Jenkins (8) have allowed for this effect for an Auger transition of the type E_{ACD} and for atoms of atomic number Z,

$$E_{ACD}(Z) = E_A(Z) - \tfrac{1}{2}\left\{E_C(Z) + E_C(Z+1) + E_D(Z) + E_D(Z+1)\right\} \qquad (1.2)$$

where $E_X(Z)$ is the ionisation energy of the level X in the atom under investigation with atomic number Z, and $E_X(Z+1)$ is the ionisation energy of the same level in the next element in the periodic table with atomic number $(Z+1)$. This formula has a typical accuracy of the order of 5 eV. Matthew (9) showed that a higher accuracy could be obtained by using the binding energy of the positive ion $E_D(Z+1)^+$ instead of the neutral level $E_D(Z+1)$.

In AES the line shape and width of an Auger peak have a strong dependance on the target and its chemical state. For example, in free atoms the broadening of the peaks is due to the transition rates of the vacancies involved i.e. life-time broadening. In this case, the peaks appear sharp and narrow above the background. As one goes into atoms in solids, the effect will depend in addition to life-time broadening, on the chemical environment which may cause additional broadening, shifting and/or modification in the shape of the peaks. For example, atomic fine structure is due to the removal of degeneracy of orbitals by spin alignment or to localised valence hole-hole interactionsin solid state. The peak shape is also affected by the density of states of the valence band and has a dependance on the bonding type i.e. ionic crystals, metals, semiconductors or adsorbed atoms (9, 10). Chemical shifts and plasmon losses or gains are due to many body interactions, with the first being a result of the interaction of the atom and the matrix while the second is due to the escaping electron (11).

1.5 THE AUGER YIELD FROM SOLIDS

The parameters that determine the collected Auger electron current from a monolayer film adsorbed on the surface of a uniform substrate can be given as follows (Bishop and Rivere (12)): consider a primary electron

beam of electrons I_b , and energy E_p incident on a flat uniform solid with density N atoms/c.c . The electron beam makes an angle Θ with the target normal Figure (1.3). The collected Auger current I_A into a solid angle Ω , assuming isotropic emission, is given by

$$I_A = I_b \, N \, \frac{\Omega}{4\pi} \, (1 - \omega) \, r \sec\Theta \, \Phi(E_p , E_A) \, \tau \, \varepsilon \qquad (1.3)$$

where ω is the fluorescence yield and is almost negligible at low energies, r is the ratio of the emitted Auger electron current to that caused directly by the incident electrons and is conventionally called the Auger backscattering factor, $\Phi(E_p , E_A)$ is the ionisation cross section of the level E_A , τ is the Auger electron escape depth, and ε is the transmission efficiency of the analyser used. In the following sections a brief discussion of the various parameters of the above equation will be given.

1.5.1 The Escape Depth of the Auger Electrons

Auger electrons are generated everywhere in the solid within the penetration depth of the primary electron beam. This depth can be of the order of a few microns but only those Auger electrons escape which can reach the surface without further energy loss. The most widely used energy range for AES is 20 - 2000 eV where Φ and i_b can be large, and, in this range the mean escape depth is only 0.4 - 2 nm (13), a property that makes AES a surface sensitive technique.

The problem of the escape depth of the Auger electrons, or more precisely the inelastic mean free path (IMFP) of electrons in the energy range 20 - 2000 eV, has received considerable attention because of its use in quantitative analysis. Several techniques have been used for its measurement (14 - 16). Figure (1.4) represents a collection of experimental data acquired from a wide range of material and at different electron

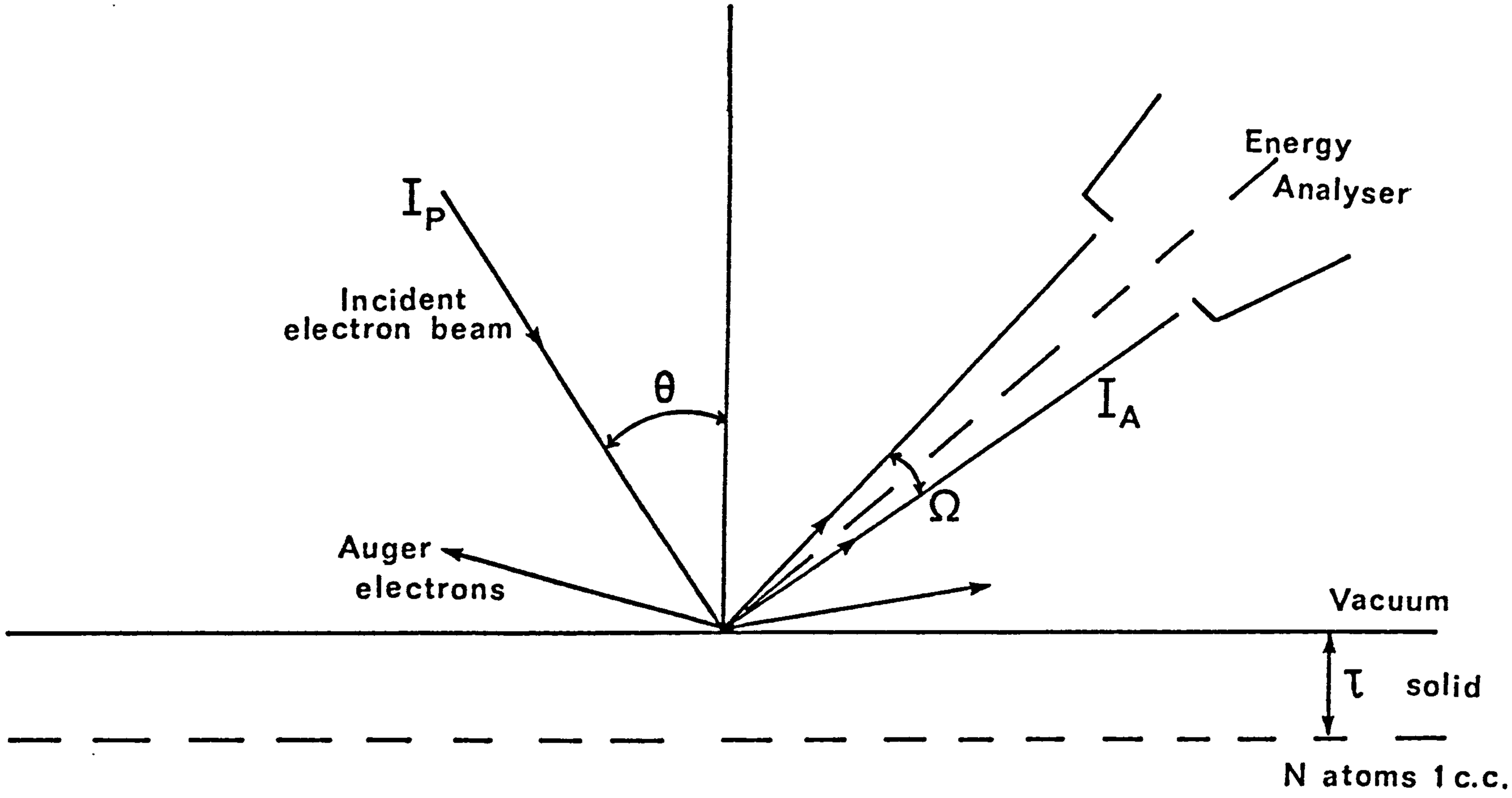

Fig. 1.3 The Auger electron current generated by a beam of electrons I_p within an escape depth τ .

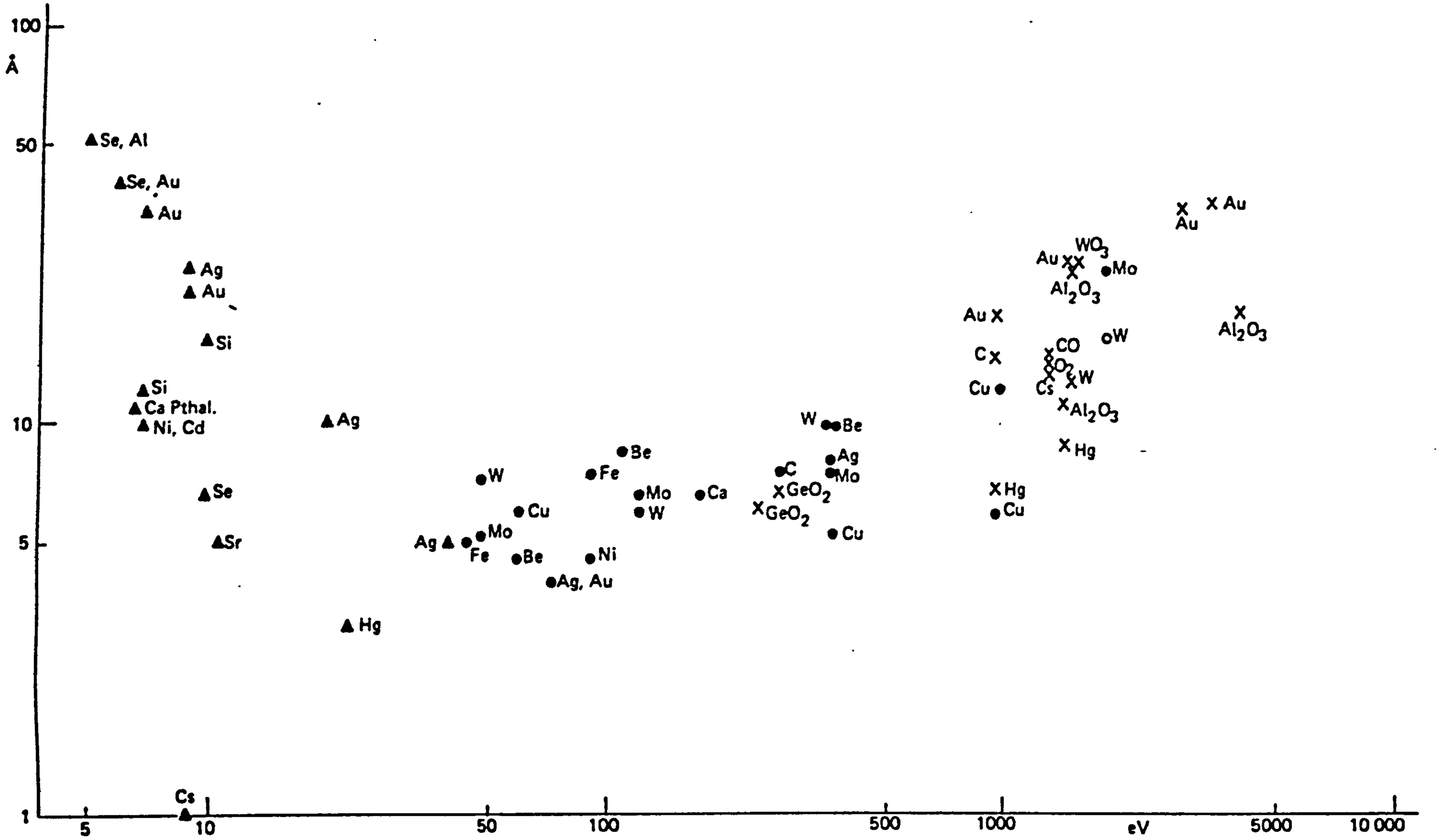

Fig. 1.4 The variation of the inelastic mean free path with electron energy (adapted from [14])

energies (14).

Several attempts have been made to relate the IMFP shown in Figure (1.4) to a universal curve (13 - 17). Recently, Seah and Dench (15) have analysed all the available experimental data to produce a set of empirical formulae for the IMFP of electrons in a given solid within the energy range 1 - 10000 eV. Using least squares fit methods Seah and Dench found that the data follow a universal curve which for elements with energies in the range 1 - 10000 eV is described by

$$\lambda_m = \frac{A}{E^2} + B\,(a\,E)^{\frac{1}{2}} \text{ monolayers} \qquad (1.4)$$

where a is the monolayer thickness in nanometers and E is the energy of the escaping electron in eV.

For pure elements A = 538 and B = 0.41, while for inorganic compounds A = 2170 and B = 0.72.

The overall root mean square (RMS) scatter factor is 1.59 but reduces to 1.36 for energies above 150 eV.

For organic compounds they found the least square scatter to occur for

$$\lambda_d = \frac{49}{E^2} + 0.11\,E^{\frac{1}{2}} \text{ mg m}^{-2} \qquad (1.5)$$

with an RMS scatter factor of 2.1.

In the case of gases, the authors recommend the use of the nearest equivalent of the above equations.

1.5.2 The Ionisation Cross-section

The ionisation cross-section is the function that relates the efficiency of ionisation of a netural atom by electrons of energy E_p, to the flux of incident electrons. Several attempts have been made to obtain a universal formula for the ionisation cross-section. The most widely

used expressions are those due to Worthington and Tomlin (18) and Gryzinski (19). The expression due to Worthington and Tomlin is an empirical formula based on a modified Born approximation, while Gryzinski's expression is based on a semi-classical model. Powell (20) has reviewed several other experimental and theoretical expressions that have been used.

The above two expressions have the general form of

$$\Phi\ (E_p\ ,\ E_A) = \frac{A}{E_A^2}\ F(U) \qquad (1.6)$$

where $U = \frac{E_p}{E_A}$, E_A is the binding energy of the electron in the level being ionised. F(U) is a function that describes the dependence of the cross-section on the incident energy and A is a constant in the Gryzinski cross-section and varies with the principal quantum number of the excited level in the Worthington and Tomlin model. Figure (1.5) shows the variation of the function F(U) with U for the two models described above. This figure also compares the theory with experimental data obtained by Gallon (21) for Si and Ag . The cross-section is shown to rise sharply in both models from the threshold to a maximum at nearly U = 2.6 and 3.3 for the Worthington and Tomlin and the Gryzinski models respectively and then decrease more slowly. The experimental data tends to follow the Gryzinski model more closely than the Worthington and Tomlin model, but the general trends are almost the same for both. Smith et al (22) have shown that a universal curve is a reasonable approximation except for levels having high angular momentum. Vraaking and Meyer (23) have found that for the k-shells, the cross-section scales as E^{-2} and for L_{23} shells it has an $E^{-1.6}$ dependence.

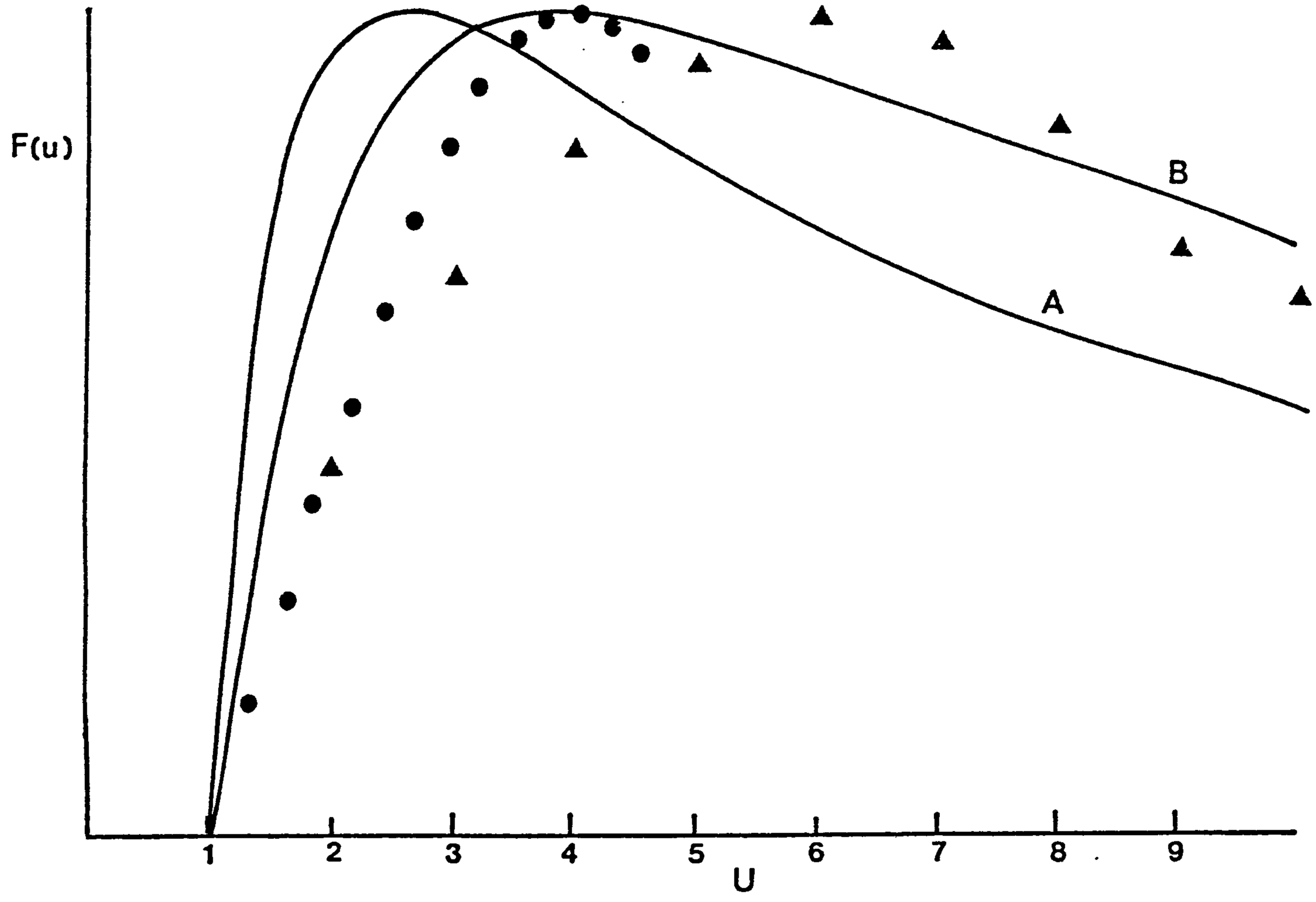

Fig. 1.5 The dependence of the ionisation cross section Φ on reduced energy U. (A) Worthington and Tomlin (18). (B) Gryzinski (19). (▲) Silicon, (●) Silver. After (21).

1.5.3 The Backscattering Factor r

In addition to the direct effect of the incident electrons, the Auger yield is enhanced by elastically reflected electrons and those loss electrons with energies greater than E_A. Bishop and Rivère (12) accounted for this positive contribution by a backscattering factor r (r > 1)

$$r = 1 + \frac{I_B}{I_p}.S. \qquad (1.7)$$

where I_p, $I_{B.S.}$ denote the Auger signal intensities due to primary and backscattered electrons respectively. The value of r depends upon the material, the primary electron energy and its angle of incidence.

Considerable attention has been paid recently to quantitative AES and hence the enhancement of the Auger yield by the backscattered and energetic secondary electrons. Monte Carlo techniques used in the EMPA and SEM have been extended to AES: (12, 106,197).

In the present work (Chapter 5) r has been estimated theoretically for a number of materials and at different energies using MC techniques. The agreement with other published data(197) at 10 keV is satisfactory (i.e. 10 - 15%) because of the different models used in the calculation.

Hall and Morabito (24) have used an empirical relation between r and the atomic number of the material suggested by Reuter (25)

$$r = 1 + 2.8\,\eta\left(1 - 0.9\,\frac{E_b}{E_p}\right) \qquad (1.8)$$

where η is the backscattering coefficient and E_b is the binding energy of the excited electron. An agreement to within a factor of X2 with low energy measurements (< 3 kV) (21) is achieved.

Several experimental methods for measuring r have been proposed (21, 23, 26). Figure (1.6) shows r values obtained by Smith and

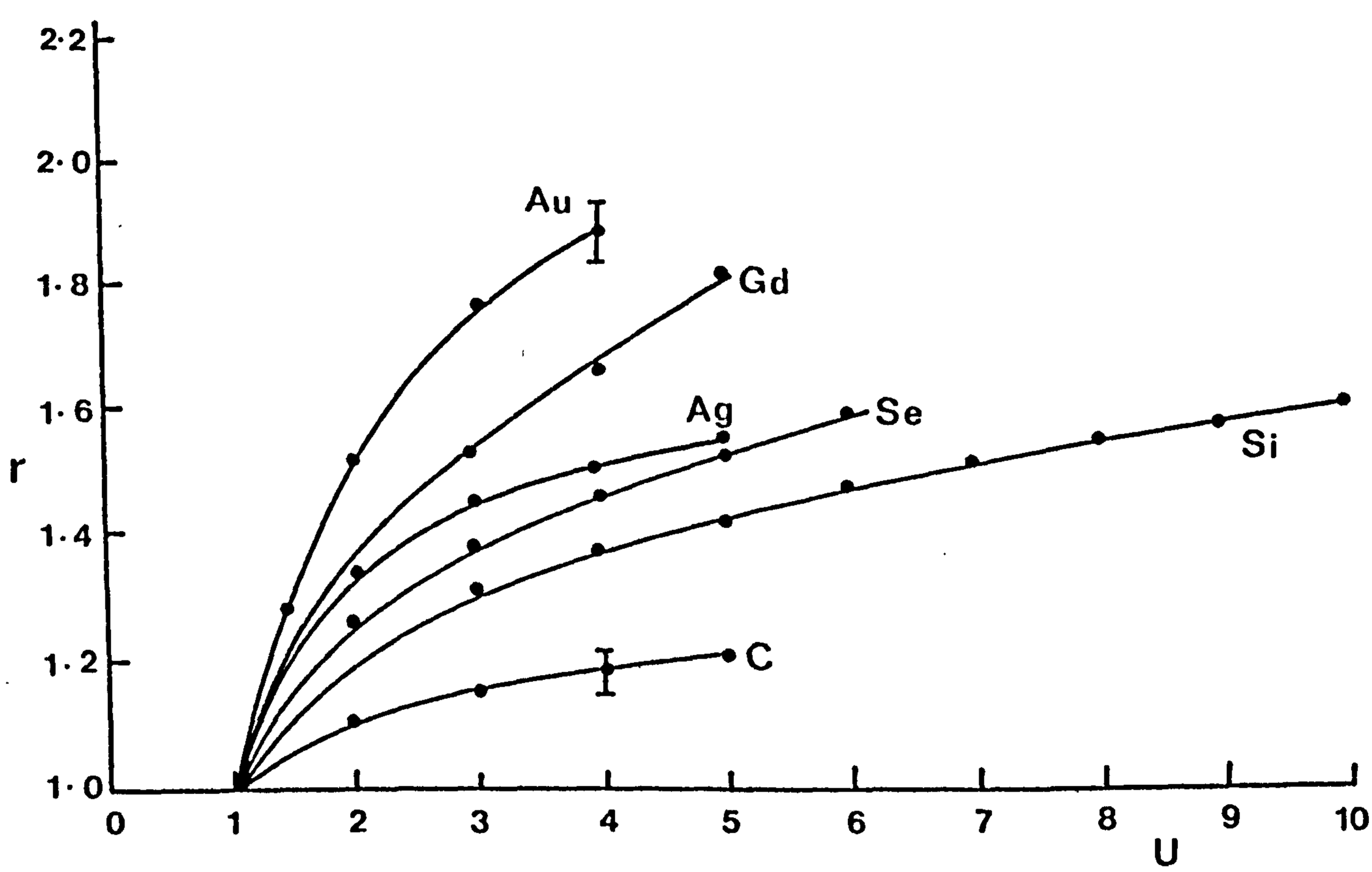

Fig. 1.6 The backscattering factor r as a function of U at low energies (after Smith and Gallon (27)).

Gallon (27) for a number of materials. To the author's knowledge, no experimental data is available at present in the energy range 10 - 30 keV, where most SAM instruments are used. This is because of the difficulty of extending existing methods such as that by Gallon (21) which is based on the LEED optics, to the high energy and low beam current region of SAM.

1.6 ELECTRON SPECTROMETERS

The criterion for an AES analyser should be high transmission, the subtended solid angle Ω as large a fraction of 2π steradian as possible, and good energy resolution with ΔE considerably smaller than the width ΔE_A of the Auger peak. Magnetic and electrostatic energy analysers have been used separately or in combination as Auger analysers (28). Siegbahn et al (29) have used magnetic analysers, but these are big in volume and expensive to make. Electrostatic analyers on the other hand are widely used in AES, for their simplicity in terms of construction and operation. Electrostatic analysers can be divided into two groups, the dispersive analysers and the retarding field analysers. Electrostatic analysers will be briefly reviewed here and the reader is referred to the original publications for more details (30 - 32). In addition, a comparison between analysers that are widely used in SAM will be given in Chapter 2, while a description of the analyser used in this work will be given in Chapter 3.

1.6.1 The Retarding Field Analyser (RFAs)

Figure (1.7) depicts the retarding field analyser, an instrument devised for Low Energy Electron Diffraction (LEED). It consists of three (or four) spherical section grids made of fine stainless steel mesh of about 80% transparency. The specimen is placed at the centre of curvature

of the spherical grids and usually kept earthed. The first grid also is kept earthed, allowing a field free region around the specimen. If grid two is held at a potential -V, then all electrons with kinetic energy E > eV will reach the third grid which is also held at earth potential. These electrons are then accelerated to the collector which is normally held at +250 volts to prevent the loss of secondary electrons. So the output of the analyser which is the current flowing to earth through the collector for electrons of energies greater than E will be

$$\int_{E}^{E_P} N(E)\, dE \qquad (1.9)$$

where N(E) is the electron energy distribution.

As mentioned earlier (section 1.2), the energy distribution is differentiated in order to reduce the background effects. This is done by superimposing onto the analysing voltage a small AC modulation voltage (2 - 10 Vrms) with a frequency of the order of 1 - 10k Hz. Assuming a gaussian Auger peak of standard deviation σ, and a modulating voltage ($k \sin \omega t$), Taylor (30) derived an expression for the current in the first and second harmonics given by

$$i(E) = i_A/(2\pi\sigma)^{\frac{1}{2}} \exp(-E^2/2\sigma^2) \qquad (1.10)$$

where i_A is the collected current and E is the analysing energy. For a full discussion of the use of LEED optics as an Auger spectrometer see reference 30. The resolution of the instrument ($\Delta E/E$) is typically 2.5% This can be improved to about 0.5% by the addition of a fourth grid which reduces field penetration to the second grid. The signal to noise ratio of this analyser is low due to the fact that all electrons with energy above the analysing energy E are collected. These excess electrons are an additional noise source to the system. This in fact is the main disadvantage of the retarding field analyser. The popularity of the apparatus

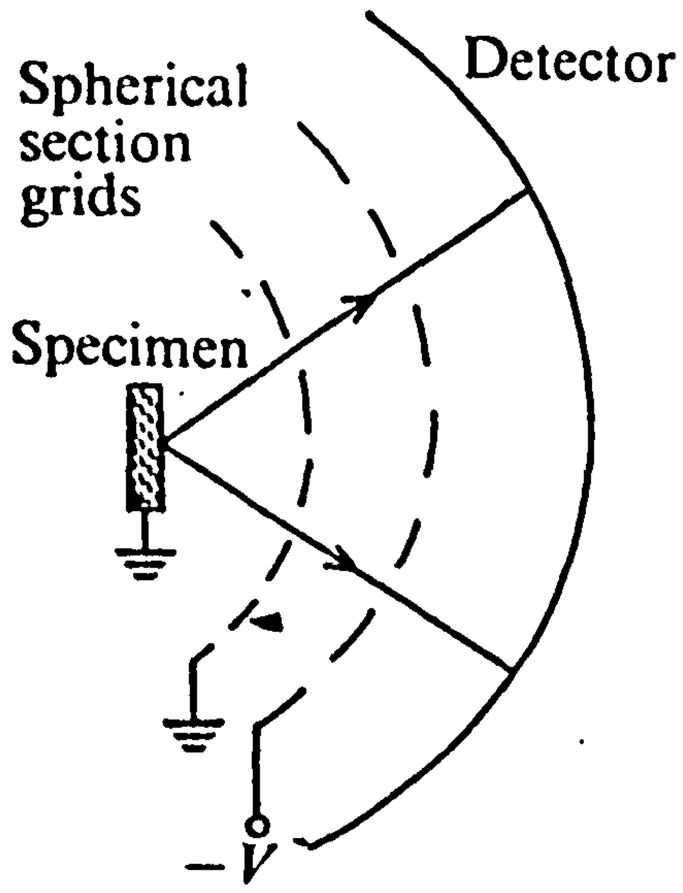

Fig. 1.7 The retarding field analyser (RFA).

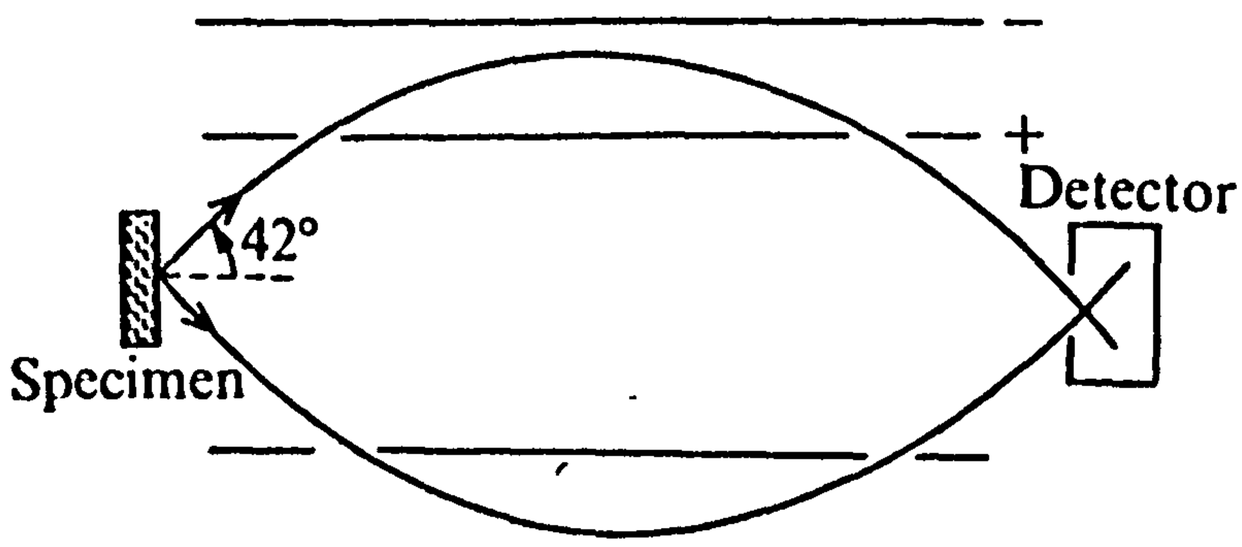

Coaxial cylinders

Fig. 1.8 The cylindrical mirror analyser (CMA).

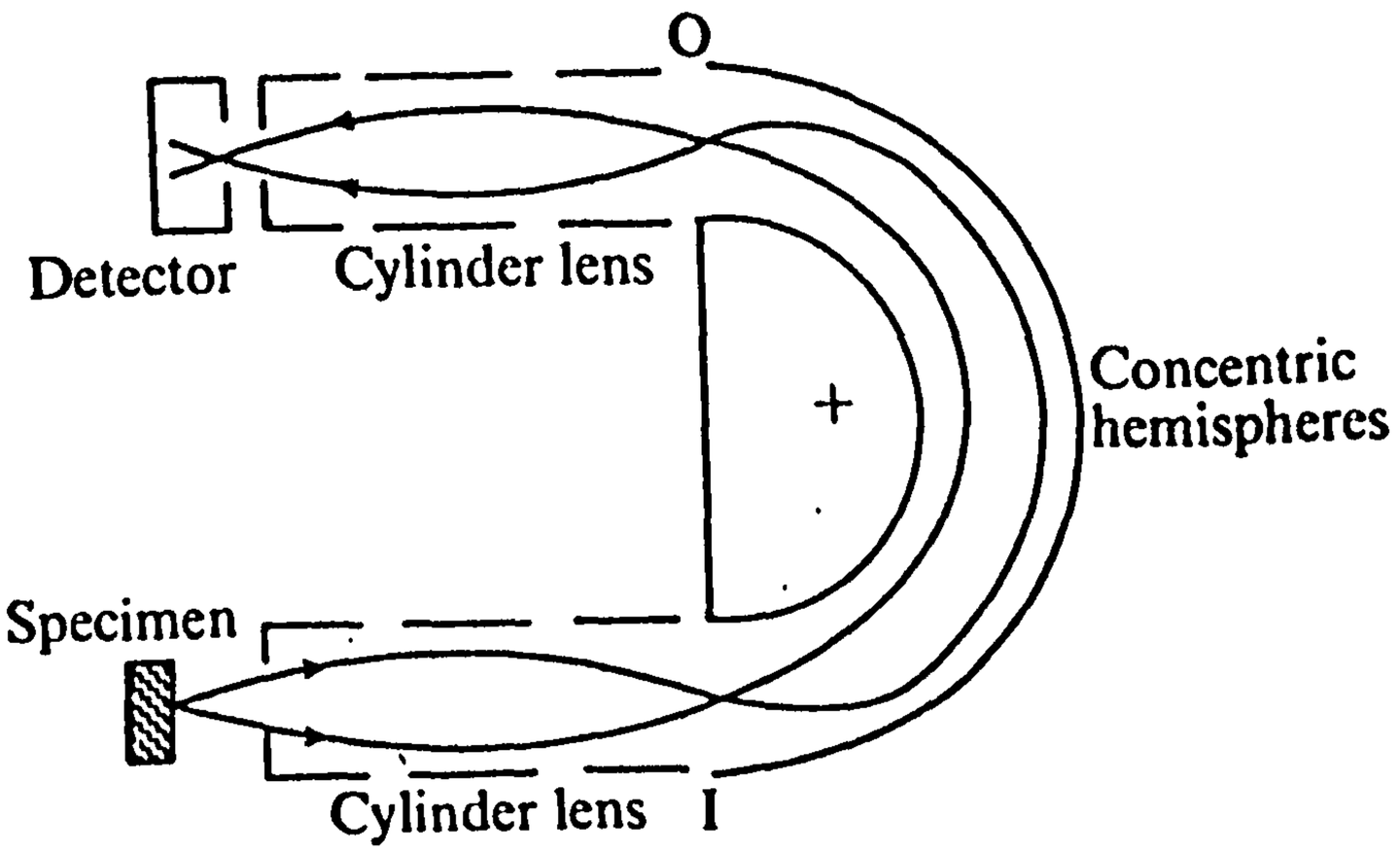

Fig. 1.9 The concentric hemispherical analyser (CHA).

has not dropped yet due to its existence as a LEED analyser and its simplicity.

1.6.2 The Dispersive Analysers

a. The Concentric Hemespherical Analysers, (CHA)

In this group of analysers, only electrons in a narrow band of energies E to E + ΔE are transmitted. This property improves the S/N ratio for the same collected current. Figure (1.9) shows a schematic of the CHA. It consists of two hemispheres of radii R_1 and R_2 which are at potentials V_1 and V_2 respectively. The field between the hemispheres will tend to converge electrons of certain energy from one point at the entrance to a focus at a diametrically opposite point at the exit. If, however, the electrons entering the hemispheres are made to retard through input electron lenses, then the product of the entrance area and entrance solid angle, so called the "entendue", can be increased without degrading the analyser resolving power. The output of the analyser is of the form N(E). By applying a modulating voltage of frequency f at the sample or the electron lenses and detecting the f component of the collected current, the differential distribution N'(E) is obtained.

b. The Cylindrical Mirror Analyser, (CMA)

A schematic of the CMA is shown in Figure (1.8), which consists mainly of two co-axial cylinders. The inner cylinder is normally grounded and has two cylindrical gridded apertures suitably positioned along its length. A negative potential Va is applied to the outer cylinder, so secondary electrons with energy E from the specimen entering the first aperture are refracted towards the second aperture and come to a focus. The addition of an annular slit at the focal position will allow only electrons with energy ΔE around E to reach the collector. The current

reaching the collector will be

$$I(E) = G\ \Delta E\ N(E) \qquad (1.11)$$

where G is a constant for the geometry used. Again, the output of the analyser will be of the form N(E). The same voltage modulation technique discussed earlier can be applied to the CMA to obtain the differential of the energy distribution N'(E).

The CMA has been the most popular electron spectrometer in the field of AES over the last decade because of its simplicity in construction and operation compared to the CHA and the higher SNR with respect to the RFA. Recent reports on the use of the instrument for quantitative AES analysis have shown big discrepancies in measuring kinetic energy and intensity ratios of Auger peaks (33, 34). The reasons for such difficulties is the lack of calibration methods and operating procedures for the instrument. In particular the positioning of the specimen on the optical axis of the spectrometer, the change of the analyser work function as a result of deposited material on its walls during ion sputtering and the inadequate magnetic shielding particularly with low energy electrons are some of the technical problems encountered.

1.7 METHODS OF EXCITING AUGER ELECTRONS

Auger electrons can be generated by different sources of which electrons and X-rays are the two most widely used. Electrons however are more favourable than X-rays. The reason is that high flux electron beams with currents of up to 100 μA and energies ranging from several electron volts up to 5 keV are easily obtained. The ability to focus and deflect electrons makes the use of electrons more convenient by assisting the positioning of an electron spot on any part of the sample. In addition

electron sources are cheaper and simpler to construct than X-ray sources in this energy range.

Another factor that determines the choice of one source with respect to another for a particular application is the ionisation efficiency. For example, conventional X-ray sources (Mg K_α , Aℓ K_α) have relatively high photoionisation cross-sections for binding energies a few hundred volts below the exciting energy, but are relatively inefficient ionisation sources for levels of binding energy of a few hundred electron volts (35). In spite of the fact that the photon fluxes of these sources are smaller than the electron fluxes readily attainable from electron guns, photon sources appear to give superior Auger spectra in the energy range to the exciting photon energy. The reason for this observation is that electron sources lead to high secondary electron backgrounds due to primary electrons suffering multiple loss; the electron beam excited spectra have inferior signal to background characteristics and, since the shot noise in the signal is determined by the signal plus background, much of the advantage of the high electron fluxes is lost.

At lower Auger energies ($\lesssim$ 500 eV) the photoionisation cross-sections from conventional sources fall off, while the electron ionisation cross-sections increase (particularly if the energy of the electron is adjusted to ~4 times the ionisation threshold). This makes electron beam excitation superior to excitation by the conventional photon sources in the highly sensitive regime below 300 eV.

An alternative source that has not been used for the excitation of Auger electrons, to the author's knowledge, is synchrotron radiation. Synchrotrons and their associated storage rings are high flux continuum sources with a typical beam flux of the order of 10^{12} - 10^{14} photons/sec/eV/m rad/m rad. Matthew and El Gomati (36) have suggested the use of unmonochromatized synchrotron radiation as an alternative to electron

beams for the excitation of low energy Auger transitions. Using a figure of merit incorporating the ionisation cross-section and the source's flux they found that unmonochromatized radiation is about 10X - 1000X more sensitive than an electron source for the excitation of L and K shell Auger transition. Such a source should be useful for the analysis of small concentrations of impurities at surfaces.

1.8 THE USE OF AES FOR CHEMICAL ANALYSIS

Lander suggested in 1953 the use of Auger electrons for surface chemical analyses, but his suggestion was not realized until the introduction of the electronic differentiation technique to the electron energy distribution by Harries in 1968. Since then AES has been a valuable analytical tool in areas of research and industry where the chemical composition of surfaces is of importance, both from the qualitative and quantitative points of view. A brief introduction to some areas where AES has been applied will be given below. Full description of these can be found in the relevant papers.

1.8.1 Qualitative Analysis

Surface cleanliness has been one of the most extensive applications of AES. For example, conventional methods for cleaning semiconductor surfaces, such as silicon, which is used for the fabrication of inte grated circuit devices involved degreasing, chemical etching in HF acid and further washing. Analysis by AES showed a large carbon peak and smaller peaks indicating the presence of oxygen, Sulphur and Phosphor us on the surface. Gallon and Matthew (7) showed that flashing the Si to 1100° C for 15 sec followed by annealing to 600° C for 10 min led to the disappearance of all except traces of phosphorous and carbon.

Since the demonstration by Weber and Peria (6) of using existing LEED optics for the detection of Auger electrons, AES has been an important complementary technique in LEED studies. Using AES has shown surfaces that were previously considered clean because of their good (1X1) LEED patterns to contain many impurities (37).

The segregation of impurities at surfaces and particularly at grain boundaries is another interesting application. For example, the formation of an ordered structure as observed by LEED can be the result of diffused impurities to the surface rather than reconstruction of the clean surface (38).

1.8.2 Quantitative Analysis

The use of AES in quantitative analysis has not been on the same scale as in qualitative analysis due partly to the lack of well established methods, because of the developing nature of the technique, but mainly due to the uncertainties involved in the measurement of the various parameters that constitute the Auger current from a sample. Some of these parameters have been reviewed in section 1.5. Quantitative methods used in AES have been recently reviewed by Chattarji (3), and Howell (197).

The accuracy of these methods range between 10 - 50% depending on the complexity of the method and the accuracy of the prepared standards used in the calibration. It should be mentioned that an accuracy similar to other techniques, such as X-ray fluorescence, may not be achieved with AES particularly in the near future because of technical difficulties (e.g. the measurement of Φ , r , and τ). Nevertheless, some information is better than none.

CHAPTER 2

THE SCANNING AUGER ELECTRON MICROSCOPE (SAM)

2.1 INTRODUCTION

The rapid recognition of AES as a technique for surface chemical analysis with high sensitivity suggested its combination with the scanning electron microscope (SEM). This was mainly to take advantage of the fine electron beam of the SEM to obtain spatially resolved chemical information. The technique is called the scanning Auger electron microscope (SAM) and its philosophy is as follows.

In an electron probe, the interaction of the incident electrons with the specimen gives rise to several signals, e.g. secondary electrons, X-rays, backscattered electrons and Auger electrons, to name but a few. The collection of one of these signals to control the brightness of a spot on a cathode ray tube (CRT) rastered in synchronism with the incident electron beam, is what gives the probe a specific name, e.g. SEM, EMPA or SAM. Hence, SAM is in principle an SEM fitted with an Auger electron detector. However, it differs from the SEM in that chemically specific information is produced by SAM, while the contrast in the SEM image is determined by several factors some of which are topography, atomic number variations and work function variations. The advantage of SAM over EMPA on the other hand is its surface specificity due to the short mean free path of the Auger electron. In fact SAM and EMPA should be looked at as two complementary techniques, with the former yielding surface information while the latter yields bulk information.

In this chapter, the properties of SAM will be discussed from a theoretical point of view, starting with representative examples showing the importance of the technique in the study of scientific and

technological problems. In addition, various techniques that help to obtain quantitative and correct mapping in SAM will be reviewed, (i.e. separating topographical effects, beam current fluctuations in field emission probes, backscattering contribution and chemical diffuseness). Finally, the design philosophy of a UHV high spatial and energy resolution SAM will be defined. These will constitute the specifications of the first instrument designed and built at York.

The principle and present state of SEM have been described by several authors (40, 41) and hence will not be mentioned here.

2.2 WHY SAM?

Before we proceed any further in the description of SAM it is instructive to justify the need for such a technique and particularly the case for imaging, hence the answer to the above question will be two fold. The first is that application of SAM to various problems in Physics, Metallurgy, Chemistry and Electronics has yielded information which could not have been obtained by any other technique.

An early and still active application of SAM is the study of surface and grain boundary segregation. An example of this is given by Seah and Hondros (42) who studied the segregation of Sulphur to inter-granular fracture surfaces of iron-tin alloys. By identifying the grain surfaces which are free of sulphur, the authors were able to test theories of surface segregation and find an additive (Manganese) to eliminate the segregation of sulphur from grain boundaries. Several other examples on the same subject have been reported (43, 44).

Another area of great technological importance where SAM has been applied is micro-electronics, such as fabrication techniques and the identification of impurities that cause failure of integrated circuits

can be monitored (50).

The second part of the above question deals with the importance of imaging, which, as will be seen later, is a long process due to the low level of the Auger signal in comparison with, for example, either the secondary electrons or X-ray signals, being of the order of 10^{-5} of the former and about 10^{-2} of the latter. Although it has been argued that point spectra and line scanning are almost sufficient to extract all the required information with a SAM, recent experience with technologically challenging materials and high resolution instruments suggests that this is not entirely true. The advantages of imaging over line scanning can be summarised as follows:

i) For a quick test to identify the presence of a small percentage impurity (or additive) that segregates to the surface along grain boundaries in low contrast pollycrystalline samples, one would run a line scan across the selected area to be analysed, as schematically depicted in Figure 2.1. Although the presence of the segregant will be detected in this case, the low signal level in addition to it being only one or two points may easily get it confused with the noisy background as shown in (b). On the other hand imaging of the feature, although still with a low level signal, will show a steady but consistant rise of the signal along the boundary as shown in (c). In this way one exploits the ability of the human eye to filter the noise and establish the presence of the chemical and can later average many line scans across the feature for subsequent quantitative analysis, an experiment one would not do in the first place if one was not sure of the presence of that chemical. An illustration of this example is found in the segregation of Zr in Ni Cr Aℓ/0.6% Zr alloys. It was only possible through Auger imaging to identify the presence of

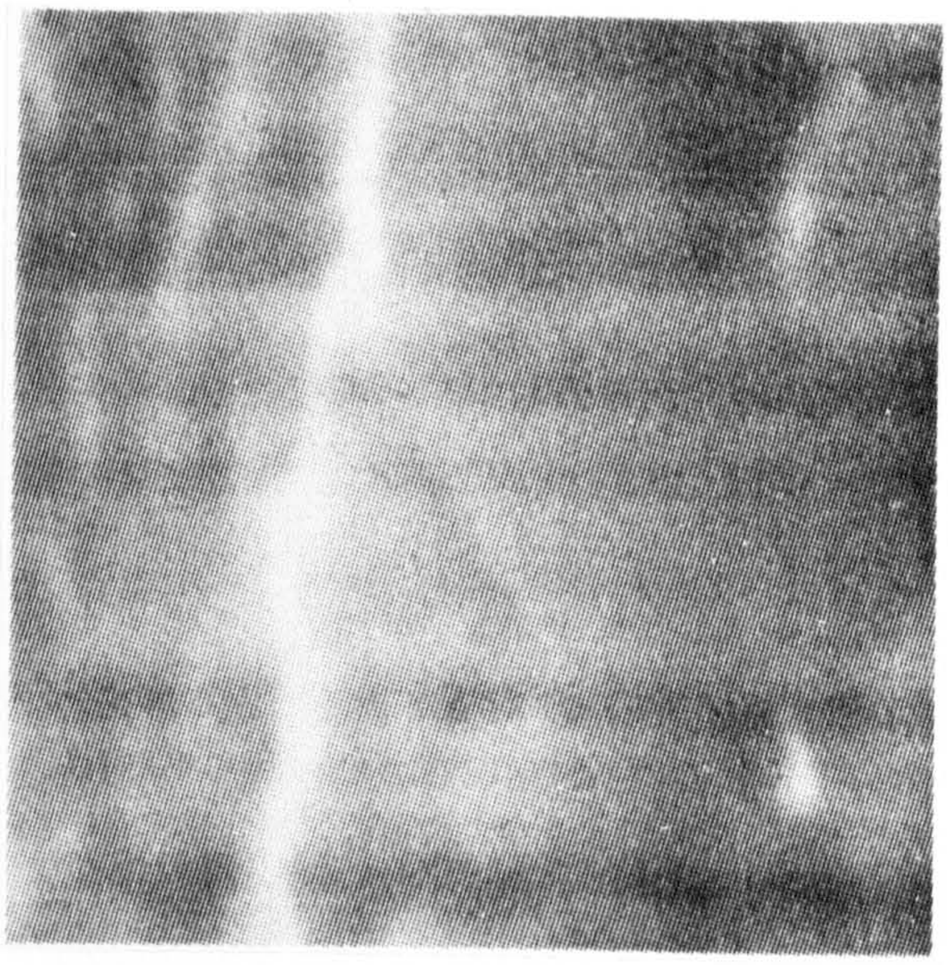

d

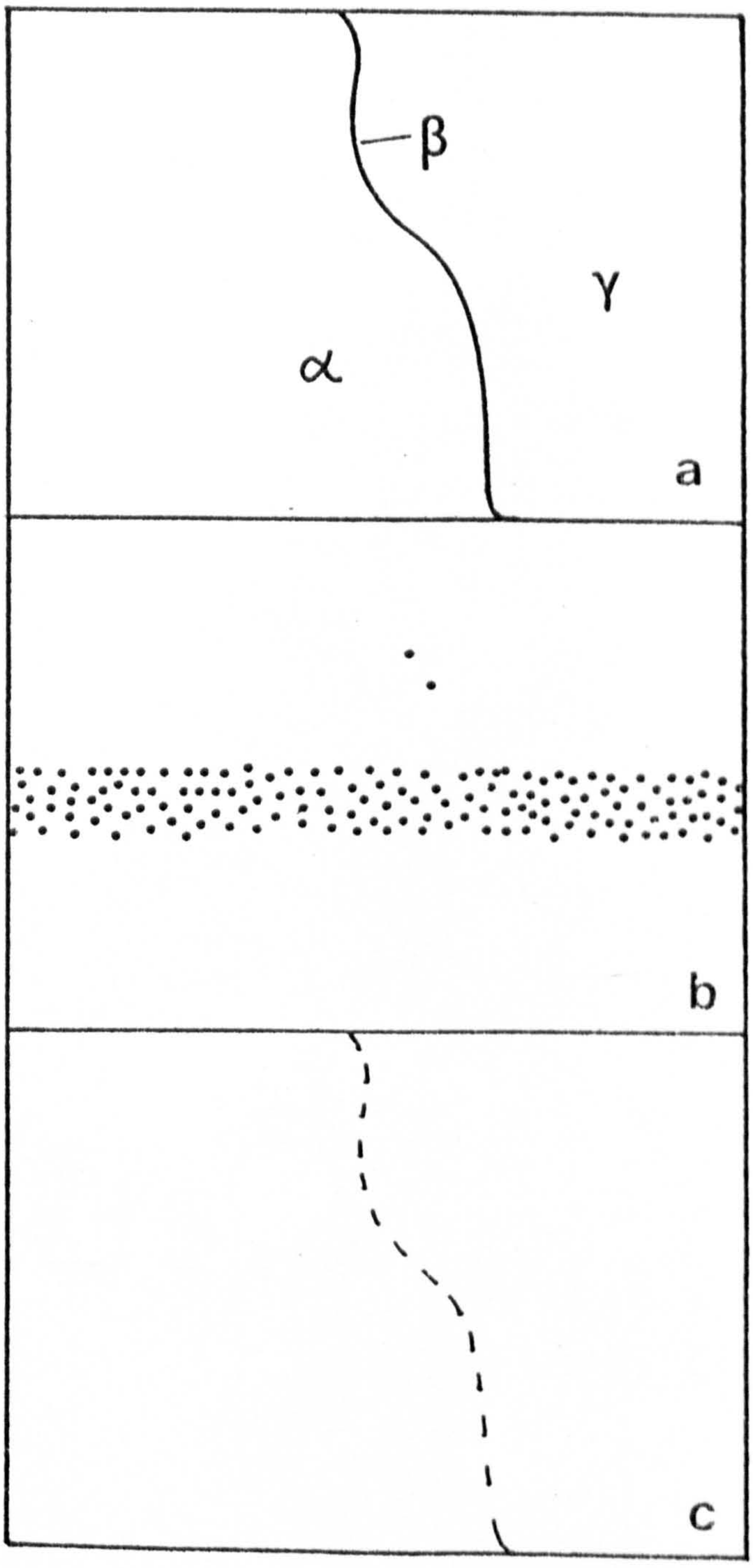

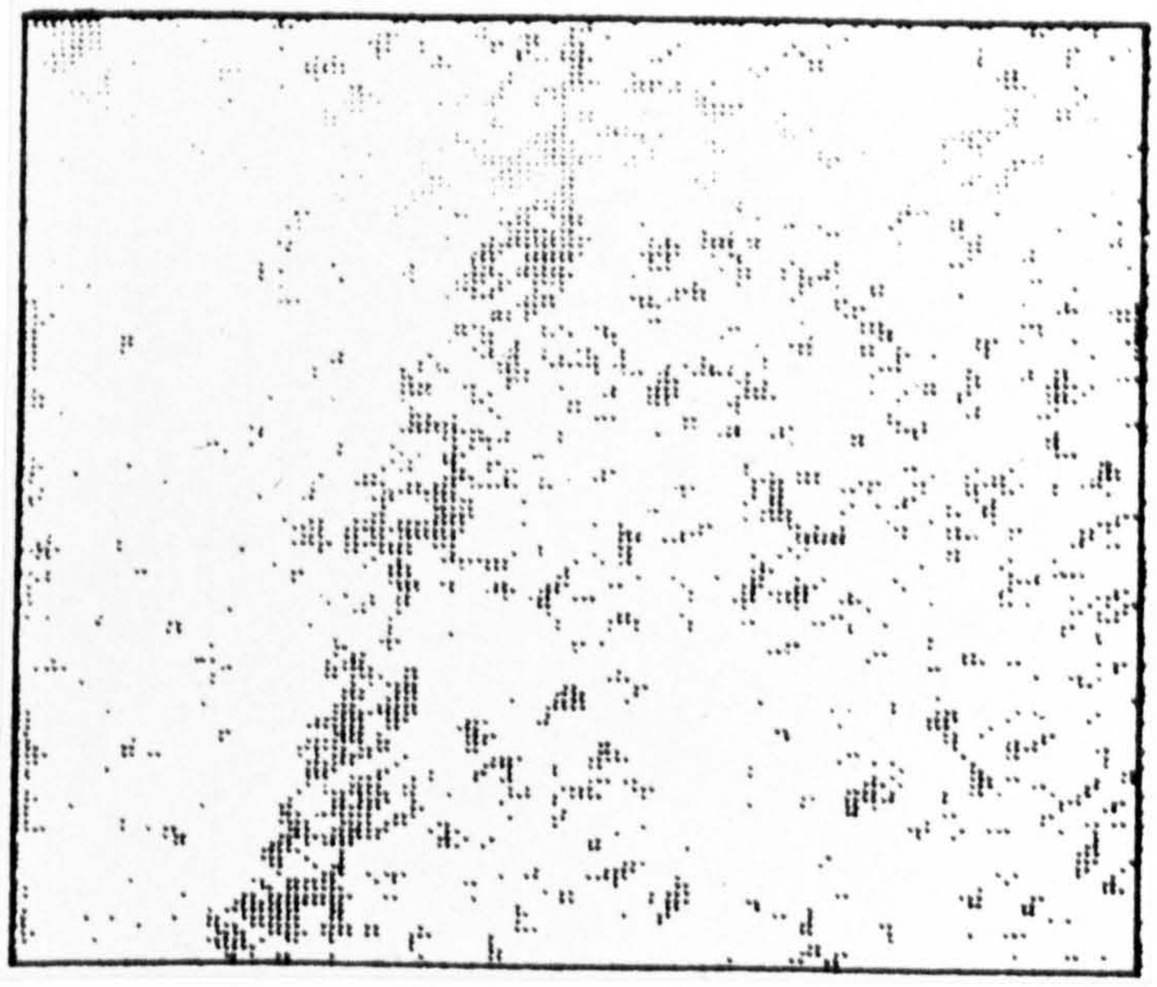

e

Fig. 2.1 The detection of a small percentage impurity (or additive) that diffused out to the surface along grain boundaries. (a) Schematic of SEM area where α and γ are low contrast areas and β is the grain boundary. (b) is an Auger line scan along x in (a), and (c) is an Auger image of the segregated chemical. (d) and (e) illustrate the segregation of Zr in Ni Cr Aℓ - .6% Zr after Larson et al. (45).

the Zr on the surface (45) as shown in (d) and (e).

ii) The time taken to identify spatially the presence of a chemical can be comparable in the two cases, but with more information in the case of imaging. An illustration of this is depicted in Figure 2.2, showing the segregation of Ni to the surface of La_7 Ni_3 specimen. Upon heating the specimen to ~ 700°C -800°C for a few minutes, Ni has diffused out to give an inhomogeneous distribution of the two materials on the surface. Figure 2.2(a) is an SEM micrograph of a selected area, and (b) is a 128 points line scan across the image with 20 m sec dwell time per point. In order to improve the S/N and allow any surface inhomogeneity to be detected, line (c) was collected in about 2 minutes (512 points with 200 m sec per point). As can be clearly seen the large La feature on the left hand side can be easily identified but the smaller one on the right hand side can still be confused with the noisy background. For further improvement of S/N an average of 4 similar scans to that in (c) is presented in (d) with a total collection time of about 8 minutes. On the other hand, an La Auger image of the same area with 128 x 128 pixels and 20 m sec/pixel as shown in (e) can be collected in about 6 minutes and clearly shows the two La features and with an estimate of their spatial distribution that can be correlated with the SEM image shown in (a).

iii) Another advantage of imaging is demonstrated in the case of high resolution instruments in the presence of specimen drift (usually due to stage stability). The information in this case is not lost but merely misplaced. Figure 2.3(a) is a low magnification example of this effect taken during development of the second instrument built at York and identified as stage instability.

Furthermore, at high resolution averaging of several scans to improve

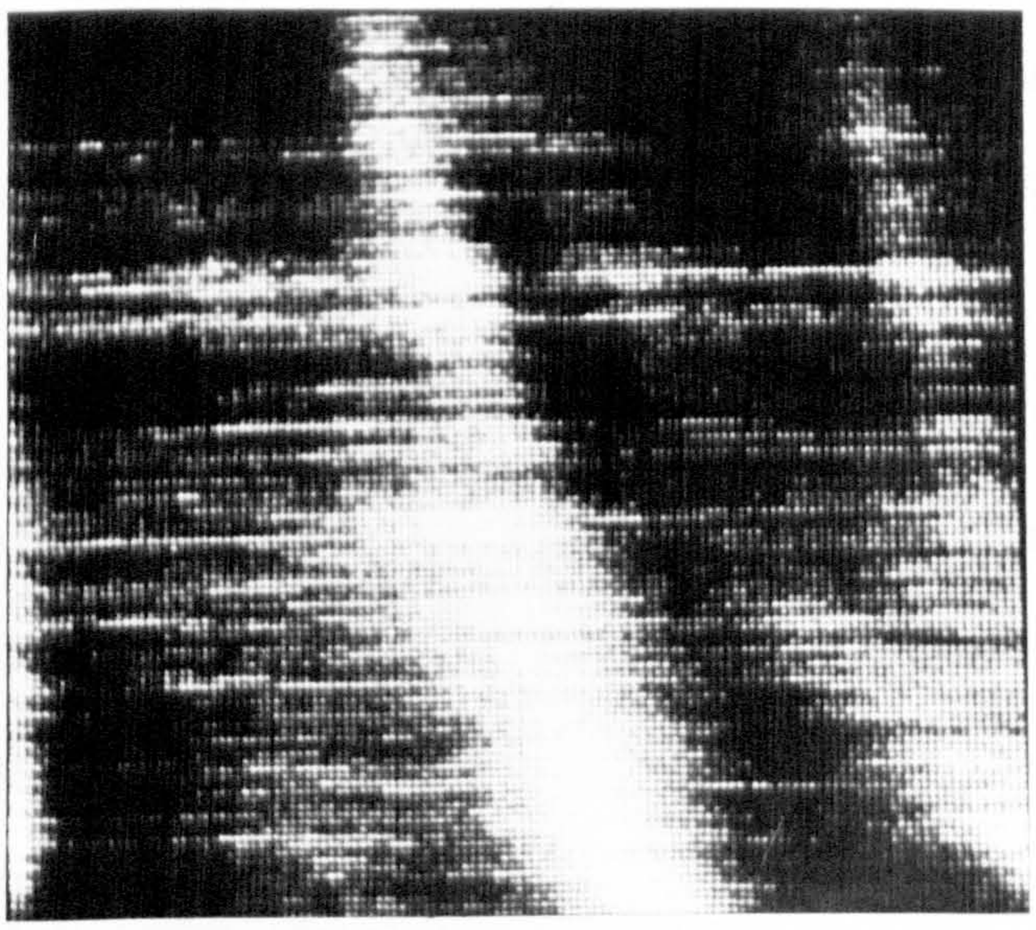

a

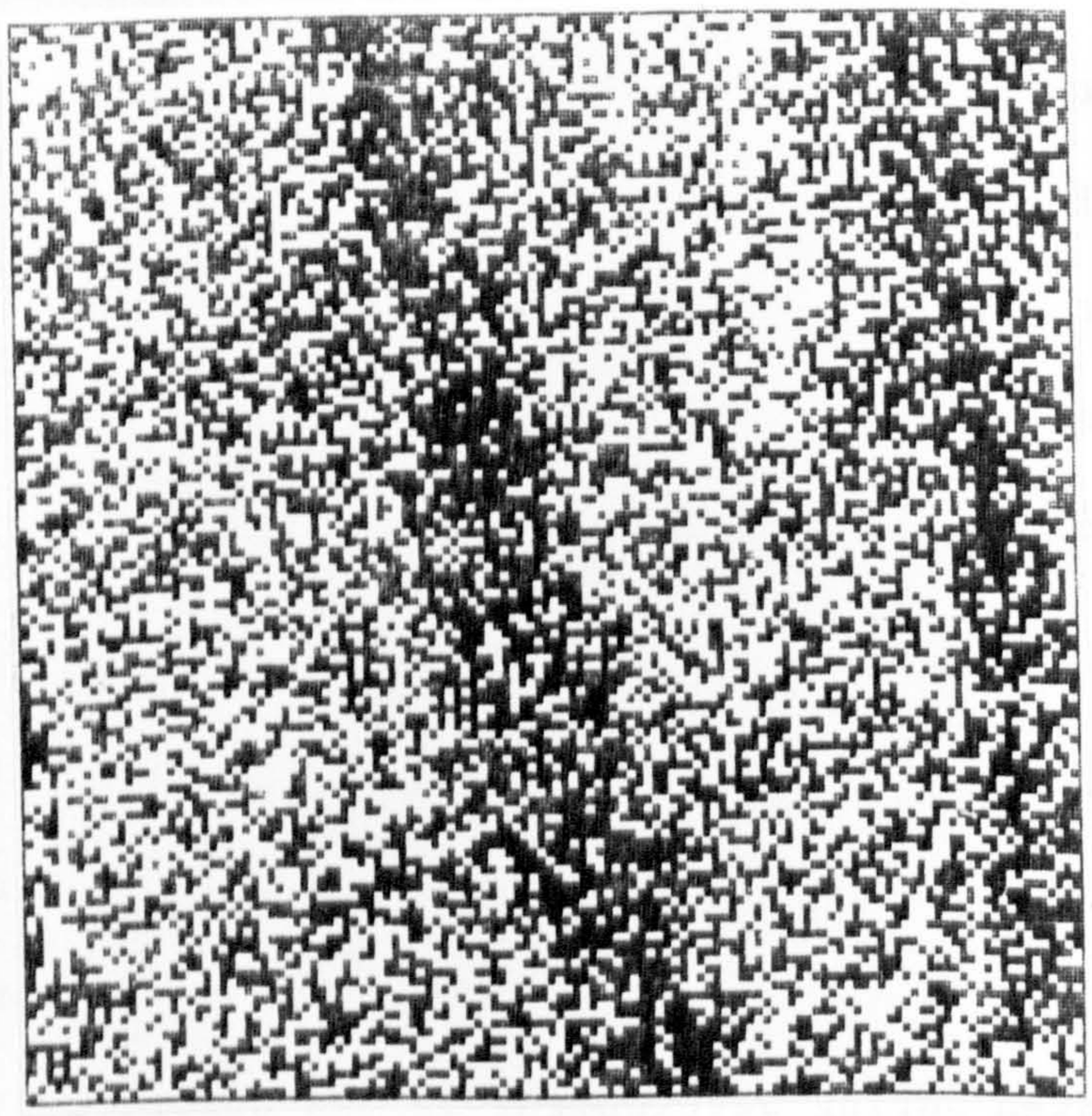

e

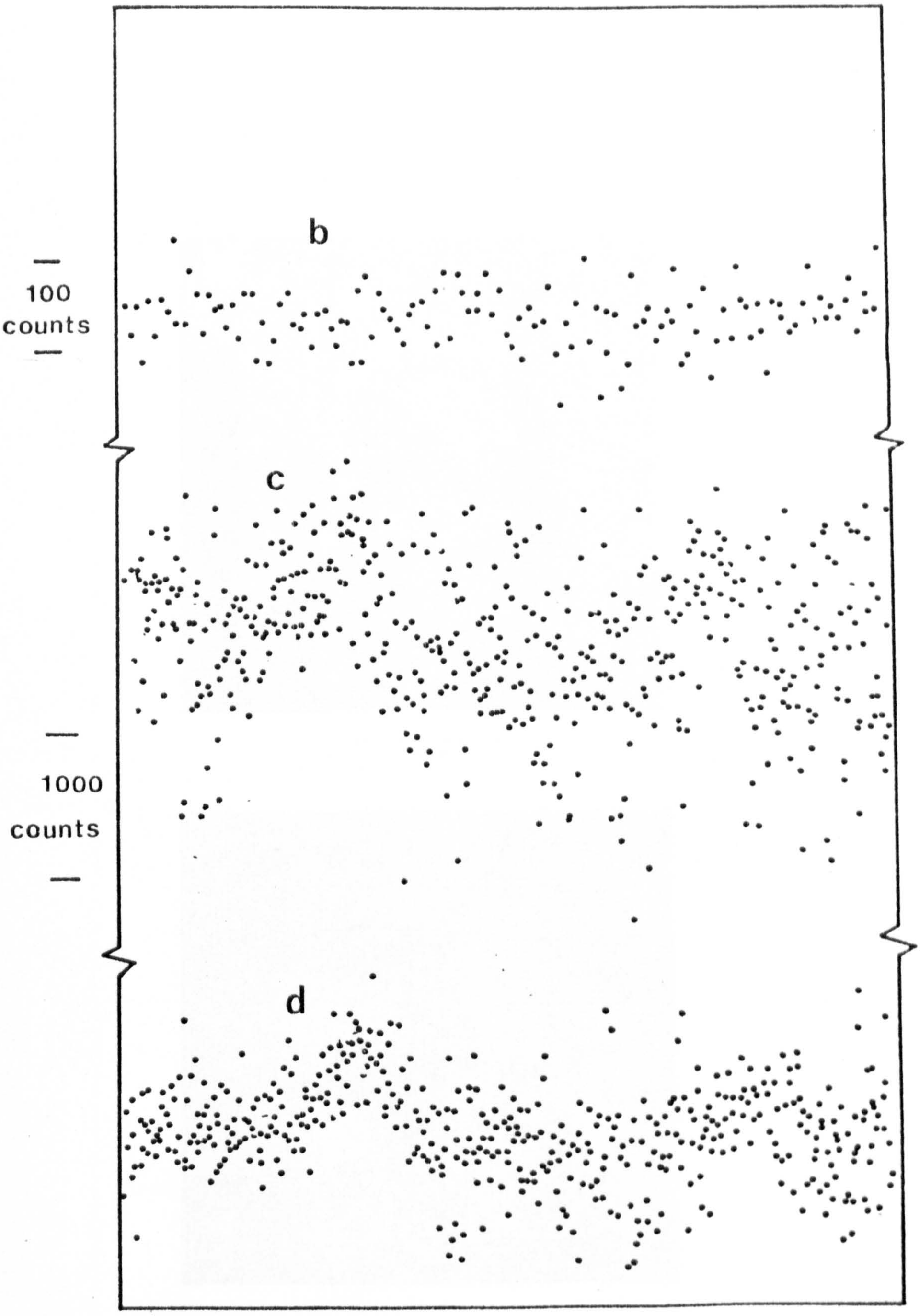

Figure 2.2 Comparison between time taken to identify spatially the presence of a chemical in SAM.
(a) SEM micrograph of a La_7Ni_3 specimen heated at 700°C for few minutes. The image was collected during the same time as the Auger image shown in (e) below and depicts beam current fluctuations.
(b) Line scan along A - A in (a) above. 20 m sec dwell time/pixel. 128 pixels.
(c) 512 pixel line scan, 200 m sec/pixel.
(d) Average of four scans as of (c).
(e) La Auger image, 128 x 128 pixels, 20 m sec/pixel.
Ep ~ 20.3 keV, I_b = 3 nA.

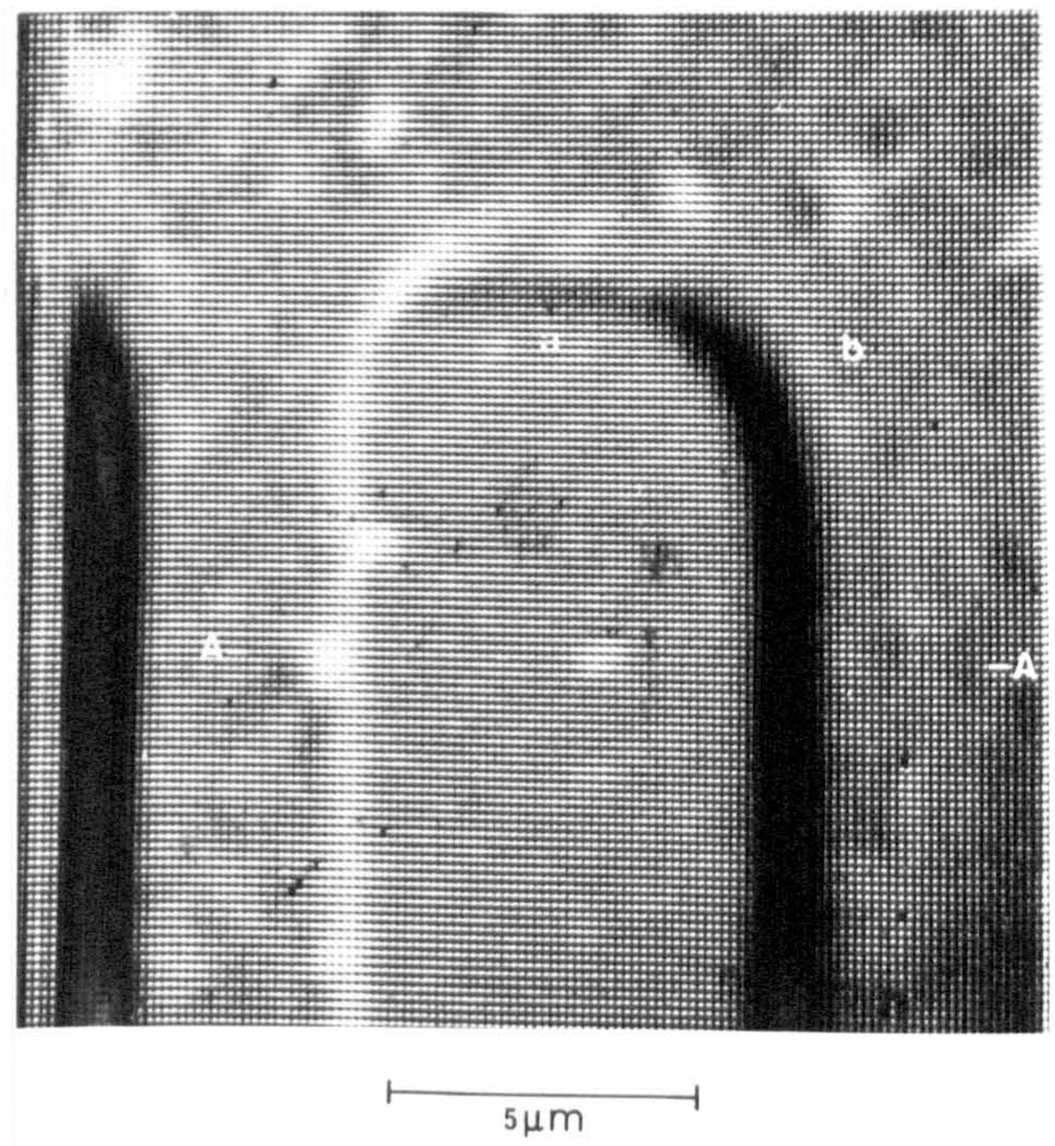

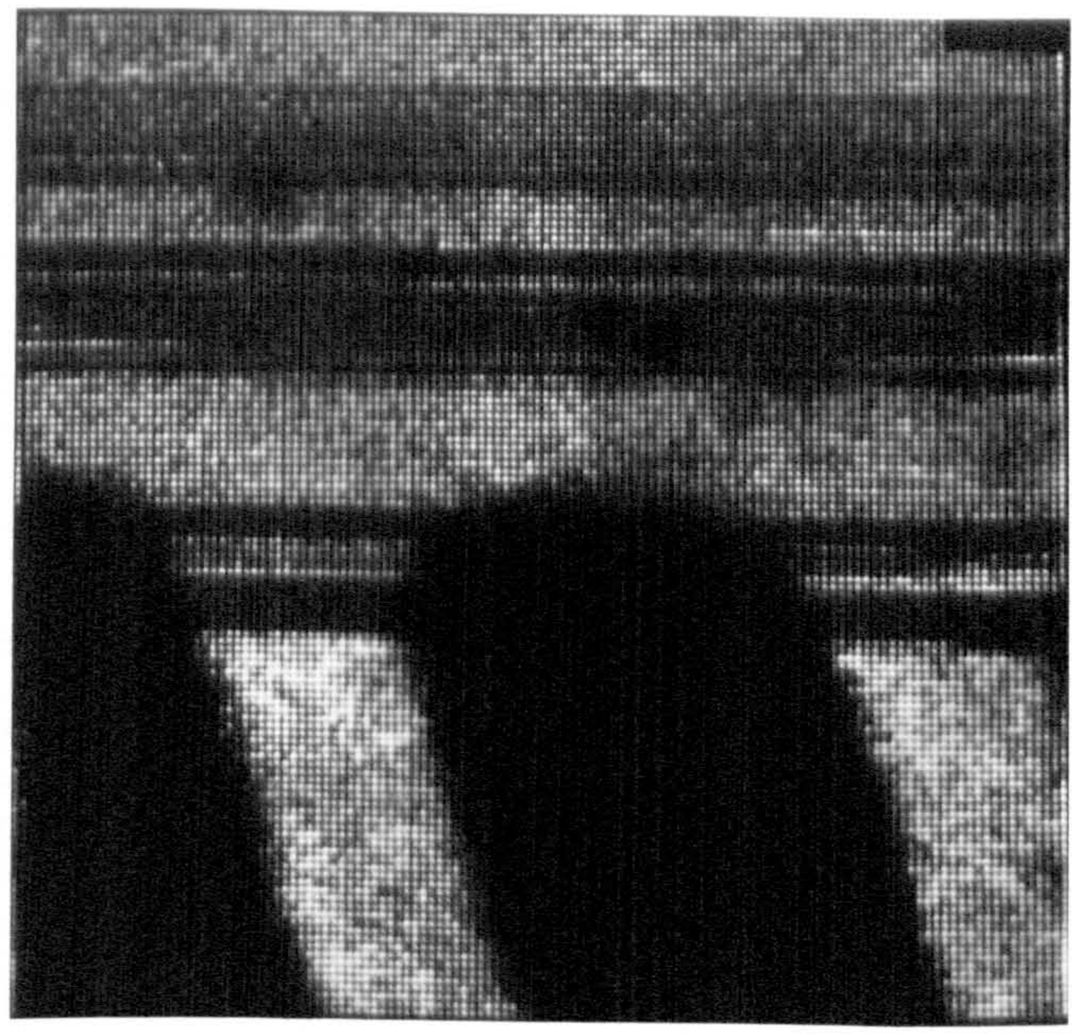

Figure 2.3(a) Example of the advantage of imaging at high resolution in the case of specimen drift, showing an Auger image of Aℓ on SiO_2. In this case the information is not completely lost but merely misplaced and can for example be correlated with an SEM image collected simultaneously.

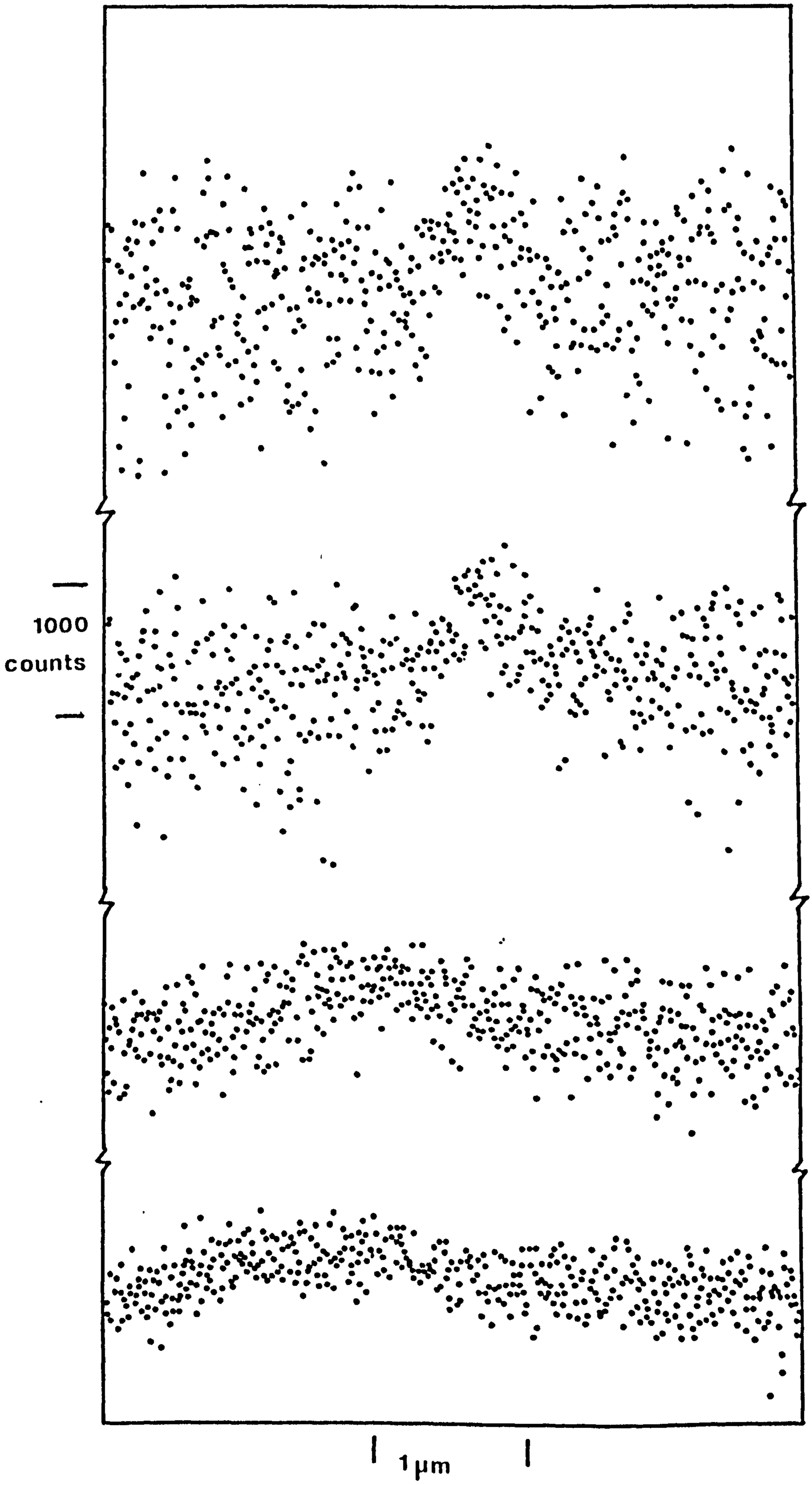

Fig. 2.3(b) Line scans of an La feature of an La_7Ni_3 specimen depicting the reduction and smearing of the La signal due to specimen drift after (i) 1, (ii) 2, (iii) 4 and (iv) 8 scans. 512 points 200 m sec/point.

the S/N can result in incorrect estimates of the spatial extent and concentration of an element as depicted in Figure 2.3(b). In this case, specimen drift by about 1 micron to the left was detected in about 20 minutes and has led to a reduction in the signal height in addition to smearing.

iv) Imaging also allows quantitative estimates of the proportional coverage of an element in comparison with its bulk concentration to be done more easily than with line scanning combined with the SEM. This point is clear in the case of low contrast specimens or small chemical concentrations as shown in (i) above, or in the study of binary alloys such as La_n Ni_m system. Both heating and gas adsorption are known to cause diffusion of one element to the surface in different concentration to that of the bulk (84).

v) Finally, extraction of information from noisy data because of low signal levels or in the case of electron beam instability as in field emission probes, is much easier in imaging than with line scans as shown in (i) and (ii) above. This is due to the use of filters to control the grey levels in an image combined with the ability of the human eye to filter noise and recognise a pattern.

From the foregoing discussion it is evident that SAM is a useful technique for a wide variety of problems of great scientific and technological importance. The case for imaging in comparison with line scanning shows that it would be advantageous in some applications to have facilities for Auger imaging in a SAM, in spite of its longer collection and processing time.

2.3 THEORETICAL CONSIDERATIONS

The quality of a SAM picture will be mainly examined with respect to the following quantities: the spatial resolution, the sensitivity, the contrast, the frame scan time and the magnification. These quantities, however, are governed by the instrument parameters which are: the spot size, the primary beam current and energy, the maximum solid angle within which the Auger electrons can be collected, and the efficiency of the analyser.

2.3.1 Contrast and Signal to Noise Ratio (S/N)

In an ideal situation, the output signal of a system should have no noise associated with it. Unfortunately, this is not the case in reality. An output signal always has some noise combined with it. Although several techniques have been devised to separate signal from noise, an amount of noise will always be mixed with the signal.

There are several sources of noise that one faces in electron microscopy. The first is associated with the electron beam and arises from the random emission of electrons from the emitter. As the total current drawn from the emitter decreases, the statistical fluctuations of the arrival of the electrons at the specimen increase, and so the noise increases. This is a fundamental effect, and can be reduced only by allowing more time for a measurement.

The second source is that associated with the specimen, in terms of additional statistical fluctuation characteristic of the secondary electron emission process. Finally, there is noise associated with signal collection and processing systems. With careful design, one can almost eliminate the last source of noise in an ordinary SEM (41).

In microscopy, the amount of noise that can be tolerated depends on the amount of contrast required in the image that is to be detected. Figure 2.4 shows the variation of the output signal with position for ideal and real systems. The definition of noise δN , signal S and the variation of signal δS are also shown. Following Booker (40), the contrast C and signal to noise ratio S_1 are defined as follows

$$C = \frac{\delta S}{S} \qquad (2.1)$$

$S_1 = \frac{S}{\delta N}$ = ratio between the rms signal snd rms fluctuation due to noise

Figure 2.4(b) shows a real system, where an amount of noise δN is superimposed on the signal. As δN increases, δS will become less distinct, hence hard to detect. Rose (46) suggested that the eye can detect a change in the signal δS in a micrograph if

$$\delta S > 5\ \delta N \qquad (2.2)$$

The factor 5 is related to the probability that a picture element will be in error by one grey level as a result of noise through the following expression (41):

$$\text{Prob. error} = \tfrac{1}{2}\left(1 - \text{erf}\ \frac{K}{2\sqrt{2}}\right) \qquad (2.3)$$

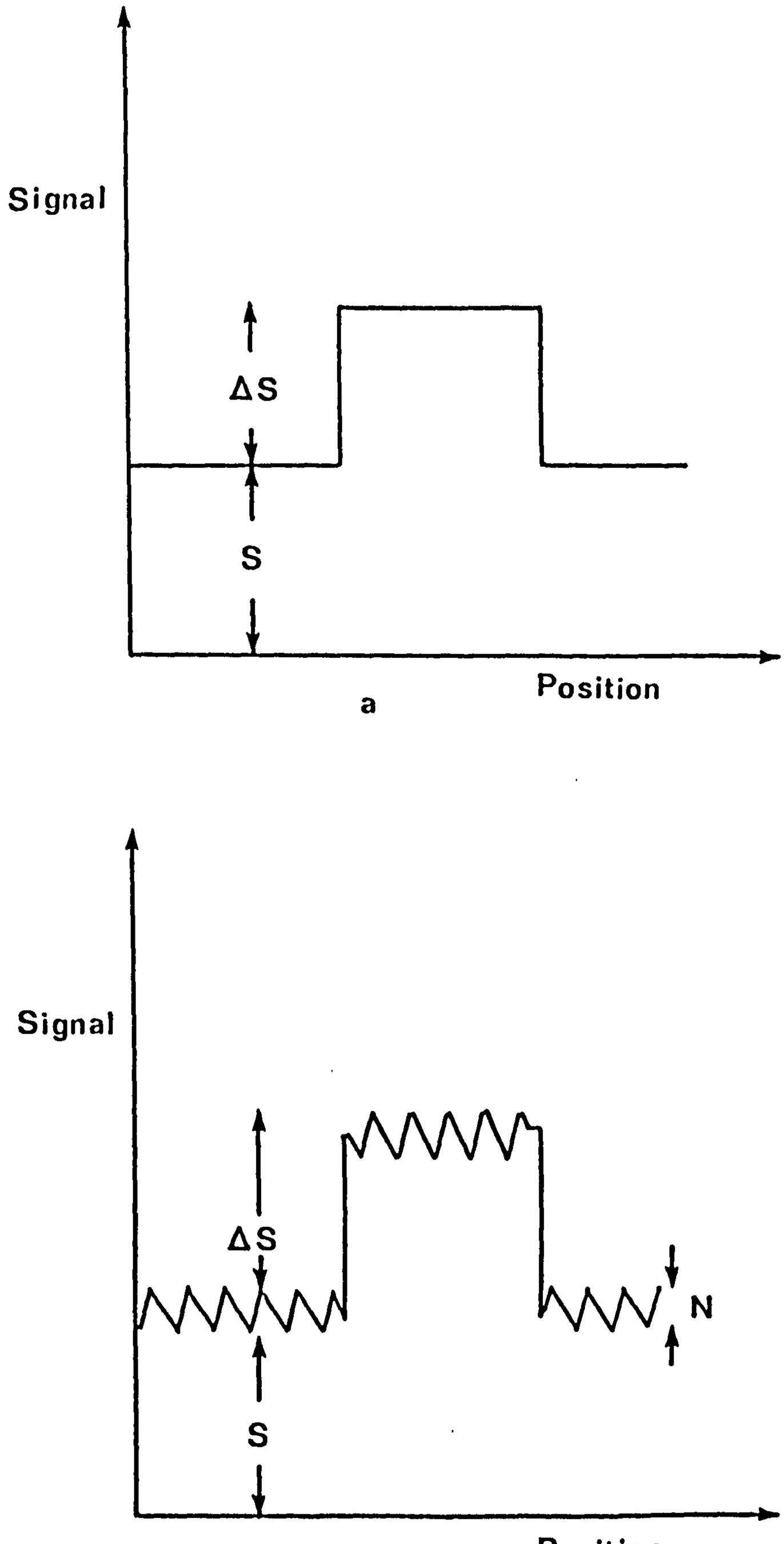

Fig. 2.4 The variation of an output signal for (a) ideal and (b) real systems.

where $$\text{erf } x = \frac{2}{\sqrt{\pi}} \int_0^x e^{-y^2} dy$$

and K is the ratio between the grey level separation and the rms fluctuation caused by noise. For K = 5, the probability error will be 1 in 160.

Let us estimate the noise in the picture which arises from the different sources discussed above, i.e. the electron beam, specimen, and the detection system. If n is the total number of electrons in the beam, then the rms fluctuation in the beam will be $\sqrt{n}$. Rose's criterion then becomes

$$\frac{\delta S}{S} > 5\ \delta N/S \tag{2.4}$$

i.e. $$C > 5\ \frac{\sqrt{n}}{n}$$

The noise arising from within the specimen will add a factor of at most 2 to the above equation (41), hence

$$n > \frac{100}{C^2} \tag{2.5}$$

2.3.2 The Auger Current

Equation (1.4.1) of Chapter 1 described the relation between the current I_A in an Auger peak and the incident beam current I_b . An estimate of I_A can be obtained for the Oxygen $K L_{23} L_{23}$ peak at 505 eV for a mono-layer of oxygen on Fe at 20 KeV primary excitations. The cross-section $\Phi(E)$ for K-shell ionisation is nearly 10^{-20} cm^2 (using Gryzinski), the back scattering factor $r \simeq 1.5$, $n \simeq 2 \times 10^{15}$ atoms/cm^2, and sec $\theta \simeq 2$ for $\theta = 60^o$. This gives $I_A \simeq 10^{-4}\ I_b$ into 4π sterradian. In practice, one only collects a fraction of this depending on the geometrical collection factor of the analyser as well as its efficiency. Values of the order of 10^{-3} are typical of this effect. So the collected Auger current in an Auger peak is only of the order of $10^{-7}\ I_b$. For a probe current of 10^{-8} A ,

this means an Auger current of about 10^{-15} A. This current will be superimposed on a background current of the order of 10^{-11} A due to the secondary electrons. So the efficiency of production of Auger electrons is very low compared to secondary electrons, which are used for imaging in SEM. This fact puts a demand for high probe current to avoid embarrasingly long scan times in SAM. On the other hand, and for certain specimens, there is a limit to the current one can use in the smallest spot size obtainable with an instrument without damaging the specimen. This topic will be discussed in a later section.

2.3.3 Frame Scan Time (T_F)

To estimate T_F, let us assume a frame containing M points in an array. If the dwell time per point is τ, then

$$T_F = M\tau \tag{2.6}$$

For an image of contrast C, following Booker (41), the collected number of electrons per image point in a time τ is given by

$$\frac{n_A^2}{n_A + n_B} > \frac{100}{C^2} \tag{2.7}$$

where n_A is the number of Auger electrons and n_B the number of electrons due to the background in the Auger spectrum. Combining equations (1.4.1) and (2.6) with inequality (2.7), we obtain

$$I_b\, T_F > \frac{100\ Me\left[1 + \frac{n_B}{n_A}\right]}{C^2\ N\ \Phi\ r\ \omega\ \sec\theta\ \Omega\ \varepsilon} \tag{2.8}$$

where e is the electronic charge and the rest of the symbols are as defined in the above mentioned equations.

There are a number of factors that contribute to the above inequality, namely, sample properties (N, ϕ, r, ω), instrumental properties

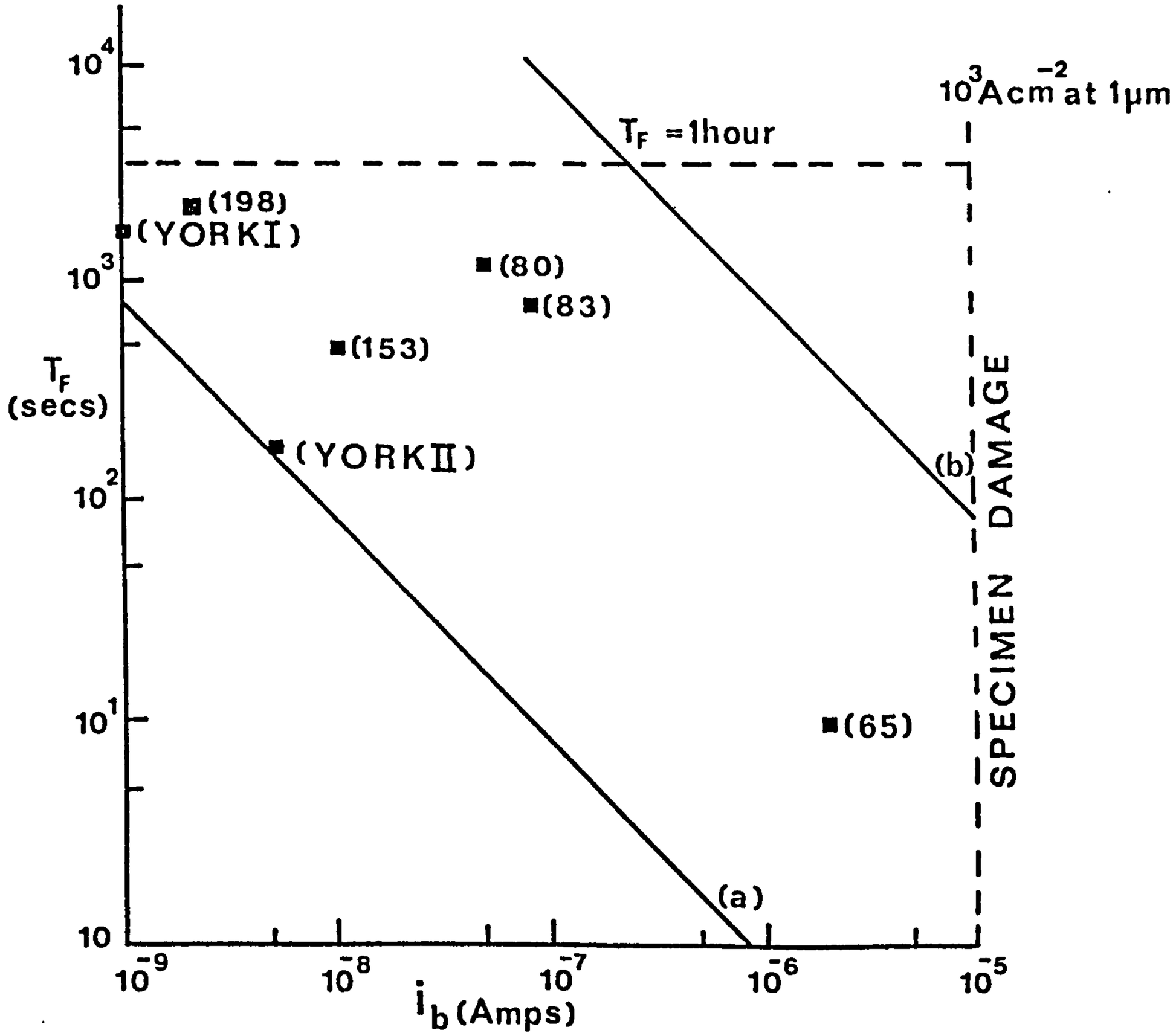

Fig. 2.5 The relation between frame scan times T_F and beam current I_b for different image densities.

(Ω , ϵ , θ) and finally the quality of the image required (C, M).

Figure 2.5 shows the relation between T_F and I_b for poor and high quality images. The figure is drawn for a monolayer of oxygen on a metal surface (assuming $K L_{23} L_{23}$ Auger yield), with $r = 1.5$, $C = 1$, $\frac{n_B}{n_A} = 5$. Line (a) is for 100 x 100 points frame with an analyser having Ω = .1 . Line (b) is a high quality image of 10^6 points with Ω = 0.01 . From the above Figure 2.5 it is clear that long frame scan times will be necessary even with beam currents of up to 10^{-6} A.

2.4 THE PRIMARY BEAM ENERGY AND SPOT SIZE

The relation between the electron energy and beam diameter will be discussed in more detail in Chapter 7. For SAM several effects have to be taken into consideration. These are, the electron energy, the size of the Auger signal and its relation with frame scan time and specimen damage, and the effects of backscattered electrons on resolution. These points will be treated further in other parts of this work. However, considering only the relation between the beam diameter and the spatial resolution in SAM, using Monte Carlo calculations (Chapters 4, 5), it was found that the latter is limited by the diameter of the electron beam. Primary electron energies and backscattered electrons will degrade the resolution but only by a factor of the order of 2. Furthermore, since the collected Auger signal is about 10^{-15} A, (in a practical system assuming a beam current of about 10^{-8} A), then the criterion for the beam should be a current of about 5 - 10 nA in a spot of the order of tens of nanometers.

For the purpose of fulfilling this requirement, it will suffice at this stage to compare a few of the most widely used electron probes. Figure 2.6 depicts the relation between beam current and diameter for some

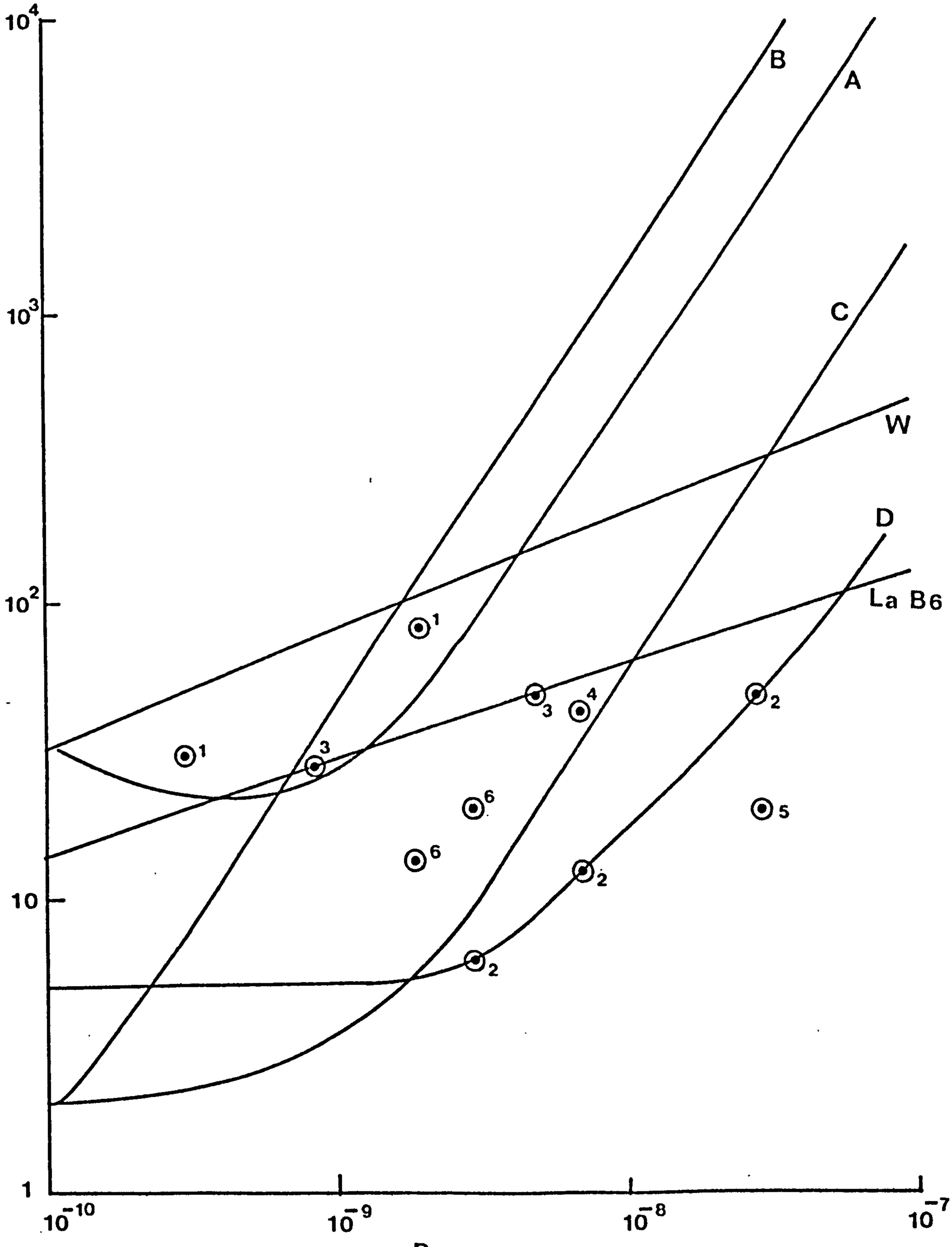

Fig. 2.6 The relation between beam current and diameter of several existing electron probes.
(1) Browning et al. (59), (2) Venables and Janssen (148), (3) Christou (82), (4) Orloff and Swanson (157), (5) Kuo and Siegel (195), (6) Venecklasen etal (133)
A two element field emission gun with optimum aperture (chapter 7), B, C(113) and D(148) are two element lens with magnetic lenses.

of these systems. Field emission probes, preferably with magnetic lenses, are shown to give the highest beam current (10^{-9} A) into the smallest spot (5 nm). The proper shielding of the magnetic field and the physical dimension of the shield will decide the merits of such a system when using a specific energy analyser like the CHA. As will be seen later, (Chapter 5), primary electron energies of about 20 keV have the least effect on resolution. It would also be useful to be able to vary the electron energy of the focussed spot for either reducing charging effects in insulating specimens or for the study of backscattering effects, to name but two applications.

2.5 SPECIMEN DAMAGE

The above discussion has led to the requirement of a beam current of the order of 10 nA in a spot diameter of less than 100 nm. This corresponds to an electron dose of the order of 10^2 C/cm^2 . It is well known that electron beam induced processes of the sample, such as decomposition, electron stimulated desorption (ESD), adsorption, heating and charging are both specimen and electron dosage dependant. Since AES is a surface sensitive technique any beam induced changes on the surface will be evident and important in analysis.

For example the decomposition of Aℓ under electron bombardment into Aℓ and $Aℓ_2\ O_3$ with electron beam dose in excess of 10 C/cm^2 at 5 keV has been reported (47), while a value of 10^2 C/cm^2 is given as the maximum permissible dose for $Si\ O_2$ (48). Lower doses of the order of 5×10^{-4} C/cm^2 have been reported to cause decomposition in condensed multilayers of $(CH_3)_2\ O$, CH_3OH and $H_2\ O$ (49).

Electron stimulated adsorption in the form of cracking of hydrocarbons at the surface and the subsequent build-up of carbon contamination

has been a common experience in surface science and electron microscopy. Joyce and Neave (50) reported the adsorption of C on Si surface under electron bombardment, while Coad et al (51) reported on the enhancement of oxygen adsorption on Si surfaces under electron bombardment, but no threshold for a destructive dosage was given in either case. The formation of Ni_3C on Ni samples with a dose of the order of 4×10^{-3} C/cm^2 has also been reported (52).

Diffusion of impurities out to the surface from the bulk under electron bombardment is another form of specimen damage. Chang (53) has reported the diffusion of P from SiO_2 / 0.5% P by electron bombardment at 3.1 keV, 5×10^{-2} A/cm^2, while Mróz (54) reported the diffusion of sulphur from Ni at 1.1 keV and 7×10^{-3} C/cm^2.

The temperature rise in a specimen under electron bombardment depends on its thermal conductivity, density and specific heat, and can amount to a few hundred degrees centigrade (55). Hofmann and Zalar (56) have observed interdiffusion in Au/Ag sandwich films which were exposed to an electron beam of about 15 mW and 175 mW.

Another problem associated with electrom bombardment is specimen charging, particularly for insulating materials. Charging is usually correlated to the electron energy and angle of incidence and not on electron density. However, insulating particles of the order of microns in size can lead to inaccurate analysis in AES (57, 58).

From the foregoing discussion, if one takes into consideration that during imaging the usual dwell time per pixel is 20 m sec; some of the above stringent conditions of electron beam dosage, considered for a stationary beam, will have to be relaxed. This will allow a wide variety of samples to be examined without a change in their chemical composition. In addition, operational precautions such as good ultra high vacuum conditions and minimising exposure time of the surface region to be studied will

have to be taken into consideration by the analyst.

2.6 SAM ELECTRON ENERGY ANALYSERS

Generally speaking, any analyser commonly used in AES can be used in SAM. On the other hand, demand for high transmission, large solid angles of collection, lack of physical obstraction, and preferably good energy resolution necessitates some types of analysers being excluded. Table 2.2 lists some of the important parameters for some of the currently used Auger energy analysers. The retarding field analyser, although the most widely used in AES to date, can not be used in high resolution SAM. The reason is the large "shot noise" contribution arising from detecting the total current for $E > E_A$. This gives a threshold current of nearly $1\mu A$, while a beam current of nearly 10^{-8} or less is anticipated. The cylindrical mirror analyser (CMA), and the concentric hemispherical analyser (CHA) will be compared below when used in SAM. The reasons are commercial availability and simplicity of operations for the CMA in addition to it being the most widely used analyser in reported SAMs, while the instrument built in York uses a CHA. A comparison of the two analysers gives the following.

1) The working distance of the CHA is much larger than that of the CMA being ~10 mm and 4 mm respectively. The small distance available for the CMA places constraints upon the design of the sample manipulator and the last aperture of the scanning electron gun. These geometrical constraints usually mean that the axis of the CMA is well away from the surface normal of the sample. This in turn can cause a reduction in the collection efficiency of the analyser by a quoted factor of up to ½ (59).

2) CMAs are usually operated with an electron multiplier as a detector and with the first dynode of the multiplier at ground potential.

This configuration is chosen to minimize potential penetration from the electron multiplier into the output aperture of the CMA and the consequent degradation of energy resolution. One effect of choosing this configuration is that the kinetic energy of electrons reaching the multiplier is just the Auger energy. As the pass energy E is reduced to observe Auger electrons with energies below 200 eV the gain of the multiplier falls quite rapidly and the electron spectrum is correspondingly attenuated.

3) The standard CMA is an instrument with constant resolving power , $E/\Delta E$. At low energies the bandwidth ΔE of the analyser becomes substantially narrower than the Auger peak width, thus signal is lost. For the purpose of microscopy it is important to maximize the signal to noise ratio and an analyser of constant bandwidth is more useful. The CHA is an instrument which can be operated in either mode, constant bandwidth or constant resolving power.

4) The field of view of the CHA can be arranged to be 0.5 mm compared to few tens of microns for the CMA.

5) The CMA is relatively easier in construction and operation compared with the CHA.

Type of analyser	$\Omega/2\pi$	resolving power	scan speed	SNR	field of view	working distance
RFA	.1 - .4	60 - 500		Low	—	—
CMA	.01 - .11	200 - 2000	up to 20 kV per sec	High	100 μm	4 mm
CHA	.01 - .1	500 - 8000	up to $\frac{1000\ eV}{sec}$	High	.5 mm	10 mm

RFA = Retarding field analyser

CMA = Cylindrical mirror analyser

CHA = Concentric hemispherical analyser

Table 2.1 A comparison of some useful properties of electron spectrometers.

2.7 SIGNAL PROCESSING

The above treatment suggests that one would detect an Auger current of the order of 10^{-15} A or less in high resolution SAM. This by itself is not an easy problem from signal recovery point of view. In addition, the problem could be even worse when one adds the contributions of backscattering, topographical effects, angle of incidence, primary energy and chemical diffuseness in the collected signal. Unless provision is made to separate the contribution of the above effects, the results obtained will be less useful.

In the following we will review briefly some of the techniques used for signal processing in SAM, as well as methods that compensate for the above mentioned effects.

2.7.1 Modulated Versus Unmodulated Spectrometers. N(E) vs N'(E)

It is common practice in AES to modulate the potentials of the energy analyser and detect the component of the output signal at the modulation frequency. This technique results in a signal proportional to the differential N'(E) of the electron energy distribution. The advantages will be a reduction of the background effects below the Auger peak in the spectrum and making the Auger peak more visible against a more slowly varying background.

The other alternative is to detect signals proportional to the energy distribution N(E). This has the advantage of checking the performance of the analyser by displaying the data in log N(E) versus log E, which yields linear background above the Auger peaks (57). In particular the background has some useful information and varies with beam energy and the sample atomic number (60). Further, the N(E) data can always be differentiated to compare with other published N'(E) data.

Prutton (61) has compared the energy resolution as well as the expected signal to noise ratios for modulated and unmodulated energy analysers assuming cosine modulation. He found that for a given shape and width of input function and a given spectrometer window δ, there is a maximum in the signal H at a particular size of modulation m. The signal increases as both the modulation and spectrometer window are increased. For the unmodulated spectrometer, an increase in the measured current will be expected as the spectrometer's window is increased.

	Unmodulated		Modulated			N(E)
	δ	FWHM	δ	m	$2\epsilon_p$ [(a)]	FWHM
Gaussian	0.68	2.54	0.68	2.1	3.2	2.355
Lorentzian	1.00	2.82	1.37	3.3	5.5	2.000

(a) $2\epsilon_p$ is a measure of the width of N'(E) distorted by the dynamic instrument response function r(E) * g(E).

Table 2.2 A Comparison of the Performance of Modulated and Unmodulated Analysers. Values Tabulated to Yield Half of the Maximum Possible Output Signal.

Table 2.2 (61) gives the values of the spectrometer window δ for unmodulated spectrometer, and δ and m for modulated spectrometer. It can be seen from the above Table that one requires large values of m to achieve the same output as in the unmodulated case. Over-modulation will, however, degrade energy resolution. In reality the ultimate decision of whether to modulate the analyser or not will depend on the actual peak and background shapes found in practice.

2.7.2 Electron Detectors in SAM

There are various types of detection schemes in use for SAM. Electron multiplier, channeltrons and phosphorscreen/photomultiplier combinations have been used in either analogue or pulse counting modes. Pulse counting is certainly preferred at probe currents below 10 n A. Analogue detection becomes more favourable as the probe current increases, where it becomes impossible for pulse counting at higher currents than 100 n A. Pulse counting however has the advantage of direct interfacing for digital processing. Todd et al (62) have compared pulse counting for N(E) mode with analogue detection for N'(E) mode at low beam currents (1 n A) and same S/N ratio. They found that a reduction of nearly 5 times in recording time is feasible using pulse counting in N(E) mode. For present electrostatic field emission guns, typical beam currents are of the order of few n A, in less than 100 nm spot. Hence pulse counting will be preferable in such systems.

Another technique aimed towards improving signal to noise ratio, is accumulation and smoothing of spectra. This technique will be extremely useful when working with very small beam currents. Mogami (48) shows an improvement of an order of magnitude when using this method.

2.7.3 Beam Brightness Modulation (BBM)

Le Gressus and Massignon (63) and Mogāmi (64) have described a method similar to chopper amplification technique used in optical measurement for use in SAM to improve S/N and minimise specimen irradiation damage. A high frequency square wave current is supplied to a beam blanking coil placed beneath the electron gun. This causes the primary electron beam to be periodically modulated. If the analysed signal (an alternating current) is fed to a lock-in amplifier followed by a phase sensitive detector (PSD), then the output spectrum will be of the N(E) type. The

advantage of this method lies in the use of the PSD, which eliminates noise signals after modulation. Mogami (64) compares S/N for Ag - MNN peaks using BBM and the N'(E) mode. An improvement of nearly 6 times was achieved by the use of BBM over N'(E). This technique is equivalent to counting in principle. Another way to employ this technique in field emission electron probes is to operate the emitter in the pulse-emission mode and take advantage of its higher emission current with respect to continuous emission. Alternatively, in the case of continuous emission mode, the beam can be electrostatically blanked by applying a deflecting signal at the scanning system used.

2.7.4 Topography

It is to be expected that surfaces examined by SAM will usually be far from ideal crystal surfaces. Topographical variations on the surface can lead to false conclusions of chemical concentrations on the surface, unless compensated for. A number of methods for the removal of topographical contrast in SAM have been used by several authors and are as follows:

i - Seah and Lea (65) have used a colour superposition technique to compare the relative heights of the Auger peaks from two different elements in a fractured surface. They showed that the relative intensity of two Auger peaks depends less on orientation than individual peaks. No quantitative information about the extent of the technique's compensation for topography was given.

ii - Janssen et al (66) have used a ratio technique of the analog signal N'(E) from the output of a lock-in amplifier and the CMA detected current N(E) (from an electron multiplier). Their results show compensation of topographical effects in addition to a reduction of backscattering and incident beam current effects.

iii - Todd and Poppa (67) correct for topographical effects by using the ratio of the Auger peak height to the background level on the high energy side of the Auger peak,

iv - a less effective method is to use the ratio of the Auger signal to the secondary electron (SEM) signal (59, 62). The effectiveness of this method depends on the geometrical arrangement of the two detectors involved, namely the Auger and SEM. Differences in Auger maps and SEM images have been reported (68), and are believed to be due to differences in the geometrical orientations of the two detectors.

Prutton et al (69) have compared some of the above methods using anisotropically etched silicon specimen with well defined crystallographic angles. They found that correction with the ratio $(N_1 - N_2)/(N_1 + N_2)$ where N_1 is the count on the Auger peak and N_2 on the background above the peak, yield the best results in comparison with any other combination of N_1 and N_2 (i.e. N_1, $N_1 - N_2$, and $(N_1 - N_2)/N_2$). The use of digital data acquisition and processing, as proposed here, would allow any of the above schemes to be employed.

2.7.5 Beam Current Variations

Field emitters are known to be very unstable when used in electron guns, particularly at high emission current. Usually they give a fluctuating beam current accompanied by a drop from its original value by as much as a factor of 4 - 5 (Chapter 6). Consequently, variation of the Auger yield will result.

One approach to compensate for this effect is by referencing the Auger signal to the secondary electron signal either directly from the SEM photomultiplier output (59), or from a reference detector along the

analyser's axis (48). The resulting ratio varies a little (to within 5% at most) with changes of beam current of up to 10^{-1} of its original value. An improvement of the same order as discussed above has been achieved by Janssen et al (66) using the ratio N'(E)/N(E) .

Cleaver and Smith (70) have devised a different method of stabilising the beam current in their microscope. They choose to collect the probe current from an electrode intersecting the beam. This is then used to determine the voltage applied to the emission control electrode (Wehnelt) of the gun. The disadvantage of this method is de-focussing and displacement of the electron probe as the Wehnelt potential is varied.

2.8 THE SPECIFICATION OF THE FIRST INSTRUMENT

From the foregoing discussion, it is proposed that a high spatial and energy resolution scanning Auger electron microscope capable of mapping the spatial distribution of a selected chemical on the surface of a solid could be realised. It would feature the following:

Primary electron energy	0.1 - 30 keV
Magnification	50 x - 20 K x in 10 steps
Electron beam diameter	30 - 100 nm
Energy analyser	CHA accessed by electron lenses
Energy resolution	1.0 eV
Energy range	10 eV - 2000 eV

In addition, the instrument will have facilities to compensate for beam current fluctuations and specimen topography in the recorded image. Digital techniques will be adopted to take advantage of their superiority in signal processing at low beam currents and for computer interfacing.

CHAPTER 3

THE DESIGN OF THE FIRST SAM INSTRUMENT

3.1 INTRODUCTION

The design of the first SAM instrument at York was based on a UHV field emission scanning electron microscope HB200, supplied by V.G. Microscopes, East Grinstead, U.K.. A CHA analyser (71) was added to the SEM as the Auger electron energy analyser. Circuitry for digitally scanning the electron beam across the sample surface, the analyser with its electronics, as well as other necessary electronic circuitaries, as will be described later, were all built at York.

Before proceeding with the description of the different units of the system, a brief introduction on how the imaging of the spatial distribution of a chemical species on the surface of a sample is done using SAM will first be given. A description of the various units needed to control this operation will then follow.

Firstly, an area of interest is located on the surface of the sample to be analysed using the standard secondary electron mode. The microscope control is then changed to the Auger mode and energy spectra from selected points are produced. The same area is then scanned digitally with the CHA tuned to a selected Auger peak in the spectrum, representing the element to be mapped. A channeltron (Mullard B318BL) is used to count the analysed Auger electrons. At each point of the frame, a count N_1 on the Auger peak at energy E_A, and another count N_2 on the high energy side E_B is done. A photon counter (Brookdeal 5C1) is then used to perform a digital to analogue conversion on the $(N_1 - N_2)$ count. Fluctuations of the beam current are reduced by generating a signal proportional to the beam current, using a voltage controlled oscillator (VCO) driven by the D.C.

Fig. 3.1 General view of the instrument.

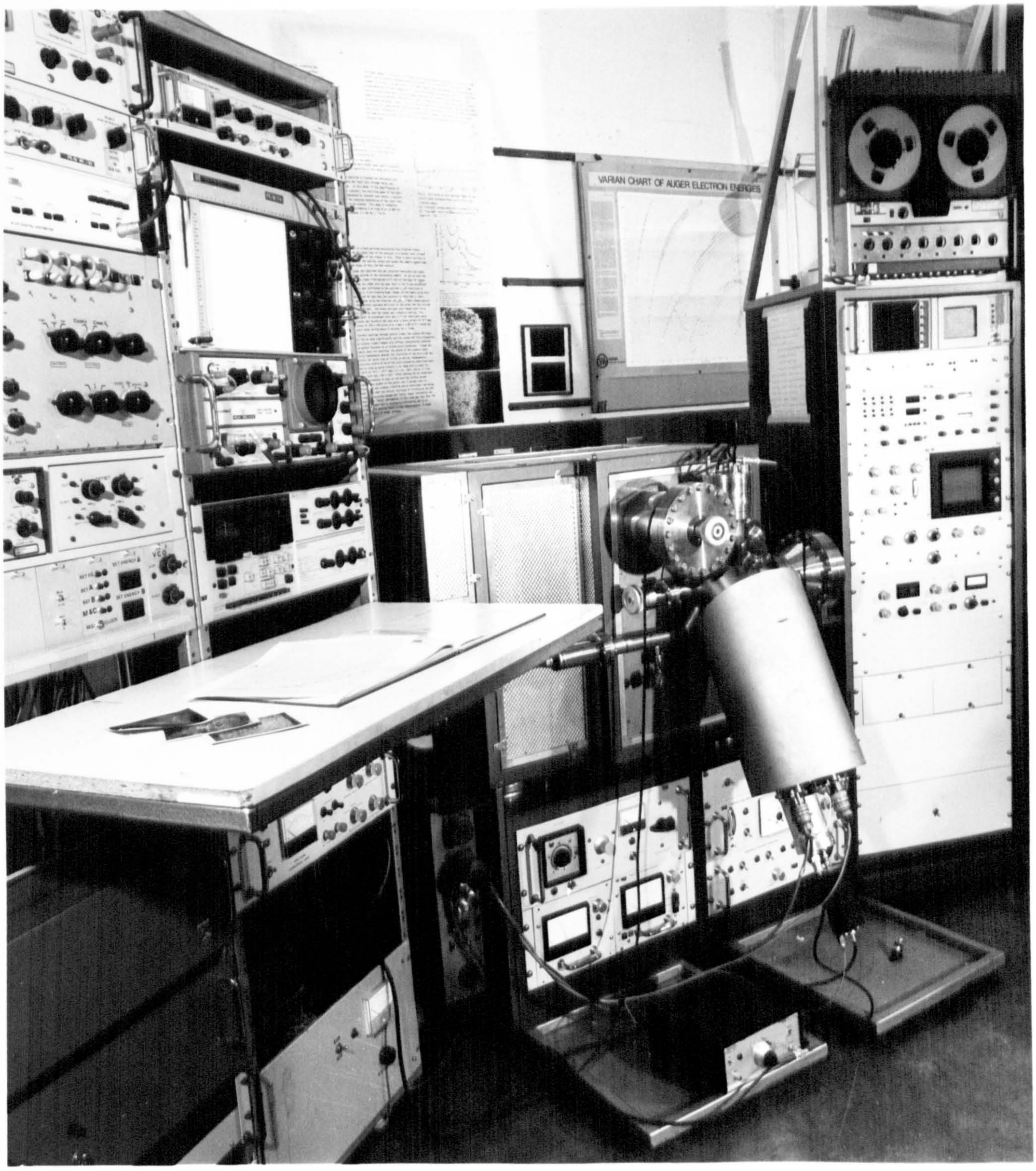
VARIAN CHART OF AUGER ELECTRON ENERGIES

level of the HB200 photomultiplier as its input. A third channel in the photon counter is used to perform a digital to analogue conversion on the output of the VCO. This is then used to divide into the Auger current $(N_1 - N_2)$. The resulting signal from this operation is used to bright up the display.

The different units that control the above operation will be described below. Description of the various electronic circuits of the SEM will not be given, as these are standard commercial facilities.

Figure 3.1 shows a layout of the instrument which consists of the following.

3.2 THE HB200 SCANNING ELECTRON MICROSCOPE (SEM)

The specifications of the SEM are as follows:

(i) The vacuum system is UHV for both gun and specimen chambers. It is of stainless steel and mu-metal construction throughout. Bake-out facilities are provided.

(ii) An electrostatic field electron emission probe of diameter about 35 nm and sufficient current ($\sim 3 \times 10^{-10}$ A) to display secondary electron pictures at TV rates.

(iii) Variable magnification, x 10 - x 20 K.

(iv) Variable accelerating voltage, 0.1 KV - 30 KV.

(v) Scanning speeds:

a) standard TV rates 625 lines, 50 frames/sec

b) 500 lines, 10 frames/sec

c) record, 2000 lines at speeds of 10, 20 and 40 seconds/frame.

(vi) Scanning modes: raster scan, line scan, single frame, reduced area scan, and spot only.

(vii) Electron detector: scintillator-photomultiplier assembly.

3.2.1 The Electron Optical System

Figure 3.2 is a diagram of the field emission source and the electron optics of the HB200. The field emission gun is electrostatic and of the triode type (72). Electrochemically etched (310) tungsten emitters with radii between 20 - 100 nm are normally used. The ratio between the accelerating voltage of the first anode and the emitter extracting voltage is 9 : 1. This condition places constraints on the radii of the emitters to be used. Sharp emitters of radii < 100 nm should be used to keep the extract voltage less than 3 KV. Such a requirement can be disadvantageous, and had proved so in this instrument as it makes the emitter more susceptible to discharges that are likely to destroy it. A detailed description of the HB200 field emission gun and its aberration coefficients will be given in Chapter 7.

The beam is scanned by magnetic fields from the scanning coils. This can be done either at TV rates for producing the secondary electron images, or digitally with different point arrays per frame using the Digital Microscope Control (DMC) (see section 3.5.a). An eight pole piece magnetic stigmator is used for correcting residual astigmatism. The optical column has two angular stops at the back of the second anode of sizes 100 μm and 300 μm. A beam current of 3×10^{-10} A into a spot of ~ 35 nm diameter is obtained. This current was found to be low for Auger imaging (see arguments of the required current for Auger imaging discussed in Chapter 2). With the removal of the smaller aperture (100 μm), a beam current of $\sim 6 \times 10^{-9}$ A with 5×10^{-5} A emission current was obtained. As a result the beam diameter was increased to about 100 nm.

The vacuum chamber is made of mu-metal in order to reduce the effects of magnetic fields, and is vac-brazed to stainless-steel conflat flanges. An extension of the specimen chamber to carry the CHA was added at York. This required another shield of 1 mm thickness to be used

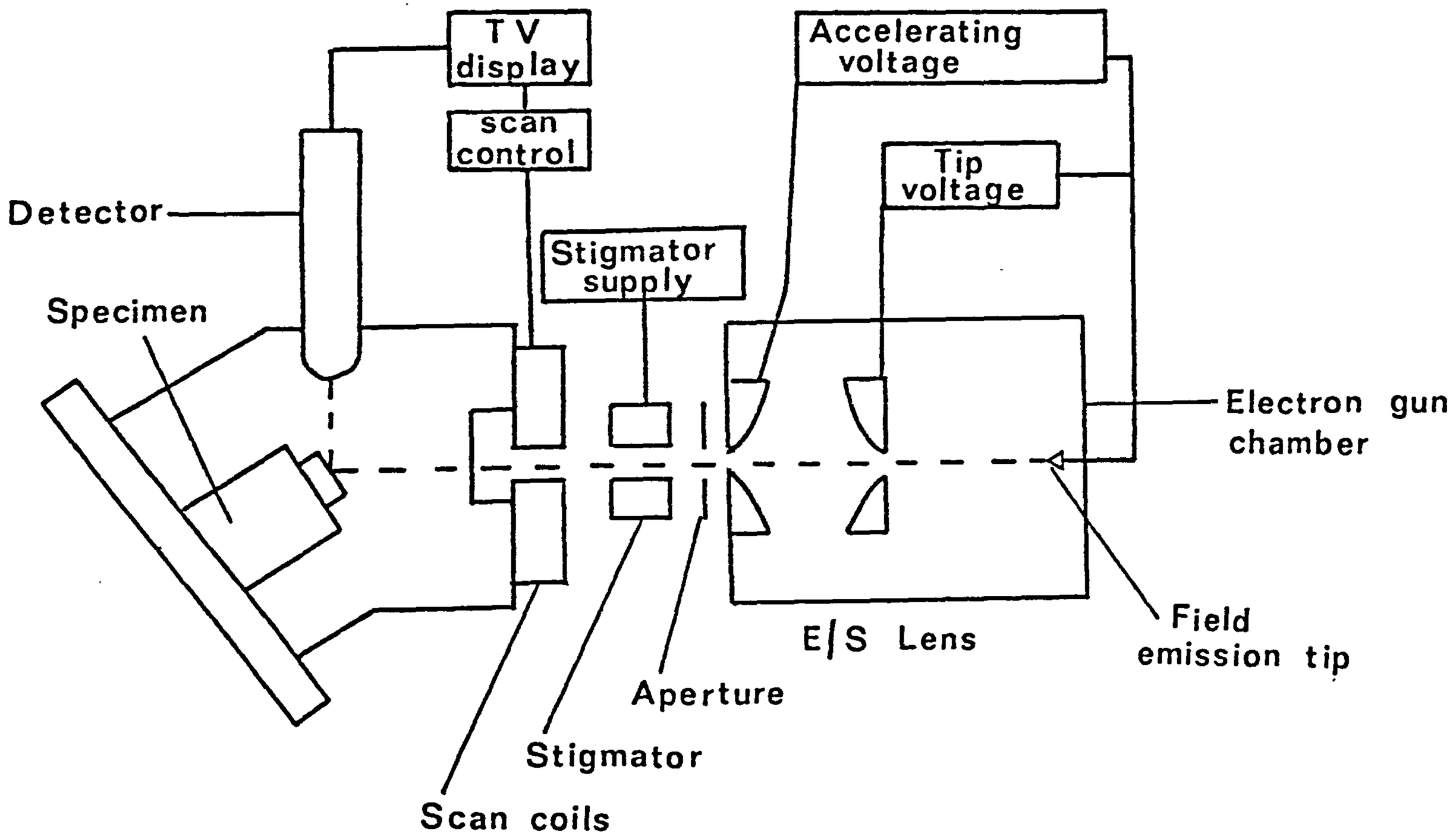

Fig. 3.2 Schematic of the electron column of the HB200 SEM.

externally. As a result the field inside the chamber was reduced to less than 5×10^{-6} Tesla.

A differential aperture and a gate valve isolate the gun from the main vacuum chamber. The former is pumped with a rotary pump-sorption trap combination to a pressure of 10^{-3} torr and with a 30 litre per second ion-sublimation pump combination to a pressure down to 3×10^{-10} torr upon baking to a temperature of 170° C for at least 16 hrs. The ion gauge is mounted next to the ion pump and hence not measuring the pressure around the emitter volume which is likely to be higher. This has been confirmed by the behaviour of the emitter which was found to be noisy at the above gauge reading, contrary to investigations carried out in a separate test chamber which showed a more stable emission (by a factor of the order of 5) at the above pressures.

3.2.2 The Specimen Chamber and Gas Handling Stage

The specimen chamber of the HB200 is not of optimum design for SAM. The volume provided is very small and so does not enable a variety of experiments such as RHEED, LEED, thin film deposition or ion sputtering to be carried out in situ. In addition few ports were available that can be used for the essential attachments (e.g. the analyser, the manipulator, a viewing window, and a gas admittance access). Figure 3.2 shows the part of the specimen chamber occupied by the analyser. The position of the analyser limits angles of incidence that can be used to be in the range of 65° - 90°. This constraint degrades the resolution that can be obtained from a beam of diameter d, to be not better than 2.36 d.

A gas handling unit was added to the existing chamber. It consists of a sorption pump and a gas flask that can be replaced. The use of ion getter pumps in the system limits the variety of gases that can be used, particularly Argon.

The chamber is pumped by a rotary pump to a pressure of 10^{-3} torr and with a 60 litre / sec ion-sublimation pump combination to a pressure of nearly 4×10^{-10} torr upon baking to a temperature of 170^{o} C. The low bake-out temperature is necessary for the channeltron.

3.2.3 The Electron Detector

The electron optical column described above can deliver currents of up to 6×10^{-9} A in a probe diameter of about 100 nm. This is sufficient for displaying a standard SEM micrograph at TV rates. A scintillator-photomultiplier assembly is used for this purpose. The scintillator is made of a glass disk 30 mm in diameter and coated with a layer of luminescent material (type YCS70, Levy West Labs., U.K.), the photomultiplier is type 7524B, made by EMI. A fine stainless steel mesh of 80% transparency is mounted in front of the scintillator (intercepting electrons coming from the specimen). It is used for either accelerating low energy secondary electrons to improve the SNR of the image, or preventing them from reaching the collector in the case of collecting backscattered electrons. A bias voltage variable from -100 volts to +200 volts is used for this purpose.

The whole assembly is mounted about 20 cms above the specimen position and at right angle to the probe. This does not make a direct line of sight with the generated electrons nor does it correspond to the same geometrical collection as the CHA.

3.3 THE ELECTRON ENERGY ANALYSER

An electron energy analyser of the concentric hemispherical type (CHA) is added to the IIB200 microscope. The analyser is a modified version

of that described by Bassett (71). The modifications are firstly, the input lens which is increased to four elements and secondly a channeltron electron multiplier (Mullard B318BL) at the output lens to allow for electron counting.

To understand the reason for the modifications to the lens it is desirable to describe first the factors determining the resolving power of the analyser.

Following Bassett et al (73) and Kuyatt and Simpson (74) the resolving power of the CHA can be described as follows, (two element input and output lenses are assumed, but the same principle applies for more elements)

$$\frac{1}{\zeta_h} = \frac{S}{2R_o} + \alpha_h^2 \qquad \text{for } \alpha_h^2 > \frac{1}{2\zeta_h} \tag{3.1}$$

and

$$\frac{1}{\zeta_h} = \frac{S}{2R_o} \qquad \text{for } \alpha_h^2 < \frac{1}{2\zeta_h} \tag{3.2}$$

where ζ_h is the resolving power of the hemispheres, S is the diameter of the circular input and output apertures, R_o is the mean radius of the hemispheres and α_h is the beam pencil angle at the hemispheres. α_h is controlled by an angle stop which defines the input angle of the beam at the lens α_1 . By use of Helmholtz-Lagrange equation, α_1 and α_h can be equated as follows:

$$\alpha_1^2 V_1 = \alpha_h^2 V_2 M^2 \tag{3.3}$$

where M is the linear magnification of the lens. Further, if d is the diameter of the object, then

$$S = Md \tag{3.4}$$

hence, (3.2) becomes

$$\frac{1}{\zeta_h} = \frac{Md}{2R_o} \tag{3.5}$$

following Heddle (75), the overall resolving power is given by

$$\zeta = \zeta_h \frac{V_1}{V_2} \tag{3.6}$$

if (3.3) and (3.5) are combined, then

$$\alpha_{1M}^2 = \frac{2 R_o^2}{\zeta_h^3 d^2} \frac{V_2}{V_1} \tag{3.7}$$

where α_{1M} is the maximum value of α_1 for any given R_o , ζ_h , d and voltage ratio.

From (3.7) it is clear that the smaller d is, the bigger α_1 that can be used, resulting in an increase in the collection efficiency of the analyser. This increase does not degrade the resolving power ζ_h provided that the input lens is not overfilled.

The three element input lens magnification was designed by Bassett (71) to be X 8 , to take advantage of the condition stated above. With this arrangement, the analyser's field of view was restricted to few microns across. This was due to field penetration from the first gap in the input lens to the input aperture. As a result the magnification was found to be much larger than X 8 . A pragmatic solution was to use a four element input lens with a crossover of the image before the analyer's entrance plane (59). This lens has a variable magnification in the retardation range 1 : 1 - 1 : 40. A field of view of nearly 0.5 mm across is achieved. A schematic and a photograph of the modified analyser are shown in Figure 3.3. The input and output slits of the lenses are set parallel with dimensions equal to 4 mm x 2 mm and 8 mm x 4 mm respectively. This arrangement gives a collection efficiency of nearly 1.6% of the electrons emitted from the target into 2π steradians. The transmission efficiency of the analyser is better than 80%.

An advantage of this analyser is the ability to operate it in two

Fig. 3.3(a) A photograph of the CHA.

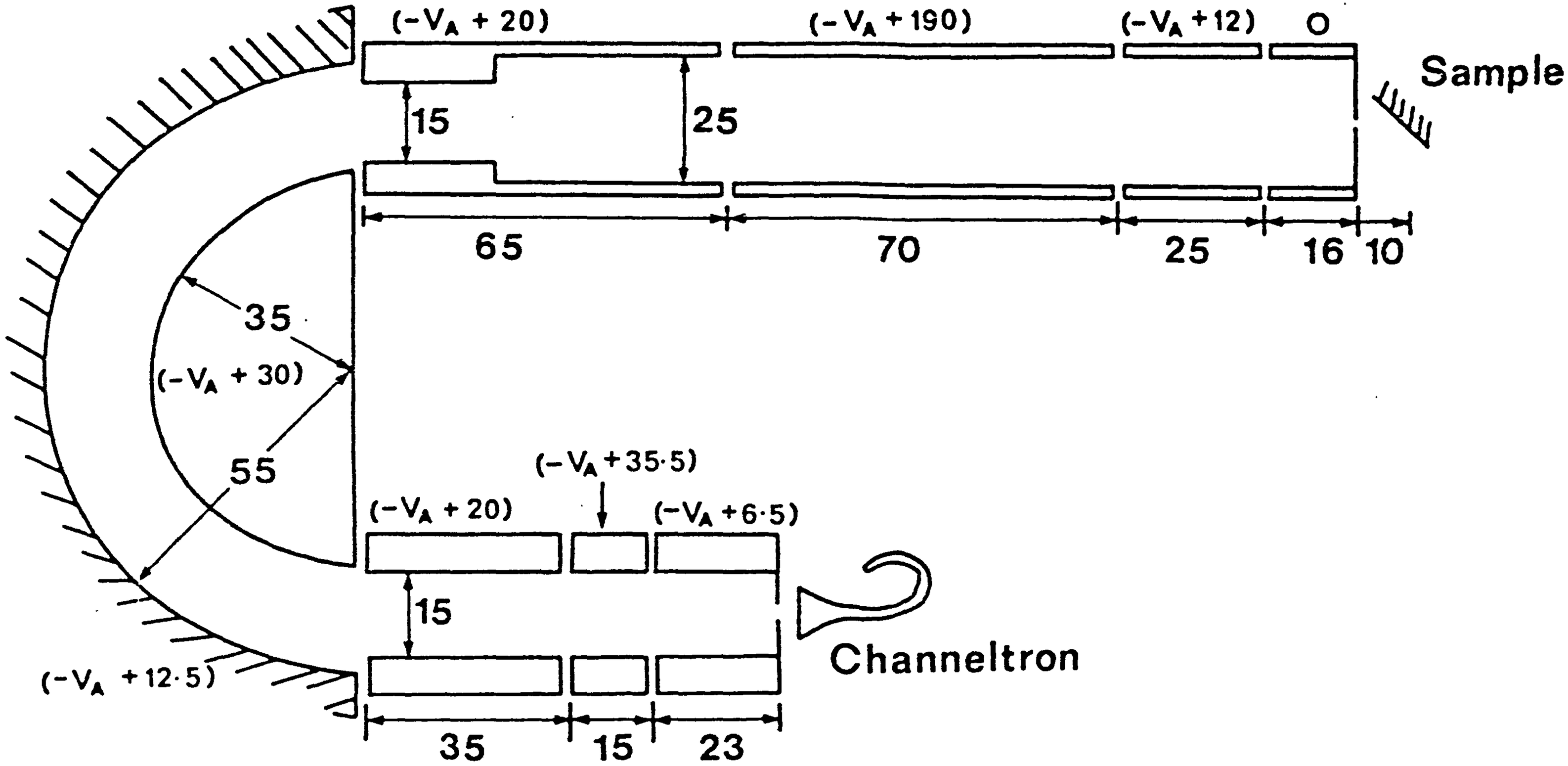

Fig. 3.3(b) A schematic of the CHA depicting the dimensions and voltages on the various elements for one mode.

different modes by simply changing the potentials on the lens elements (externally). These modes are:

(i) The constant pass energy mode.

Varying the input lens ratio (to retard) enables the analyser to scan a spectrum. This mode gives an approximately constant bandwidth ΔE. This is useful for faithful reproduction of N(E) and for obtaining large Auger signal strength at low energy. In this mode, with the pass energy set equal to 20 eV , the window ΔE has a FWHM value of 2 eV, which is roughly constant between 20 eV and 800 eV. τ was determined by using as the electron source a hot filament mounted at the input lens.

(ii) The constant resolving power mode.

With fixed input lens voltage ratio, the pass energy is scanned to record a spectrum. In this mode, the analyser has a constant resolving power $E/\Delta E$, which is favourable for obtaining large Auger peaks at higher energies. As it is used now the input lens acts as a two element lens in the second mode with a retardation ratio of 15 : 1 to make it focus. Comparing this figure with the first mode where the analyser is set to 20 eV, it can be seen that a crossover between high and low energy regions occurs at 300 eV. This means that the largest Auger signal strengths below 300 eV are obtained in the constant window mode, while above 300 eV they are obtained in constant resolving power mode.

The analyser is made from non-magnetic stainless steel (Immaculate 5). The outer hemisphere radius is 55 mm and the inner is 35 mm. The overall outside diameter is 126 mm so it is easily passed down a 6 inch I.D. tube. The lenses are supported on ceramic rods and the hemispheres supported on sapphire balls. The analyser is mounted on an 8 inch conflat

flange, with UHV welded bellows for alignment.

A triax cable is used to bring the signal from the back of the channeltron to the vacuum wall. The triax was found to be necessary for minimising radio frequency interference from the scan coils as well as from external r.f. sources. The voltages for the hemispheres and the lenses were derived through a chain of resistors from two different power supplies corresponding to the two different modes of the analyser. For the constant resolving power mode, a fast-slewing programmable power supply (Kepco type BHK2000) was used. In the constant energy window mode a Kepco OPS2000 programmed via a single diode breakpoint function generator was used. Figure 3.4 shows the circuit diagram of the analyser's electronics. High voltage emitter follower transistors are used. These were found to supply the high currents required to drive long co-axial cables. Rise times of about 100 perμsec are obtained at the analyser, this corresponds to slew rates of about 2×10^5 volts/sec. With the simplified resistor chain (Figure 3.4) the OPS2000 power supply is preferred to the BHK2000. The OPS is nearly 4 times faster than the BHK.

3.4 THE SPECIMEN MANIPULATOR

A simple specimen manipulator shown in Figure 3.5 was designed and built at York. It has an energy absorbing rod to locate the specimen. This had to be a 25 cms long tube packed with 5 μm alumina powder. Under no movement in the laboratory and with the microscope standing directly on the concrete floor, a residual amplitude of vibration of the order of 40 nm was measured (76). The manipulator had a limited linear motion in the three perpendicular directions due to the short bellows used. The bellows act as a pivot, after a 2 - 3 mm linear translation, movement in a

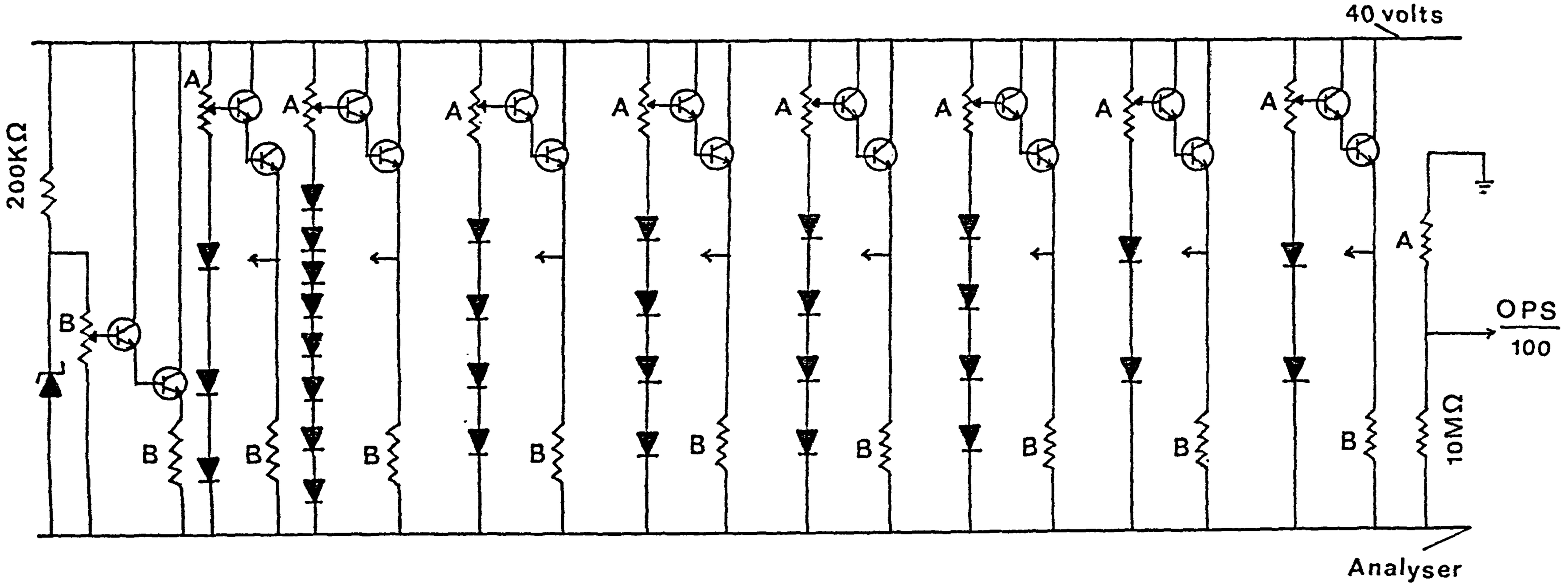

A = 1MΩ

B = 100KΩ

All Transistors BF259

Fig. 3.4 Circuit diagram of the CHA power supply.

perpendicular direction starts. To overcome these problems, two modifications were thought desirable. The first is to add or replace the existing bellows to a length that provides at least 6 - 8 mm translation in the three perpendicular directions, (i.e. a bellows of at least 15 cms long). The second modification is a stage that minimises vibration. Figure 3.6 depicts the designed stage. The idea of the stage is to make the rod effectively shorter with freedom to move in any direction. This can be achieved via the sapphire balls that can slide between two flat surfaces, in order to avoid cold welding. However, neither solution was tested due to difficulties with the vacuum chamber described earlier. The difficulties experienced by the specimen manipulator had necessitated fixing the sample at the first element of the input lens. A sample holder was designed that allows for the specimen to be heated in situ, for cleaning purposes.

3.5 THE SYSTEM ELECTRONICS

One of the features of this SAM is digital scanning of the beam as well as digital signal processing, because of the advantages described in Chapter 2. This in turn required alteration of the signal circuitry of the microscope. In addition, off-set circuits, a voltage controlled oscillator, video amplifiers and signal routing circuitry were also built. Figure 3.7 shows a block diagram of the system electronics. Generally speaking, the system is controlled through two units:

1) The digital microscope controller (DMC) which provides all the system timing and determines the type of display obtained (i.e. Auger, SEM, SEM + Auger, or spectrum).
2) The energy programmer, which determines the required voltages at the

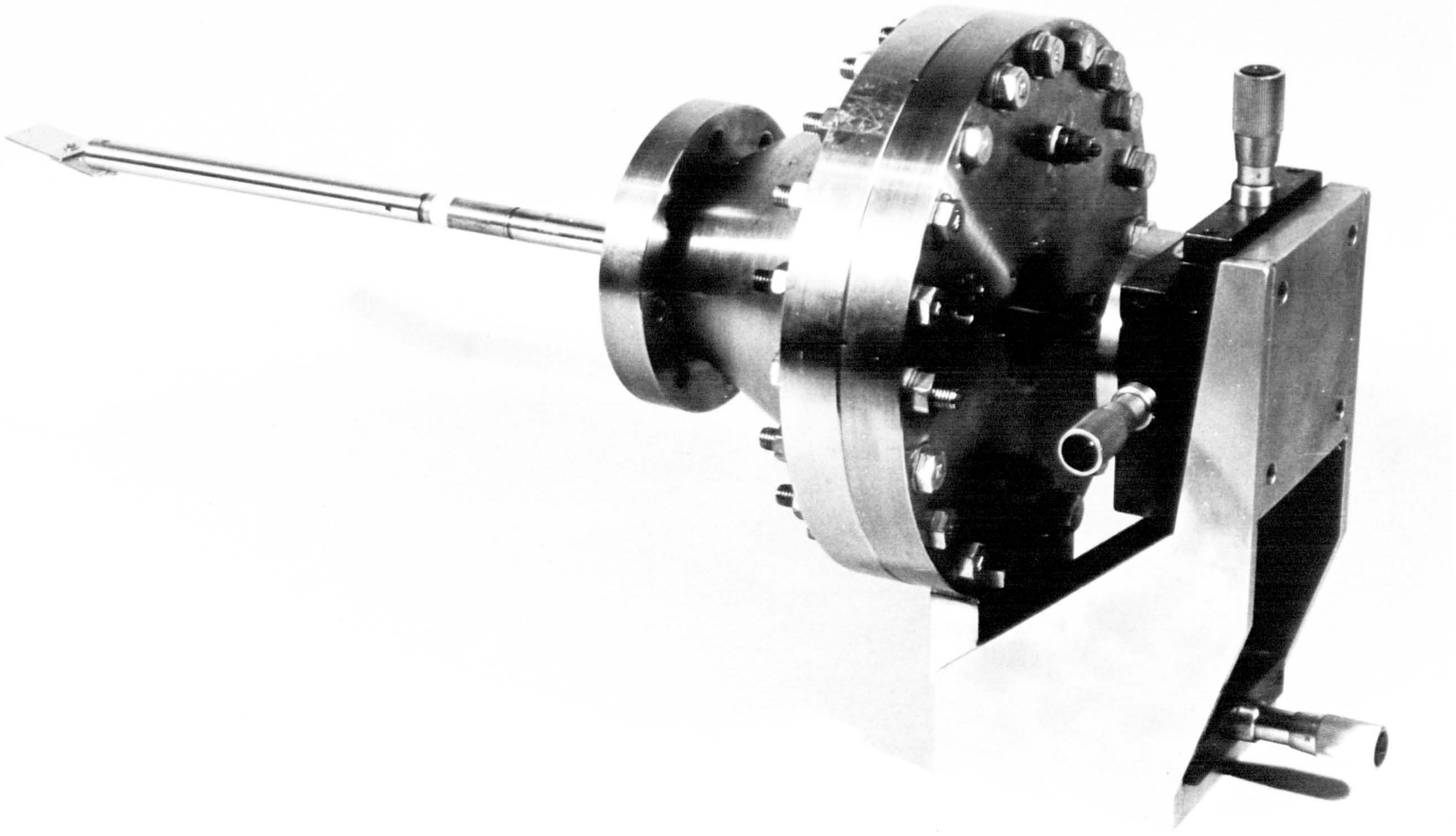

Fig. 3.5 The specimen manipulator of the first instrument

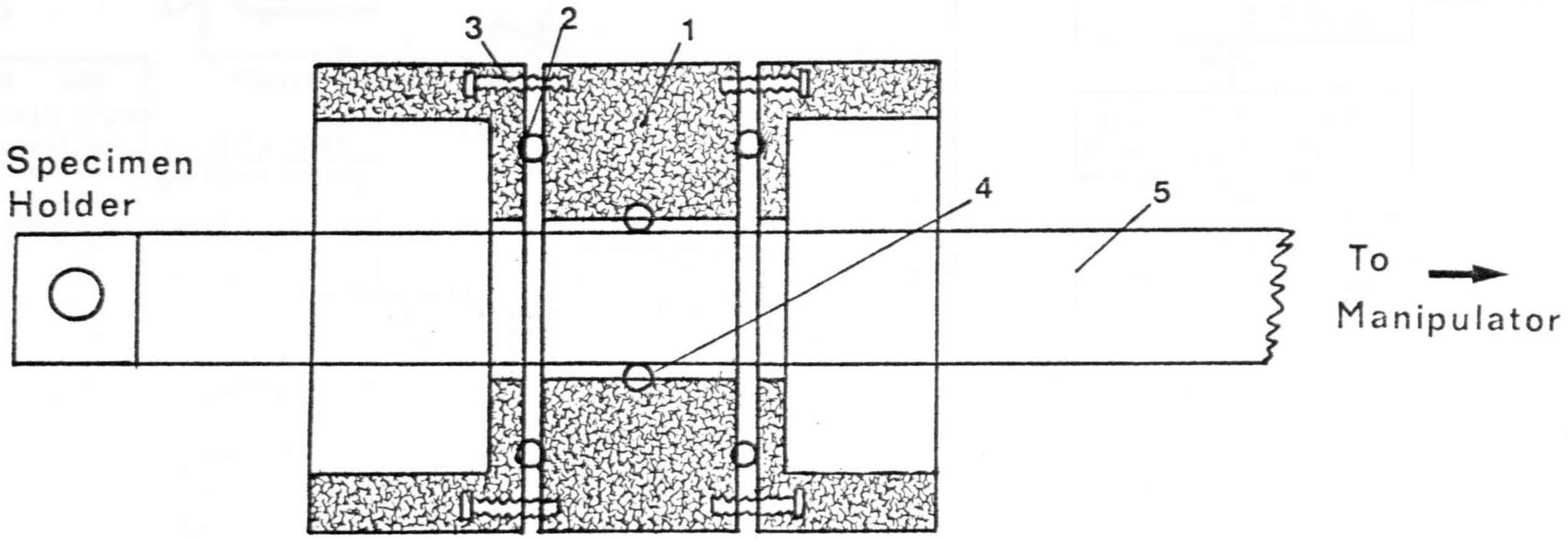

Fig. 3.6 A stage for reducing specimen vibration and to allow for correct translation in the orthogonal directions of motion.
(1) Stainless steel. (2) and (4) Sapphire balls. (3) Stainless steel bolts and phosphor-bronze spring. (5) Alumina packed tube.

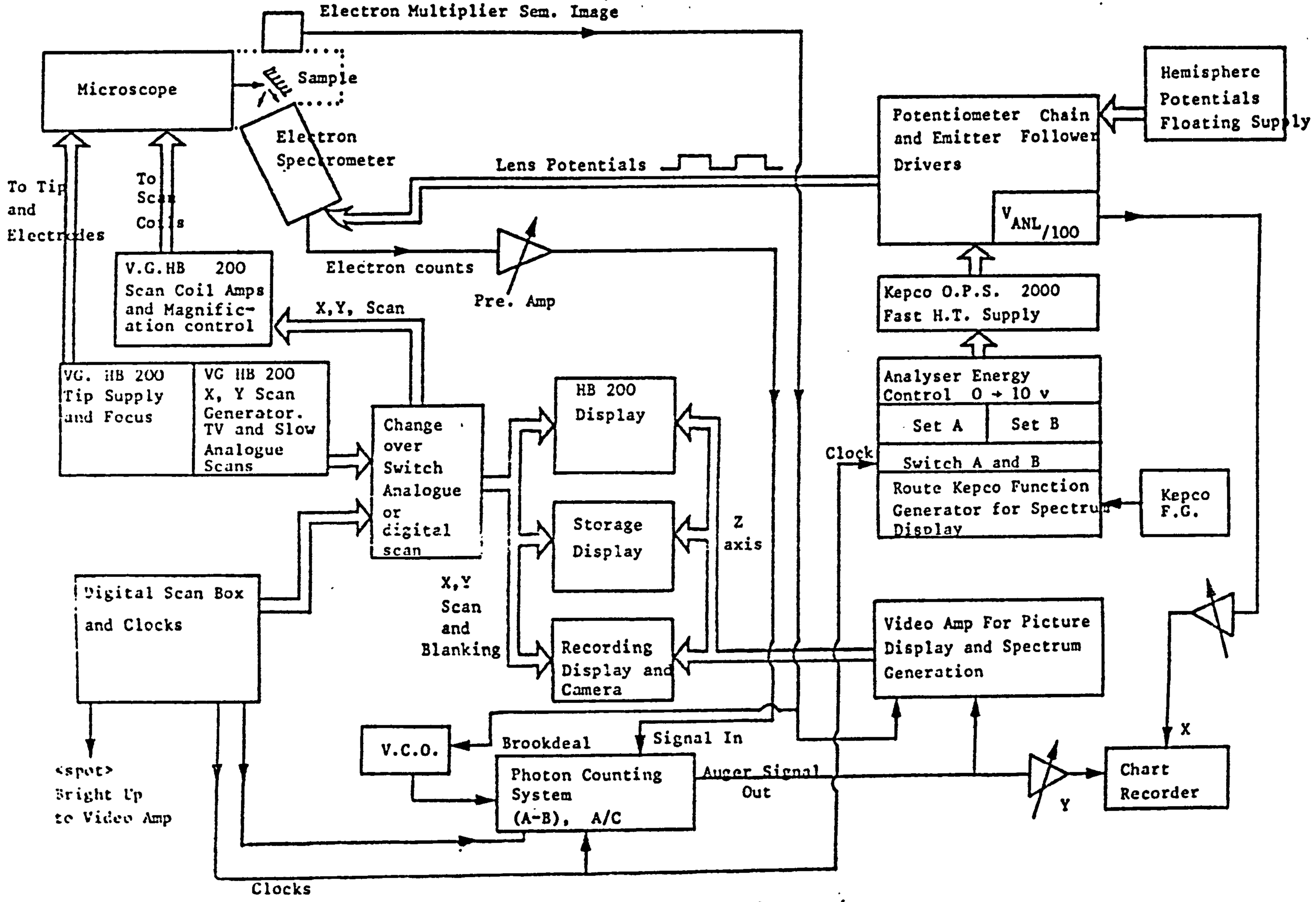

Fig. 3.7 Block diagram of the system electronics.

CHA analyser.

The author has designed and built some of the required circuits namely, the energy programmer, the VCO, the off-set facilities and the trigger, while the rest of these circuitries were all designed and built by R. Browning.

3.5.1 The Digital Microscope Controller

Figure 3.8 depicts a block diagram of the DMC with its frame and line scan generators. The main function of the DMC is providing digital scanning of the electron beam in place of the analogue and TV scans of the V.G. scanning control. It contains over 200 integrated circuit chips, and can be easily interfaced with standard TTL digital equipment. A manual that fully describes the unit, its operation with detailed circuit diagrams, has been written as an internal report (77).

In addition, the DMC provides the following:

(i) Point arrays from 32 to 1024 in 6 steps in x and y directions independently.

(ii) Dewell times on each point of the frame from 10 μs to 1 s in 6 steps.

(iii) Choice of running or single frame.

(iv) Choice of running or single line at a selectable address.

(v) Choice of a point at a selectable address.

(vi) Choice of bright up of the displays at the selected address point either in the SAM or SEM image so that points of interest can be identified. The selected address is displayed.

(vii) Pulses of a half dwell time in length which switch between the energies E_A and E_B selected by using the energy programmers and which gate the photon counter to form counts N_1 and N_2.

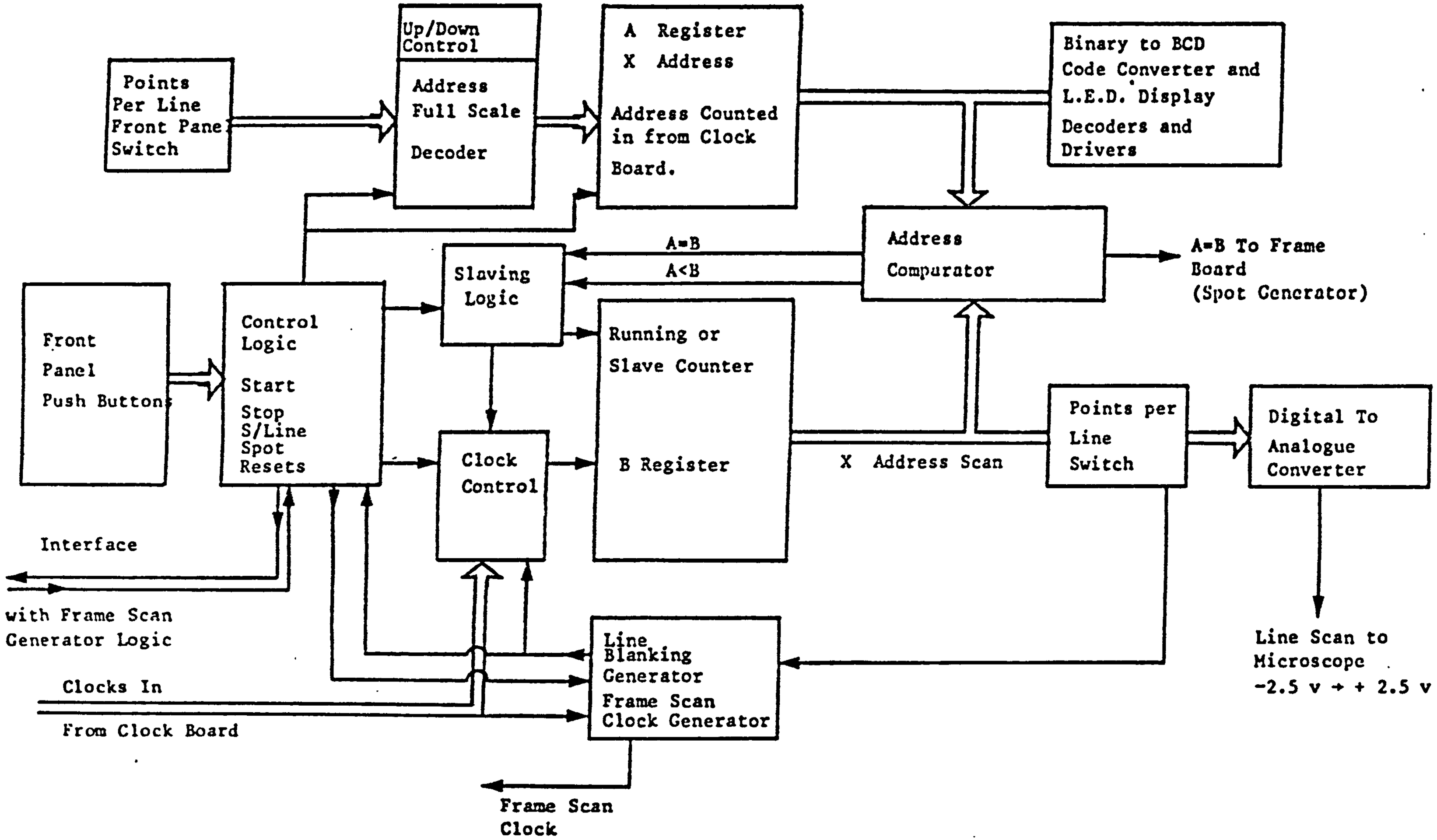

Fig. 3.8 Block diagram of the digital microscope control (DMC) showing (a) line scan generator board
(b) frame scan generator board.

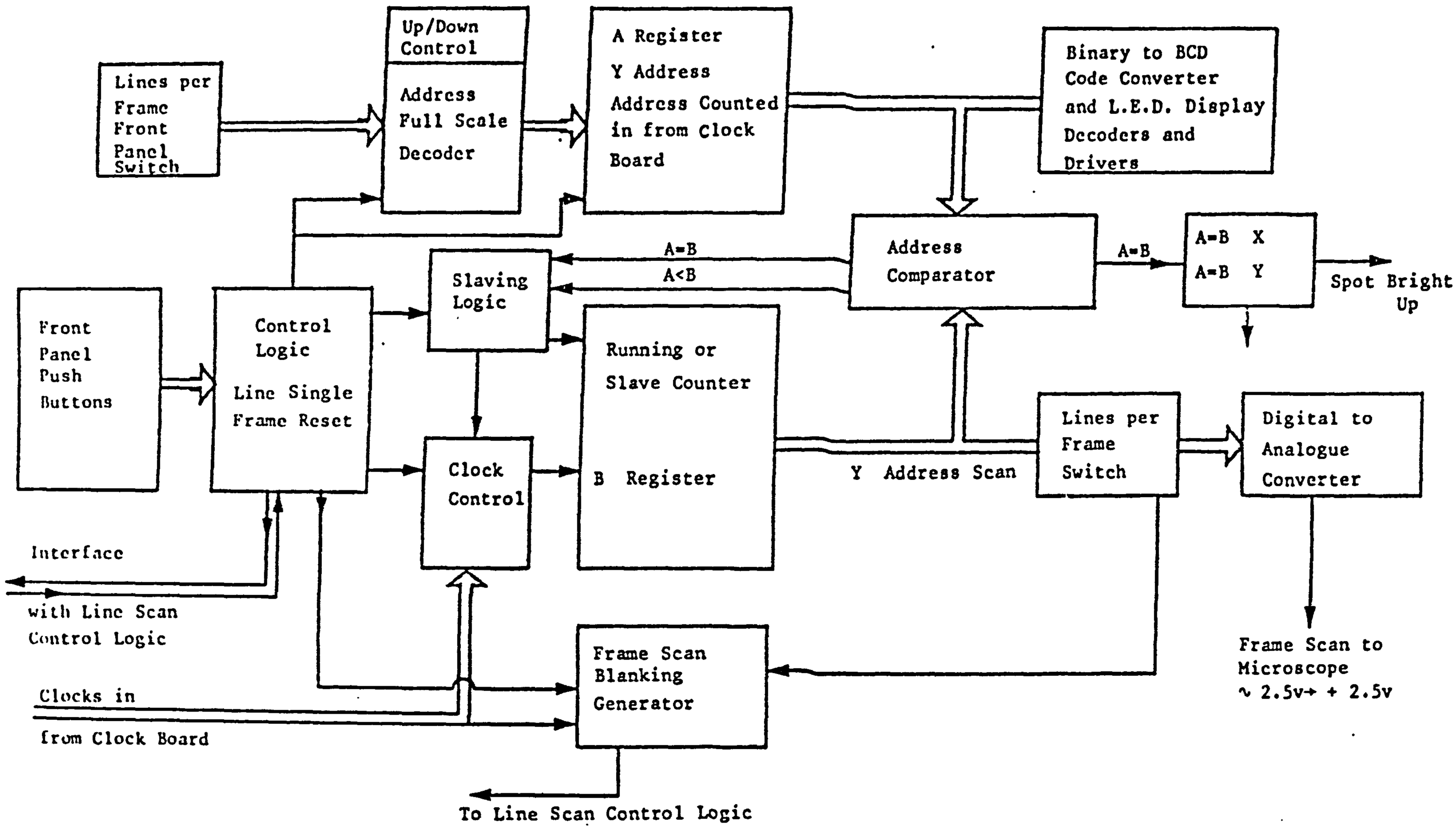
Lines per Frame Front Panel Switch
Up/Down Control
Address Full Scale Decoder
A Register
Y Address
Address Counted in from Clock Board
Binary to BCD Code Converter and L.E.D. Display Decoders and Drivers
A=B
A<B
Slaving Logic
Address Comparator
A=B
A=B X
A=B Y
Spot Bright Up
Front Panel Push Buttons
Control Logic
Line Single Frame Reset
Running or Slave Counter
Clock Control
B Register
Y Address Scan
Lines per Frame Switch
Digital to Analogue Converter
Interface
with Line Scan Control Logic
Frame Scan Blanking Generator
Frame Scan to Microscope
∿ 2.5v→ + 2.5v
Clocks in
from Clock Board
To Line Scan Control Logic

FIG. 3·8b

3.5.2 The Energy Programmer

This unit determines the time sequence of potentials at the CHA. Figure 3.9 depicts a circuit diagram of the energy programmer. It provides the following modes of operation.

(i) Analyser driven by linear voltage ramp from the high voltage power supplies (Kepco BHK2000 or OPS2000) via a single diode break point function generator (Kepco FG100). This mode is used in spectrum display.

(ii) Analyser held at energy E_A or E_B. This mode is used to set up E_A and E_B (described above) whilst the spectrum is displayed. Digital helipots at the front pannel are used to set up the required energy.

(iii) Analyser switched between E_A and E_B during a dwell time determined by the DMC. This mode is used during Auger imaging. The output of the programmer is displayed in a digital voltmeter. The programmer was arranged to drive the two power supplies, BHK2000 and OPS200. The voltage output of the former was found to be noisy at high switching speeds (10,100 ms). At the moment the OPS2000 is used. All modes described above can be obtained with push buttons coupled with LED's.

3.5.3 The Video Amplifiers and Signal Routing

A schematic of this unit which consists mainly of video amplifiers and offset circuits is shown in Figure 3.10. It can provide the following functions:

(i) Give signal switching to the displays so as to allow for the following to be displayed at the turn of a switch

a - scanning electron micrographs.

b - scanning Auger electron micrographs, or

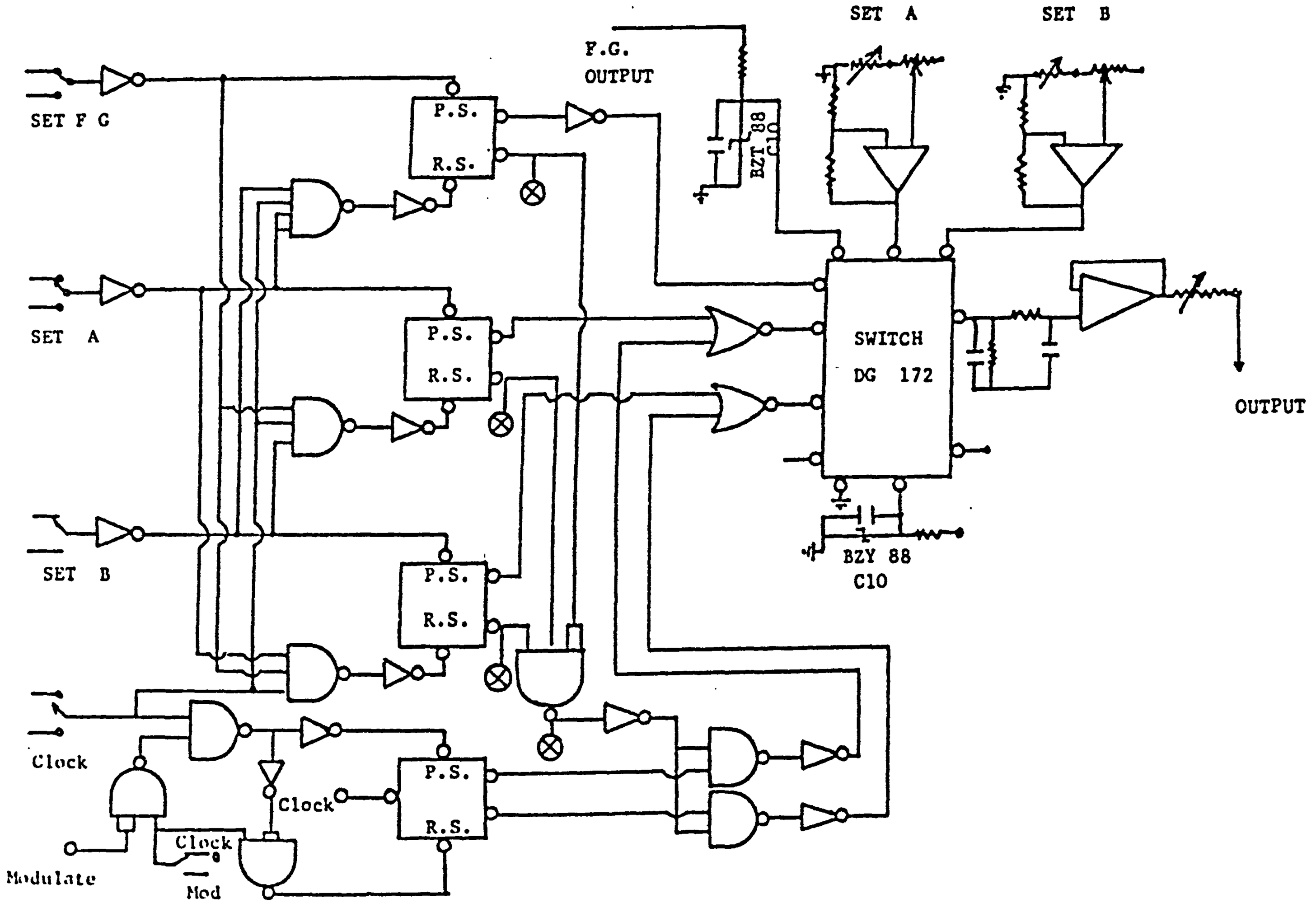

Fig. 3.9 Circuit diagram of the energy programmer.

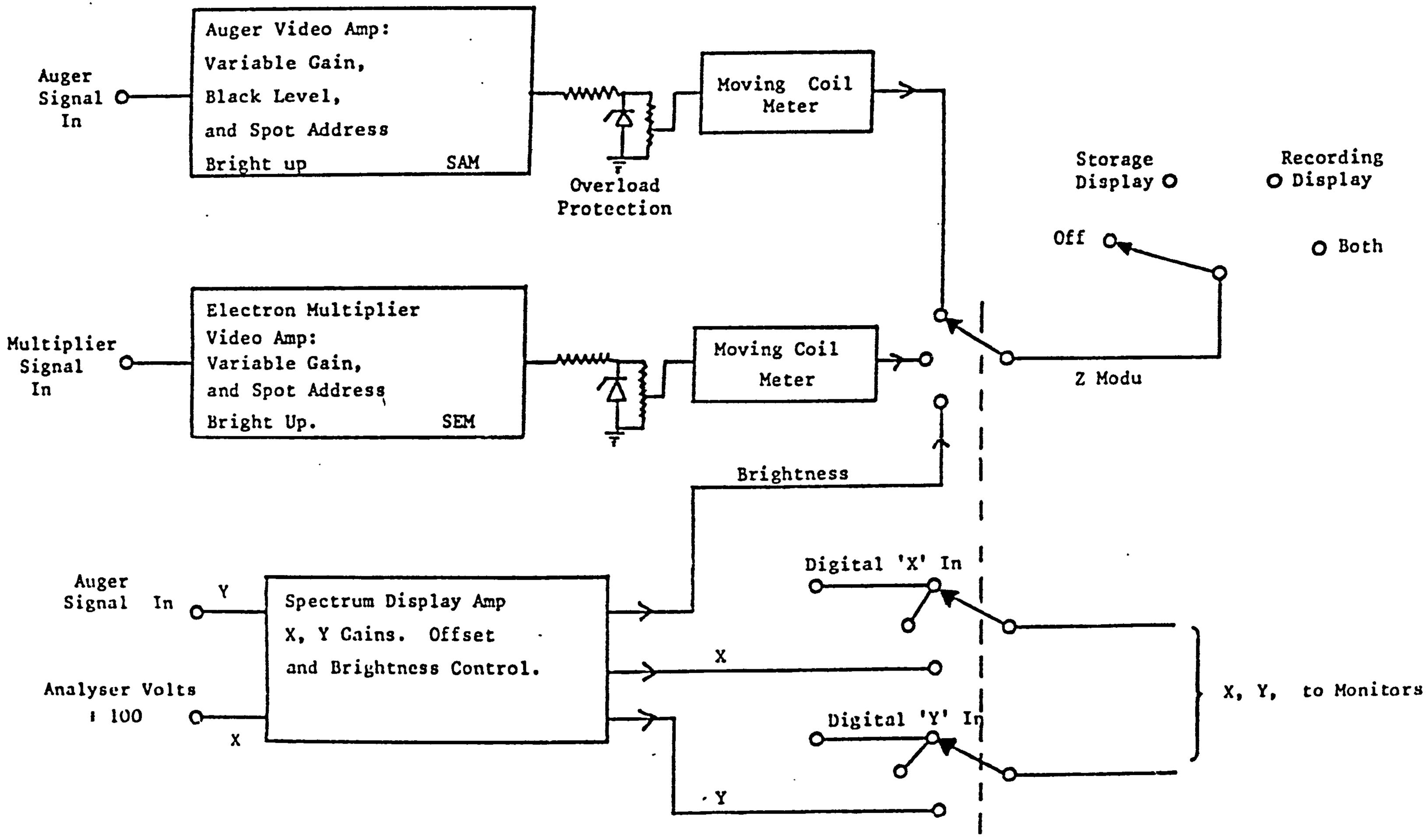

Fig. 3.10 Block diagram of the Video amplifier.

c - the electron spectrum.

(ii) Provide video gain for the correct display brightness.

(iii) Provide black level control.

(iv) Provide a video signal indication on meters as a guide for choosing the photographic exposure times.

3.5.4 X and Y Offset Circuits

It is always useful to be able to select a limited spectral region of the displayed spectrum and fill the display with it. Two amplification and offset circuits that can provide this facility were incorporated. The circuit diagram of this unit is shown in Figure 3.11. Both amplifiers have maximum gain of 100, a bandwidth of 3 Hz, and a maximum offset of effectively 1000 volts. The D.C. stability of the unit is better than 0.1 μv/sec.

3.5.5 Trigger Circuit

At low beam currents, the signal to noise ratio can be very poor (see discussion in Chapter 2). One way of overcoming this difficulty, without loss of high resolution, is by accumulation of spectra by repeated scans and then averaging the obtained spectra. A Nicolet 1020 digital averaging oscilloscope can provide such a facility. To interface the microscope with the Nicholet 1020, a trigger circuit was required. A circuit diagram of the trigger is shown in Figure 3.12. The output of the trigger is 4 volt square wave. This technique however, is not used routinely in SAM; nevertheless, it adds a useful facility to the instrument.

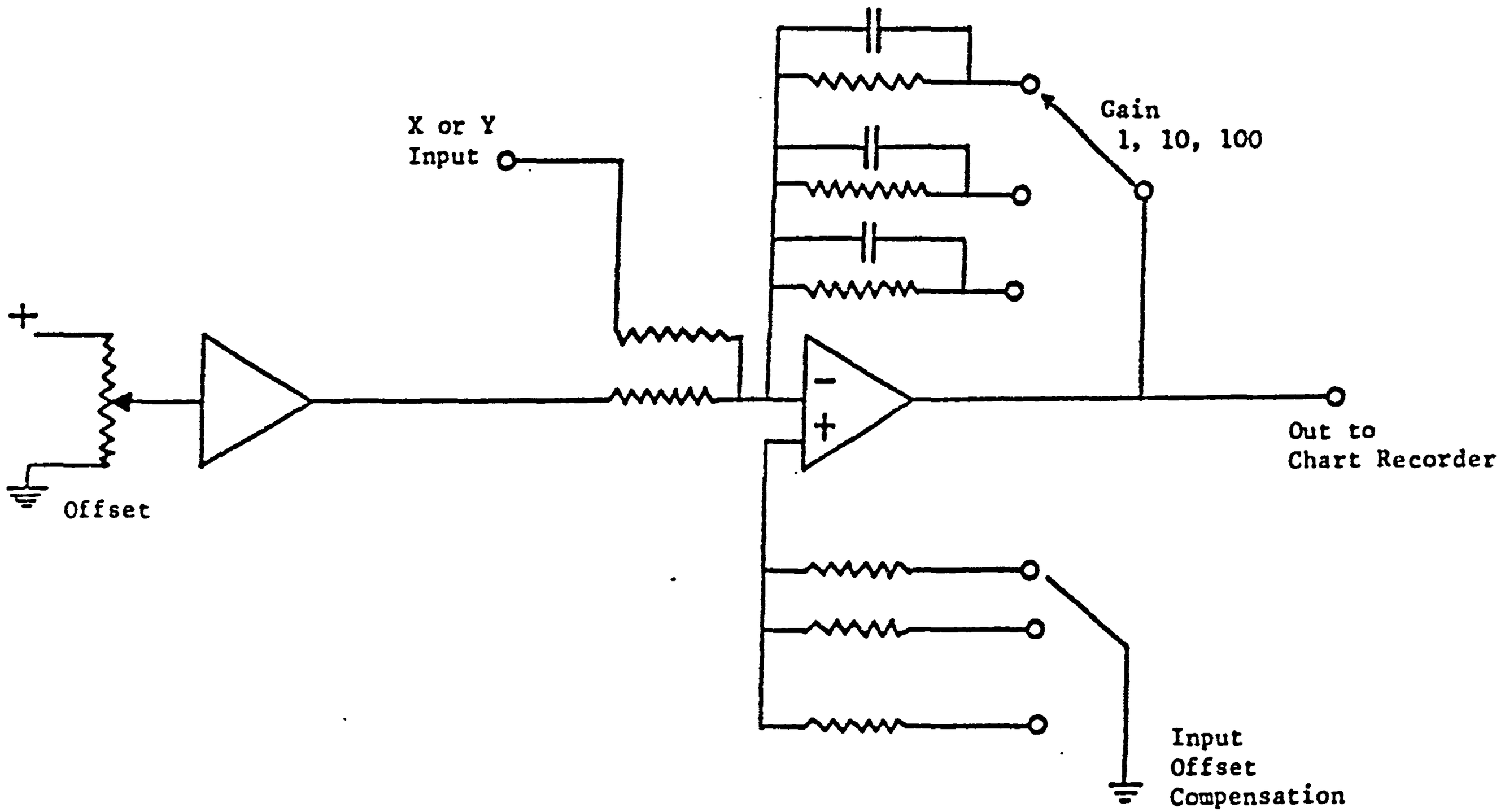

Fig. 3.11 Circuit diagram of off-set circuit.

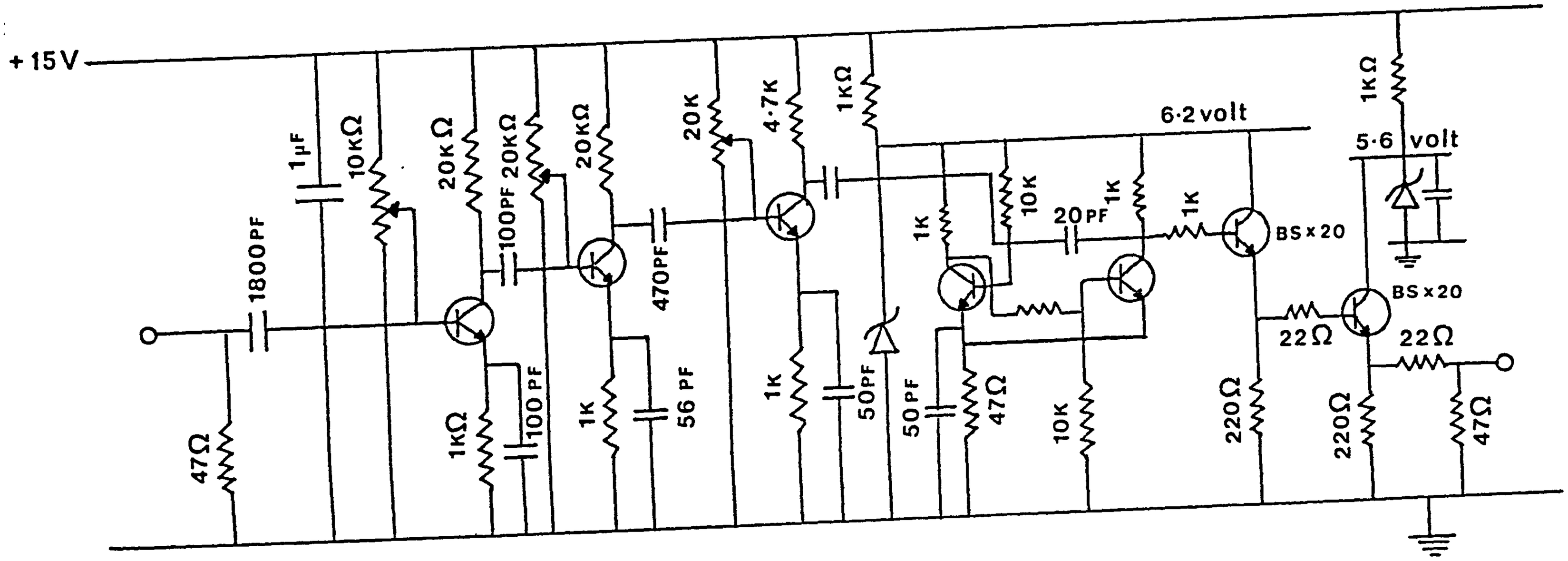

All Transistors BF×89
unless specified

Fig. 3.12 Circuit diagram of the trigger facility.

3.5.6 The Voltage Controlled Oscillator (VCO)

Although the field emission source is capable of delivering high current density in a smaller probe diameter than the conventional thermal emitter, it has an associated difficulty with it. This in fact is an expected difficulty with the present state of anode materials and vacuum conditions. As a result of gas adsorption onto and sputtering of metal atoms from the emitter tip, there is unsteady beam current. This effect can be reduced to a minimum, for meaningful mapping, if the Auger signal can be divided by a signal proportional to the fluctuating beam current. To correct for this effect in this instrument, the output from the scintillator/photomultiplier detector used for the SEM is taken as the signal proportional to the beam current. The SEM output is used to derive a voltage controlled oscillator which produces pulses at a frequency C proportional to the beam current. At the end of a data acquisition time (during the recording of a spectrum, or at the end of a dwell time during the recording of an image) a current derived from C is converted to an analogue level and divided into the output of the photon counter ($N_1 + N_2$) for spectra, ($N_1 - N_2$) for images, by using a standard analogue divider. As described in the last chapter, this division in addition to reducing the noise due to beam current fluctuation, reduces the effects of topographical contrast in the Auger image. Figure 3.13 depicts a schematic of the voltage controlled oscillator (VCO). A temperature compensated non-linear amplifier control is added to the VCO to improve its linearity (better than 1% of inputs between 0.1 and 3.0 volts). It has variable dispersion, but is conveniently used with 1 MHz per volt of input from the SEM photomultiplier. Figure 3.14 demonstrates the correction gained by using this method for a deliberately ten-fold reduction in beam current.

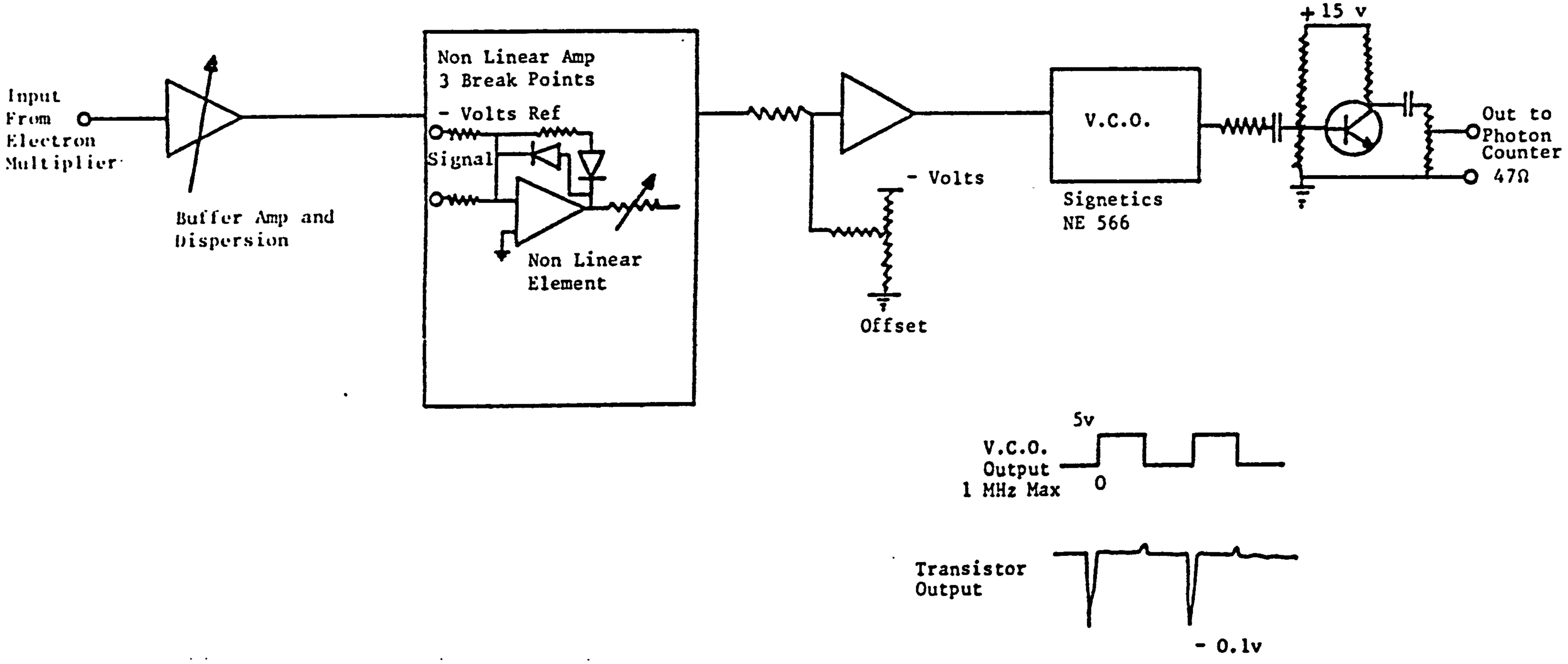

Fig. 3.13 Circuit diagram of the voltage controlled oscillator (VCO).

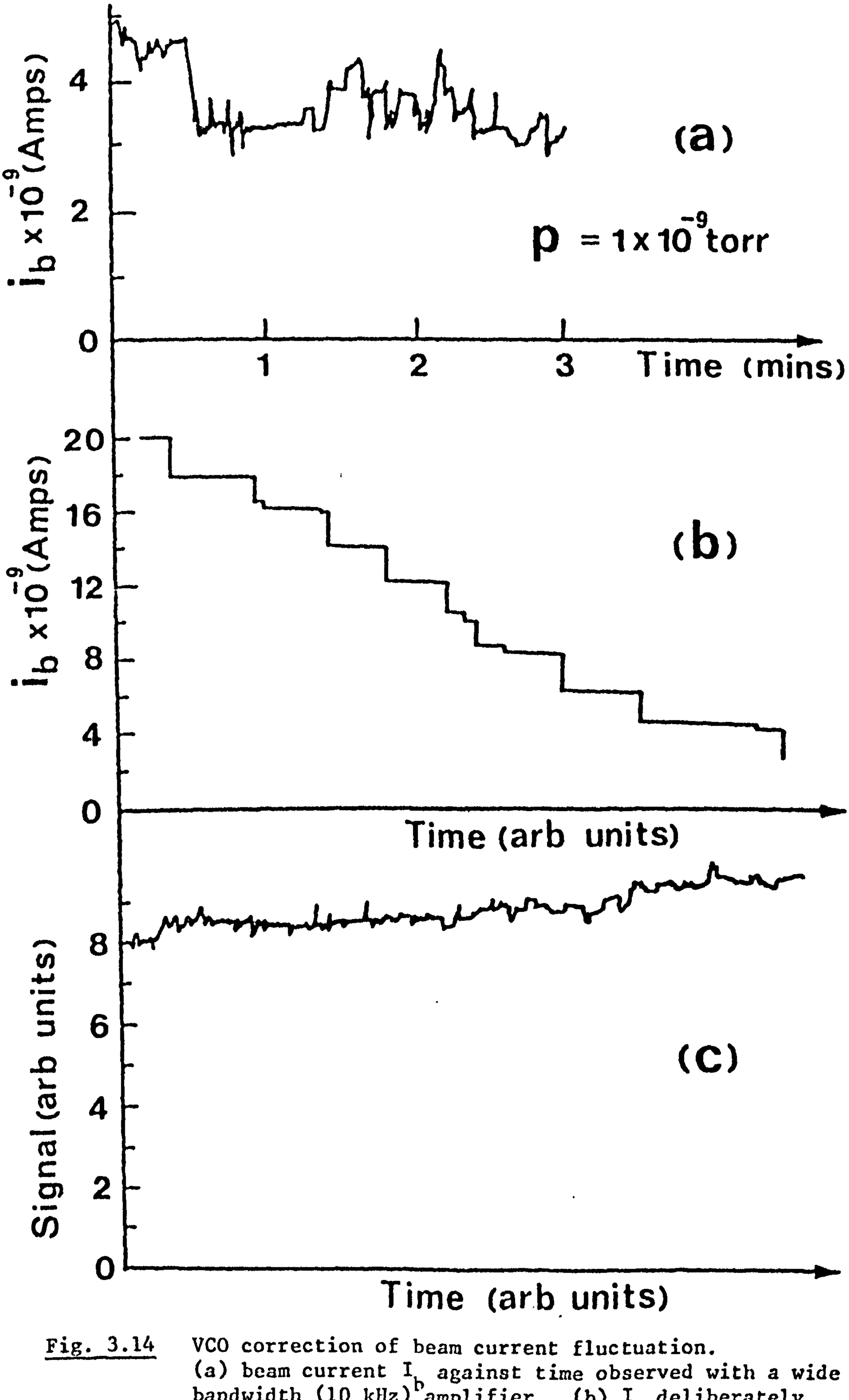

Fig. 3.14 VCO correction of beam current fluctuation. (a) beam current I_b against time observed with a wide bandwidth (10 kHz) amplifier. (b) I_b deliberately changed in successive steps over a factor of ten in size. (c) Carbon KVV Auger signal divided by the VCO signal derived from I_b. I_b changing as given in (b).

3.5.7 The Racal Store 7 Recorder

The inconvenience of repeating frames of times above 15 minutes can be avoided by recording the image on a magnetic tape as it was generated. Three channels of a Racal Store 7 instrumentation recorder are used to record the synchronization and brightness levels of an image at a speed of 2.4 cm/sec. Play-back to the visual and photographic displays can then be carried out at speeds of 20.3 cm/sec and 15 2 cm/sec. This method gives a useful reduction in display time which assists in setting up the displays for photography. In addition, it reduces the beam dosage of a sample which in turn assists in obtaining truthful images.

3.5.8 The Displays

Three displays are used in this system. The HB200 display which was supplied with the microscope. This is used for selecting the area of interest for analysis in the secondary electron mode. A storage display which is used for presenting the Auger image for visual purposes and for presenting spectra during fixed point chemical analysis. This is a Tektronix Model 605 storage display. It has variable persistance time up to about 15 minutes and about 12 tones of grey level scales. The third display is a Tektronix Model 602 which is used for good quality image photography.

3.6 THE PERFORMANCE OF THE FIRST INSTRUMENT

3.6.1 The Vacuum System

As has been described earlier, and because of the use of field electron emitters, the gun chamber is isolated from the main vacuum system

by a gate valve and a 300 μm differential aperture. As a result a pressure level of about 10^{-3} - 10^{-2} with respect to the main vacuum system can be maintained at the gun during operation and about 10^{-9} torr with the main chamber at atmospheric pressure with the gate valve closed.

After 16 hrs of bake-out at about 170^{o} C, a base pressure of about $3 - 5 \times 10^{-10}$ torr is achieved in both systems. It was found that this is sufficient to operate the emitter with emission currents of the order of a few micro Amps (i.e. display a SEM image at TV rates), but emission instability of up to 20 - 50% results for an increased emission current to a few tens of micro Amp (i.e. the requirement for Auger imaging). Furthermore, a deterioration of the pumping speed of the ion pumps was noticed after a few years of use giving a pressure limit of 8×10^{-10} - 10^{-9} torr. Inspection of the ion pump's anodes showed both discolouration and wear. Regeneration of the anodes by glass beads blasting resulted in very little improvement in this case.

The most serious problem with the vacuum system was a recrystallization of the brazed joint between the mu-metal of the vacuum chamber and the stainless steel conflat flange carrying the CHA, as a result of the heavy weight of the latter. Crystallites of the order of 1 - 2 mm were visible. This caused a vacuum leak to develop during bake-out, which limited the system pressure to about 5×10^{-7} torr. This situation has prevented the use of the instrument as a SAM and was an important factor in the decision to re-design and construct the second instrument.

3.6.2 The Field Emission Gun

The use of the field emission gun as an SEM probe was successful apart from the deterioration of the pumping speed of the ion pump with time. A resolution of the order of 35 - 50 mm was obtained when the instrument was first delivered. The removal of a 100 μm limiting aperture has increased

both the beam current and diameter to 5 x 10^{-9} A and 100 nm respectively.

In the Auger mode, where a large amount of emission current of about 40 - 50 μA is needed to give a beam current of the order of a few nA, it was found that the emitter has to be operated for a few hours with gradually increasing emission to the above value before a stable emission of about 10 - 15% can be achieved. This was mainly because of the inadequate out-gassing of the first anode and the low pumping speed around the emitter.

As a result of the fixed focussing ratio of the gun lens, and the limitation of the high voltage supply, sharp electron emitters had to be used. These were disadvantageous particularly with micro-discharges giving a high rate of emitter destruction. In addition it was found that, occasionally, emitters are destroyed during cleaning by being bent, while still sharp at the tip. This is thought to be due to stresses at such high fields or developing during fabrication of such small radii emitters and acting to cause it to bend in one direction during the passage of current. A reverse voltage less than that required for emitter build up was found necessary to be applied to the emitter during cleaning to reduce this effect, (i.e. by keeping the emitter in a uniform field that counteracts the mechanical stresses during cleaning). It must be mentioned, however, that such a precaution is not normally employed in conventional field emission microscopy (FEM), where much blunter emitters, (of up to an order of magnitude), to the present case are usually used.

Finally, the use of mu-metal in the construction of the vacuum system has resulted in an additional problem to that mentioned above (section 3.6a). This was a deterioration of the magnetic properties of the material due to the fact that it has been used externally. Mu-metal is known to lose its magnetic properties if it is either hardened or machined. This effect has allowed A.C. interference from the laboratory mains and

other equipments to increase the effective electron beam diameter by about a factor of 3x - 4x.

3.6.3 The CHA

With the completion of the first instrument, preliminary tests were carried out to assess its performance and to establish the power of SAM and the fields that may benefit most from it. The first tests were performed on a polycrystalline titanium wire (99.99 titanium). The low melting temperature of the Ti causes it to re-crystallise with large grain boundaries. This could then be imaged. The surface was hand polished with different grades of diamond grit (to 1 μm particles size) to produce a thin section at its centre. The sample was mounted, in a holder, on the first element of the input lens with provisions for in situ heating.

The FWHM of the energy distribution of elastically scattered electrons from the titanium surface was measured to test the energy resolution. Figure 3.15 shows a comparison between the constant band pass mode with 20 eV pass energy and the constant retardation mode with the input lens focusing at 15 : 1 retardation. It was found that the performance of the four element input lens is dominated by its aberrations. This effect has caused the FWHM of the elastic peak to increase from 2 eV when measured at 30 eV to about 2.6 eV at 1000 eV (59). A computer simulation of the characteristics of this analyser is being carried out at the moment. The preliminary results confirmed the aberrative nature of the lenses but suggest that different sets of lens potentials are visible that should give better focusing (78).

A constant resolving power of about 130 was obtained when the input lens was operating in the two element mode with constant retardation of 15 : 1. In this mode, the analyser's transmission falls sharply for incident energies below 200 eV, so restricting its use. The deterioration in the

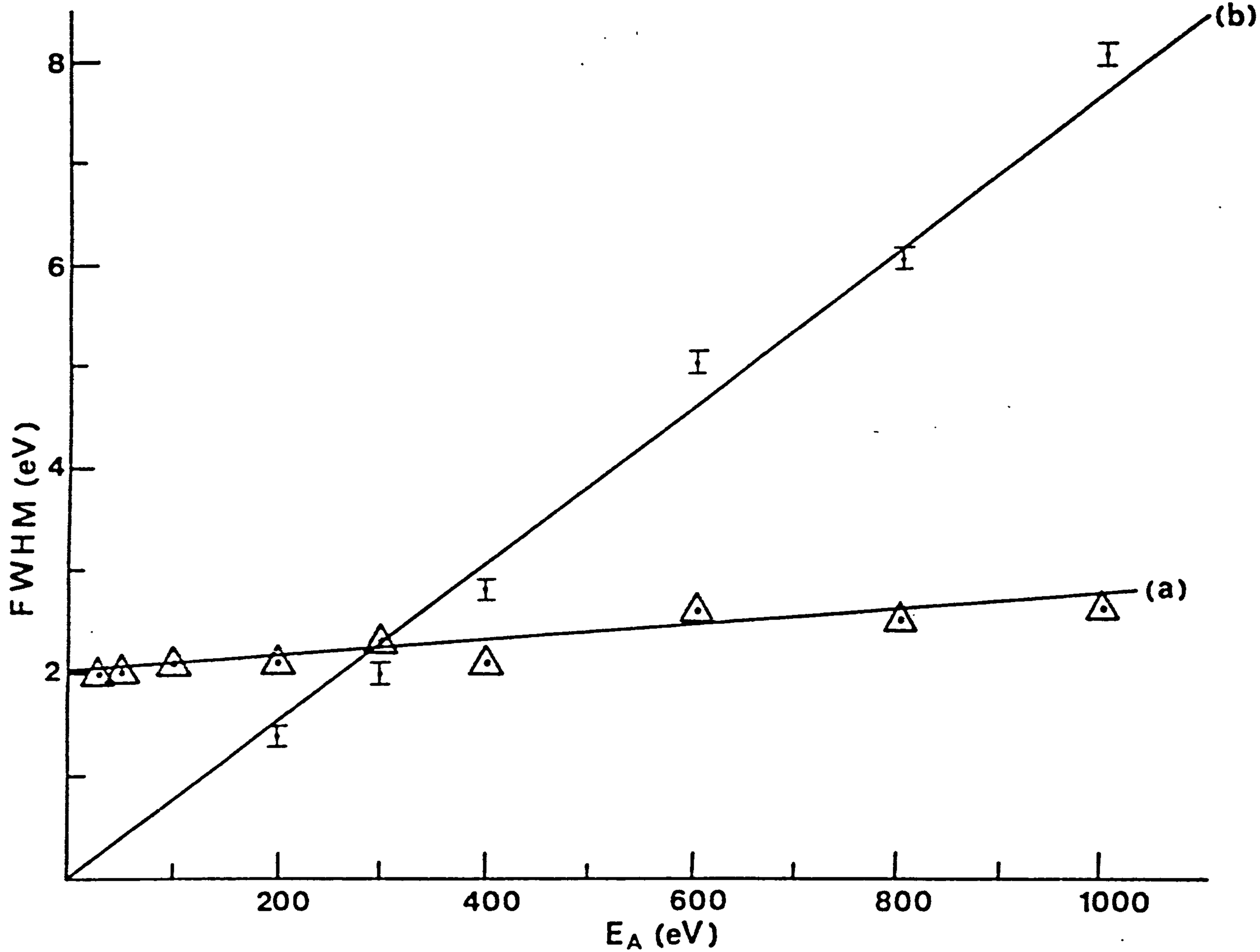

Fig. 3.15 Full width at Half Maximum (FWHM) of the elastic peak scattered from a polycrystalline Ti sample.
(a) pass energy of 20 eV.
(b) constant retardation of 15 : 1. $\Delta E/E \approx 130$.

analyser's transmission was caused by residual magnetic fields in the gap between the hemispheres and in the output lens. A serious misaligning effect was found as the kinetic energies in the hemispheres and the output lens fell below 13 eV and about 1.5 eV respectively. However, such a fault should be easy to remove by using an improved magnetic screening in the critical regions.

The Ti sample was heated to a dull red colour for a few minutes to remove part of the overlay carbon and oxygen. Spectra obtained from a fixed point on the titanium surface, for both modes, after the above treatment is shown in Figures 3.16(a), (b). Titanium, oxygen and sulphur Auger peaks are observed. The signal to noise ratio in the spectra are close to those expected for shot noise in the collected current. Figure 3.16 demonstrates the serious degradation of transmission below 200 eV in the constant resolving power mode. A comparison between oxygen peak heights in Figures 3.16(a), (b), shows an increase of about 90% in the constant resolving power mode. This increase however is due to the fact that the window ΔE is about 3.8 eV in the constant resolving power mode and 2.4 eV in the constant window mode. By taking the ratio of the electron count per unit window width for the two modes, and by using Figures 3.16 and 3.17 together, the relative efficiencies of the two modes can be obtained. This relative efficiency peaks at about 300 eV at a value of 1.5, the constant resolving power mode having higher efficiency than the constant bandwidth mode. This results from the magnetic field effects upon the two element mode operation at low energies, and to the magnification of the four element input lens which rises as the energy falls.

3.6.4 Auger Imaging

Before the titanium sample was heated, a small region of very low contrast was observed in the SEM image. Spectra from within this region and

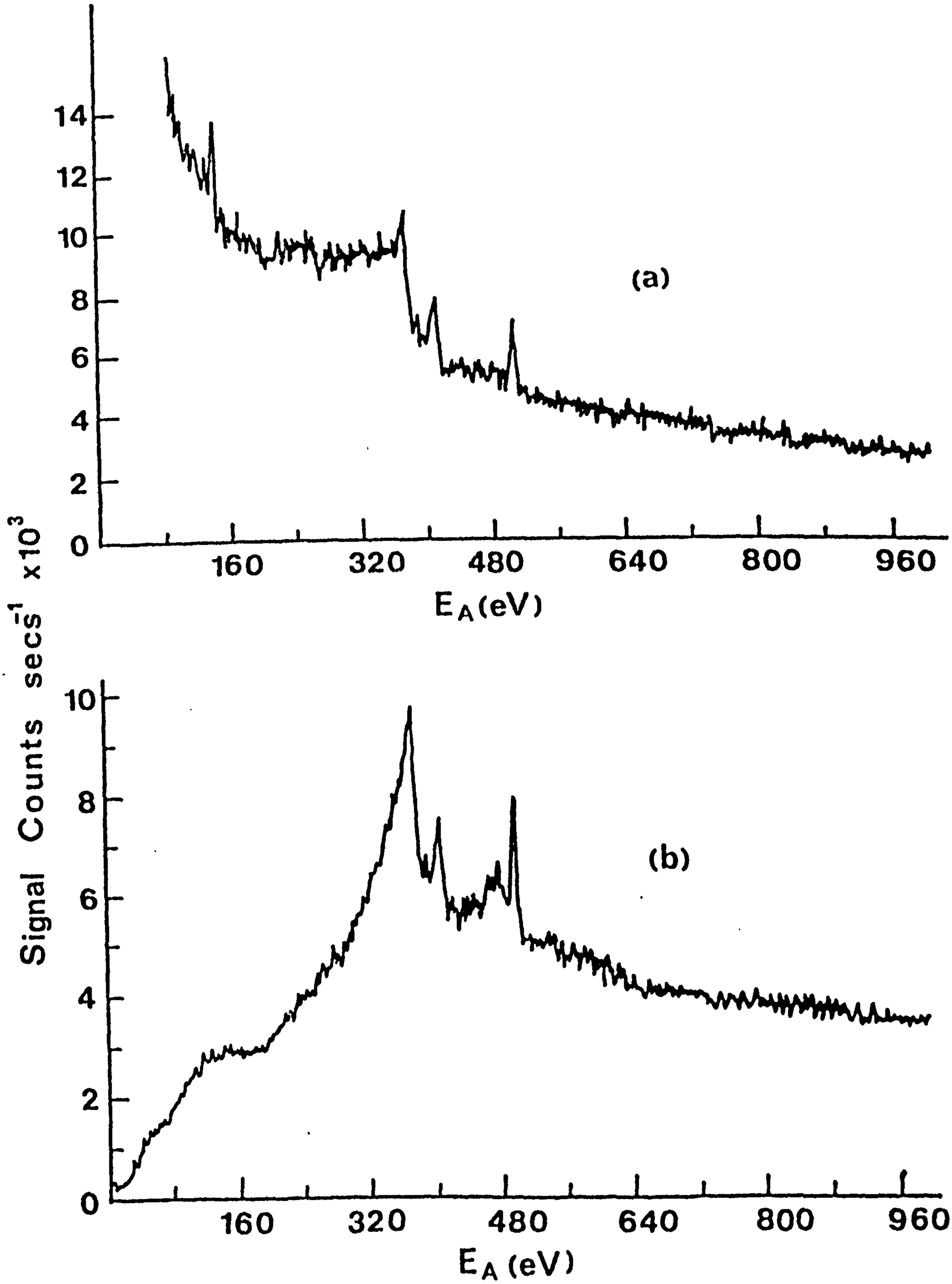

Fig. 3.16 Spectra from Ti sample after heating to about 700°C for few minutes. Sweep rate 7 eV s^{-1} ; Ep = 25 keV ; I_b - 6 nA, count time 1 sec. (Constant band pass mode E_A = 20 eV. (b) Constant resolving power mode ρ = 130.

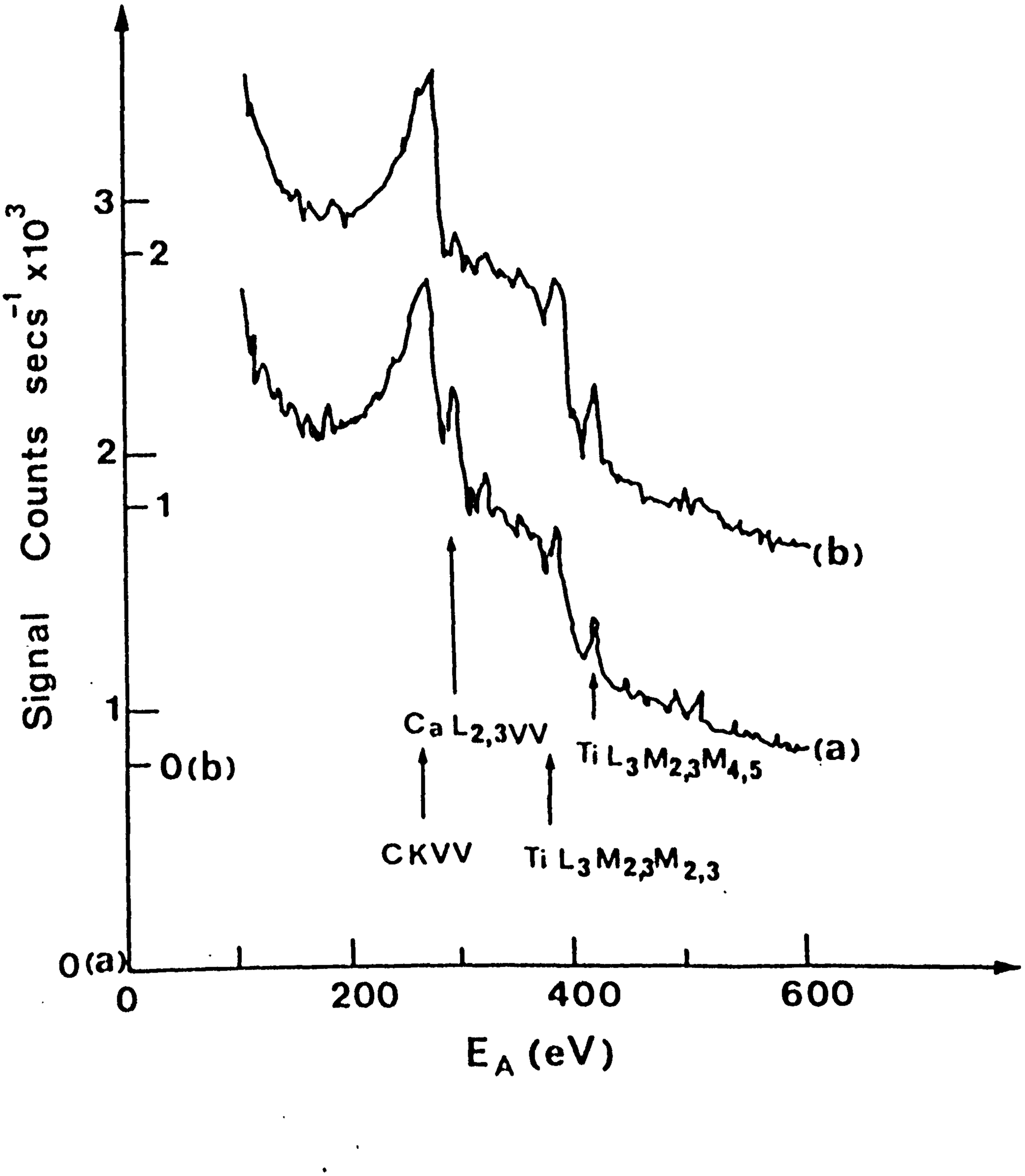

Fig. 3.17(a) and (b) Spectra on and near a region of low contrast in the SEM of Fig. 3.19(a). I_b = 1 nA, $\tau = 10^{-1}$ s ; T_F = 27 min.; E_A = 288 eV ; E_B = 296 eV ; E_p = 25 keV.
(a) Spectrum on the region. ΔE = 2 eV.
(b) Spectrum off the region. ΔE = 2 eV.

beside it were taken in the constant window mode. Figure 3.17 shows the results obtained using a beam current of 10^{-9} A which gave rise to about 2000 counts/sec, ΔE = 2 eV, and primary energy of 25 KeV. The strong carbon peak suggests the presence of an overlayer of carbon on the surface. Comparing spectra in Figures 3.17(a), (b) revealed the presence of a chemical species on the low contrast region which is not present in the background Figure 3.16(b). This was attributed to the calcium L_{23} VV transition at 288 eV. The peak to background ratio was about 0.14 at the above conditions. The presence of calcium was not expected, (compare with Ti spectra in Handbook for Auger spectra (79)), but it could be due to the polishing process used. This region was thought to be interesting, and an attempt was made to test the SAM imaging using it. Figure 3.18 shows frame scans of 128 x 128 pixels with a dwell time of 0.1 second per point, E_A = 288 eV and E_B = 296 eV giving about 27 minutes per frame. The presence of C , S , and Ti in the two spectra of Figure 3.17 suggests that the Auger images obtained are of a calcium patch on a titanium surface contaminated with both sulphur and carbon. When an attempt was made to image either carbon or sulphur on titanium, no structure in the obtained images could be found. From these observations it was believed that these materials were uniformly distributed over both the titanium and the calcium.

Further heating was applied (through several stages amounting to a total of 1 hr) in order to clean the sample and to cause some further structure at the grain boundaries to appear. As a result, the sulphur KVV Auger transition at 150 eV grew significantly while the carbon KVV almost disappeared. An SEM image is compared with a sulphur Auger image in Figure 3.19. Although a spatial resolution of 0.4 μm per point could be obtained in Figure 3.19(b), no well defined concentration gradients of sulphur could be observed in the Auger image. Figure 3.20 shows a spectrum taken from the most intense region in Figure 3.19(b).

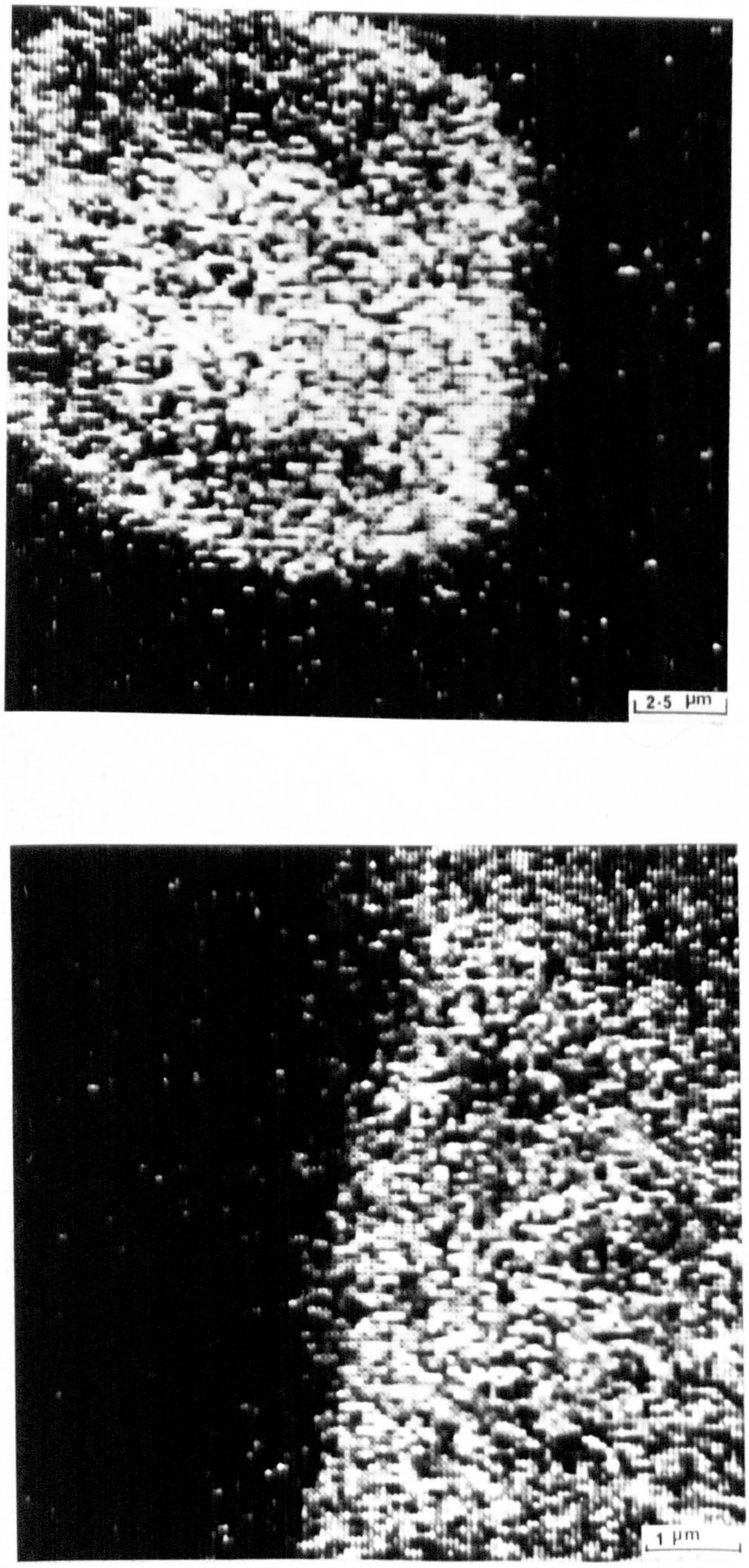

Fig. 3.18 Frame scans on and near a region of low contrast in the SEM image (Fig. 3.19(a)). Conditions as in Fig. 3.17. (a) Ca Auger image 128 x 128 pixels. (b) Auger image on the edge of the bright region in (a).

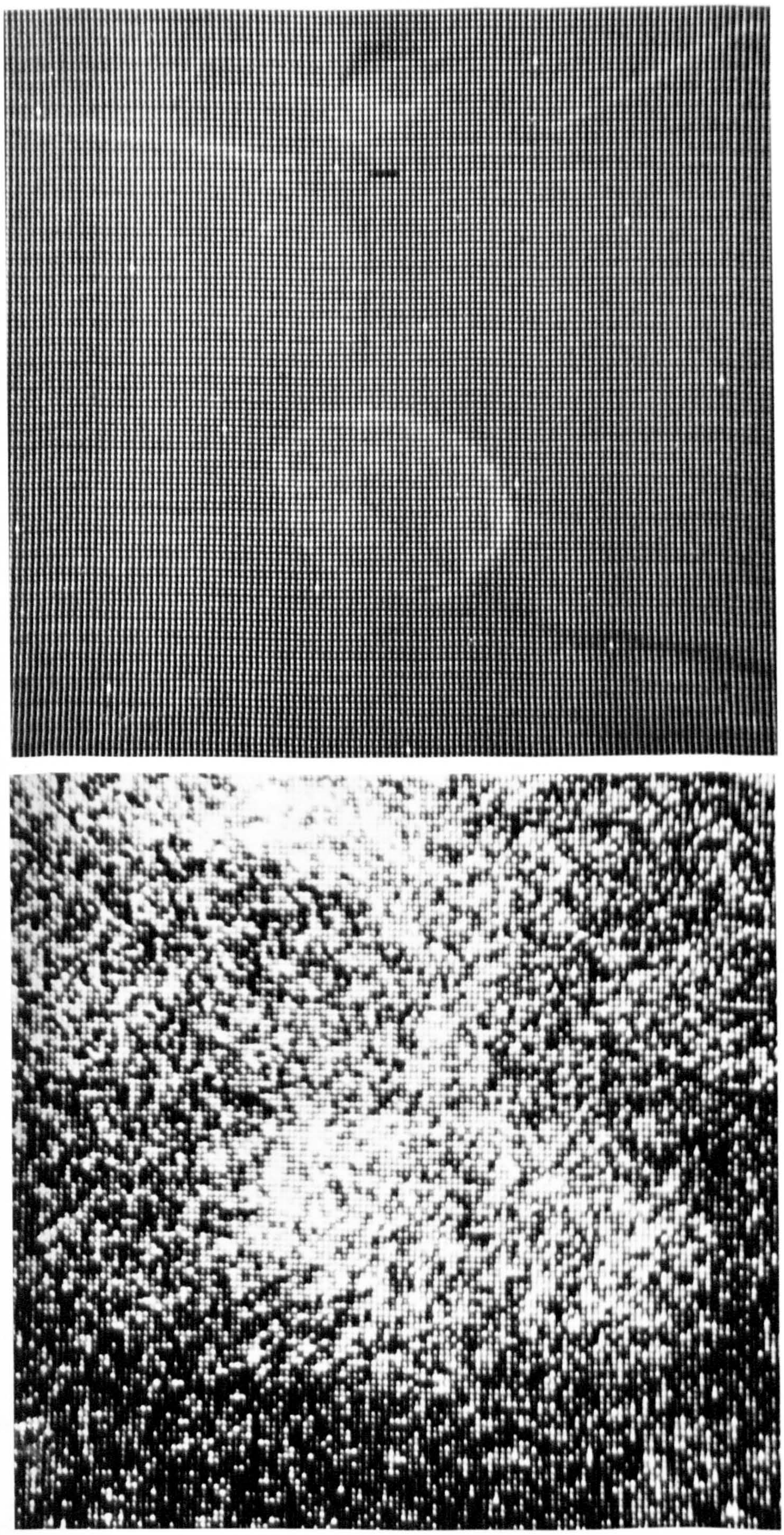

Fig. 3.19 Frame scans of (a) SEM image of low contrast feature. (b) Sulphur KVV Auger image of (a) above after heating the sample to ~700°C for few minutes. I_b = 5 nA, $\tau = 10^{-2}$ sec, E_A = 150 eV, E_B = 160 eV.

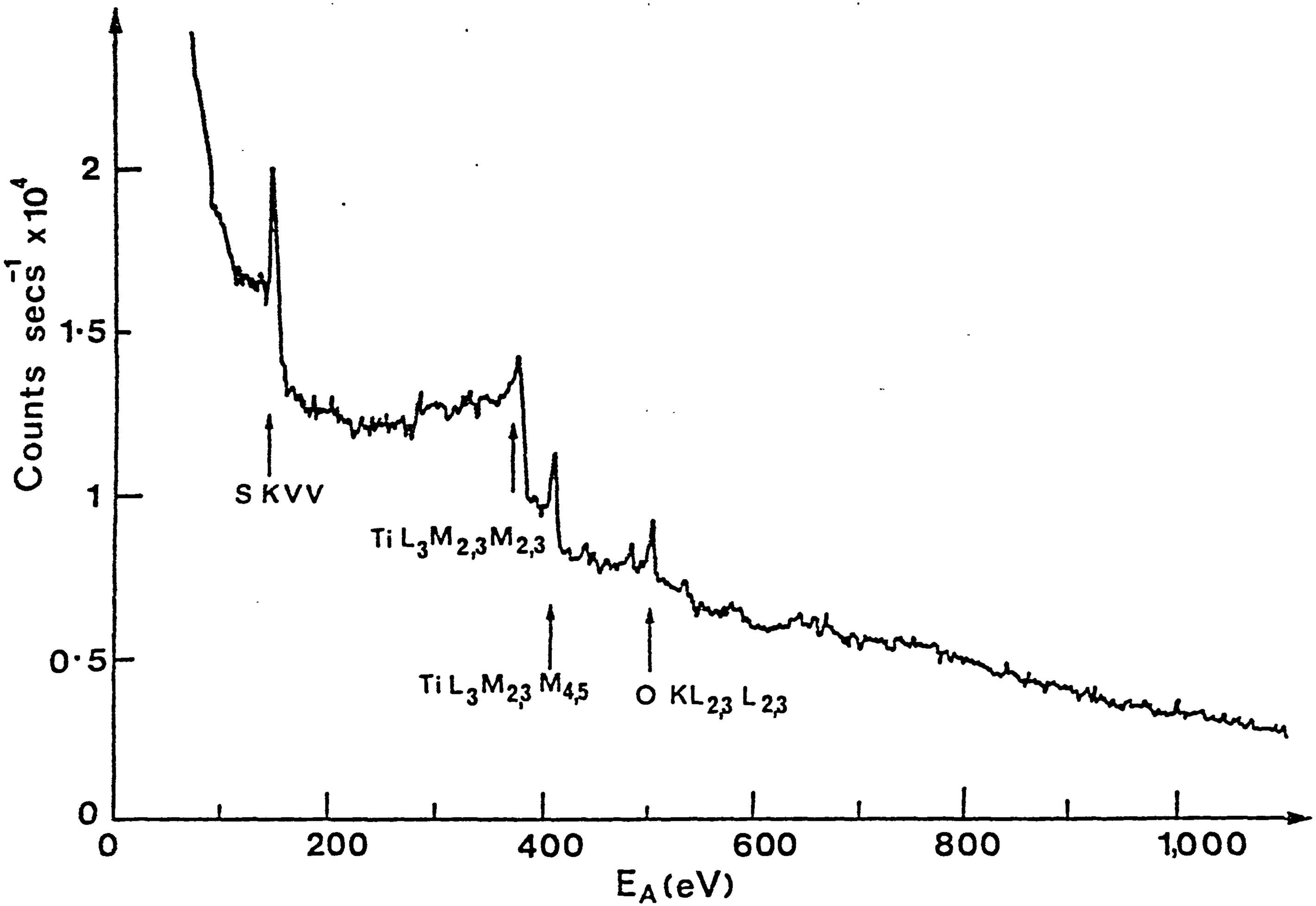

Fig. 3.20 Spectrum of region most intense in Fig. 3.19(b) conditions as in Fig. 3.19 but $\tau = 10^{-1}$s, sweep rate is 10 eV s^{-1}.

3.6.5 The Spatial Resolution

At this stage of development, an estimate of SAM spatial resolution is important for its evaluation against other analytical techniques, such as EMPA.

Line scans in the SEM mode revealed that the spatial resolution was about 100 nm. In the Auger mode however, there was no feature that could be used to test the spatial resolution. An attempt to form a sharp chemical edge of Au/Si or Ag/Si was not successful (see Chapter 5).

Generally speaking, and in the case of detecting small isolated particles, or for determining the minimum gap size between two extended particles, the primary beam diameter with a useful signal to noise ratio will be the main factors in determining the spatial resolution, assuming normal incidence electron beams. Backscattering in this case will be almost negligible. For edge resolution on the other hand, other factors should be included in determining the resolution. These are, the angle of incidence, the primary energy and the orientation of the edge with respect to the scan direction. The extent of the effects of these factors on the spatial resolution of SAM will be dealt with in more detail in the following chapters.

3.7 DISCUSSION

Over the past few years a number of scanning Auger electron microscopes have been reported. A quantitative comparison of these instruments with the one reported here is rather difficult because of inadequate data available about the other instruments. However, some properties of interest for SAM, which are usually quoted are listed in Table 3.1 for some of the reported instruments. These were chosen on the grounds that they feature UHV conditions, a sub-micron resolution, and Auger maps were

Author	Spatial Resolution nm	I beam Amp	Energy Analyser	Electron Gun	Signal Processing	Frame Scan Time (min.)
MacDonald et al (80)	5000	2.5×10^{-8}	CMA	T	Analogue	102
Christou (82)	500	1×10^{-9}	CMA	T, FE	Analogue	21
Ishida (83)	700	8×10^{-8}	CMA	T	Analogue	15
Venables et al (68)	30	2×10^{-8}	CMA	FE	Analogue	8.5
Browning et al (59)	100	5×10^{-9}	CHA	FE	Digital	28
Mogami (64)	70	5×10^{-10}	CMA	T	Analogue	——

T = Thermal electron source

FE = Field electron emitter

Table 3.1 A comparison of some reported SAMs featuring submicron resolution UHV conditions and facilities for Auger mapping.

presented. An exception to the above criteria is the instrument reported by MacDonald (80). This is particularly interesting to include in the comparison in order to shed some light on how much the technique has developed since its introduction.

From the above table it is clear that a great improvement in resolution and frame scan times has been achieved since the first instrument was reported. The improvement is a direct result of the use of field electron emitters as electron sources. This is due to the fact of their higher brightness in comparison with conventional thermal emitters. It must be emphasized however, that a thorough investigation on the use of field emitters as electron sources in SAM is needed. This is because of the larger amount of emission current needed in SAM compared with conventional SEM. As the emission current increases the energy distribution of the emitted electrons changes to a higher value (81). In addition, the stability of the emitted electrons deteriorates.

An investigation on the use of different field electron emitters in high current probes with necessary conditions for electron current stability of a few percent will be given in Chapter 6.

A comparison of different electron sources for high resolution SAM was reported by Christou (82). This comparison is not correct for the following reason. With reference to Figures 1 and 2 of Christou, the Au M_5 N_7 N_7 Auger transition at 2024 eV is given for three different electron sources with the same beam current. However, it is to be expected that different spot sizes would result due to different probe designs, energy spread, etc., hence changing the current density and causing a different SNR to be obtained for each source. No details of spot size were given in the above comparison.

All the reported instruments were based on a CMA system. The present instrument is the only one to use a CHA. It has been shown that a

properly designed CHA with input and output electron lenses is advantageous to use in SAM. The trade-offs in such a choice would be complexity and cost in comparison with CMA.

One area that has not been developed yet is computer controlled systems. With the complexity of the technique as well as the amount of data acquired, a computer controlled system should prove useful. The next stage of development of the present instrument would feature such a facility.

3.8 CONCLUSION

A digital scanning Auger electron microscope incorporating a concentric hemispherical analyser (CHA) has been constructed. A beam current of 10^{-9} - 10^{-8} A in a spot of diameter of about 100 nm has been achieved. These figures allow Auger images of the order of 16000 pixels to be obtained in frame scan times of the order of 27 minutes. The instrument has facilities that compensate for beam current fluctuations and topographical interference from the examined surfaces.

The performance of the instrument can, however, be improved by some modifications to the existing system. Particularly the specimen chamber has shown great inflexibility in performing experiments or techniques complementary and sometimes essential to SAM. These are, ion sputtering, gas admittance, in situ evaporation of thin films, LEED, and RHEED. In addition inadequate magnetic shielding which resulted in a deterioration of the resolution of the microscope as well as the analyser, and the recrystallization of the vac-braze have limited the use of the instrument.

A new multiport chamber that avoids the above mentioned constraints was designed, as will be described later. The whole instrument is enclosed by magnetic coils which makes the magnetic field at the centre less than

5×10^{-7} T .

The field emission gun supplied by V.G. Microscopes could also be improved. The improvements are by incorporating a higher speed pump to cope with the gas load produced, proper outgassing of the first anode, and possibly the use of a different field emitter that offers higher brightness at lower voltages. Alternatively, a new design could prove useful, with higher resolution in addition to the above mentioned modifications, (Chapters 6 - 8).

The problem of high resolution SAM has not yet been justified. Energetic backscattered electrons give rise to Auger electrons in addition to the primary beam. It is not known if these backscattered electrons put a low limit of resolution in SAM, as is the case in EMPA. Christou (82) has claimed an order of magnitude degradation on the spatial resolution of SAM due to backscattered electrons. But no theoretical justification of these measurements has been reported yet.

This point is important for the quantification of SAM at this stage. In addition, the results would direct developments of electron probes for SAM. And for this study it would clarify whether or not a new design of a field emission gun would be beneficial. The next two chapters will be concerned with this problem.

CHAPTER 4

THEORETICAL INVESTIGATION OF THE EFFECTS OF THE BACKSCATTERED ELECTRONS ON THE SPATIAL RESOLUTION OF SAM

4.1 INTRODUCTION

High spatial resolution is one of the features which can favour one analytical technique to another. In the Electron Micro Probe Analyser (EMPA) for example, the sample to be analysed is bombarded with a beam of electrons of kinetic energy between 10 - 30 KeV. As the electrons penetrate the sample x-rays are generated up to a few microns from the point of impact with the emission concentrated around the centre of a pear-shaped source. For Copper at 29 KeV, Reed (85) found that the best obtainable resolution with EMPA is 1.1 μm. The low resolution of the technique can be attributed to two reasons. The first has a physical nature in that the collected x-rays come from the pear-shaped emission source whose radius is the dominating factor in determining the resolution. The second reason is less important and is in part technical. The efficiency of the x-ray production per incident electron is typically between 10^{-3} - 10^{-2}. This requires a high density of incident electrons which means a large electron beam diameter.

The resolution of the Scanning Electron Microscope (SEM) on the other hand depends largely on origin of the collected signal. In the secondary electron mode a resolution of better than 2.5 nm can now be easily achieved. In the low loss mode where high energy backscattered electrons are the collected signal, Wells et al. (86) show a point to point resolution of 3 nm and an edge resolution of 1.5 nm.

The problem of SAM resolution is more complicated than in either EMPA or SEM. It has been shown in Chapter 1 that the Auger process is an alternative, (to x-ray production), for relaxation of an ionized atom.

This means that the Auger electrons are produced within the same volume as the x-rays. Although x-rays suffer from absorption as they emerge from the target, a big fraction can still be collected. This absorption depends on energy, the atomic number and composition of the sample and can be an order of magnitude less than the generated signal (87). Auger electrons which suffer energy losses of more than 3 - 5 eV appear in the background as secondaries. As a result, the efficiency of production for the collected Auger electrons is worse than for x-rays, being usually 10^{-5} - 10^{-4} per incident electron. This means that the collected Auger electrons come from the top few atomic layers which causes the technique to be surface sensitive. These electrons are produced in one of four ways. Most are produced directly by the incident electrons, some by elastically scattered electrons, some by energetic secondaries and some by backscattered electrons. The size of the contribution from the last three ways is referred to in the literature as "the backscattering factor" r which has a value between $1 < r < 2$ depending on the target material, energy and angle of incidence of the electron beam. The effect of these electrons on SAM resolution was not known before this work. A similar situation as in EMPA may arise where a lower limit of resolution results due to the back-scattering radius of the backscattered electrons rather than the electron beam diameter.

Christou (82) has compared different electron sources for high resolution SAM. His conclusion is that the limit of the spatial resolution in SAM is ten times the probe diameter. He attributes this result to the effects of energetic backscattered electrons. Christou's conclusion was based on experimental measurements which did not seem well characterised for the test. Two points in particular were not clear in his experiment. The first is that the edge sharpness of the test sample (sputtered 5-µm gold dots on a silicon substrate) was not defined. At high resolution a

sharp chemical edge is necessary. The second point concerns beam diameter which seems to have been deduced from aberration coefficients of the optical column rather than being measured. In addition no theoretical investigation was available for comparison and support of the experiment.

The present chapter is a theoretical investigation of the effects of the backscattered electrons on the spatial resolution of SAM. The aim of the work is to establish whether a low resolution limit in SAM exists or not. The answer to this question should set the criteria for a new electron probe to be used in the second instrument.

The method of calculation should be similar to that employed in EMPA since both techniques share the same principle of electron scattering in the sample. At the early stages of development of EMPA, simplified scattering models were adopted. These gave a good qualitative understanding of the scattering process. Quantitatively however, and with the development of EMPA, a more accurate approach was needed. Green (88) was the first to apply Monte Carlo techniques to the problems of Electron Probe Microanalysis. His results showed the potential of the method. Many attempts have followed that of Green which proved the technique to be probably the most basic theoretical approach for the understanding of electron scattering in EMPA and SEM. With this picture in mind, it was decided to apply Monte Carlo techniques to the Scanning Auger Electron Microscope situation.

4.2 CHOICE OF THE MODEL

There is a wide choice of different Monte Carlo approaches that have been used. The complexity of the different models depends on the scattering theory adopted. Bishop (89) and Shimizu et al (90) have used a multiple scattering approach. The idea of this approach is to replace the

effects of a number of single scattering events that cause the electron to travel a distance ΔS within the solid by a single event occuring at some arbitrarily selected point within the step. The general agreement between theory and experiment using this approach is very good, especially with low atomic number materials, but rather poorer for high atomic number materials as a consequence of the use of Rutherford cross-section which is a poor approximation for heavy elements. This method requires large computers in order to handle the tables containing angles of equal scattering probability.

Krefting and Reimer (91) have used a single scattering approach. In order to improve agreement with experiment especially for heavier elements they have used the exact Mott elastic scattering cross-section for scattering angles greater than 10^{o}. Energy losses greater than about 100 eV were treated as single scattering events. Their results agreed well with experiment and as expected for heavier elements, but that was at the expense of the computer time required.

Curgenven and Duncumb (92) have described a model suitable for small computers. The model is based on a simplified multiple scattering formalism with the use of fixed step length. Several workers have demonstrated the usefulness of Curgenven and Duncumb's relatively simple approach (93, 94) and comparable results with other Monte Carlo calculations as well as experiment were obtained.

It should be mentioned that the criterion for setting up a Monte Carlo model is to introduce as many simplifications to the scattering process as possible without significantly affecting the end result. Furthermore, since Monte Carlo calculations are statistical in nature, the bigger the number of events simulated the better the accuracy of the results obtained. Taking into account the low efficiency of the Auger electron production in the target, a simple model would enable one to

improve the S/N of the results by increasing the number of electron trajectories for a given simulation time in comparison with more realistic models. Based on these points, the approach of Curgenven and Duncomb was favoured.

4.3 DESCRIPTION OF THE MODEL

4.3.1 Introduction

In the electron-solid interaction, there are two distinct processes which cause the electron to lose energy and change its direction randomly. The first is the elastic scattering by the nucleus (Rutherfore interactions). This is responsible for most of the angular scattering of the electron. In this process the scattering is dominated by small angle events. Each electron has a completely Random trajectory determined by its approach geometry and energy or momentum. In a Monte Carlo approach, each scattering event is treated randomly. In addition, the scattering process can also result in some electrons being backscattered out of the target. These backscattered electrons enhance the production of Auger electrons and may set a limit on the obtainable resolution of a SAM. The second process is the inelastic scattering of the incident electron with orbital electrons. This process causes the incident electrons to lose energy continuously with very little angular deflection.

Enhancement to the Auger electron yield due to energetic true secondaries is ignored. The reason for this is based on results obtained by Koshikawa and Shimizu (95) who found that low energy true secondaries are centred within a few nm's of the point of incidence of the primary electron beams. Most of these electrons have energies around 5 eV, which is inadequate for Auger excitation. Koshikawa and Shimizu have also found

that the number of high energy secondary electrons drops rapidly with increasing energy. For the case of copper at 20 eV, the number drops to nearly one tenth of its value at 5 eV. Very little is known about the spatial distribution of high energy secondaries >50 eV. However, the results of Koshikawa and Shimizu reproduced in Figure 4.1 suggest that an extended uniform distribution for high energy secondaries would be a reasonable estimate. Based on these conclusions and by considering only Auger lines above 500eV, it was decided "safe" to ignore the contribution to the Auger yield by true secondaries at this stage. Finally, the target was assumed to be continuous.

4.3.2 Angular Scattering of Electrons

Following Curgenven and Duncomb, angular scattering of electrons in the sample is regarded as being due entirely to elastic scattering from the nucleus. Most Monte Carlo models have incorporated a screened Rutherford cross-section to describe this process. To simplify the calculation, Curgenven and Duncomb chose to use the Rutherford formula in its unscreened form. This choice makes it unnecessary to store large arrays of previously computed scattering angles, as in Bishop (89) or Shimizu et al (90) models. The Rutherford scattering formula may be written as

$$\cot {}^{\beta}/_{2} = \frac{13.9\ PEp}{Z} \qquad (4.1)$$

where β is the scattering angle, P is the impact parameter in nm (i.e. the closest distance the electron would approach the nucleus if no deflection occurred), Ep and Z are as defined earlier. The errors introduced by using a Rutherford single scattering law, by treating all angular scattering as elastic and by ignoring screening are partially corrected by choosing the maximum impact parameter to force the Monte Carlo calculations to

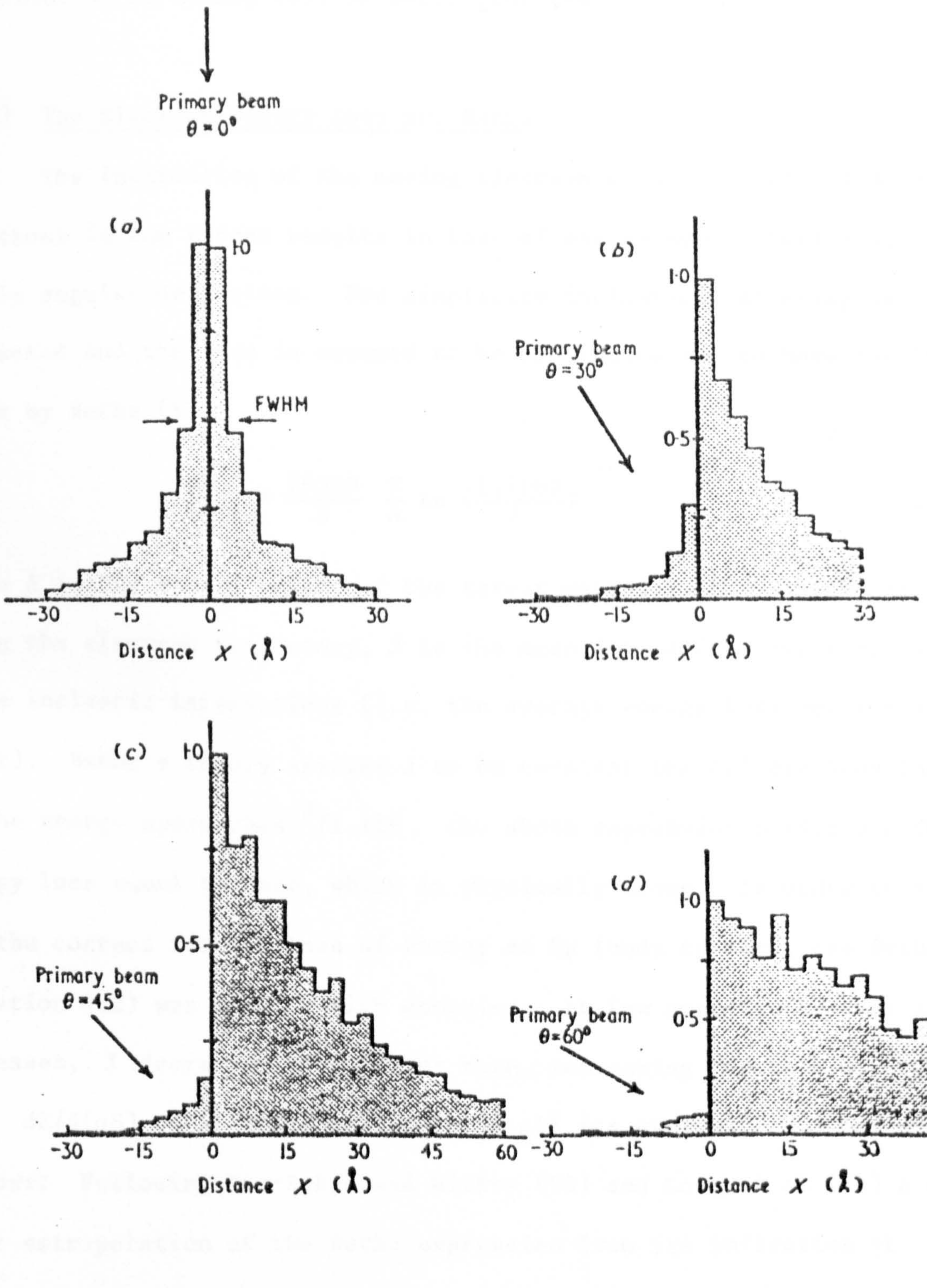

Fig. 4.1 The lateral distribution of secondary electrons for various values of θ (after (95)).

result in the experimentally measured value of the backscattering coefficient η of Bishop (89) or Darlington (96).

4.3.3 The Electron Energy Loss and Range

The interaction of the moving electron with the core and band electrons in the target results in loss of energy by excitation with very little angular deflection. For simplicity inelastic scattering is neglected and the loss is assumed to be continuous and to have the form given by Bethe (97),

$$\frac{dE}{d(\rho S)} = \frac{78500}{E} \frac{Z}{A} \ln \left(\frac{1.166E}{J}\right) \qquad (4.2)$$

where A is the atomic weight of the target material, (ρS) is the distance along the electron trajectory, J is the mean ionisation potential for these inelastic interactions (i.e. the average energy loss per inelastic event). Bethe's theory assumes J to be constant for all electron energies. As the energy approaches $^{J}/1.116$, the above expression predicts a rate of energy loss equal to zero, which is physically wrong. In order to allow for the correct rate of loss of energy as Ep tends to zero, the Bethe law (equation 4.2) was used at high energies. At low energies however as E decreases, J decreases at a faster rate, increasing the rate of energy loss $dE/d(\rho S)$ until the electron loses all its energy. This was done as follows: Following Rao-Sahib and Wittry (98) and Love et al (94) a parabolic extrapolation of the Bethe expression from its inflection at $E/J = 6.338$ to the origin has been performed. Figure 4.2 shows the relation between the rate of energy loss $dE/d(\rho S)$ versus E/J of the Bethe expression and its modifications. The modified Bethe formula can be written as

$$\frac{dE}{d(\rho S)} = \frac{-62360}{E^{\frac{1}{2}}} \frac{Z}{A} \frac{1}{J^{\frac{1}{2}}} \qquad (4.3)$$

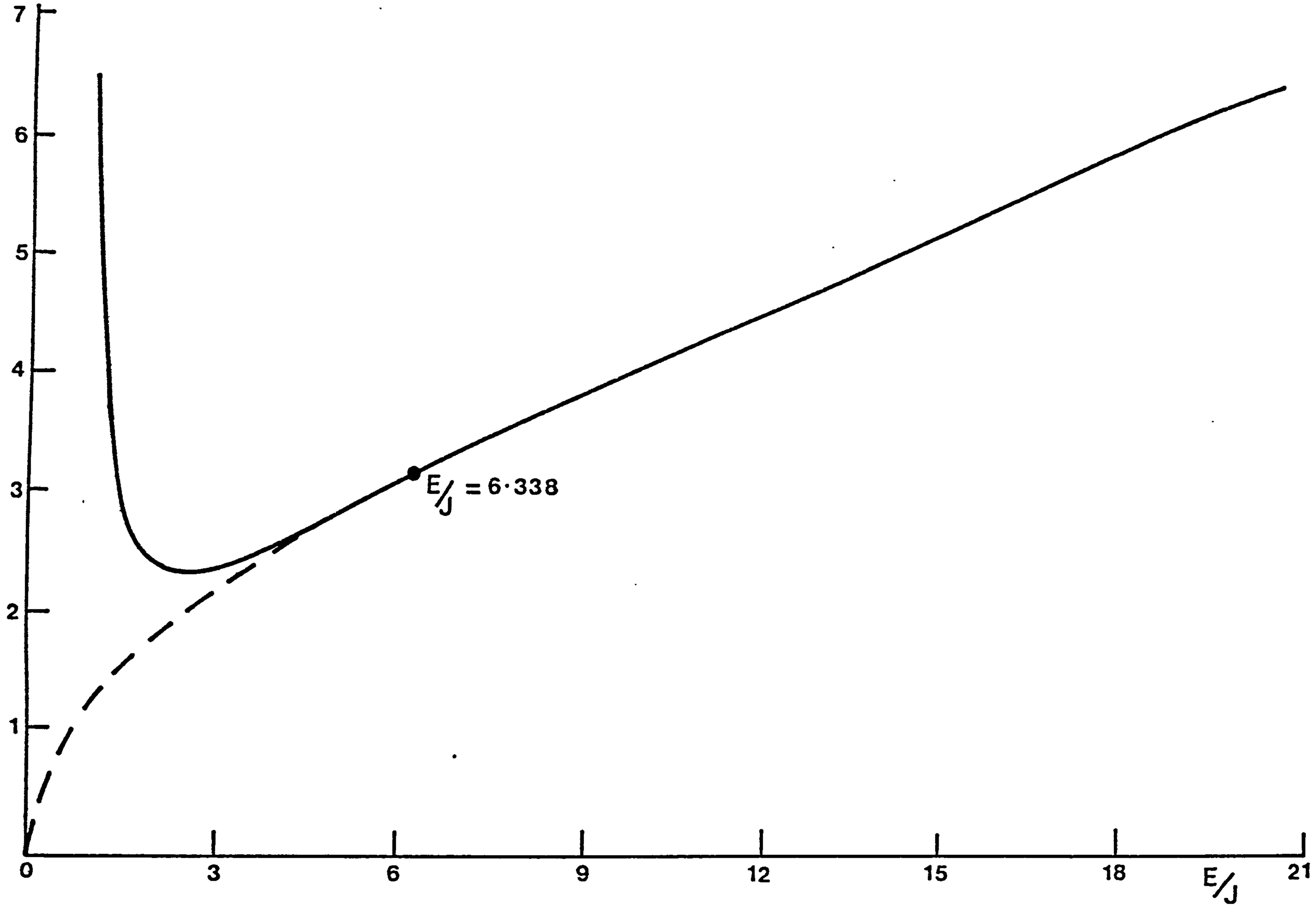

Fig. 4.2 Plot of the rate of energy loss d(ρs)/dE vs E/J of the Bethe expression (97) and its modification (98) at low energies.

A constant value of $J = 13.5\ Z$ was assumed. This choice was based mainly on the theoretical predictions of Bloch (99) and the empirical expression given by Duncomb and Da Casa (100). Equations (4.2) and (4.3) are used to determine the maximum electron range in the solid $(\rho S)_{max}$ at a given energy using

$$(\rho S)_{max} = -\int_{o}^{E_o} \frac{1}{dE/d(\rho S)}\, dE \qquad (4.4)$$

The range of each electron was divided into 100 steps in the target as a compromise between the true number of scattering acts and the time required for the computation. No significant difference was found for a number of steps higher than 100 at 20 KeV.

The electron energy at each step was evaluated numerically using the fourth order Runge-Kutta method. At the ℓ^{th} step the energy is given by

$$E_\ell = E_{\ell-1} \int_{(\rho S)_{\ell-1}}^{(\rho S)_\ell} dE/d(\rho S)\ .\ d(\rho S) \qquad (4.5)$$

4.3.4 The Auger Ionisation Cross-section

Electrons reaching a region within an Auger escape depth of the surface are allowed to ionise atoms with a Gryzinski cross-section (19) for the process. This cross-section was chosen because it provides a satisfactory fit to experimental data (20, 21) and is given by

$$\Phi(u) = \frac{\sigma_o}{E_c^2}\ \frac{1}{U} \left\{\frac{U-1}{U+1}\right\}^{3/2} \left(1 + \frac{2}{3}\left(1 - \frac{1}{2U}\right) \ell n\left(2.7 + (U-1)^{\frac{1}{2}}\right)\right)$$

$$= \frac{\sigma_o}{E_c^2}\ g\ (U) \qquad (4.6)$$

In this equation U is the reduced energy E/E_c and E_c is the initial state energy for the Auger process in question. The magnitude of the cross-section constant σ_o was determined by fitting the maximum cross-section $\Phi_{max}(u)$ to the maximum values given by either Lotz (101) or Worthington and Tomlin (18). This was based on the assumption that almost all cross-section models have nearly the same maxima at around 3 - 5 U. In addition it should be noted that the accuracy of any given expression is not better than 10 - 20% and sometimes even worse (102). For the present work, the exact value of the cross-section is not critical as most interest is in the relative heights of signals due to primary and backscattered electrons and to the spatial extent of the backscattering effects.

4.4 STRUCTURE OF THE MODEL

Following Curgenven and Duncomb, Cartesian coordinates are used to define the position of the electron in the solid assuming the point of incidence as the origin. A typical electron trajectory is shown in Figure 4.3 and a flow chart of the computer program is given in Appendix A1. The calculated electron range (eq4.4) is divided into 100 steps, and the position of the $(L + 1)^{th}$ step is calculated as follows. Two arrays for the energy losses from the Bethe equation and the corresponding ionisation cross-section from the Cryzinski formula are set up first. A value for the impact parameter P is randomly selected between zero and the maximum P_o such that

$$P = P_o(SR)^{\frac{1}{2}} \qquad (4.7)$$

where SR is a pseudo random number in the range 0 - 1. It is assumed that electrons arrive randomly over a circle of radius P_o, hence the inclusion of the square root allows for the greater probability of higher values of

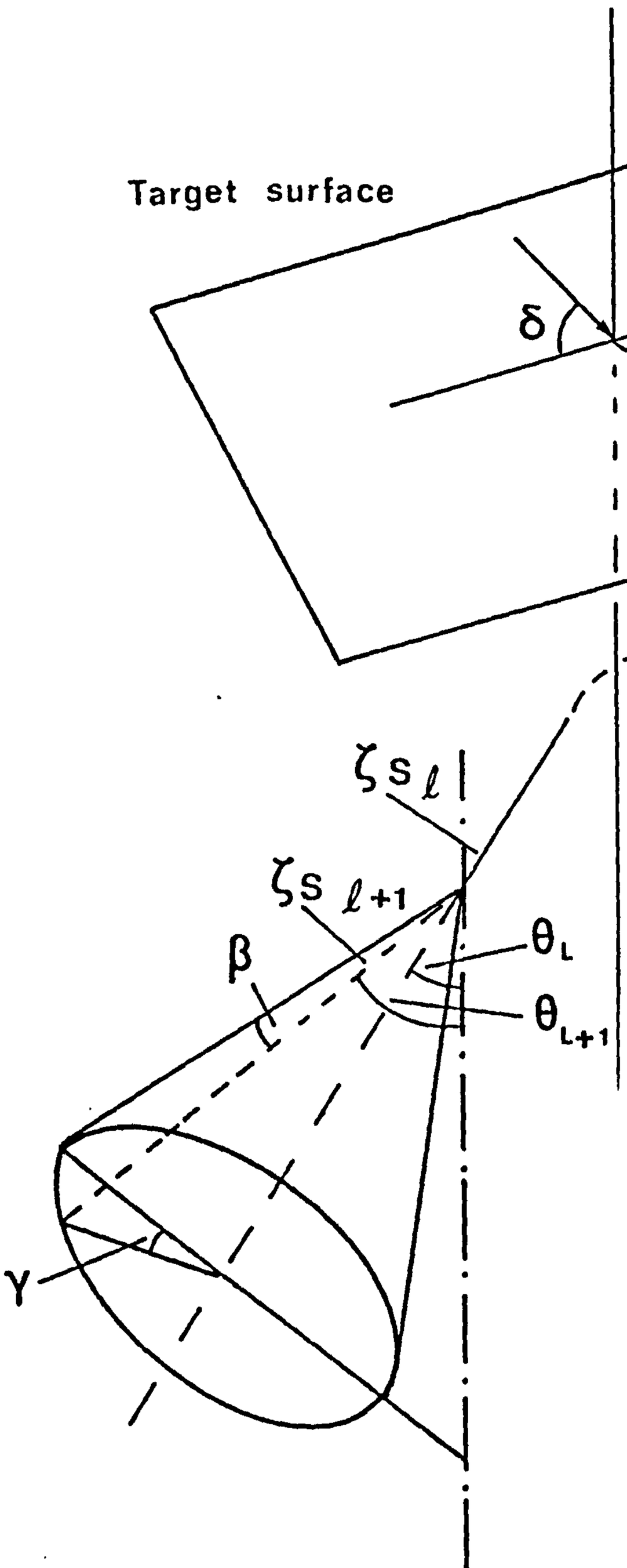

Fig. 4.3 Geometry of a typical electron trajectory in solids.

P. The maximum impact parameter Po is selected by trial and error such that the Monte Carlo program is forced to yield the experimental value of the backscattering coefficient η. The scattering angle β between the L^{th} and the $(L + 1)^{th}$ steps is then determined by substitution of P and E_ℓ in equation (4.1). Duncomb (103) suggests a value of P_o given by

$$P_o = (0.82\ Z^{0.4})/E \qquad (4.8)$$

while Love et al (94) have simplified the situation by extracting an empirical relation between the scattering angle β and the backscattering coefficient η for a wide range of P_o representing different materials. Their expression is given by

$$\tan \beta_o/2 = 0.02209 + 0.10716\eta + 0.03009\eta^2 + 0.37555\eta^3 \qquad (4.9)$$

where β_o is the minimum scattering angle for the incident electron with energy E_o. Both expressions give very good agreement with experimental η values. The expression of Love et al is more fundamental than that of Duncomb and it eliminates the necessity to pre-calculate P_o and hence it was used in the final form of the program.

The azimuthal scattering angle γ in a plane perpendicular to the direction of the L^{th} step is next determined using a second random number. Since all azimuths are equally probable, γ takes any value between 0 and 2π radians such that

$$\gamma = 2\pi\ (SR) \qquad (4.10)$$

The parameters of the spatial position of the L^{th} step (i.e. X_L, Y_L, Z_L, Θ_L, β_L) together with the two angles Θ and β calculated above are used to calculate the position of the $(L + 1)^{th}$ step using the following expression

$$\cos \Theta_{L+1} = \cos \Theta_L \cos \beta - \sin \Theta_L \sin \beta \cos \gamma \qquad (4.11)$$

At each step the electron's spatial position with respect to the Auger escape depth is checked. If the electron lies within the Auger escape depth then it is allowed to ionise the atom and a comparison between a third random number and the normalised ionisation cross-section for the Auger process in question is performed. (A normalisation factor is calculated for each transition using the Auger yield formula (1.4.1)). If the number is less than or equal to the normalised ionisation cross-section, then an Auger electron is produced and its spatial position stored on disc for subsequent processing. The electron trajectory is terminated in one of two ways. Either the electron is backscattered or the specified number of steps are completed.

The input to the program contains the following. The primary electron energy Ep, the target atomic number Z, the target atomic weight A, the angle of incidence of the electron beam Θ, the backscattering co-efficient of the target η, the initial state energy of the Auger process in question, the number of steps in a trajectory and the total number of electron trajectories to be simulated.

The output from the program depends on the question asked and the standard output usually contains the following. An array of the spatial distribution of the backscattered Auger electrons, the target's calculated backscattering coefficient η_c, and the number of Auger electrons due to:

(i) the primary electrons

(ii) the backscattered electrons

(iii) the rediffused primaries

from which the Auger backscattering coefficient x is obtained.

With very little modification to the program one can obtain electron trajectory plots (Figure 4.4) or energy distribution of the backscattered electrons. Calculations were carried out on a DEC 10 computer using a

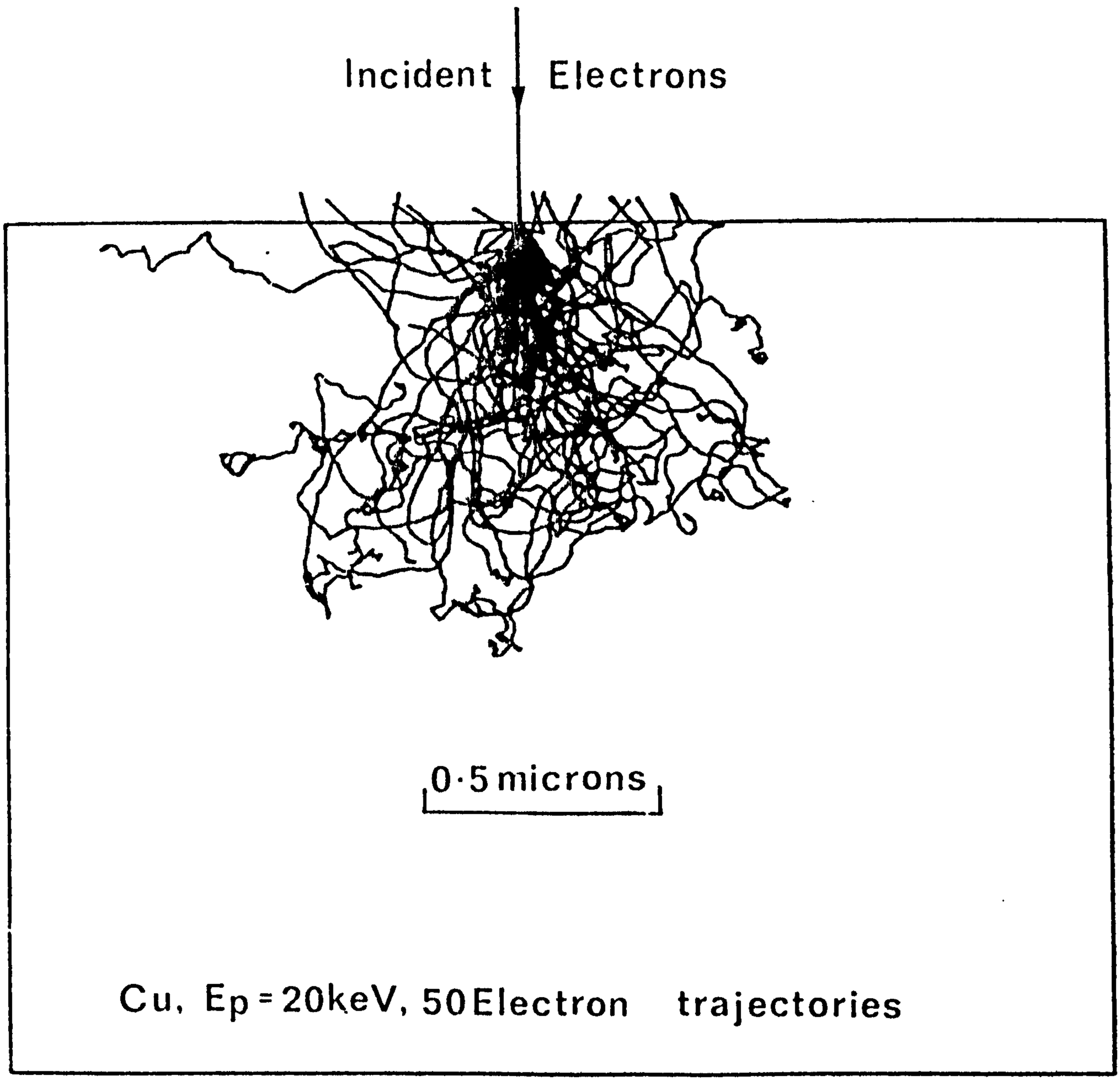

Fig. 4.4 Typical electron trajectories using the present Monte Carlo model.

random number generator which did not repeat until 2^{43}. The original random number generator of Curgenven and Duncomb was found to repeat after a few thousand. A DEC 10 library subroutine was used for the integration of the Bethe formula.

4.5 THE CHECKS OF THE MODEL

The distribution in depth and energy of the primary electrons are the important quantities in EMPA for obtaining in-depth distribution of the x-rays. For SAM however most interest is on the spatial distribution of the backscattered electrons and their energies. This comes from the fact that the Auger electron emission depends on the energy of the incident electrons, which in this case is the backscattered electrons. In order to check the accuracy of the model in the present work, a comparison between calculated electron energy distribution of backscattered electrons and experimental values was done for a range of targets of differing atomic numbers Z. Figure 4.5 shows a comparison between the Monte Carlo and the experimental results of Darlington for Aℓ, Cu and Au at normal incidence. The agreement with experiment is good. Figure 4.6 shows trajectories of 100 electrons incident upon Aℓ, Cu and Au targets at normal incidence. The interaction volume predicted by the model is in very good agreement with previous observations in EMPA and SEM.

The use of the Rutherford scattering cross-section at the energies reported here does not affect the accuracy of the calculation greatly. This is based on the observation of the energy distribution of the backscattered electrons which was found to peak near the primary energy with fewer electrons at energies below 5 KeV. This effect is shown more clearly for high atomic number materials. The model however was extended to low energies to compare backscattering factors calculated with those measured

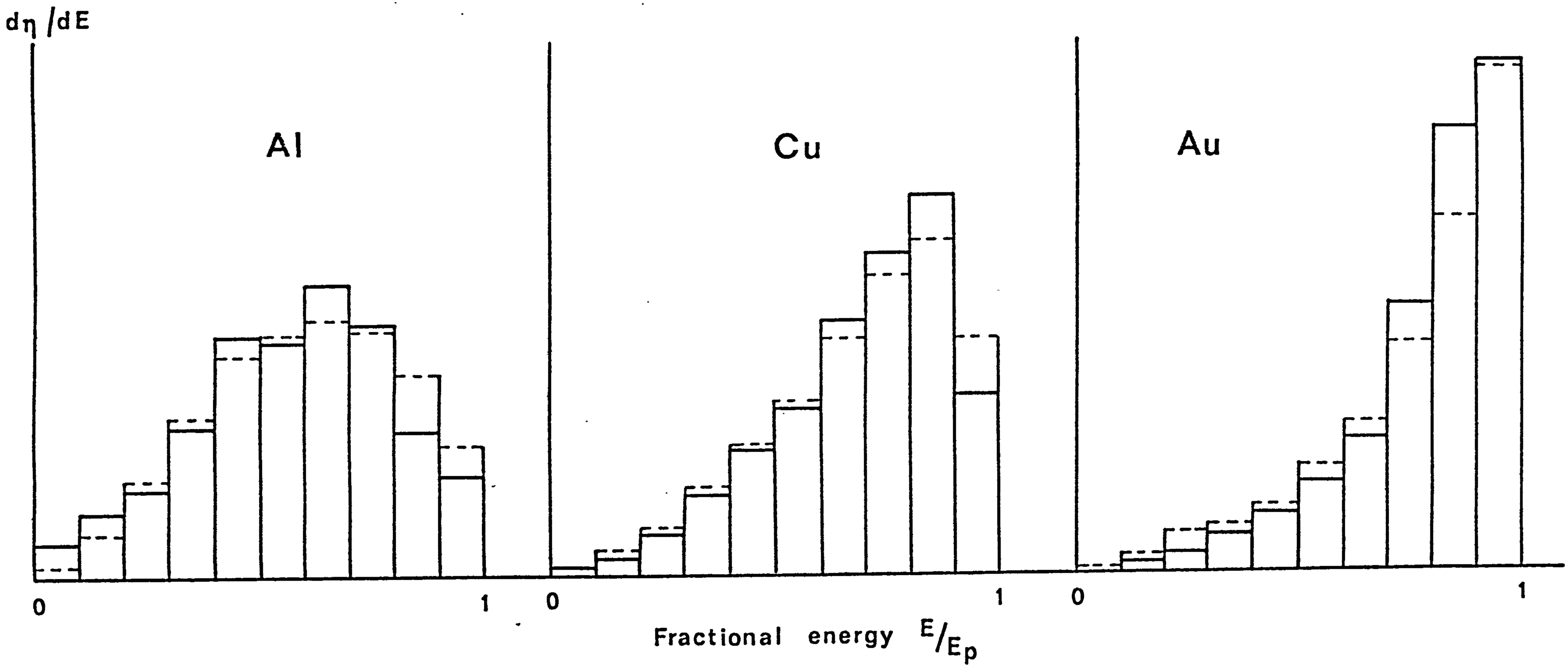

Fig. 4.5 Comparison of electron energy distribution of Aℓ, Cu and Au at normal incidence. Histogram is present calculation and dotted line is from Darlington (96).

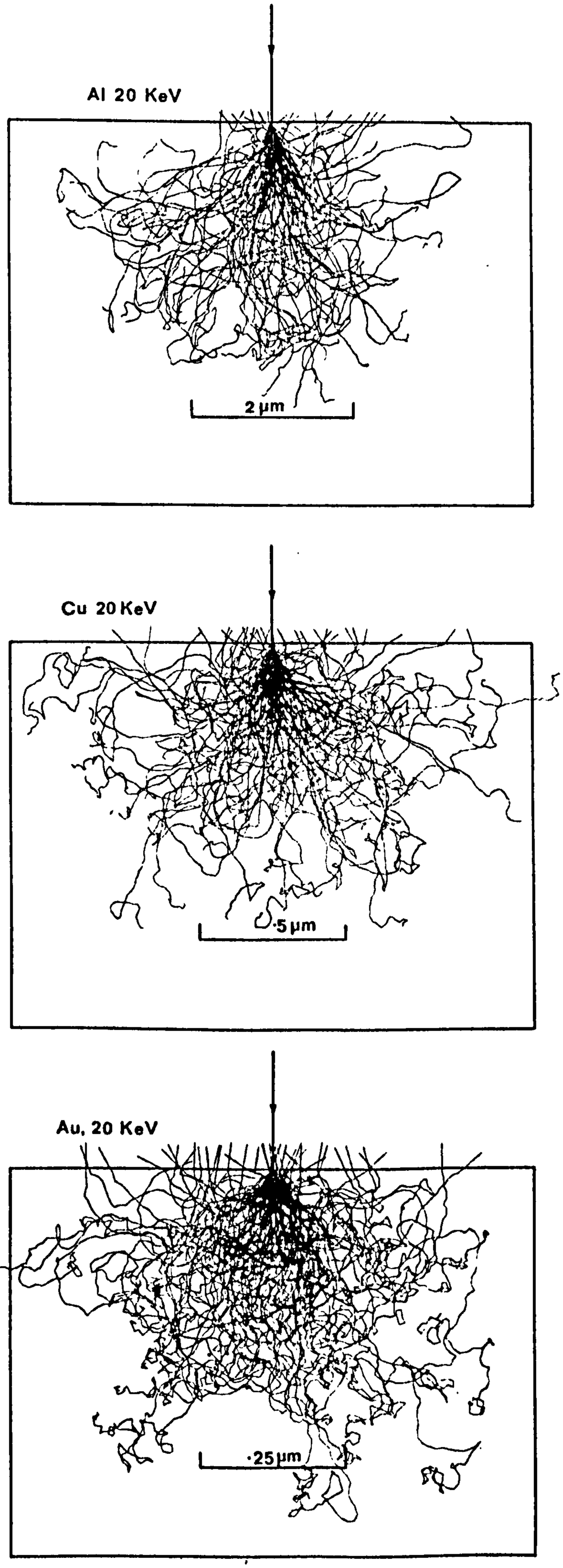

Fig. 4.6 Electron trajectories of 100 incident electrons at normal incidence for (a) Aℓ , (b) Cu and (c) Au.

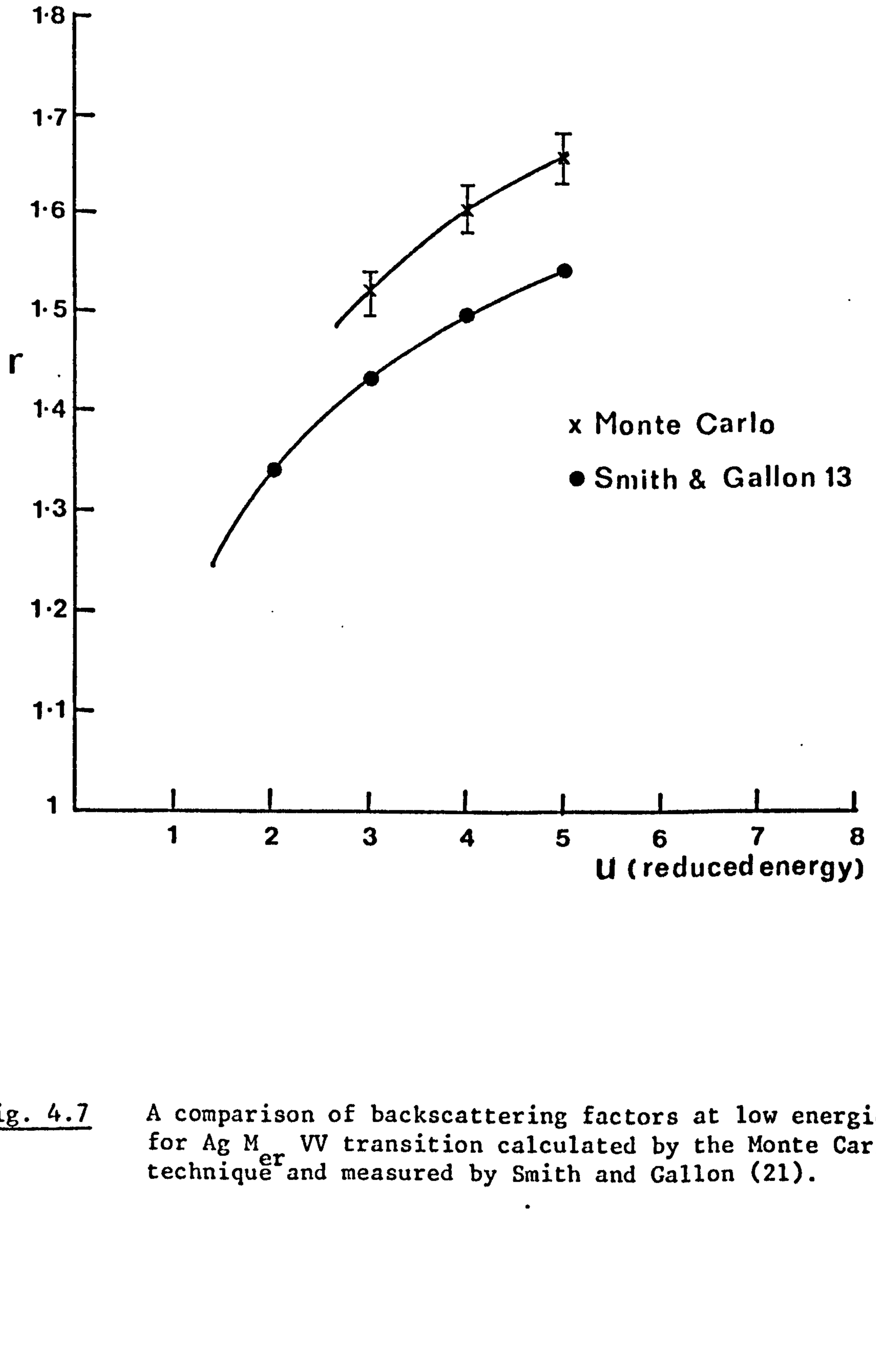

Fig. 4.7 A comparison of backscattering factors at low energies for Ag M_{er} VV transition calculated by the Monte Carlo technique and measured by Smith and Gallon (21).

by Smith and Gallon (21). This comparison has been made for the Silver M_{45} VV Auger transition and the results are summarised in Figure 4.7. A compromise was sought between fitting the backscattering factor η and the largest step possible for these low energies. The step length was usually in the range 1 - 3 nm. The calculated backscattering factor is over-estimated but not grossly. This is not surprising as the Rutherford cross-section is quite wrong for these low energies. The inclusion of a differential scattering cross-section as reported by Shimizu et al (105) should correctly represent scattering acts at low energies. The above observations, in addition to the consistency of the calculated backscattering coefficient has led to the conclusion that the model is reasonable in describing the electron-specimen interaction and hence in the calculation of the spatial resolution of SAM.

4.6 RESULTS

4.6.1 Electron Energy Ranges

Electron trajectories and the spatial distribution of Auger electrons have been calculated for aluminium, copper and gold. The data required for the calculations is summarised in Table 4.1. The equations (4.2) and (4.3) were used to calculate the electron range for different primary energies. The results are listed in Table 4.2 where they are compared with the values given by Murata (104) at 20 KeV. The difference between the two sets of ranges is due to the use here of the value 1.166 as coefficient for E in equation (4.2) where Murata uses the value 2, which is correct only for heavy ions (85). In any case, the backscattering data obtained in the present work was insensitive to changes in range of the order shown in Table 4.2. Figure 4.8 shows the relation between the

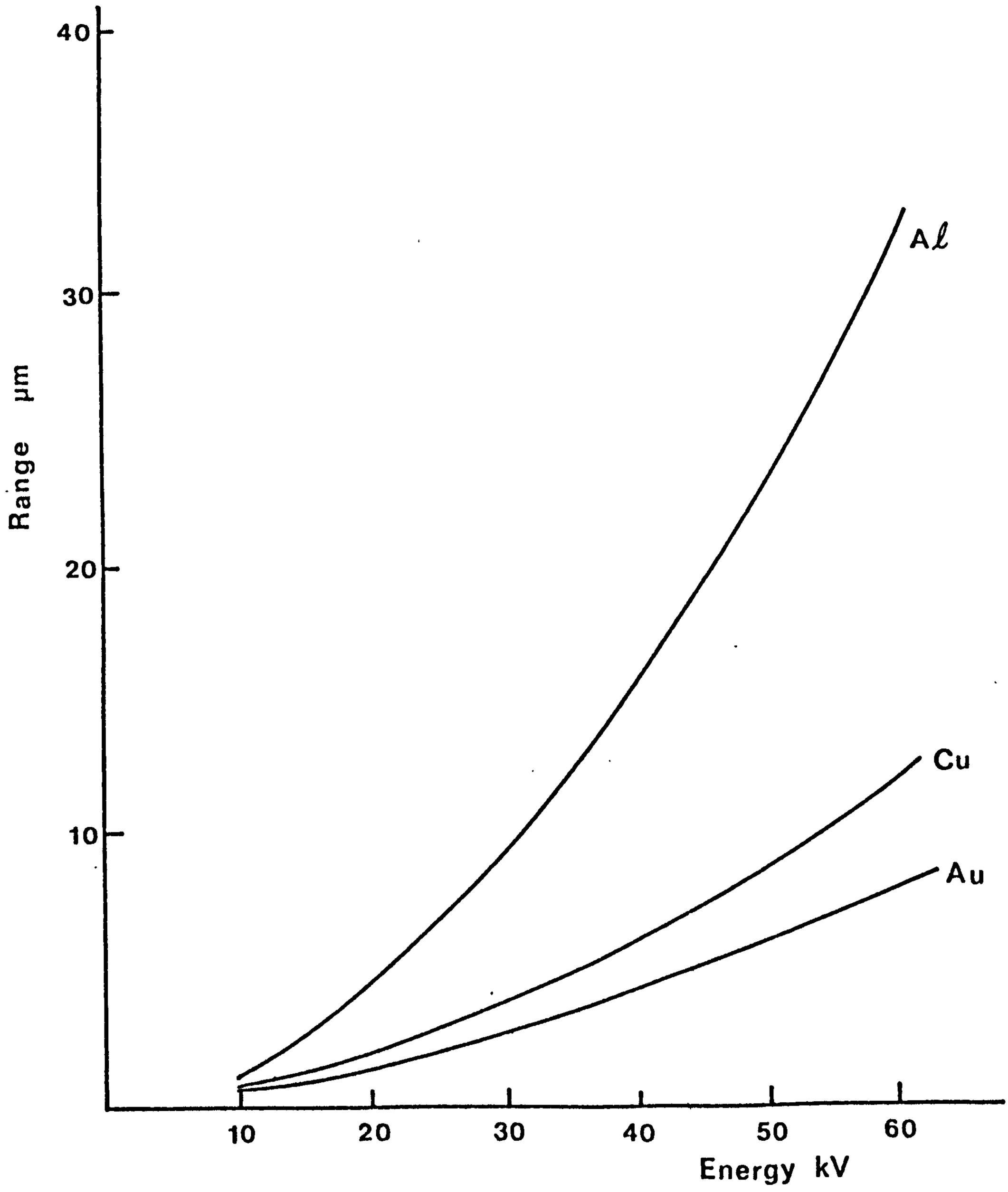

Fig. 4.8 Electron energy range versus energy for Aℓ, Cu and Au.

Property	Material			Reference
	Cu	Al	Au	
Back-scattering factor, η	0.309	0.164	0.507	Reed (85)
Mean ionisation potential, J (eV)	392	176	1067	Love et al (94)
Auger process	L_3VV	KVV	$N_{6,7}VV$	Bearden and Burr (107)
Auger initial state energy, E_c (eV)	931	1560	84	Bearden and Burr (107)
Auger escape depth τ (A)	12	28	6	Powell (102)
Maximum ionisation cross section, $\sigma_{0\,max}$ ($cm^2\ eV^2 \times 10^{-14}$)	11.7	7.3	9.2	Gryzinski (19) Worthington and Tomlin (18) Lotz (101)

Table 4.1 Data used to calculate the Auger electron emission.

Element	Present calculation	Murata's result
Aluminium	4.54	3.90
Copper	1.79	1.49
Gold	1.36	1.04

Table 4.2 Electron ranges in microns for a primary beam energy of 20 keV compared with those due to Murata (104).

electron range and energy for a number of different materials.

4.6.2 The Spatial Distribution of the Auger Electrons

The Auger emission spatial response functions of Aℓ, Cu, and Au targets to a delta function in the width of the primary beam are shown in Figure 4.9. It is assumed that electrons are incident normally on the target surface. The distribution can be divided into two parts. The first is a delta function at the origin of size determined by the Auger yield for the primary beam. The second is a broad region surrounding this delta function and is due to the backscattered electrons. The background region has a spatial extent in the range 0.2 μm in the case of Au to nearly 2.5 μm for Aℓ in good agreement with backscattered calculations due to Murata (104). Even though the emission of Auger electrons due to backscattering is concentrated near the origin, the size of the background is still very small compared with the signal at the origin which is caused by the primary beam - an effect which is not unexpected and which suggests that the spatial resolution will be dominated by the size of the primary beam. In addition there appears a "halo" around the central peak (for Au this can be seen near 100 nm and for Cu near 200 nm in Figure 4.9) which corresponds to a similar "halo" in the backscattered electron distributions calculated by Murata.

In practice finite beams of different diameters are used which necessitates the response function of Figure 4.9 to be convoluted with the beam profile. Because the δ-function part of the spatial response function of the target is so large compared to the broad backscattered part this convolution will divide the behaviour of the target into three types. These are:

(i) If the incident beam is very broad compared to the radius of the backscattered part of the spatial response function, then the

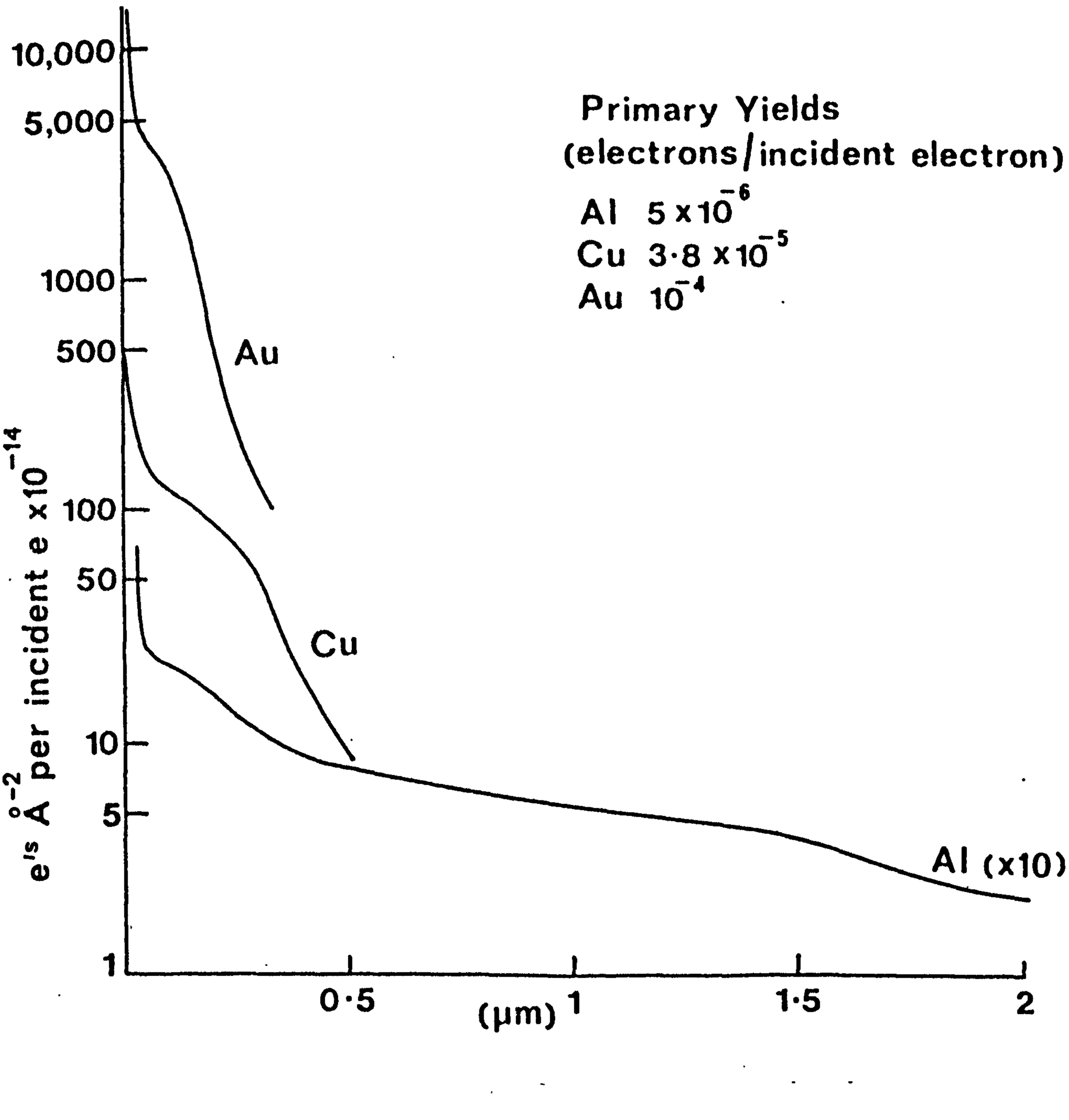

Fig. 4.9 The spatial distributions of Auger electrons for Aℓ, Cu and Au due to an infinitesimally wide beam. Ep = 20 keV at normal incidence.

Auger yield is simply raised by the backscattering factor r and the broadening effects of the target are negligible.

(ii) If the incident beam is very narrow compared to the backscattering radius then the source profile is reproduced in the Auger profile which is also surrounded by a very low disc due to backscattered electrons. The flux of Auger electrons from this disc is very small compared to the flux from the region containing ionisations due to the primary beam but it extends to the backscattering radius (0.2 - 0.5 μm).

(iii) If the beam size is comparable to the backscattering radius then the Auger electrons come from a region which is broadened and enhanced by backscattering.

Case (ii) above is of most interest for this study. A quantitative estimate of the spatial effects of backscattering can be obtained by using the spatial response functions $R(\vec{r})$ which causes the Auger process utilised in the image. The spatial image function $H(\vec{r})$ is then given by:

$$H(\vec{r}) = S(\vec{r}) * R(\vec{r}) * C(\vec{r}) \qquad (4.12)$$

In this equation, * represents the convolution operation. In order to gain physical insight into the factors controlling $H(\vec{r})$ it is useful to estimate case (ii) above under the following constraints:

(i) $S(\vec{r})$ is Gaussian of half-width σ, given by

$$S(\vec{r}) = S(x,y) = \frac{s'}{\sigma_1 \sqrt{2\pi}} \exp -\frac{(x^2 + y^2)}{2\sigma_1^2} \qquad (4.13)$$

(ii) $R(\vec{r})$ as given in Figure 4.9 is approximated by a δ-function due to primary yield plus a Gaussian of half-width σ_2 due to backscattering

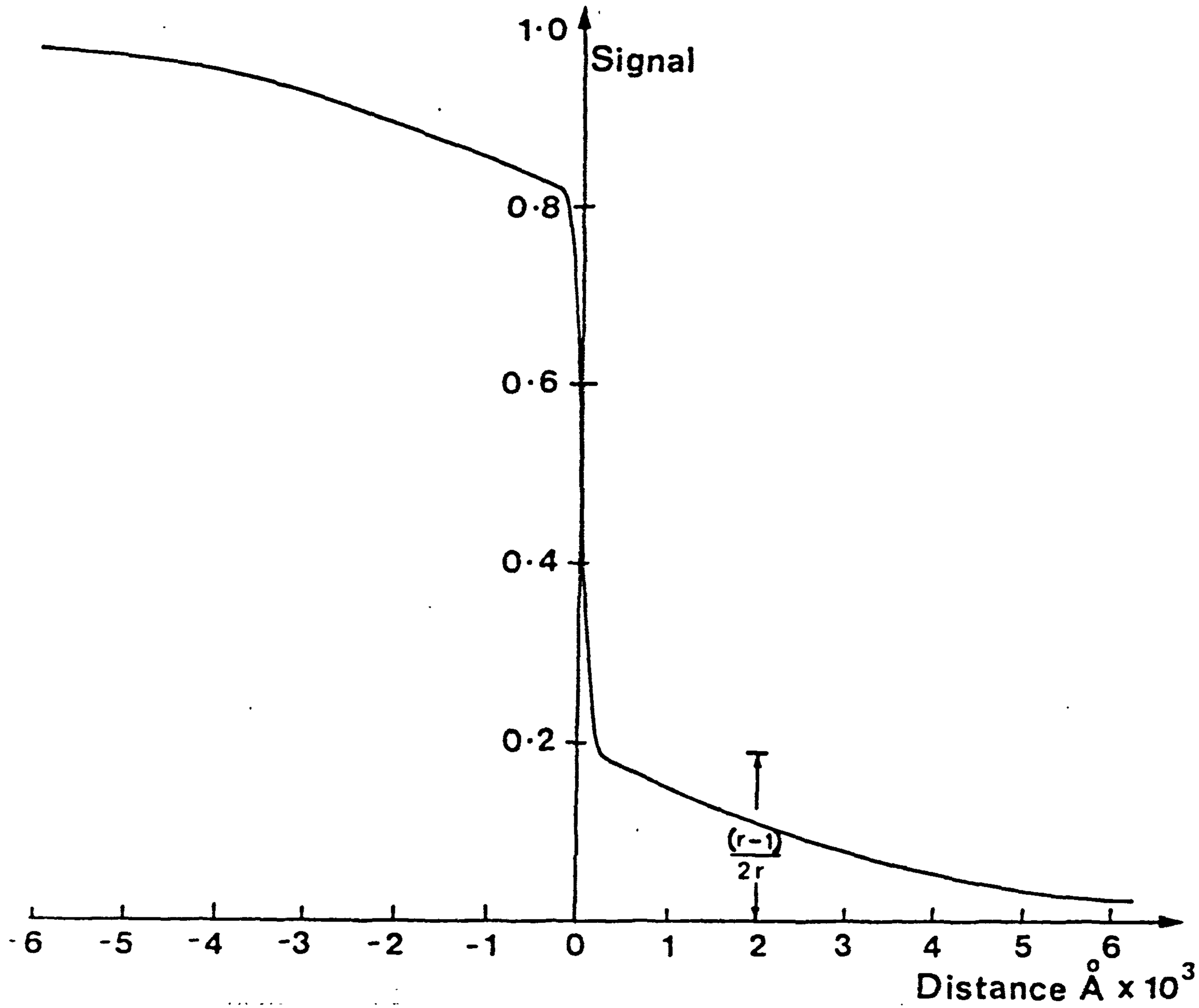

Fig. 4.10 The variation of an Auger signal due to a Cu step along y = o for a surface in the (x, y) plane. Beam half width - 10 nm, backscattering assumed as a Gaussian of half width - 400 nm and r - 1.6 .

yield, such that

$$R(\vec{r}) = R(x,y) = a\ \delta(x,y) + B(x,y) \qquad (4.14)$$

$$B(x,y) = \frac{I_B}{2\pi\sigma_2^{\,2}} \exp - \frac{(x^2 + y^2)}{2\sigma_2^{\,2}}$$

(iii) $C(\vec{r})$ is simply a step function in the surface composition profile. The step is conveniently placed along $y = o$ for a surface in the (x,y) plane such that

$$\left.\begin{aligned} C(\vec{r}) = C(x,y) &= C \quad X < o \\ &= 0 \quad X > o \end{aligned}\right\} \qquad (4.15)$$

Equation (4.12) can then be evaluated analytically and the result is (see Appendix A2),

$$H(x) = \frac{K}{2r}\left\{ \operatorname{erf} \frac{x}{\sqrt{2}\,\sigma_1} + (r-1)\ \operatorname{erfc}\ \frac{x}{\sqrt{2}\,\sigma_2} \right\} \qquad (4.16)$$

where K is a simple constant determining the Auger yield well into the composition step. This result is illustrated in Figure 4.10 for a Cu step and a primary beam having σ_1 = 10 nm. Using Figure 4.9, σ_2 has been taken as 400 nm and the backscattering factor r as 1.6.

In microscopy, edge resolution is defined as the distance between point x% and the point (100 - x)% of the maximum signal produced by scanning an infinitesimally wide beam across a sharp edge. In high resolution SEM, x can be taken as small as 3 - 5. We adopt here the same definition of edge resolution as in SEM but with larger x values. The reason is that in SAM one is forced to accept signal to noise ratios no higher than about 10 or else the time taken to produce Auger images can be inconveniently long. This means that a consistent criterion for the spatial resolution should be, for instance, the spacing Δ_{50} between 25% and 75% of the maximum signal. In this case, the example of Figure 4.10 would show a spatial resolution controlled by σ_1 not by σ_2. In the steeply sloping region near the step H(x) takes the form

$$H(x) \approx K \left\{ \frac{1}{2} - \frac{1}{\sqrt{(2\pi)}} \frac{x}{r\sigma_1} \right\} \qquad (4.17)$$

which can be used to derive an expression for the width Δ_{50}. This is given by

$$\Delta_{50} \approx 1.25\ r\sigma_1 \qquad (4.18)$$

Thus for the conditions given in Figure 4.10, Δ_{50} is 20 nm for an incident beam with σ_1 = 10 nm. The spatial resolution is degraded by the effects of backscattering but only by the backscattering factor r acting upon the incident beam and not by the large backscattering radius. However, if time is taken to produce a line scan with a good S/N, then the broadening effects of the backscattered electrons will be visible and it may be necessary then to unfold the whole spatial response function from the line-scan to get at $C(\vec{r})$.

4.6.3 The Auger Backscattering Factor "r"

The backscattering factor r calculated here is the total number of Auger electrons produced to the number resulting from primary electrons alone. Table 4.3 is a comparison between r values from the present work to other published data. The agreement at high energy with values given by (23) and (197) is good.

It should be noted that r depends on the atomic number of the target Z (or matrix), the Auger initial state energy E_c, the primary electron energy Ep and the angle of incidence Θ. Figure 4.11 shows the dependence of r on Θ for a number of different Z materials at Ep = 10, 60 KeV. As can be seen, the behaviour of r with Θ has a strong dependence on Z. The reason for this is as follows. For heavy elements, although more electrons are backscattered with increasing Θ, the actual number of ionisations due to primaries increases more rapidly than those due to backscattered electrons because of the sec Θ contribution. In addition, the energy distribution of the backscattered electrons for heavy elements

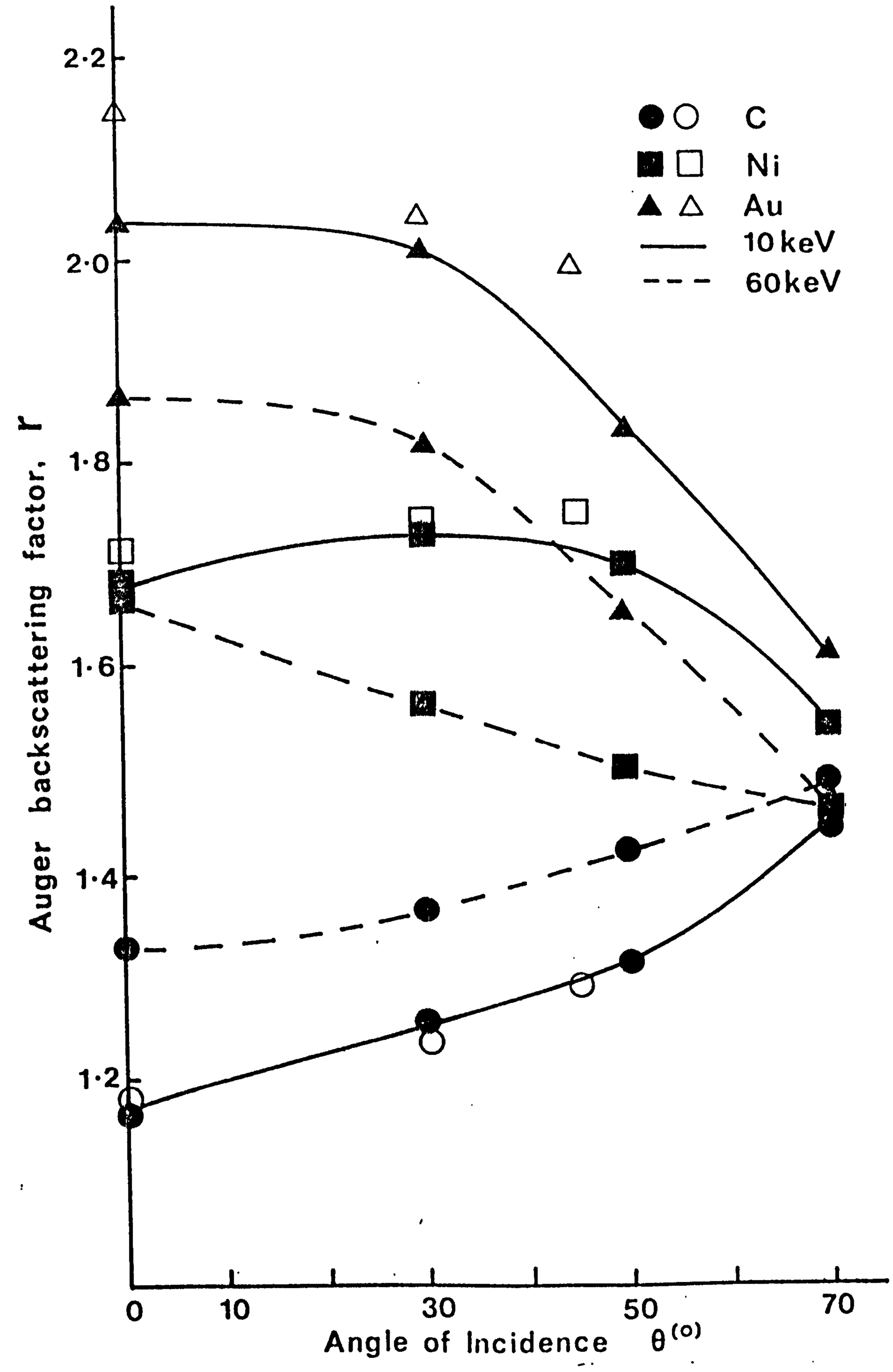

Fig. 4.11 The dependence of r on the angle of incidence θ for C, N_i and Au at Ep = 10 keV, 60 keV.

Open symbols from (197)

peaks nearer to Ep with increasing θ resulting in a reduction in their ionisation efficiency. For light elements, the energy distribution of the backscattered electrons peaks away from Ep with increasing θ. This in turn will increase the efficiency of ionisation with respect to the normal incidence case. As a result an increase of r would be obtained at angles $>50^{o}$. However, it should also be noted that a net increase in the Auger yield will be obtained with increasing θ for all Z materials.

Jablonski (108) has calculated r for a number of low Z materials in the energy range 2 kv < E < 5 kV. His results show a considerable dependence of r on θ with a maximum of r occurring at about 60^{o} - 80^{o}. He found that this maximum moves towards large angles with increasing Ep.

Element	Present work Ep = 20 keV	Bishop (23) Ep = 10 keV	Ichimura and Shimizu Ep = 10 keV	Jablonski(108) Ep = 5 keV
C	1.18 ± 0.05	1.25	1.18	1.2
Aℓ	1.4 ± 0.08	1.4	1.3	1.20
Ni	1.60 ± 0.05	—	1.72	—
Cu	1.6 ± 0.05	1.9	1.7	—
W	1.8 ± 0.1	—	—	—
Au	2.0 ± 0.1	—	2.1	—

Table 4.3 A comparison of the Auger backscattering factor r calculated here with other published data.

As mentioned at the beginning of the chapter, the present calculation does not take into account the contribution due to secondaries. At the Auger transitions considered here, this is expected to be rather negligible. Shimizu et al. (105) have investigated the role of energetic secondary electrons on Auger signals of the type LVV. Their conclusion is

that high energy secondaries are a significant source for low energy Auger signals. They also found that most of these Auger electrons are produced in the vicinity of the primary beam and hence should not degrade the resolution of SAM, in agreement with the results reported here. Unfortunately there is no experimental data available for the backscattering factor at high energies. A comparison of calculated r values with experimental data at the same reduced energy U, but with different primary energy can serve as a guide in the absence of experimental data, but should be treated carefully because of the contribution from secondaries.

4.6.4 The Effect of Angle Of Incidence on Resolution

A preliminary study of the effects of varying the angle of incidence gives similar results to those by Murata (104) for backscattered electrons. The trajectories of 100 electrons incident upon Aℓ, Cu, and Au targets at different angles are shown in Figure 4.12. As the angle of incidence is increased so the proportion of backscattered electrons reaching the escape depth for Auger electrons increases. As a result the position of the Auger spatial response function shifts in the forward scattering direction. It is interesting to note that at oblique incidence the intersection of the electron beam with the target's surface will take the shape of an ellipse. This case would, depending on the orientation of the edge with respect to the scanning direction of the electron beam, have an effect on the edge resolution. An investigation of this effect for different beam energies and angles will be given in the next chapter.

4.6.5 The Effect of Atomic Number on Resolution

The electron trajectories of Figure 4.12 show that the lighter the target material, the deeper the electron travels with fewer backscattered

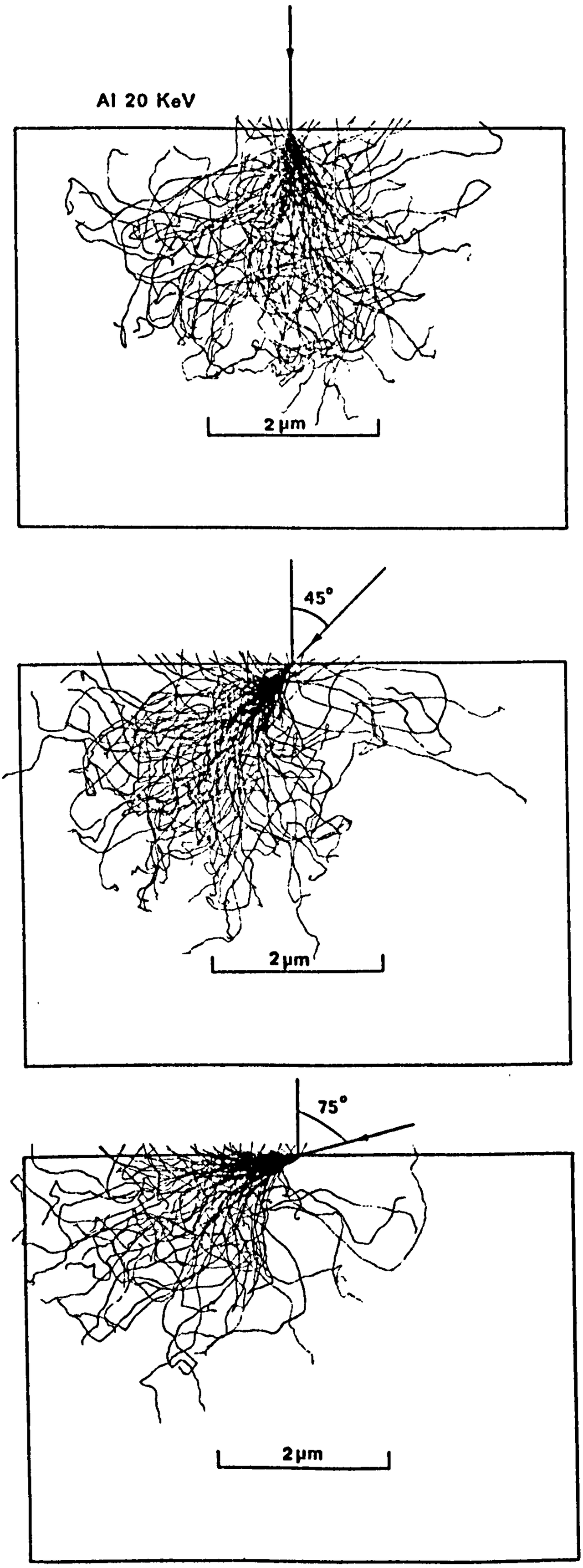

Fig. 4.12 Simulations of 100 electron trajectories at different angles of incidence for (a) Aℓ, (b) Cu and (c) Au. E = 20 keV.

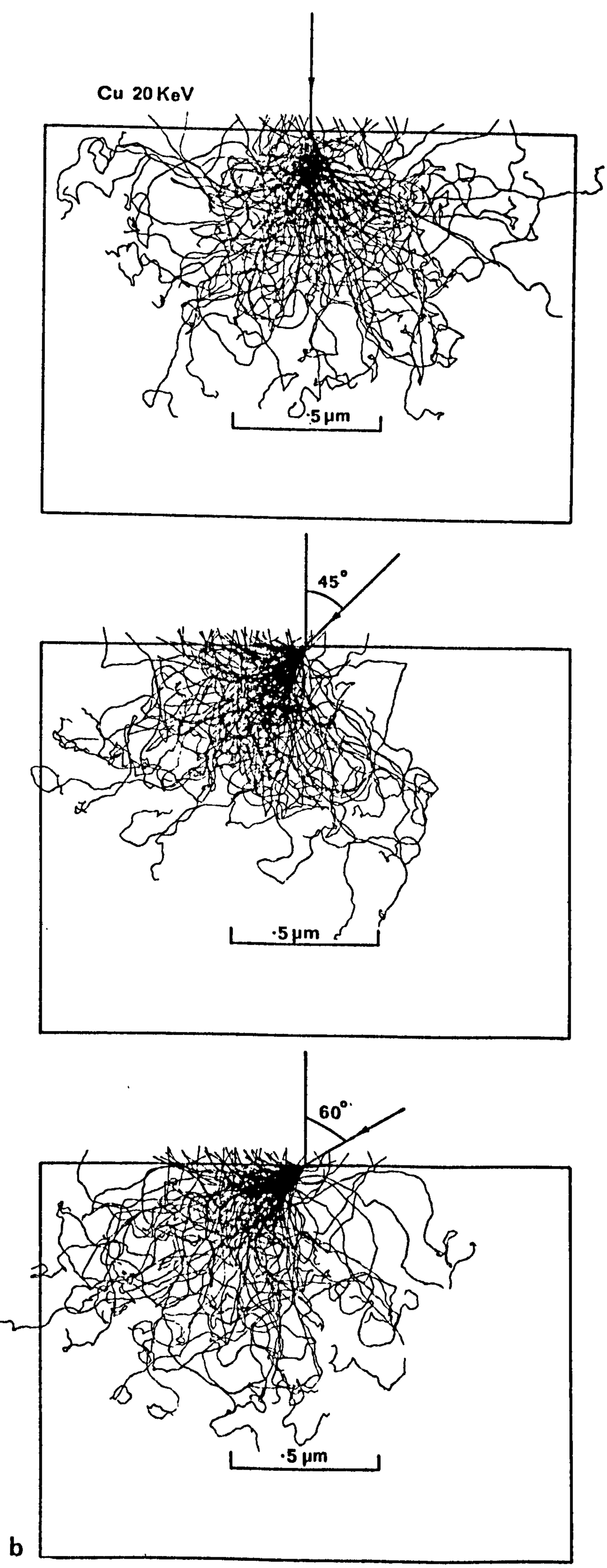

b

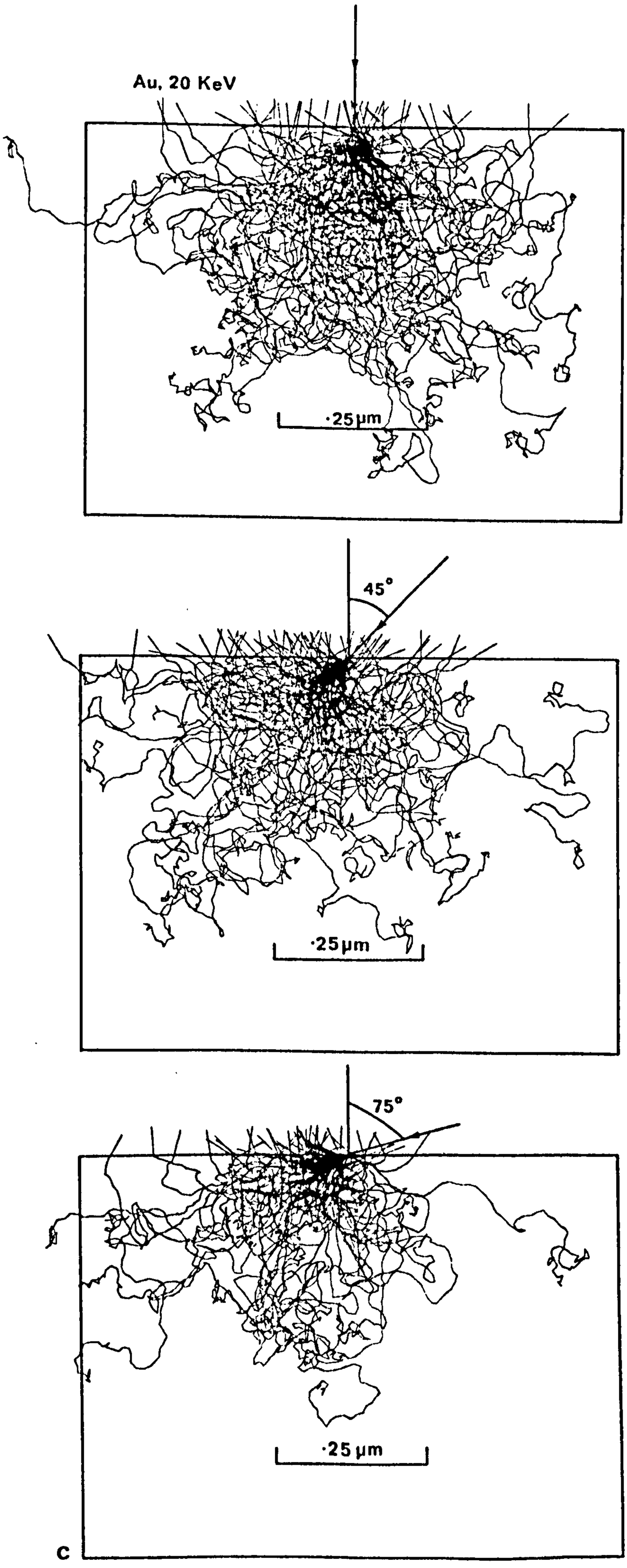

c

electrons. For the heavy elements like gold, the interaction volume is nearer to the target surface and the point of impact. This fact has led to a lateral resolution in EMPA of the order of 100 nm for the heavy elements ($Z > 40$). For light elements ($Z < 20$) the lateral resolution becomes worse as the interaction volume of the electron with the sample increases. In SAM the situation is reversed but with a much weaker effect. The variation of the Auger signal from a composition step along $y = o$ for a surface in the $x - y$ plane is shown in Figure 4.13 for two different atomic number materials. The same approximation near the edge of Figure 4.10 leading to expression (4.18) can be used here. For a beam of $\sigma_1 = 10$ nm, Δ_{50} will take the following values for the conditions given in Figure 4.13.

$$\text{For Au} \quad , \quad \Delta_{50} \approx 22 \text{ nm}$$

$$\text{A}\ell \quad , \quad \Delta_{50} \approx 18 \text{ nm}$$

These results show a slight dependence of resolution on the atomic number. The relatively improved resolution of light elements comes from the fact that the backscattering contribution is spread over a large area compared to the beam profile.

A similar effect happens for a thin film (of thickness of the order of few tens of nm's) of atomic number Z_1 deposited on a substrate of atomic number Z_2. In such a case, care should be exercised for any quantitative estimate of chemical concentrations. Kirschner (106) reports the same effect of enhancement of the Auger yield due to backscattering from a high atomic number substrate.

4.7 DISCUSSION

In this chapter, a Monte Carlo technique used successfully in

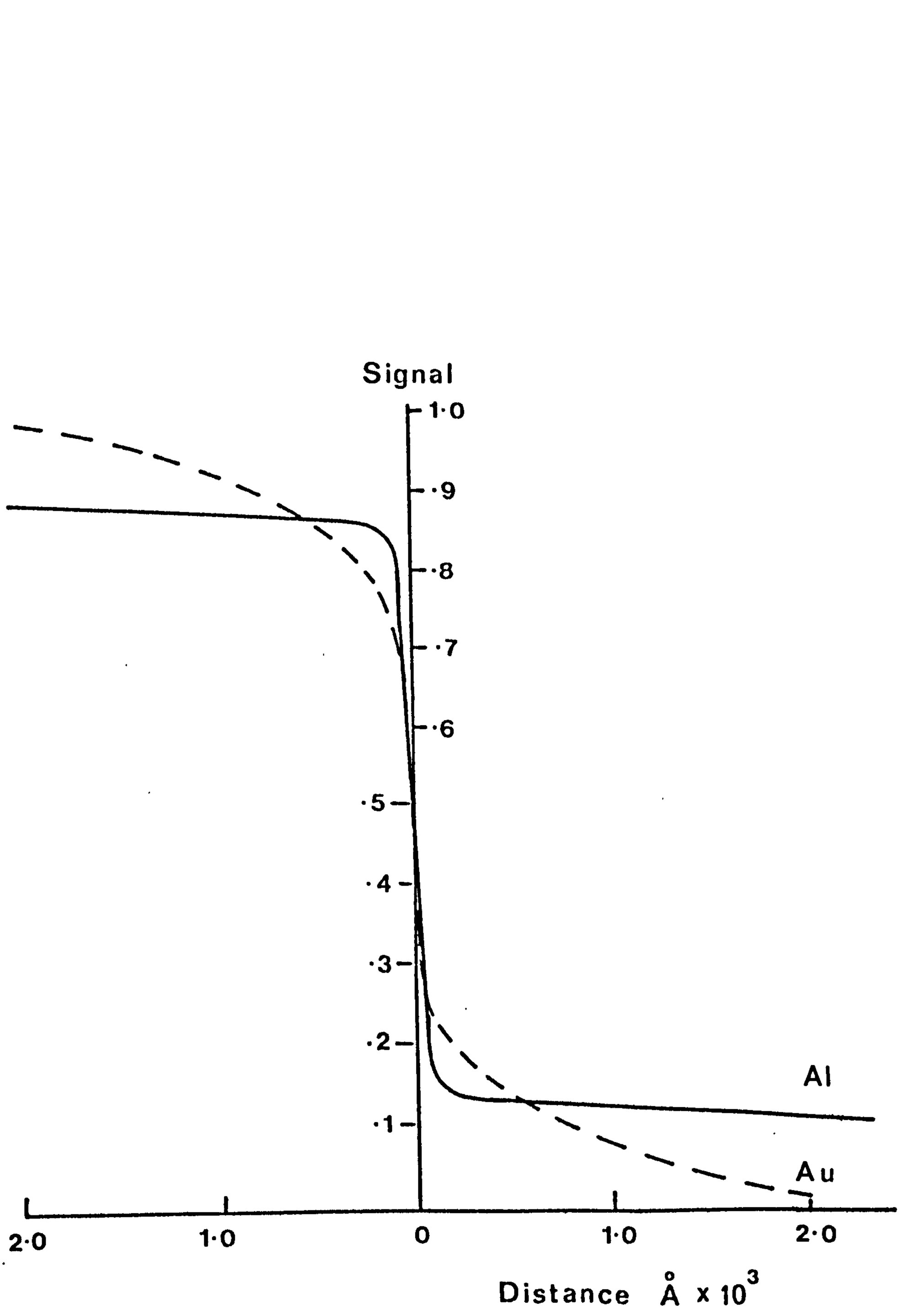

Fig. 4.13 The effect of the substrate atomic number on SAM resolution.

electron microprobe analysis and scanning electron microscopy is described. A straightforward extension of the technique to the generation of Auger electrons, in the case of SAM has shown that the spatial resolution of SAM should be limited by the diameter of the incident beam. Broadening effects due to the large spatial extent of backscattered electrons are present but at such a low level that they are unlikely to be detected with the counting statistics normally used in SAM. The results reported here suggest that the spatial resolution limits should scale to be about twice the beam size provided that the latter is small compared to the backscattering radius.

This conclusion is directly contradictory with experimental evidence presented by Christou (82), who found a resolution limit of nearly 10 x the beam diameter. In the light of the results obtained in this investigation, we can perhaps explain Christou's result. The first point is that the spot size was not measured but instead deduced from measurements of the source's brightness and the beam current which were then corrected for electron optical aberrations. Secondly, and at such low beam currents of nearly 1 n Amp , the signal to noise ratio will play an important role in the measurements. This fact was reported by Christou in his Figure (4), but not taken into consideration in the conclusion. Thirdly, no quantitative measurement of the chemical edge was given. Topographical effects can interfere with chemical information (68), and a sharp chemical edge would seem essential in this measurement. Finally, the author did not give the angle of incidence of the electron beam. Higher angles of incidence can set a limit on the obtainable resolution of SAM as will be seen in the next chapter.

Preliminary studies of the effects of varying the angle of incidence gives similar results to those by Murata (104) for backscattered electrons. The results show an enhancement of the total Auger yield with increasing incidence angle. Resolution measurements at such large

incidence angles should be treated carefully. It was also found that SAM resolution will have a slight dependence on the sample's atomic number. This effect will contribute mainly in the case of quantitative Auger electron spectroscopy.

The dominating effect of the incident beam profile has also been implied in calculations by Shimizu et al (105). In their model, Shimitzu et al have included the contribution of the high energy secondaries to the total Auger yield. For the LVV Auger electrons in Aluminium, they found that almost 50% of the total Auger signal is produced by backscattered and high energy secondaries, and about 30% for the KLL electrons. The spatial distribution of these electrons was found to extend over a much larger area in comparison with the infinitesimally wide electron beam. A similar conclusion to the finding of this work was drawn by Shimitzu et al.

Kirschner (106) has extended backscattering data for the SEM by Murata (104) to the SAM situation. For low and high atomic number materials, namely Aℓ and Au, Kirschner gives a resolution limit of nearly 100 nm. This low limit was a consequence of the rather stringent definition for the resolution adopted by the author, being between 10% to 90% of the maximum Auger signal.

It is likely that practical limits to the spatial resolution in SAM will be set by a number of factors. These will usually be the beam diameter, topography of the sample, stage stability, wandering of the emitting area on a field electron tip, stray fluctuating magnetic field causing beam displacement in addition to the obtainable signal to noise ratio.

CHAPTER 5

A THEORY/EXPERIMENT COMPARISON OF SAM SPATIAL RESOLUTION

5.1 INTRODUCTION

The effects of backscattered electrons on the spatial resolution of SAM have been calculated in the last chapter. The results obtained suggest that the spatial resolution limits are determined almost entirely by the profile of the incident electron beam and the Auger backscattering factor r. The work reported by Christou (82) was found to be inadequate for a quantitative comparison with the Monte Carlo results obtained here and an experiment to measure the variation of the Auger signal upon scanning across a sharp chemical edge was planned. However, due to limitations of the first electron probe and specimen chamber the experiment was not satisfactorily completed.

At the same time as this work was carried out Janssen and Venables (109) reported a measurement of the Auger spatial resolution of a sharp chemical boundary formed by vapour deposition. Their results were found to be interesting and a comparison with the Monte Carlo calculations was sought.

The first part of this chapter will be a description of the experimental work both at York and by Janssen and Venables (109). The second part will be on modifications to the Monte Carlo method described in the last chapter in order to compare with experiment. A distinction between different experimental geometries is presented. Calculated and measured edge profiles for Silver M_{45} VV Auger electrons are compared. In addition, preliminary tests on the role of the edge geometry on resolution with respect to the scan direction using the second instrument is also presented. Finally, the role of the primary energy, angle of incidence and sample topography on edge resolution will be discussed.

5.2 EXPERIMENTAL METHODS

5.2.1 The Experiment at York

The idea of the experiment is to form a sharp chemical edge using vapour deposition. By measuring the changes in the Auger signal upon scanning the electron beam across the formed edge, an estimate of SAM resolution, Δ50, can be made.

The inflexibility of the specimen chamber of the first instrument restricted the use in situ of well known techniques in Electron Microscopy to form a chemical boundary, such as shadowing. Therefore a different philosophy was adopted by forming the chemical boundary in a different system and then transferring it to SAM. The specimen was made of Gold and Silver films of thickness between 100 - 300 nm deposited on a silicon substrate. It was anticipated that the sample could be either cleaved in situ resulting in a clean chemical boundary or alternatively ion-milled across the boundary. Neither of the two methods was successful. The latter due to the use of getter ion pumps in the system, while in the former the film peeled off the silicon substrate. Heating the silicon substrate prior and during film deposition to form a boundary of Au - Si or Ag - Si alloy had little success as well.

A series of problems in the system (described in Chapter 3) halted any further progress on this experiment. At the same time as this work was carried out, Janssen and Venables reported an experimental measurement on the role of backscattered electrons on SAM resolution, which is a similar experiment to the one attempted in York. Their conclusion was in agreement with the theoretical predictions reported here. In view of the difficulties reported above, it was found appropriate to compare the theory with the experiment of Janssen and Venables. At the same time new designs of a multi-purpose specimen chamber and an electron probe were launched.

5.2.2 The Experiment of Janssen and Venables

Janssen and Venables have formed a sharp chemical boundary in situ using shadowing techniques as shown in Figure 5.1. Nickel spheres of diameters 0.5 - 4 μm were dropped onto the surface of a polycrystalline tungsten substrate. These spheres are used to shadow the silver vapour from aknudsen source placed 15 cms away.

It was found that the nickel spheres had welded to the tungsten surface on impact. For this reason the scans were made with the spheres in position resulting in a loss of the collected Auger electrons due to the spheres. Figure 5.2 shows the position of the analyser collection angle, electron beam and line scan direction with respect to the shadow area. For the minimum interception of the Auger electrons with the nickel spheres, the position of the line scan was at a point where the chemical edge makes an angle of $26\frac{1}{2}^{o}$ to the beam normal. It will be shown later that the position of the edge with respect to the beam normal affects the resolution. For more details on the experiment the reader is referred to the original publication by the authors.

Electron probes of diameters 5 nm and with $I_b \approx 2 \times 10^{-9}$ A or 20 nm with $I_b \approx 1 \times 10^{-8}$ A were used to produce Auger line scans of the silver M_{45} VV Auger electrons. The electron beam energy was varied between 20 KV to 60 KV in 10 KV increments at angles of incidence between 50^{o} and 80^{o}. Ratioing techniques of the Auger signal (Chapter II) were used to correct for beam current variations.

5.2.3 Experimental Results

Figure 5.3 shows Auger line scans across the Ag edge for various primary energies and incident angles for a probe of diameter approximately 20 nm. The profiles show a gradual fall-off in the Auger intensity upon crossing the boundary due to backscattering contribution. In addition

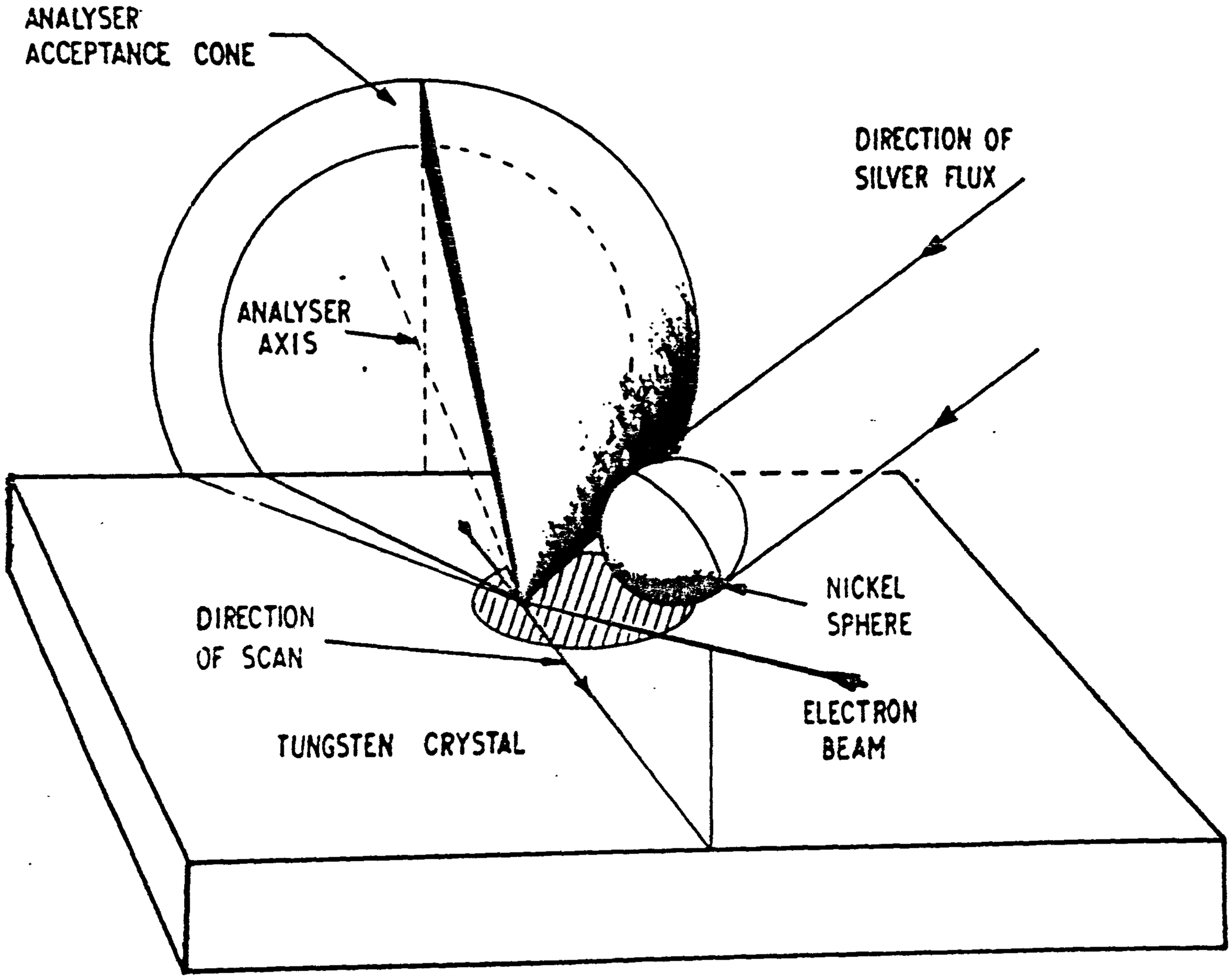

Fig. 5.1 Schematic of the experimental geometry used for the deposition of the Ag film (after (109)).

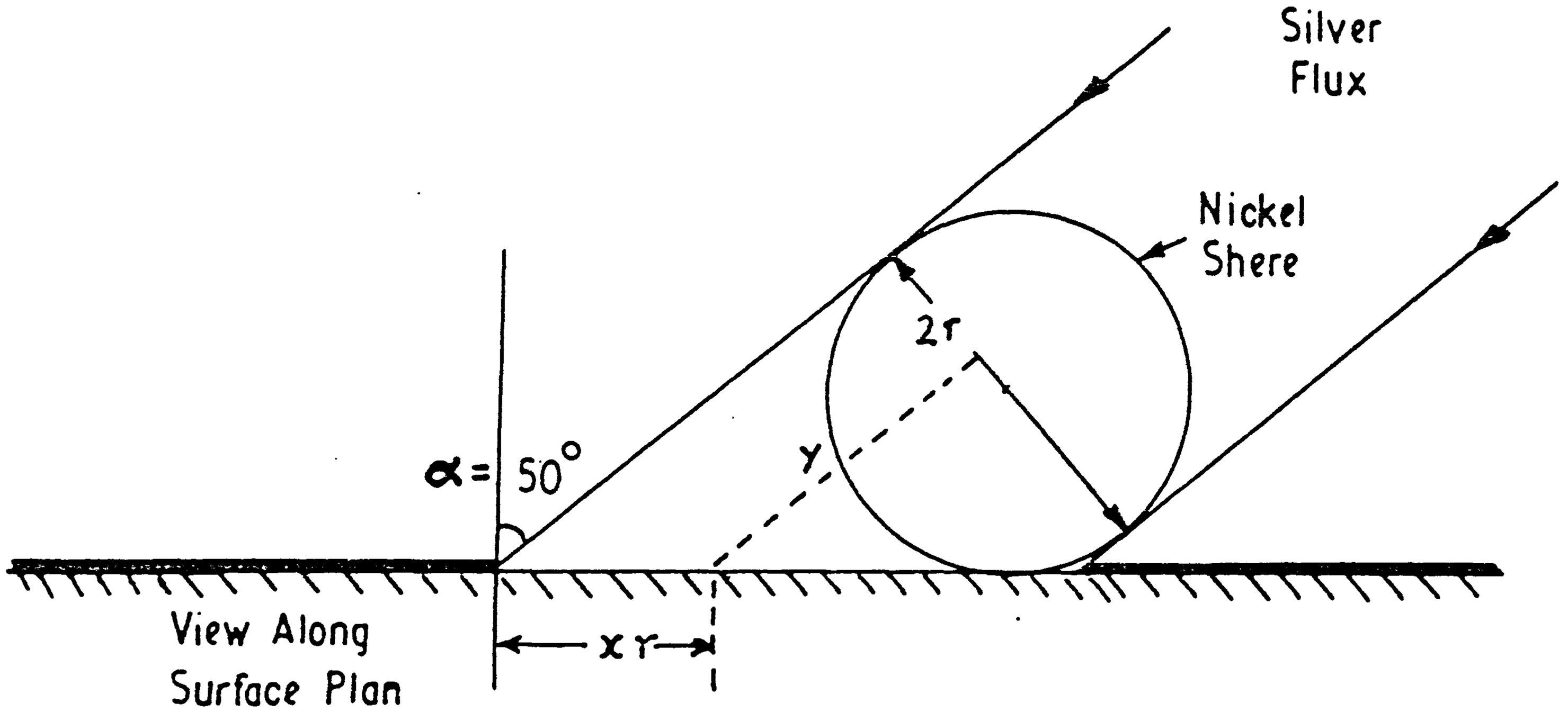

Fig. 5.2 The position of the analyser collection angle, electron beam and line scan direction with respect to the shadow area (after (109)).

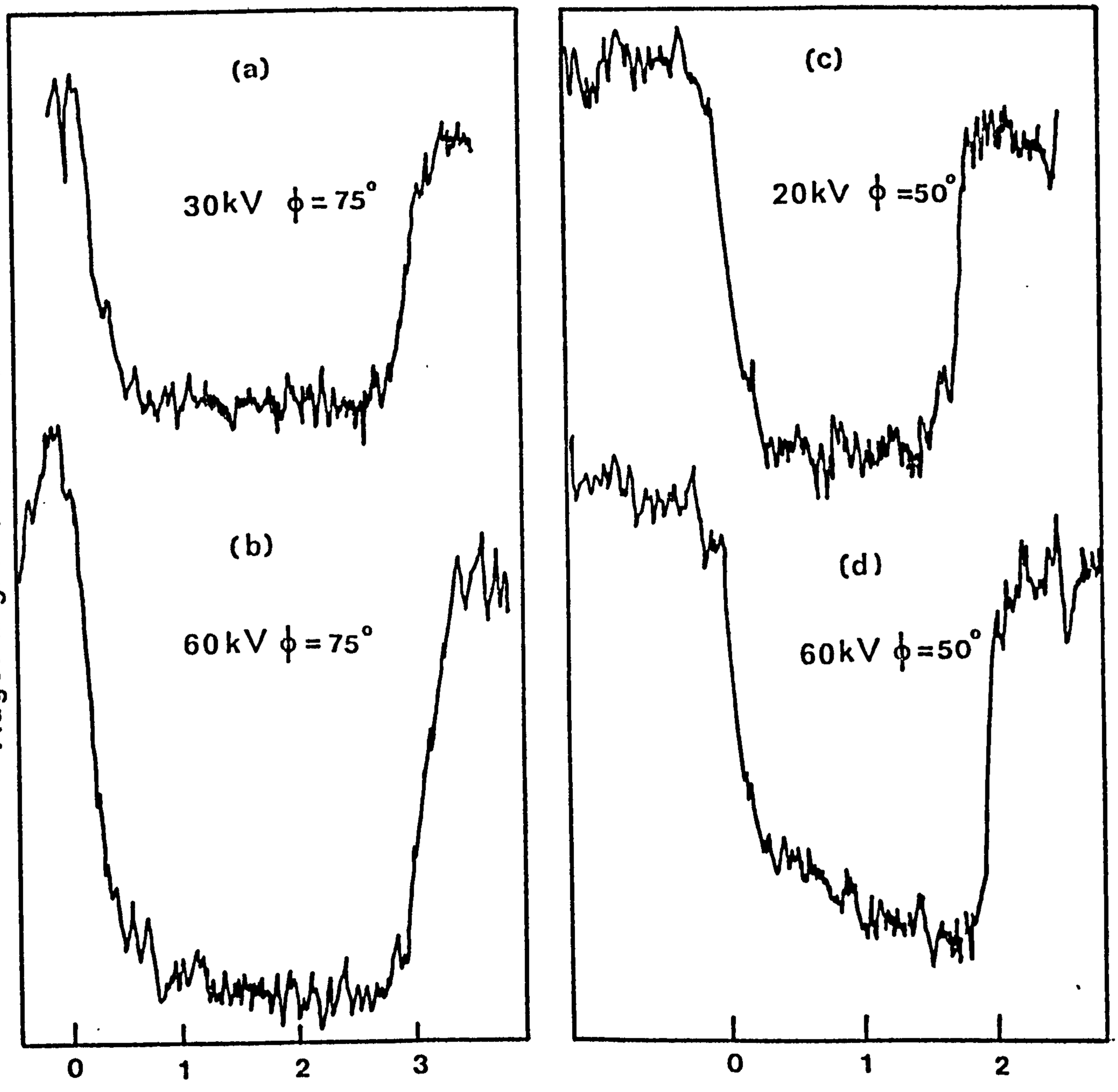

Fig. 5.3 Auger line scans across the Ag edge for various primary energies

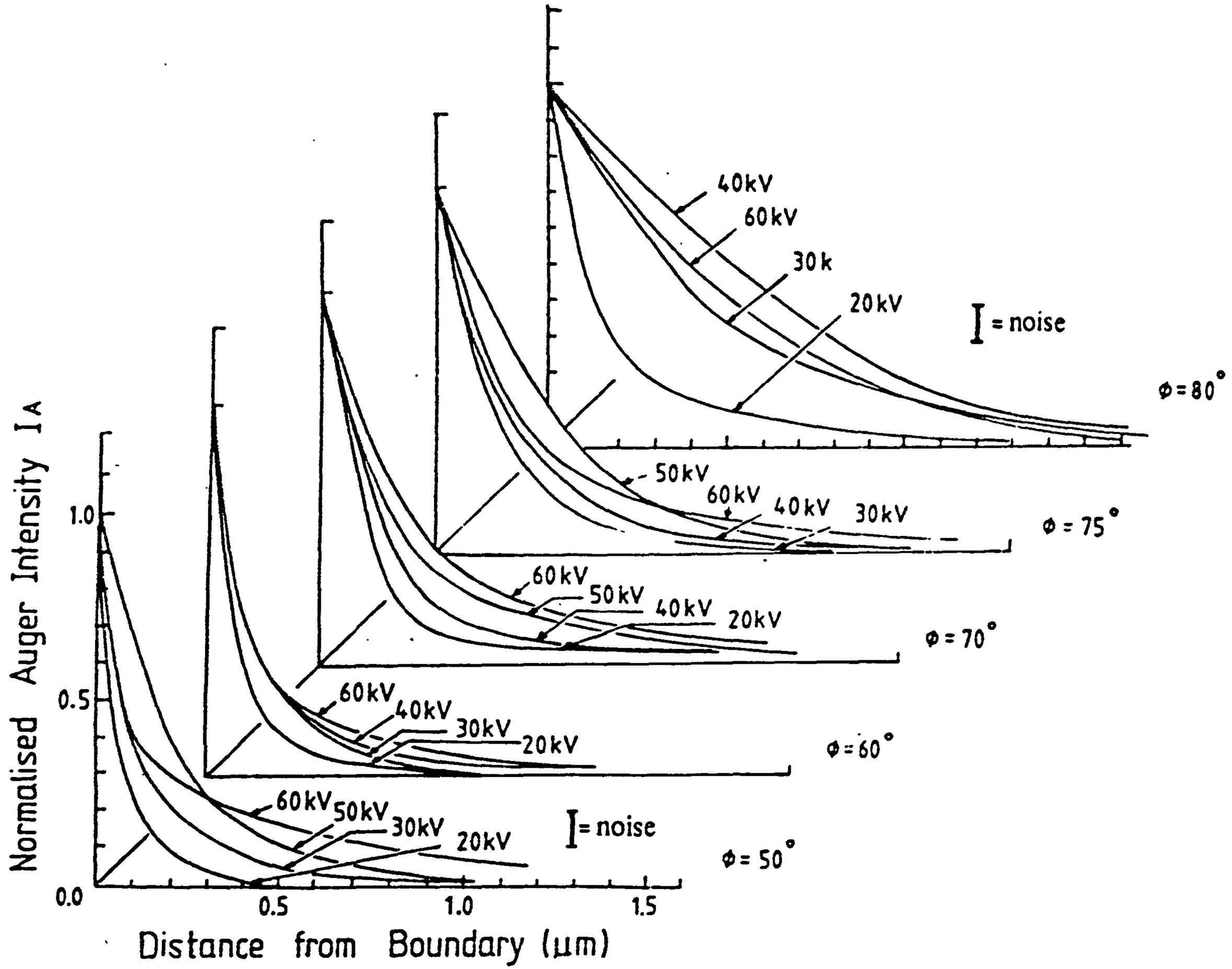

Fig. 5.4 Auger profiles of the Ag edge for different Ep and ϕ (after (109)).

the profiles are asymmetric, in agreement with the simulated electron trajectories (Figure 4.12) which shows that the backscattered electrons reach the surface in the forward direction in the case of oblique incidence. Auger profiles across the silver boundary for a range of primary energies and incident angles are shown in Figure 5.4. Janssen and Venable's conclusion from these profiles were as follows:

(i) The profiles' widths are smallest for low θ and Ep.

(ii) The width of the profile increases as either θ or Ep increases. For large θ, the asymmetry of the profiles is larger and with more backscattered electrons emitted within a small distance of the primary beam.

(iii) As θ increases, the total contribution from backscattering increases. Janssen and Venables have adopted a slightly different definition of edge resolution than the one used in this work, where they measure between 20% and 80% of the Auger signal. For tungsten with Ep = 20 KV, $\theta = 50^{o}$, their 20% - 80% resolution is ~30 nm for the 5 nm beam condition and ~50 nm for the ~20 nm beam condition. These results suggest that the Auger resolution will be essentially determined by the beam diameter.

A theory experiment comparison with two cases of the above experiment will be given in section 5.4.

5.3 MODIFICATIONS TO THE PROGRAM

In the last chapter the effects of backscattered electrons in the normal incidence case were discussed. In an actual experiment, however, constraints imposed by the size and proximity of the electron gun, the sample and its manipulator and the electron energy analyser often lead to

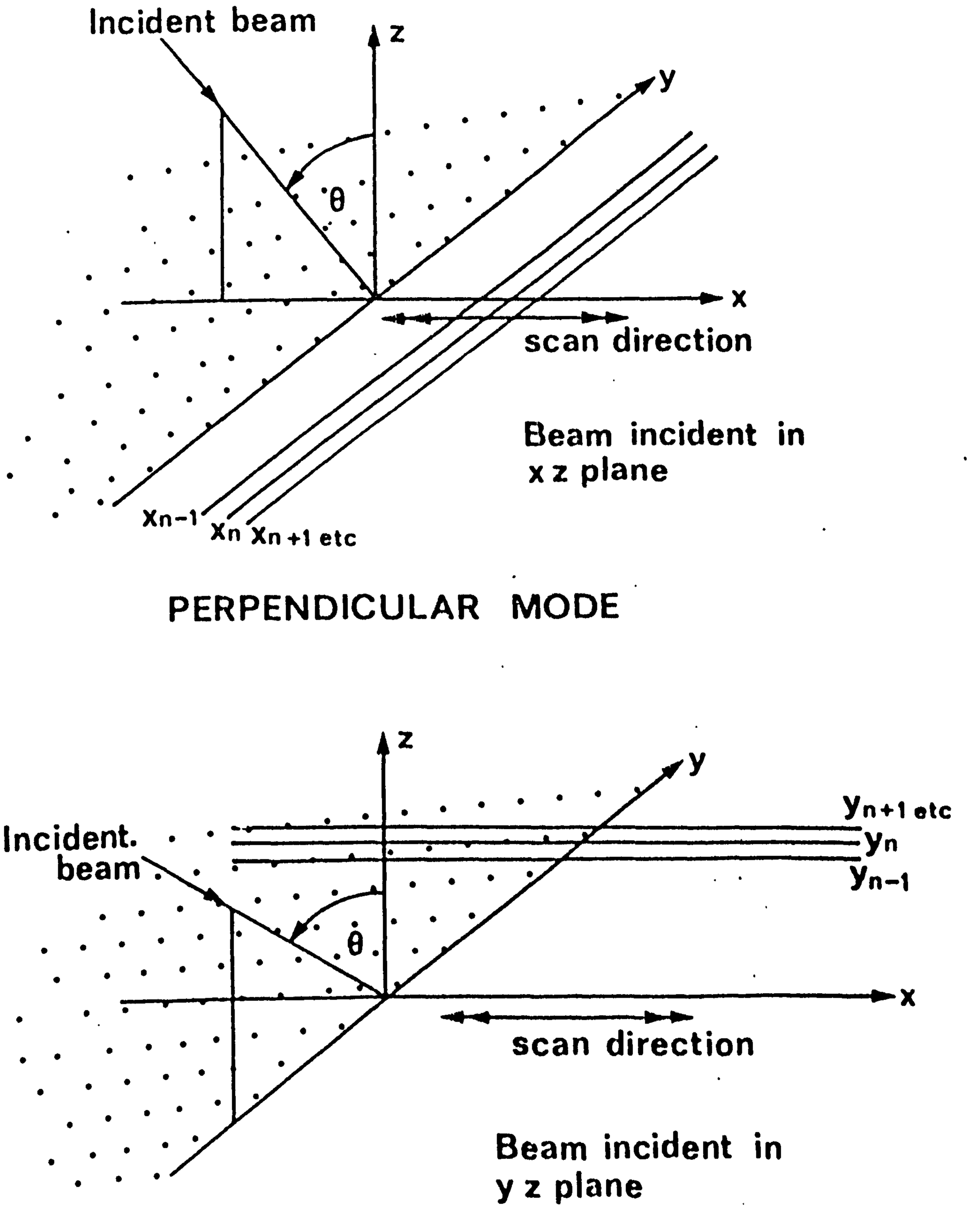

Fig. 5.5 The geometry of the incident beam with respect to the chemical edge and the scan direction.

the use of off-normal incidence. In this case there are two extreme possibilities for the detection of an edge:

(a) The plane of incidence is normal to the edge whilst the beam is also scanned normal to the edge (Figure 5.5a). This will be referred to as the perpendicular mode.

(b) The plane of incidence is parallel to the edge but the scanning direction remains normal to the edge (Figure 5.5b). This will be referred to as the parallel mode.

It is assumed for simplicity that the chemical edge is placed along the y-axis and the x-axis is in the plane of the surface and perpendicular to the edge. The x-axis is the scanning direction. The angle of incidence, θ, is defined in Figure 5.5. Auger electrons arising from ionisations caused by backscattered electrons are counted in intervals of width $(x_n - x_{n-1})$ for the perpendicular mode and of width $(y_n - y_{n-1})$ for the parallel mode. The counts C(x) and C(y) are then the Auger response functions for backscattered electrons arising from an infinitesimally wide incident beam. The total Auger response for a finite beam can be found by adding the Auger response due to the primary ionisations and then convoluting the total edge response function with the beam profile. Unlike the case of normal incidence dealt with in the last chapter, the incident beam intersects the surface in an ellipse of major axis $w \sec\theta$. The beam width is w. This elongation is important in the perpendicular mode.

In order to compare with the experiment of Janssen and Venables the spatial distribution of the backscattered Auger electrons was calculated for a Tungsten substrate at primary energies Ep of 20 keV and 60 keV. For 60 keV the primary electron range was divided into 200 steps and for the 20 keV it was divided into 100 steps. These ranges were calculated to be 8.1 μm and 1.3 μm respectively. The Auger process in question was the Ag,

$M_{4,5}$ VV transition at 355 eV. The backscattering factor η has been given by Reed (85) as 0.5 for Tungsten. At normal incidence the Auger backscattering factor was found to be 1.81 and for $\theta = 50^{o}$ it gave a value of $r = 1.6$, in good agreement with Janssen and Venables estimate. The rest of the data and the computer program were as described in the last chapter.

5.4 THEORY/EXPERIMENT COMPARISON

5.4.1 Comparison With The Experiment of Janssen and Venables

The backscattering part of the Auger response function for an infinitesimal incident beam width is shown in Figure 5.6 for both modes at the two primary energies. The experiment reported by Janssen and Venables corresponds to the perpendicular mode but with the chemical edge inclined at an angle γ of 26.5^{o} to the y-axis in Figure 5.5a. The effect of this inclination has been included in the calculation of the response function by summing the Auger electron count in strips parallel to this inclined edge. For small angles γ it can be approximated by multiplying the x-coordinate in Figure 5.6a by $\sec\gamma$. The response function thus modified was then summed to a Gaussian incident beam profile and then integrated over x to yield theoretical edge profiles. The summation procedure is a good approximation to the (exact) convolution process described in the last chapter because the widths of the incident beam and the Auger response functions are so different. The full width at half-maximum (FWHM), σ, of the incident beam was allowed to take the values 10, 20, 30 or 40 nm in order to compare with the experimental data obtained with a 20 nm beam width. The calculated profiles for 20 keV are compared in Figure 5.7 (solid lines) with the experimental data (broken line). The agreement between theory and experiment is very good, showing that the experimental

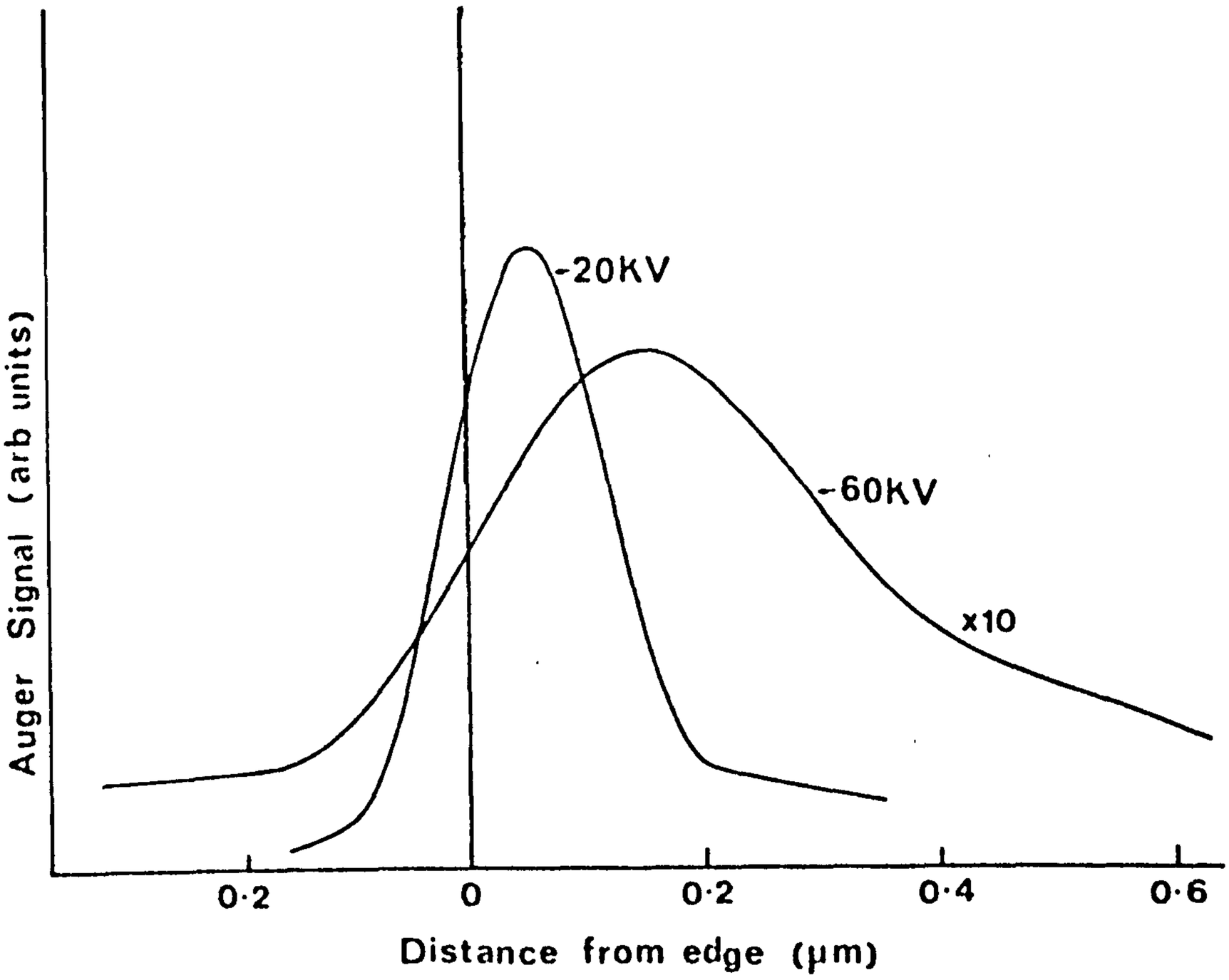

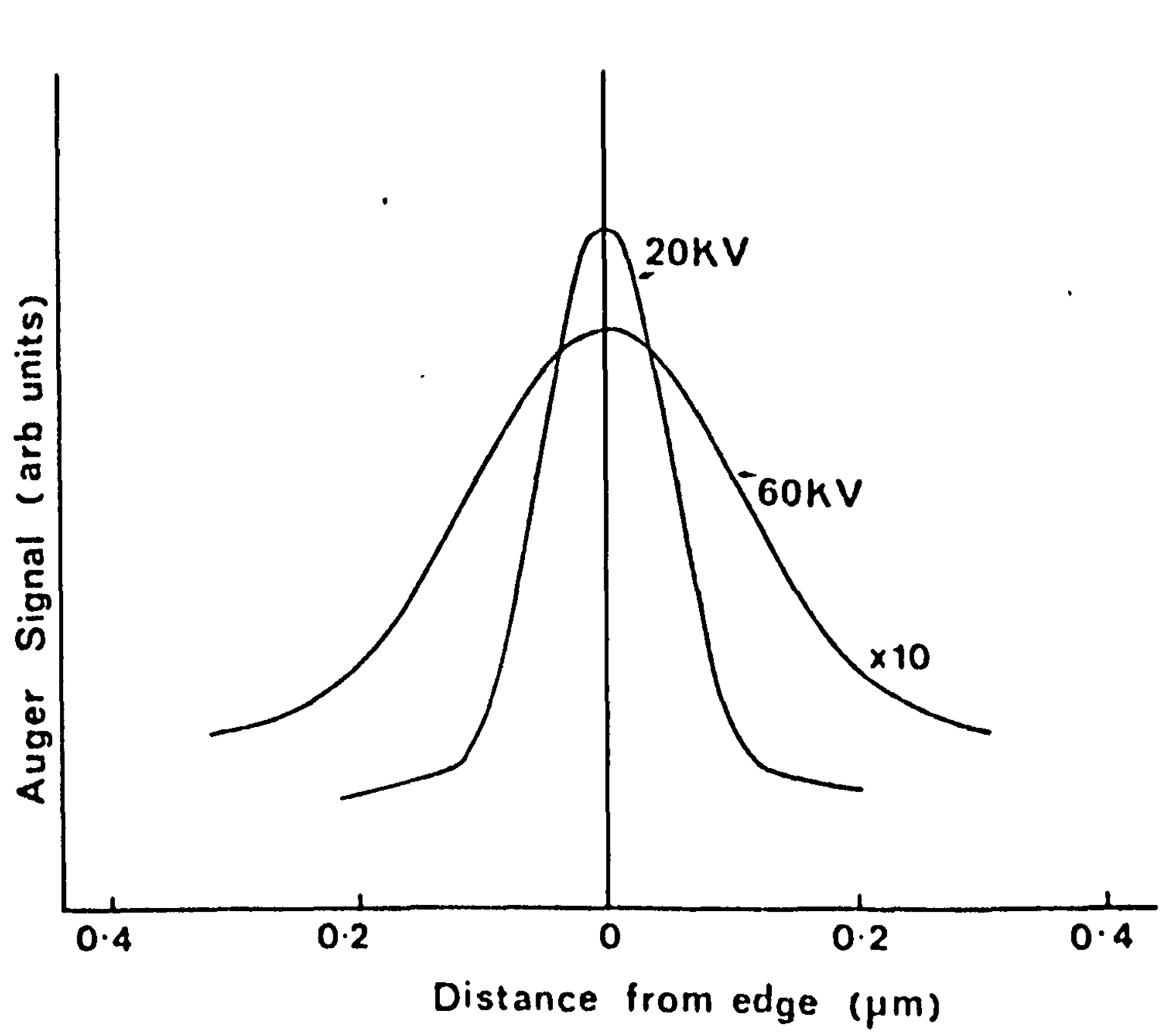

Fig. 5.6 Spatial distribution function of Auger electrons due to backscattering in the case of Ag M_{45} VV .
(a) Perpendicular mode.
(b) Parallel mode.

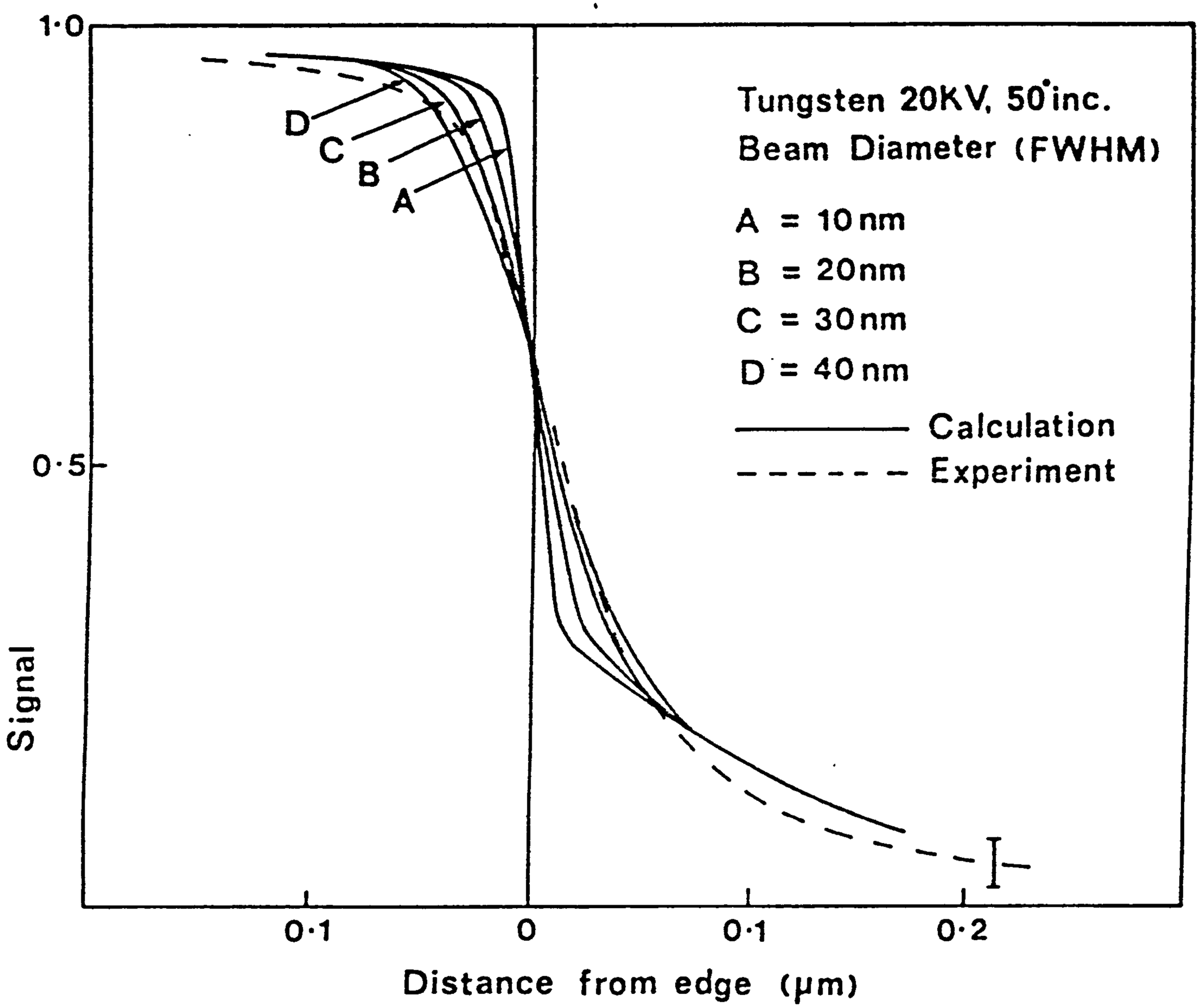

Fig. 5.7 Comparison of measured - – – - and calculated ——— edge profiles of Ag M_{45} VV at $\theta = 50^{o}$ and Ep = 20 keV. Beam assumed to be a Gaussian with FWHM ranging from 10 - 40 nm.

profile lies between the calculated 20 nm and 30 nm profiles. Using the criterion, adopted in the last chapter, that the spatial resolution in SAM, Δ_{50}, should be measured between 25% and 75% of the maximum Auger signal, the calculated profiles of Figure 5.8 show that differences in incident beam sizes can be easily detected in the resolution profiles. This observation, however, applies to fine beams as discussed in the last chapter (4.6.1(ii)). This result confirms that the spatial resolution in SAM is limited by the incident beam size as predicted earlier.

For 60 keV electrons, as shown in Figure 5.7, agreement with theory is not so good. In addition, the spatial resolution is much worse than in the 20 keV case. This loss of resolution at 60 keV could be associated with the asymmetric function of Figure 5.6a. This asymmetry is due to the forward peaked character of the electron scattering which becomes more noticeable in the Auger yield as the angle of incidence is raised. (The effect of angle of incidence on resolution will be discussed more fully in the following section.) Thus, peaking in the forward direction is displaced further from the chemical edge at 60 keV than at 20 keV. This leads to a relatively high "tail" in the edge profile which was found to extend a few microns away from the edge in the 60 keV case. At the same time the number of primary ionisations falls by a factor of about 2.6 between 20 keV and 60 keV for constant incident beam current. The consequent degradation of signal to noise ratio, by a factor of nearly 1.6, will also contribute to apparently worse spatial resolution. Nevertheless, the calculated 40 nm profile is not far from the, necessarily noisy, experimental data and generally shows the same behaviour as seen in the experiment.

The response functions at 20 keV and 60 keV for the parallel mode are shown in Figure 5.6b. In this geometry the minor axis of the ellipse formed by the intersection of the beam with the sample is what determines

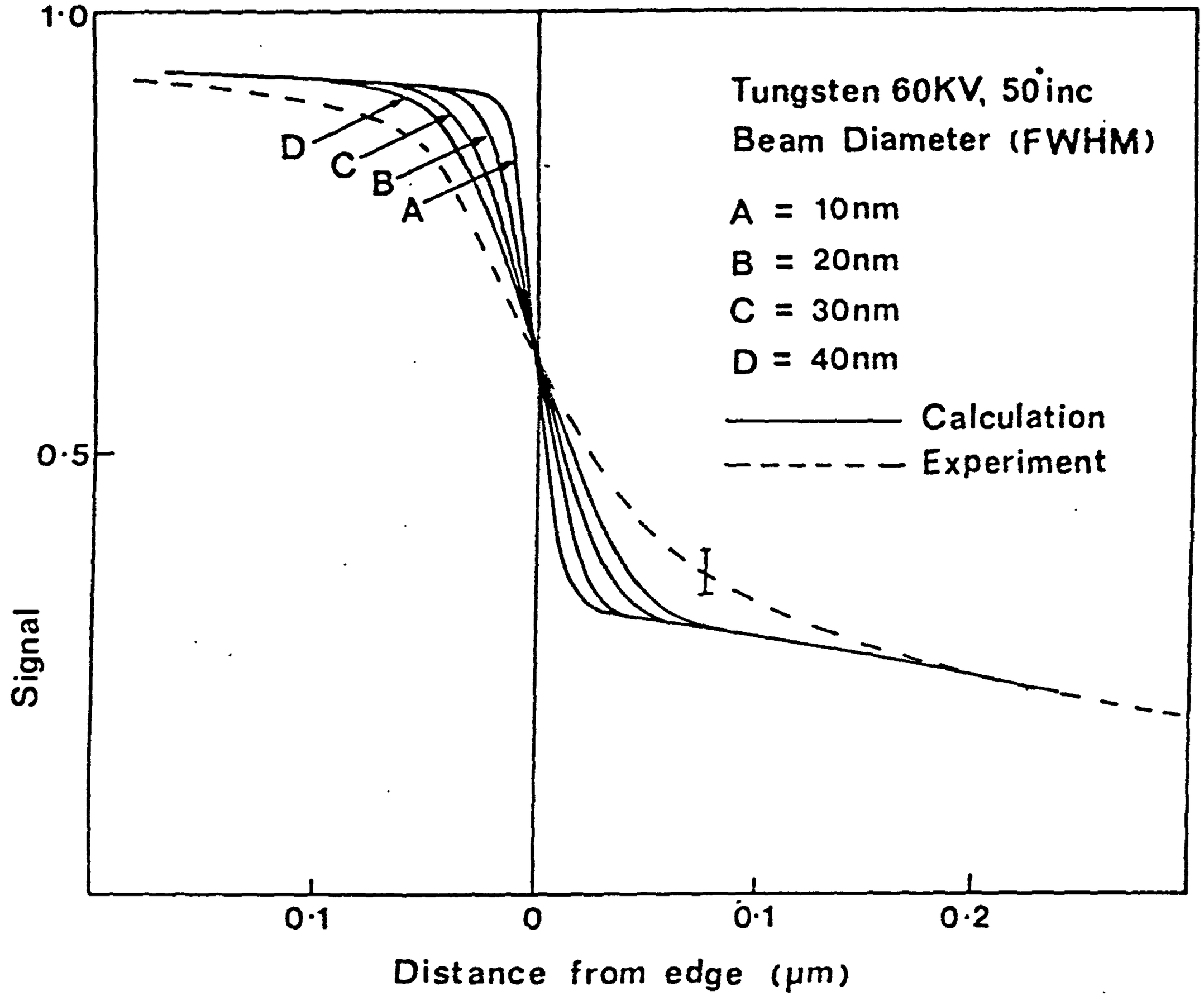

Fig. 5.8 As Fig. 5.7 but for Ep = 60 keV.

the spatial resolution. Unlike the perpendicular mode, the response function, here, is symmetric around the origin. This helps in improving the resolution when convoluted with the beam profile which is also symmetric around the origin. Figure 5.9 shows the calculated Auger profiles for this mode at 20 keV and 60 keV for the same beam size range as used in Figures 5.7 and 5.8. The profile is symmetric as expected and yields better spatial resolution than does the perpendicular mode using the same definition Δ_{50}. Increasing Auger yield with increasing θ should give improving signal to noise ratio without loss of spatial resolution if this edge geometry is used.

5.4.2 The Effect Of The Edge Orientation On The Resolution

A preliminary investigation of the effects of backscattered electrons on SAM resolution as a function of the chemical edge orientation with respect to the scan direction has been carried out using the second instrument (to be described later). The sample used was a microcircuit with an SiO_2 overlayer, estimated from the SEM picture to be about 1 - 2 μm thick, on a silicon substrate. Figure 5.10 shows the part of the sample used with the superimposed line indicating the scan direction. Although a thinner overlayer, as that used by Janssen and Venables, would have been preferable for quantitative experimentation, no gross interference from topographical effects have been seen during this experiment due to the effective normalisation technique used, $(N_1 - N_2)/(N_1 + N_2)$. In addition, the SiO_2 overlayer is cut with a sloping profile to reveal the Si as can be seen from the micrograph. An independent test with a tallystep showed the step to be about 1.6 μm in good agreement with SEM. Figure 5.11 shows the N(E) spectra of the two materials $Si(SiO_2)\,L_{23}VV$ and $Si\,L_{23}VV$, after the sample was cleaned for 45 minutes with an argon ion dose 10^{-6} A/cm^{-2}, I_b ~2 nA into a spot of a Gaussian profile with a FWHM, σ of about 250 nm and

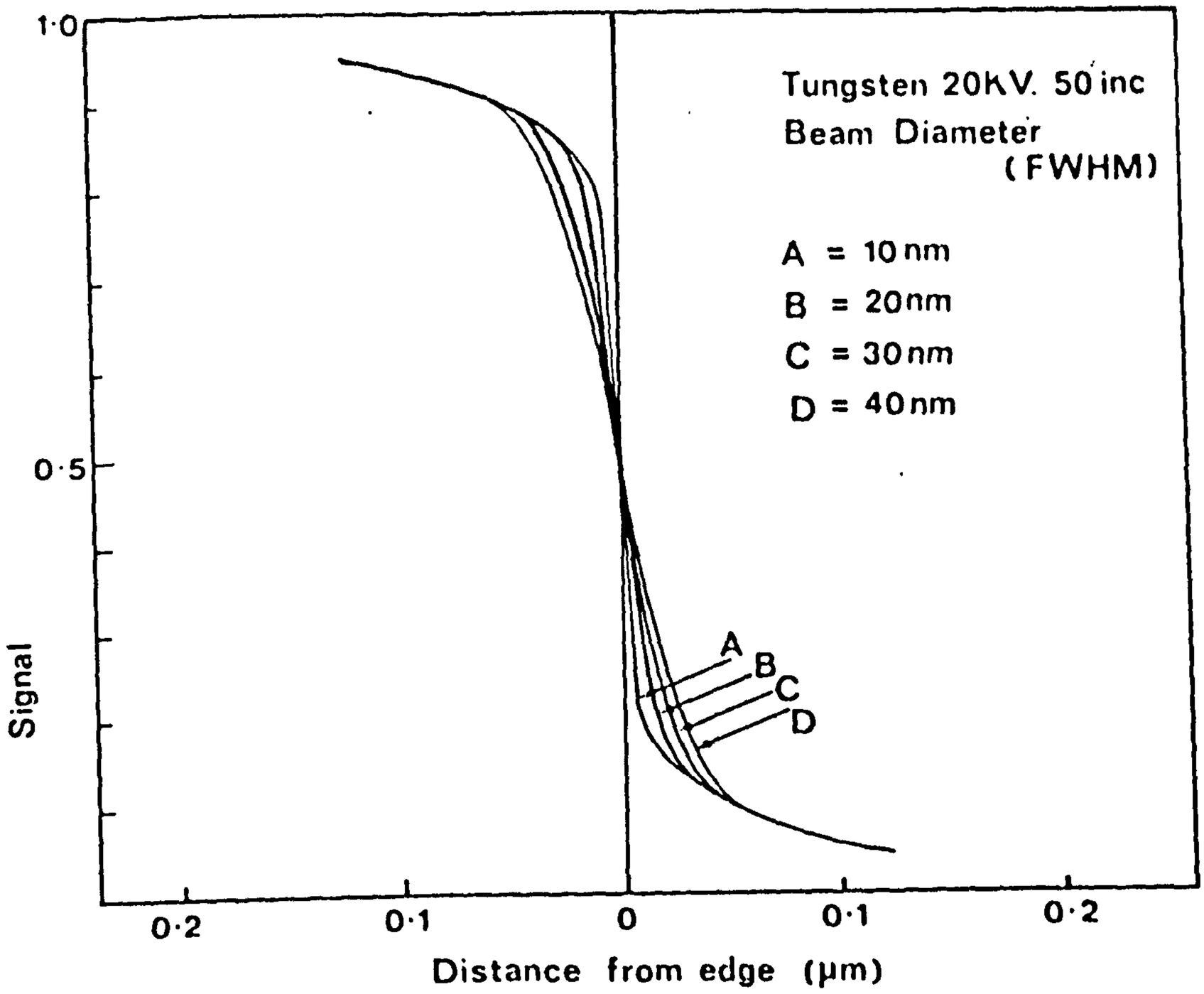

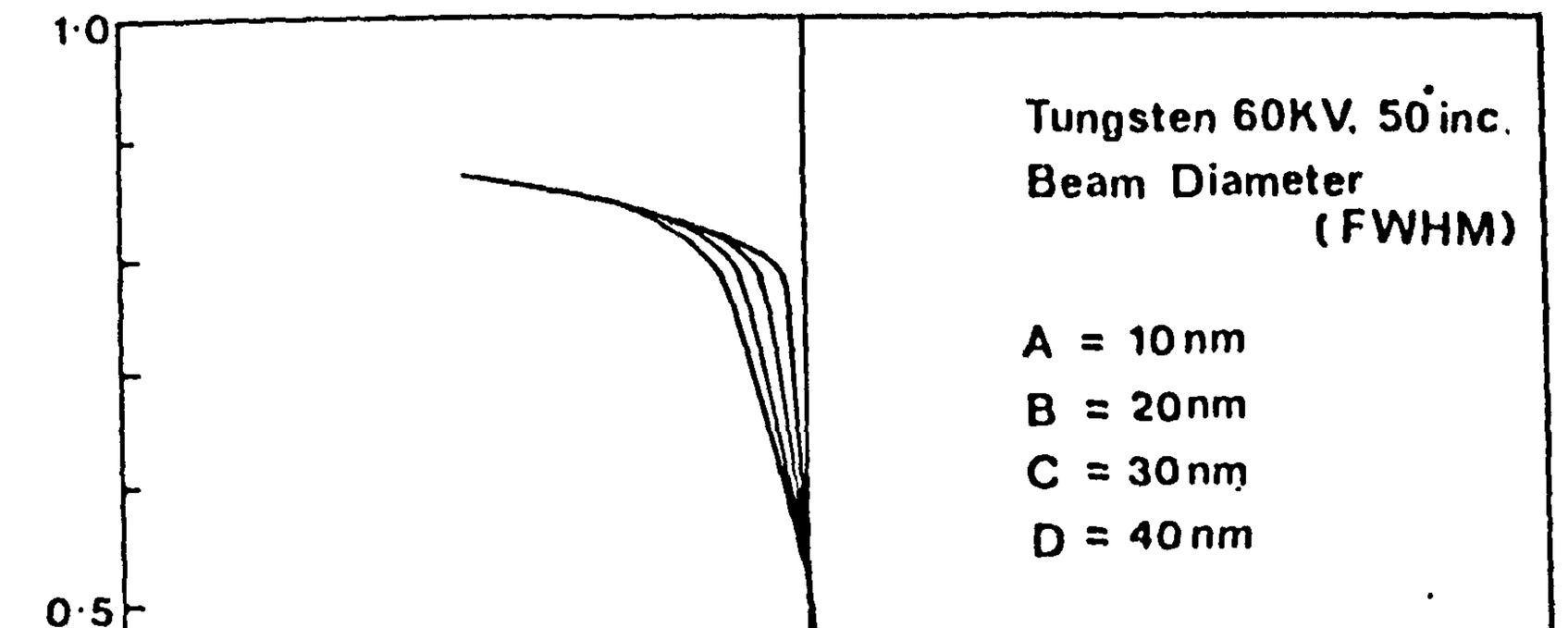

Fig. 5.9 Calculated edge profiles for the parallel mode.
(a) Ep = 20 keV, (b) Ep = 60 keV.

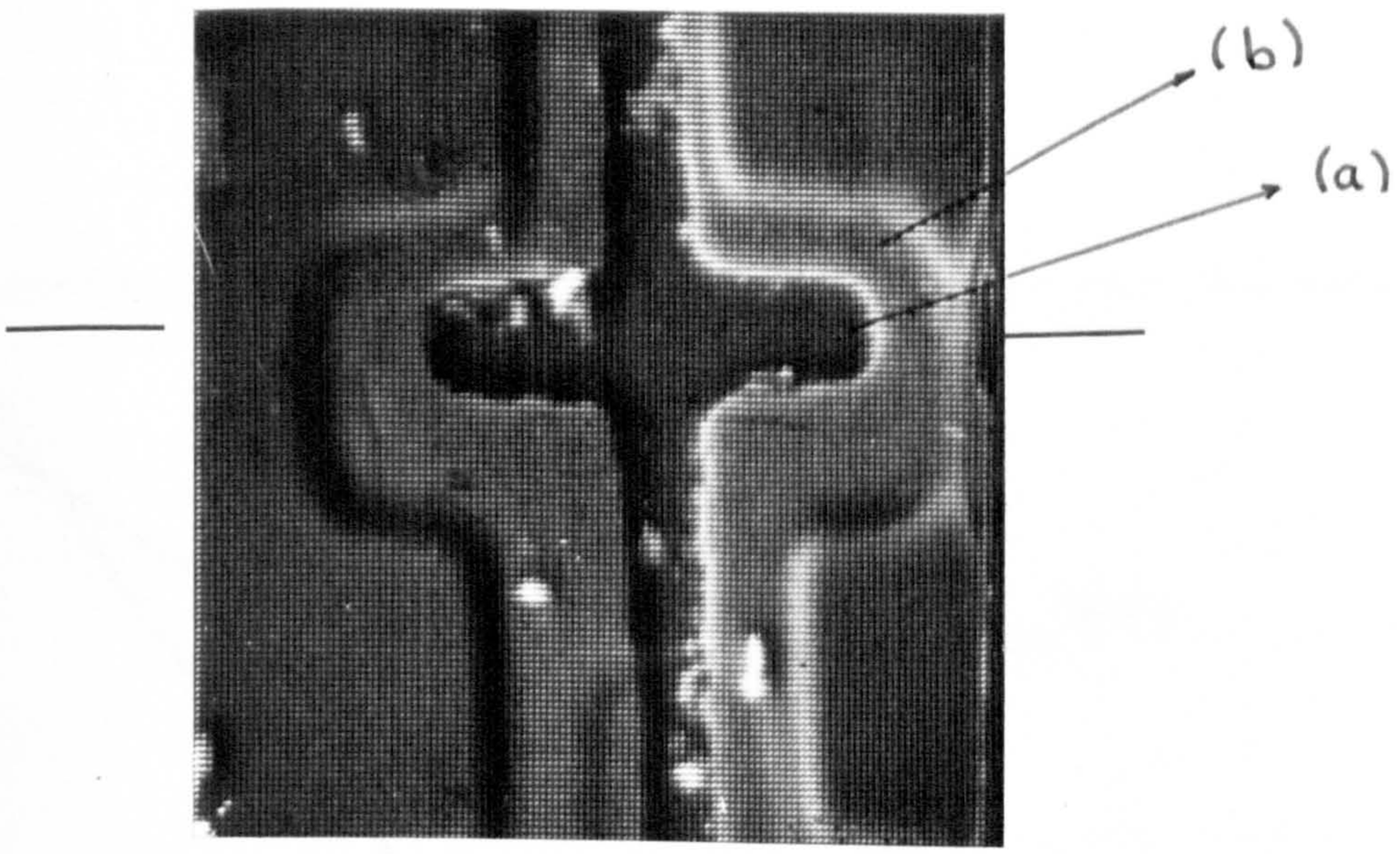

Fig. 5.10 SEM micrograph of part of the Integrated circuit, with superimposed line indicating scan direction.

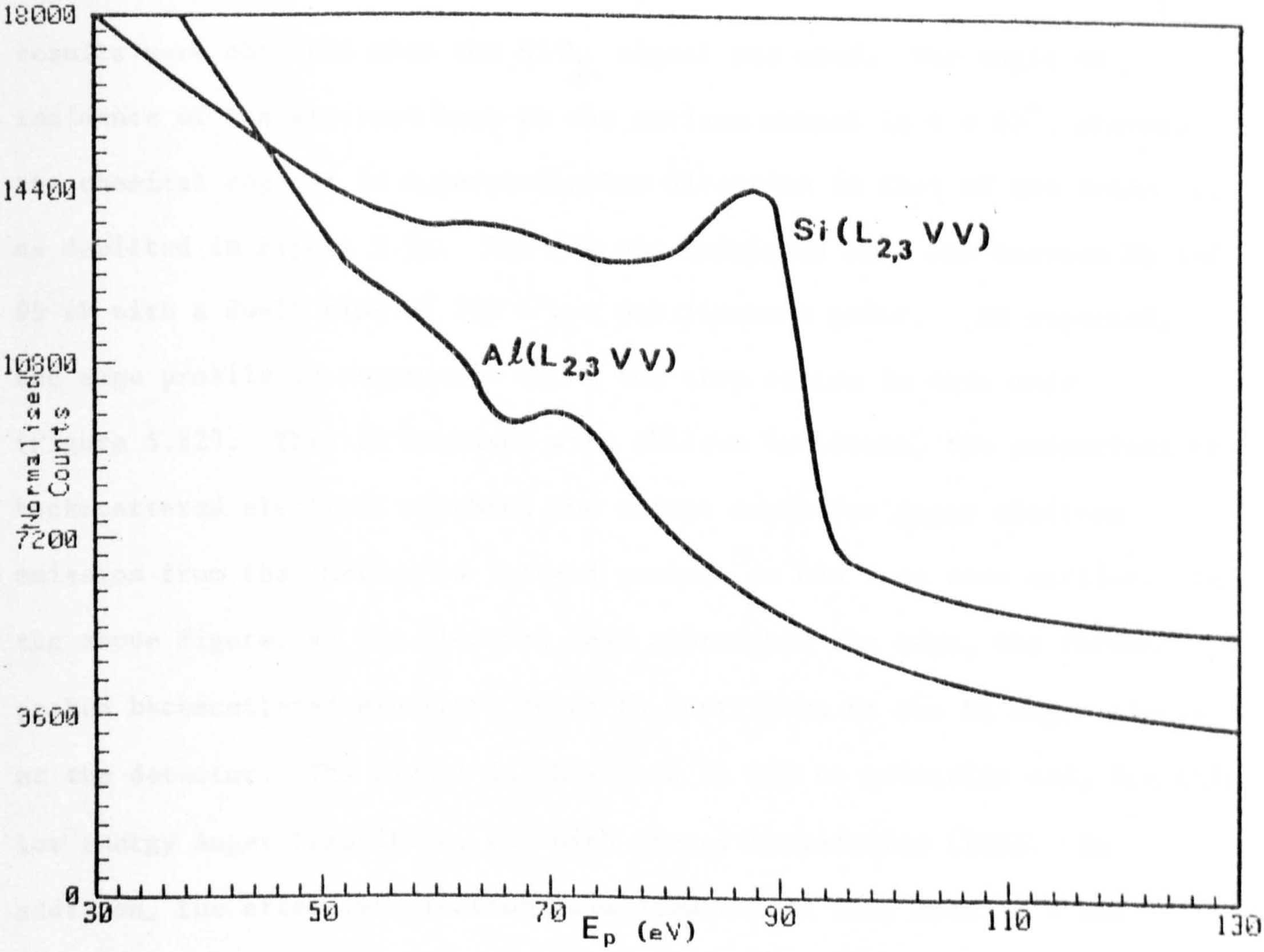

Fig. 5.11 Spectra from points (a) and (b) of Fig. 5.10 showing Si($Si\,O_2$) $L_{23}VV$ and Al L_{23} VV . I_b = 2 nA, Ep = 20 keV.

a primary energy Ep = 20 keV were used.

Figure 5.12 shows the measured edge profile in the perpendicular mode. The Si signal was chosen for the line scans because it has a greater peak height above background than the SiO_2, as can be seen from Figure 5.11. This choise improves only the linescan (S/N) , but the same results were obtained when the SiO_2 signal was used. The angle of incidence of the electron beam to the surface normal is $\theta = 45^{o}$, whereas the chemical edge is in a perpendicular direction to that of the scanning, as depicted in Figure 5.5a. The CHA was modulated at 1 kHz between 88 and 95 eV with a dwell time of 200 m sec per linescan point. As expected, the edge profile is assymetric about the step centre in this mode (Figure 5.12). This is because, with oblique incidence, the proportion of backscattered electrons reaching the escape depth for Auger electron emission from the surface is forward peaked, as has been seen earlier. In the above Figure, as the electron beam approached the edge, the forward peaked backscattered electrons cease to contribute to the Si Auger signal at the detector. The signal in this area is due to primaries and, for this low energy Auger transition, the high energy secondaries (105). In addition, the effective electron beam diameter in this mode is $\sigma \sec \theta$, resulting from the intersection with the sample. Using the same criterion for the measurement of edge resolution, Δ_{50}, Figure 5.12 gives $\Delta_{50} \simeq 950$ nm. From the Monte Carlo results of Chapter 4, formula (4.18) gives

$$\Delta_{50} \underline{\Omega} 1.25\ r\ \sigma \sec \theta$$

and assuming r to be 1.4, one obtains $\Delta_{50} \approx 630$ nm.

The reasons for the discrepancy between theory and experiment can be explained as follows: Firstly the theory does not take into account the contribution of high energy secondaries which may broaden the spatial

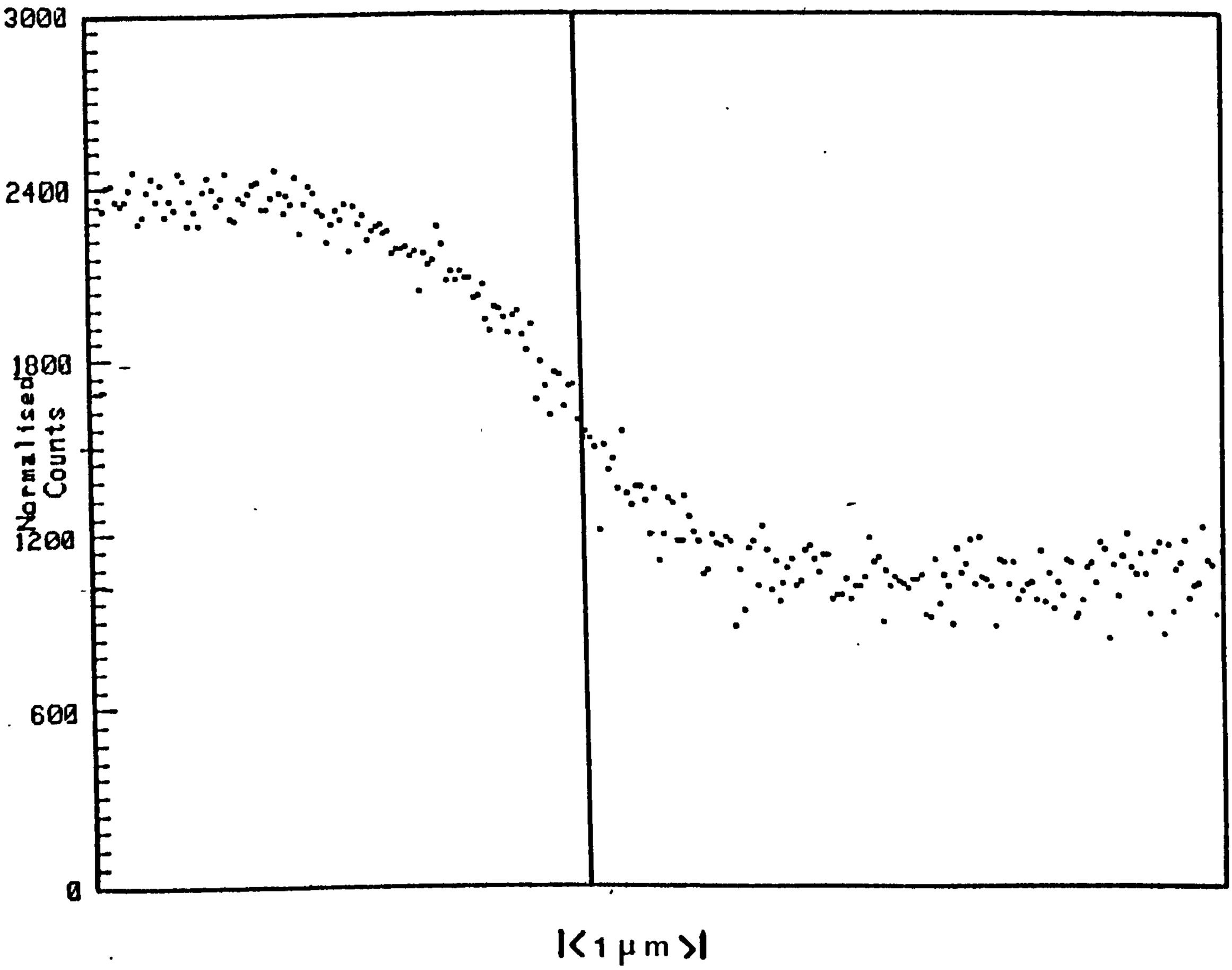

Fig. 5.12 Measured edge profile in the perpendicular mode. Dwell time is 200 m sec per point, for 256 points. The profile is the average of 2 scans. I_b = 2 nA, Ep = 20 keV.

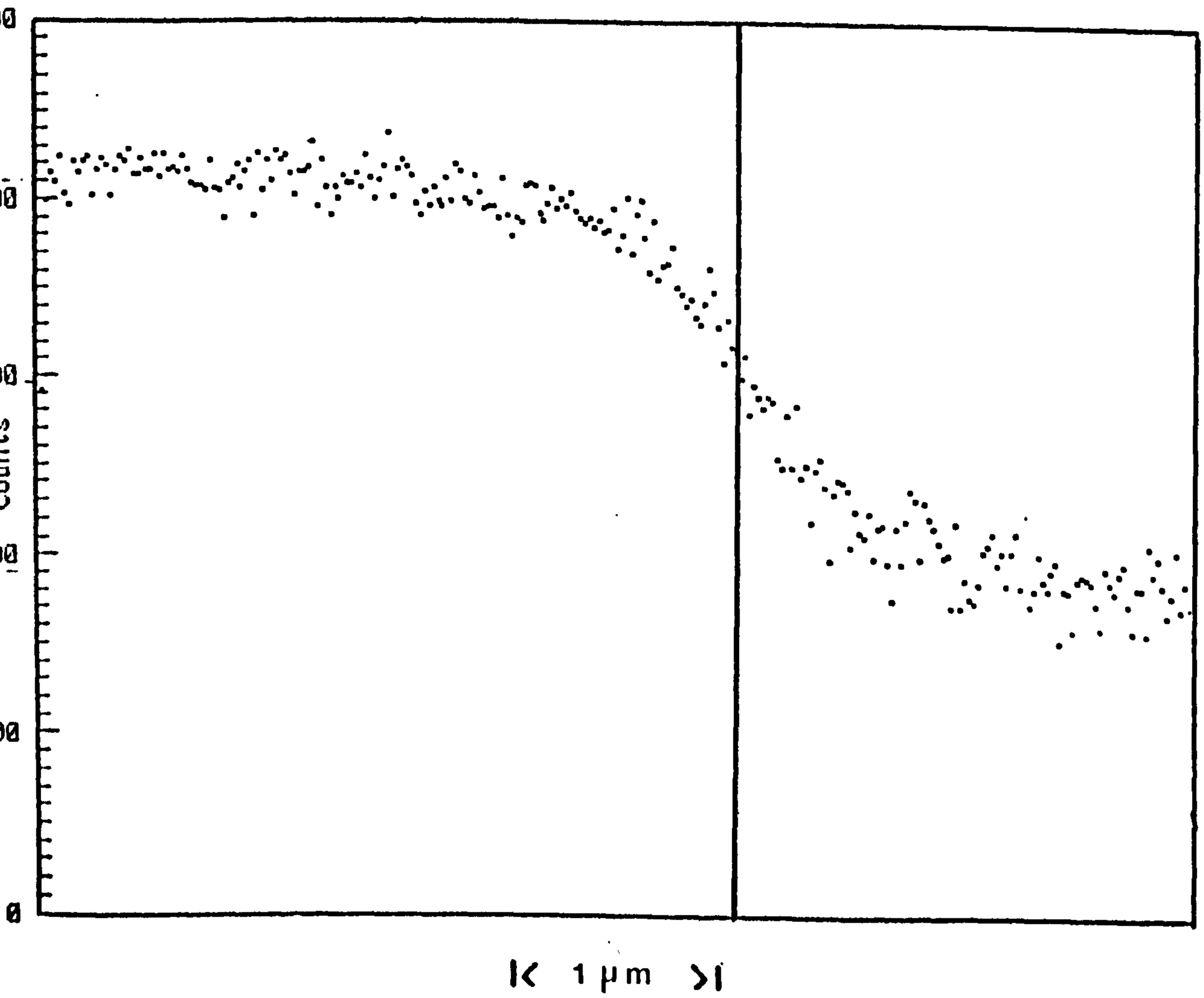

Fig. 5.13 Measured edge profile in the parallel mode. Same conditions as in Fig. 5.12.

distribution of low energy Auger electrons. Secondly the broadening effects of the forward peaking of the backscattering contribution for off-normal incidence in this mode may increase the value of Δ_{50}.

By rotating the sample in situ through 90^{o} about the azimuth, a unique capability of the present instrument, it was possible to scan the same edge as in Figure 5.12 but in the parallel mode to give the edge profile shown in Figure 5.13. In this case, the effective beam diameter is the minor axis of an ellipse, σ. Figure 5.13 shows a symmetric profile about the origin, in agreement with the theoretical results of section 5.4.1. In addition, a Δ_{50} of nearly 600 nm is found in this case. The theory suggests $\Delta_{50} \simeq 440$ nm. This discrepancy might be in part due to the contribution from energetic secondaries.

The above experiment has clearly shown that the orientation of a chemical edge with respect to the scan direction has an important influence on the spatial resolution of a SAM and must be taken into account when interpreting Auger images. However, in order to obtain more quantitative estimates of the effects of high energy secondaries a shallower topographical step at the chemical edge and a beam diameter of less than 100 nm should be used. In order to compare such an experiment with theory, the existing Monte Carlo calculations will need to be modified.

5.5 CALCULATION OF THE EFFECTS OF ENERGY AND ANGLE OF INCIDENCE ON EDGE RESOLUTION

The above results show the dependence of the spatial resolution on both primary energy Ep and angle of incidence 0 for a fixed specimen and an Auger process. This dependence is stronger in the perpendicular mode. The above technique and input data were extended in the perpendicular mode.

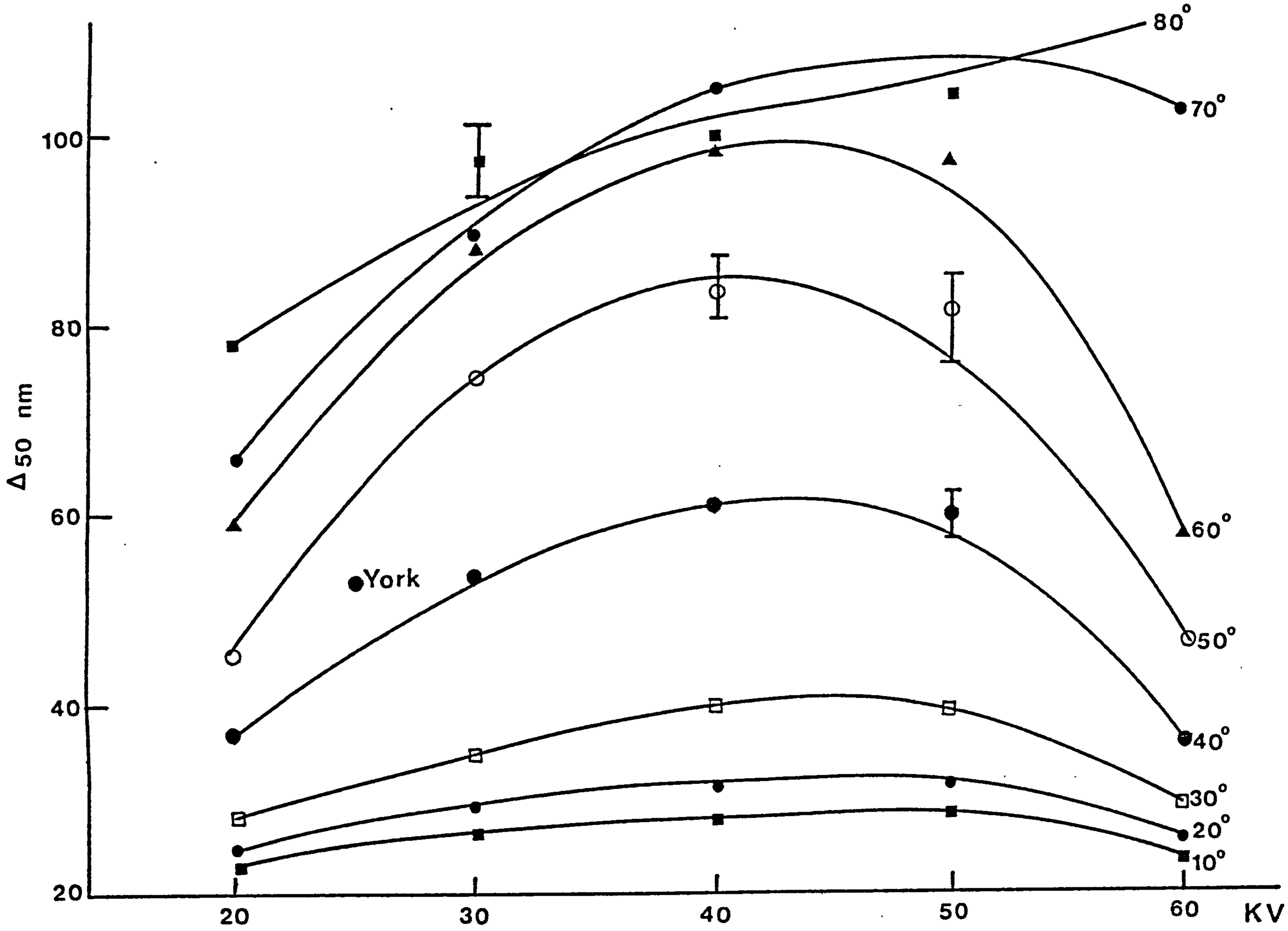

Fig. 5.14 Change in SAM resolution Δ_{50} as a function of Ep and θ for a probe 20 nm. FWHM in the perpendicular mode.

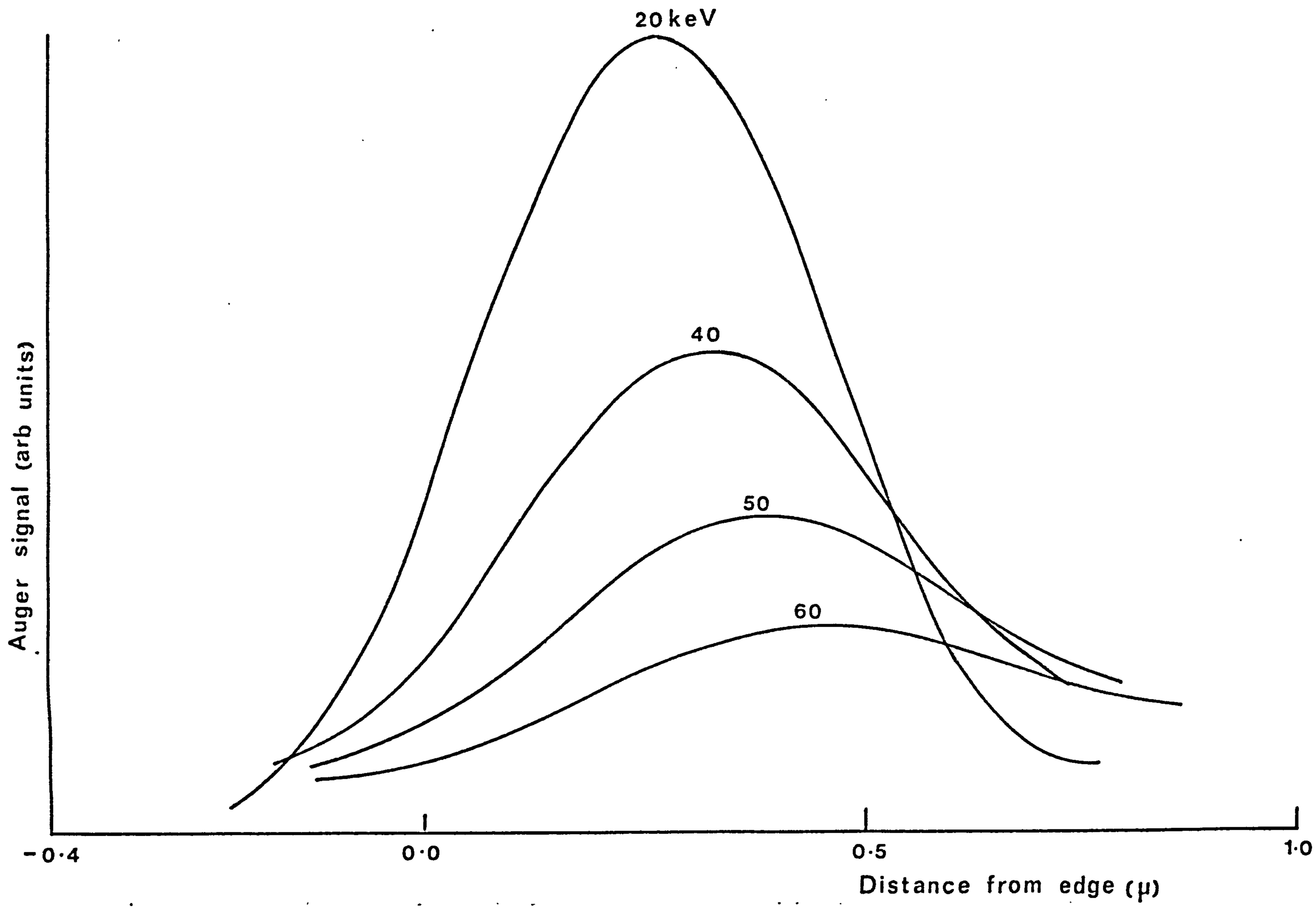

Fig. 5.15 Auger backscattering response functions for different primary energies, E_p but fixed incidence angle $\theta = 50^{o}$.

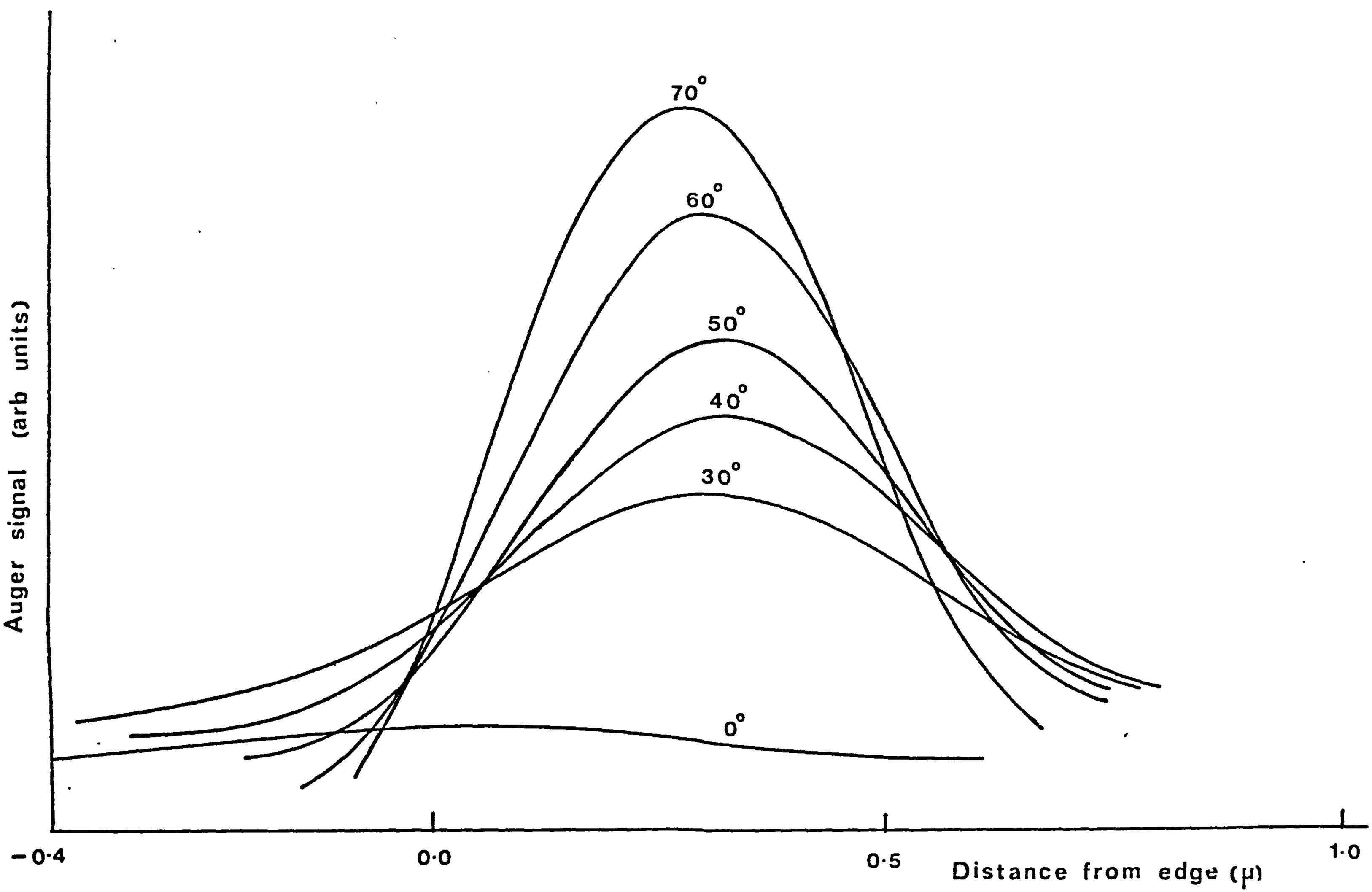

Fig. 5.16 Auger backscattering response functions for different incidence angles and fixed primary energy, E_p = 40 keV.

The ranges $0^{o} < \theta < 80^{o}$, 20 keV < Ep < 60 keV and 10 nm < ω < 40 nm have been explored. The electron range was divided into 100 steps for the 20 keV and 30 keV cases and 200 steps for the 40 keV - 60 keV cases. Figure 5.14 shows the results for the perpendicular mode and a beam of full width at half maximum of 20 nm.

It can be seen that optimum resolution should be obtained in normal incidence, in which case Δ_{50} is roughly independent of primary energy. As θ is increased the resolution is degraded until Ep is over 50 keV when Δ_{50} begins to improve again. This behaviour is seen for θ up to nearly 60^{o}. In addition to the simple projection of the incident electron beam into an ellipse of major axis ω sec θ it is believed that there are three other contributions to the behaviour of Δ_{50} for $\theta < 60^{o}$. The first is that as Ep increases, for fixed θ, the peak in the backscattering response function shifts away from the point of incidence. This behaviour is seen in Figure 5.15 for $\theta = 50^{o}$ and Ep over the range 20 keV - 60 keV. When summed with the beam profile this results in a broader and more asymmetric edge response function around the origin. This effect dominates up to 40 - 50 keV. Secondly, as θ increases for a fixed Ep, the peak of the backscattering response function will again shift, away from the point of incidence. This is shown in Figure 5.16 for Ep = 40 keV and θ values over the range 0^{o} - 70^{o}. As a result, a similar edge response function to that described above would be obtained upon summation with the beam profile. Finally, for high values of Ep the backscattered electrons are distributed over a wider surface area than at, say, 20 keV, as can be seen in Figure 5.15. Thus the height of the backscattering response function is lower with respect to the beam profile and the edge resolution tends back towards the projection of the beam width.

For $\theta > 60^{o}$ it is interesting to note that the projection of the beam width is the dominant contribution to Δ_{50}. The degradation of the

spatial resolution at these high values of θ means that the experiment is approaching the region of conventional, coarse resolution, Auger spectroscopy. In these circumstances Δ_{50} can vary rather slowly with ω. If one is forced to work in this geometry it can be beneficial from a signal to noise point of view to use an increased beam diameter, and so collect more current, at the expense of a slightly degraded spatial resolution. It should also be noted that at such high angles of incidence it will be rather difficult to eliminate the interference with chemical information due to sample topography.

In the parallel mode the only effect of increasing θ is to increase the number of ionised atoms. As the value of Ep increases the backscattering response function increases in width but is sufficiently small that the effect upon Δ_{50} is negligible.

5.6 THE EFFECT OF SAMPLE TOPOGRAPHY ON RESOLUTION

In the above calculation, it was assumed that a flat surface exists with a chemical edge of negligible height (or at most of height < the probe diameter). In reality this is not often the case. Practical specimens that are investigated in a SAM consist normally of fractured or chemically etched surfaces with topographical variations on the surface of the order of several microns. Such gross variations can lead to incorrect conclusions in quantitative measurements unless taken into consideration.

It is interesting to note that shadowing of the signal by protrusions of a particular surface will have an increasing role as the incident beam angle is increased. This is schematically depicted in Figure 5.17 for the case of a narrow collection cone angle as in the CHA. The use of a different collection geometry, as the CMA, may result in a reduction in the signal instead of a total loss for the above geometry.

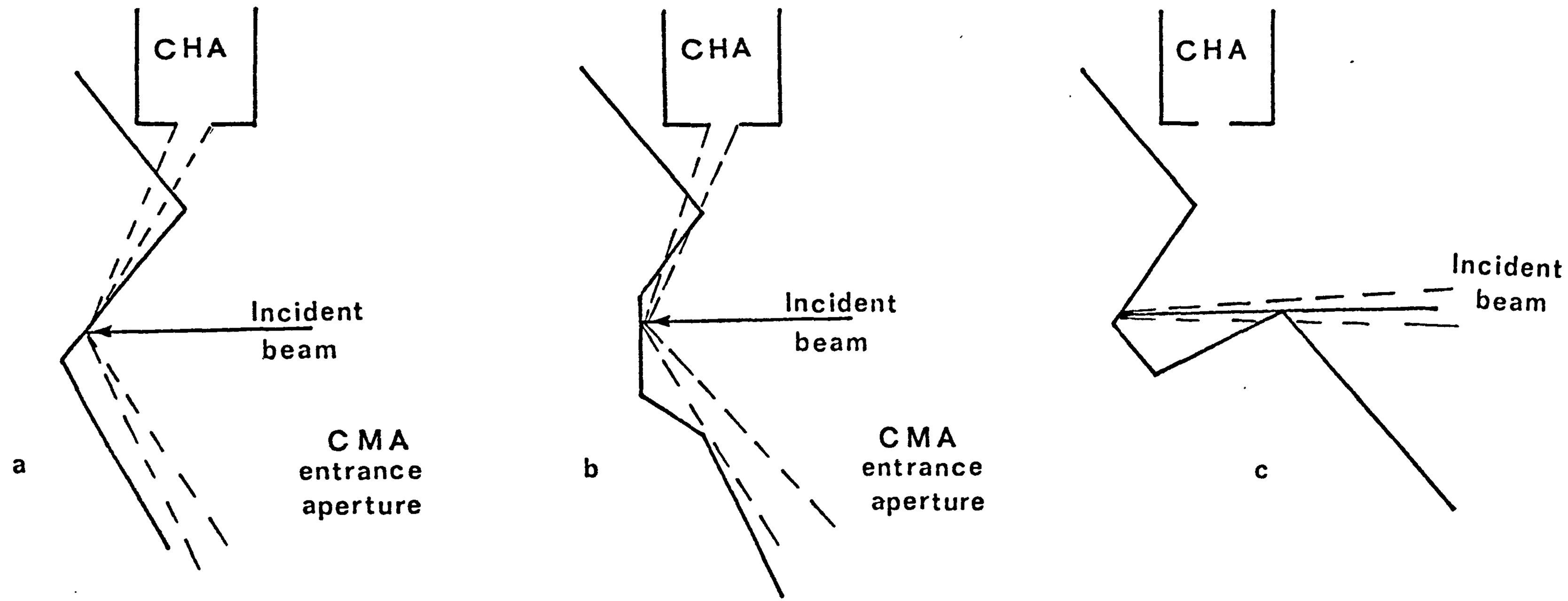

Fig. 5.17 The effect of topography on the collection of an Auger signal. (a) self shadowing (b) neighbour shadowing (c) beam obstruction.

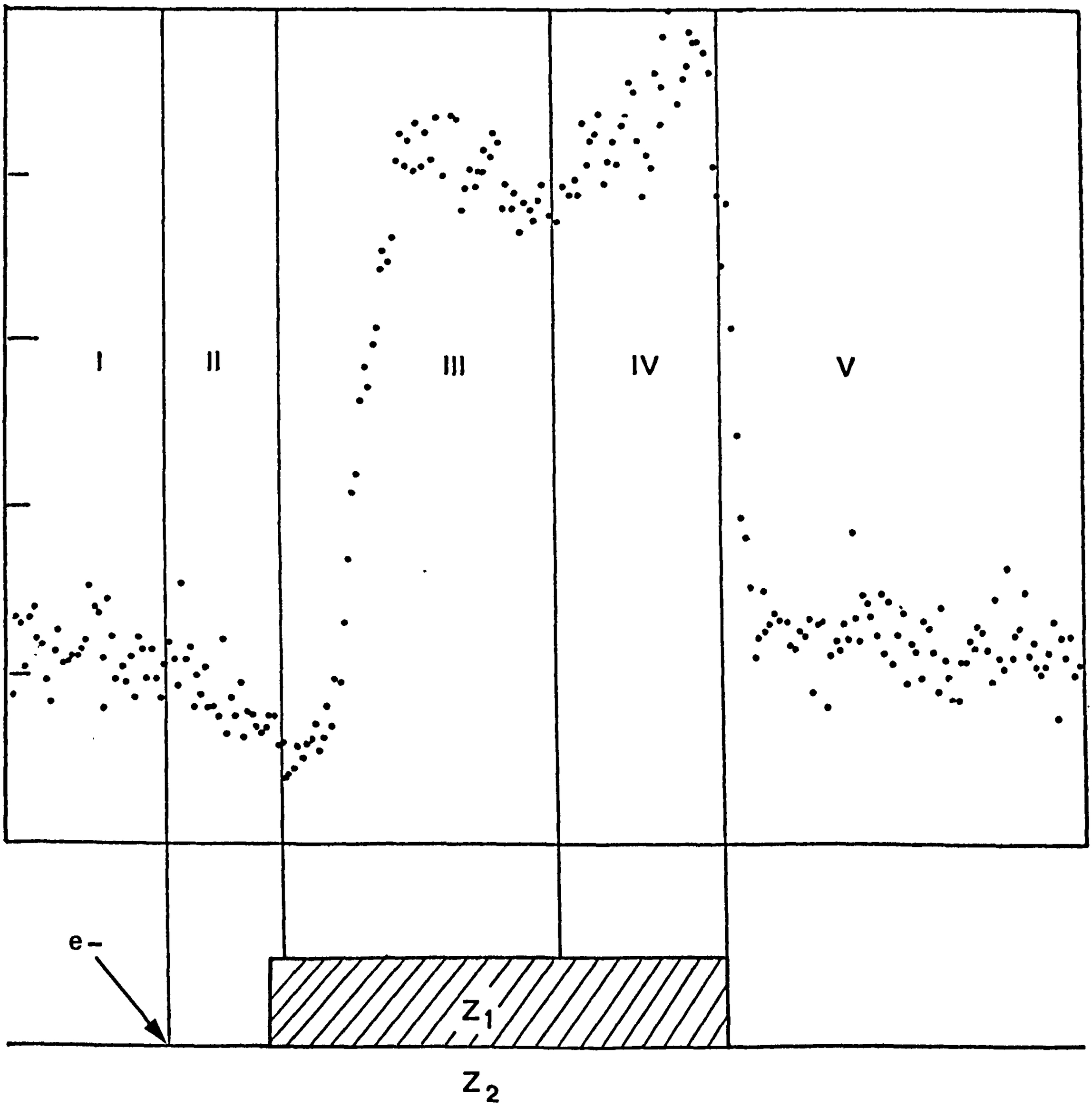

Fig. 5.18 The effect of self and neighbour shadowing on an edge profile.

Normalisation techniques of the type described in Chapter 2 can correct, with up to 10% accuracy, for simple topographical interference (69). More complicated geometries as shown in Figure 5.17c may require the use of several images (or line scans) of the same area and at different incident beam angles.

An example of shadowing effects in case a and b of Figure 5.17 above is shown in Figure 5.18. The specimen used was a plasma etched Aℓ of 1 μm thickness on an SiO_2 substrate and the edge is inclined 45^{o} with respect to both the CHA and the electron beam. The behaviour of the collected Auger signal can be classified into 5 regions depending on the point of incident electrons as follows:

i) The electron beam is on the substrate and all backscattered electrons are detectable by the CHA.

ii) As the beam approaches the edge, a drop of the signal collection by the CHA results, due to intersection by the edge (i.e. neighbour shadowing). A further drop of the signal to a minimum is obtained as the beam starts to scan the side of the edge (i.e. a combination of self and neighbour shadowing).

iii) Region 3 shows a rise in the Aℓ signal as the beam begins to scan the top of the edge. All the active interference here is self shadowing.

iv) In this region the signal is enhanced further due to the change of the electron beam incidence angle.

v) The last region shows a gradual fall-off in the Aℓ signal as the beam moves away from the edge. It is interesting to note here that part of the Si substrate, next to the Aℓ metallization, is still shadowed from the electron beam. The effect of this is to cause smearing of the edge.

An estimate of the width of the Aℓ metallization from the above results shows it to be about 7 μm (FWHM), in good agreement with estimates made with the SEM. However, a shift in the edge position in the Auger mode with respect to that of the SEM is obtained and is due to the topographic interference. The effects of such interference at high resolution could be stronger but a well designed experiment (i.e. finer probe diameter, well defined topography) will be needed. Preliminary results of one of the correction schemes $(N_1 - N_2)/N_2$ showed further smearing of the edge in the above example.

5.7 DISCUSSION

An experiment to measure the edge resolution in a SAM is described and the results are compared with theoretical predictions using the Monte Carlo techniques of the last chapter. In addition two experimental geometries for the detection of a chemical edge with respect to the scan direction are defined. The agreement between experiment and theory using a high energy Auger transition is very good. From this comparison it can be seen that the resolution limits in SAM are determined by the incident beam profile and the experimental geometry. For low energy transitions (i.e. $\lesssim 100$ eV) the agreement with theory is less satisfactory. An important reason for this discrepancy could be the contribution of high energy secondaries which was not included in the theory. Shimizu et al (105) have found that for LMM transition (i.e. < 100 eV) up to 30% of the signal is due to high energy secondaries.

Preliminary tests on the edge geometry with respect to scan direction has confirmed that the parallel mode yields a better spatial resolution in comparison with the perpendicular mode, as predicted in the theory. However, further work with probe diameter less than 100 nm and for a wide

number of substrate materials is needed. A suggested experiment here is to use the same Aℓ edge to investigate the effects of high energy secondaries with the two Aℓ Auger transitions, namely KLL (at 1390 eV) and LMM (at 68 eV). On the theoretical side, an investigation of the role of high energy secondaries on low Auger transition energies is also required.

In conclusion, if instrumental effects such as specimen drift (due to stage), beam current instability and specimen damage forcing the use of a large beam diameter can be excluded, the resolution in SAM will be controlled mainly by the profile of the incident beam. Further factors that should be taken into consideration are the geometry of the edge with respect to scan direction, the electron beam energy, the angle of incidence, the topography of the edge and finally any contribution from un-isotropic Auger emission. These will broaden the resolution in SAM but only by a factor of 2 - 3 the beam diameter, hence proving SAM to be a high resolution technique. Consequently, development of electron probes should be aimed towards a high beam current in a spot diameter of the order of few tens of nm's.

CHAPTER 6

OPERATIONAL CONDITIONS OF FIELD ELECTRON EMITTERS IN HIGH CURRENT PROBES

6.1 INTRODUCTION

The discussions in the previous chapters have established that a beam current of the order of few nA is required for short frame Auger mapping (< 500 secs), with the smallest possible spot size. Such requirements necessitate the use of a high brightness electron source. The brightness (B) is defined as the number of Amperes/ster adian/cm^2 an emitter supplies. Table 6.1 lists B values for various electron sources used in electron probes. As can be seen from this comparison, field electron emitters have a B value of at least a factor of $x10^2$ with respect to conventional sources. At the beginning of this work, field emitters were already in use as electron sources in commercial instruments (e.g. VG HB200 SEM and Welter Coates SEM). Both instruments used a single crystal oriented W(310) cold field emitter, and were based on the design of Crewe (72). Routine use of these early instruments was difficult. The reason was the lack of understanding of the requirements of field emitters as electron sources, e.g. low pressure ($< 1 \times 10^{-10}$ torr), cleanliness of anodes, the choice of emitter orientation, and the mode of operating the emitter for a particular instrument.

To convert such an instrument to a SAM, a beam current of about an order of magnitude higher than what is normally used in the SEM mode was required. This was a further constraint on cold field emitters as emission fluctuations increase with the higher emission currents needed (110).

The work in this chapter was in part to establish a reliable way of operating such emitters at relatively high emission currents ($> 3 \times 10^{-5}$ A), with an improved life time. A preliminary investigation of a different

emitter, Zr/O/W(100), and the thermally assisted field emission mode, TF, will be presented. Finally, a comparison between the merits of W(310) cold field emitters and TF emission from W(100) built up and Zr/O/W(100) will be made.

Source	Brightness (B)
Tungsten hairpin	1.5×10^5 A/cm^2 ster
La B_6	$1 - 5 \times 10^6$ A/cm^2 ster
Field emitters	$> 10^8$ A/cm^2 ster

Table 6.1 A list of brightness values of various electron sources.

6.2 THE CHARACTERISTICS AND OPERATIONAL REQUIREMENTS OF ELECTRON SOURCES

6.2.1 Thermionic Cathodes

The heated tungsten hairpin filament, W, has been the most commonly used electron source in conventional electron probes. Its properties are well documented (111). The filament is made from tungsten wire of about 125 μm in diameter and is operated at a temperature of ~ 2850 K and a pressure below 1×10^{-4} torr for a stable emission. The high temperature limits the life of the filament to a few tens of hours because of evaporation. Broers(112) shows that a brightness of about 1.5×10^5 A/cm^2/sr at 25 kV is obtained from such cathodes with a lifetime of 10 - 15 hrs. A pointed cathode can improve brightness with a slight reduction in operating temperature. This results from two effects, firstly the high surface field applied to prevent the limitation of current by space charge and secondly

the emission enhancement by the Schottky effect. Brightnesses of about 5×10^5 A/cm^2/sr at 25 kV have been reported by Brores (112) at pressures of about 1×10^{-7} torr. A source size of about 25 μm is expected for this type of emitter.

One of the important parameters of electron sources is the energy spread which determines the contribution of the chromatic aberrations to the final probe diameter. For thermionic emission, the energy distribution would be of the form

$$F(\varepsilon)\, d\varepsilon \;\alpha\; \varepsilon \exp \frac{-\varepsilon}{kT}\, d\varepsilon \qquad \varepsilon > o \qquad (6.1)$$

$$= o \qquad \varepsilon < o$$

where ε is the energy above the vacuum level, k is the Boltzmann's constant and T is the temperature in ^oK. The full width at half the maximum (FWHM) of this distribution is 2.9 kT, which for 3000 ^oK is ~ 0.27 eV. In low brightness operation figures closer to the above theoretical values can be obtained. For high brightness systems a much higher value of 4 - 5 eV is obtained (113). This broadening is in fact due to the Boersch effect (114).

Lanthanam hexaboride (La B_6), was recognised as an alternative high brightness electron source in 1951 by Lafferty (115). However, its use was restricted because of its reactivity at high temperature. In 1969 Brores (116) realized a gun in which the La B_6 cathode was heated by electron bombardment. Further improvements to the design by Ahmed (117) have allowed a reduction in the heater power. A brightness of about 5×10^6 A/cm^2/sr at 25 kV and an energy spread of about 3 - 4 eV are typical for a 1 μm diameter tip (112). No measurements of the source size was given for this emitter but for a 20 μm tip diameter, a source of ~ 9 μm diameter is given (112). A vacuum of better than 1×10^{-6} torr is essential for the operation of such emitters.

Recently, Shimizu et al (118) have devised a method to fabricate single crystal La B_6 in sharp needle-shapes suitable for field emission. Zaima et al (119) reported an energy spread of about 1 eV for a (100) single crystal La B_6 tip operated in the TF mode with a temperature between 1000 K - 1500 K. The current density was 3.9×10^5 A/cm^2 and the tip radius was estimated to be about 0.13 μm from Fowler-Nordheim plots (120). This figure was in good agreement with measurements made with an SEM.

6.2.1 Field Emitters

When a large electric field of the order of $2 - 5 \times 10^7$ V/cm is applied to a metal surface, the potential step barrier is changed into a "wall" barrier through which electrons can tunnel into the vacuum with a high current density. This effect is known as field emission. Complete discussion of the phenomena can be found in several articles (121 - 123). Figure 6.1 shows the energy diagram of electrons in a metal and the effects of an applied electric field, E. Fowler and Nordheim (120) have derived an expression relating the field emission current density J (A/cm^2), to the electric field at the surface E (C/cm), and the work function ϕ (eV). They assumed a triangular distribution and neglected the outside image force acting on the emitted electrons. If this image force is taken into consideration and a linear applied macroscopic electric field is assumed, their expression can be written as (121),

$$J = \frac{AE^2}{\phi\, t^2(y)} \exp\left(-B \frac{\phi^{3/2}}{E} \nu(y)\right) \quad A/cm^2 \qquad (6.2)$$

where
$$A = 1.54 \times 10^{-6}$$
$$B = 6.87 \times 10^{7}$$
$$y = 3.79 \times 10^{-4}\, E^{1/2}/\phi$$
$$t(y) = \nu(y) - \frac{2}{3}\, y\, \frac{d}{dy}\, \nu(y) \qquad (6.3)$$

Over the useful operating ranges of field emitters, the slowly varying functions $\nu(y)$ and $t(y)$ have the following approximate values (124)

$$t^2(y) = 1.1 \quad \text{and} \quad \nu(y) = 0.95 - y^2 \tag{6.4}$$

Field emitter cathodes are generally made of a single crystal wire of diameter about 125 μm welded to a heater loop and electropolished to a sharp point. Methods of fabricating field emitters are described in the above references (121, 122). Due to its high tensile strength to withstand the applied electrostatic stresses, and its high melting point (3670 K) , single crystal tungsten wires have been used as electron sources in field emission probe forming systems. The emitter radius typically ranges from 0.01 - 1.0 μm, depending on the particular application of the emitter. However, the actual source is much smaller than this. Crewe et al (72) have estimated the source diameter to be about 2 nm, while Cleaver (125) suggests a diameter of 1.5 nm. Wiesner (126) assumed different tip shapes and diameters and included the contributions of spherical aberration, energy broadening ΔV, and diffraction for the calculation of the source size. His results suggest a source diameter ranging from 4 - 10 nm, assuming ΔV = 0.3 eV. He found an optimum source size for a tip diameter of 0.6 μm operated at 4 kV. Recent experimental measurements of source size agree well with Wiesner's predictions (127). Stringent vacuum conditions ($< 1 \times 10^{-10}$ torr) are necessary for stable emission as will be seen later.

One of the most attractive properties of field emitters as electron sources is their high brightness compared to thermionic sources. Values in excess of 1×10^7 A/cm^2 are typical. Tamaki et al (128) have measured a brightness of 1×10^{11} A/cm^2/rad^2 from a built up W(310) emitter.

Following Young (129), the FWHM of the total energy distribution (TED) for cold field emission is given by,

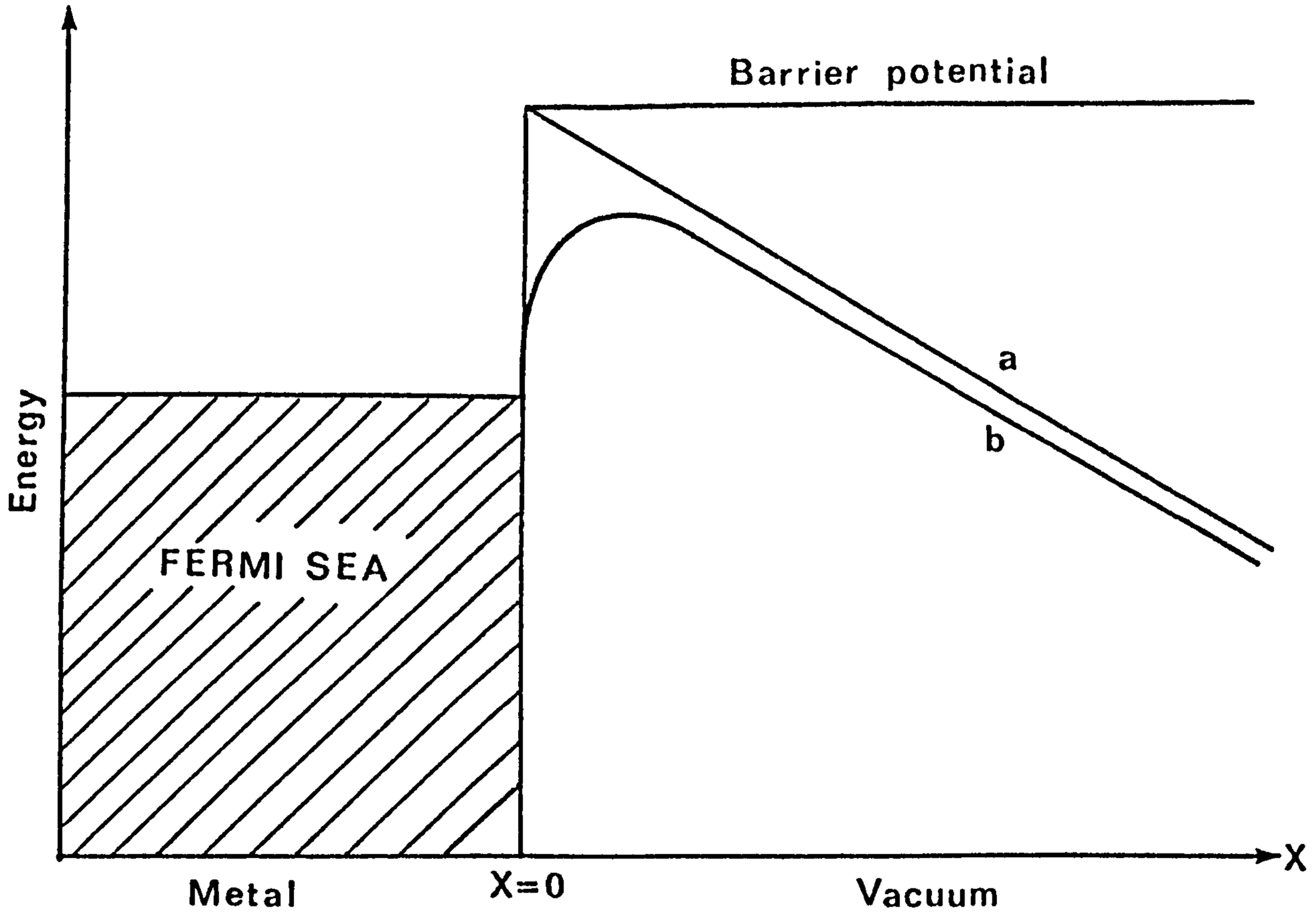

Fig. 6.1 Energy diagram for a metal electrode with an applied field. (a) Potential energy due to externalelectric field. (b) Resultant potential barrier.

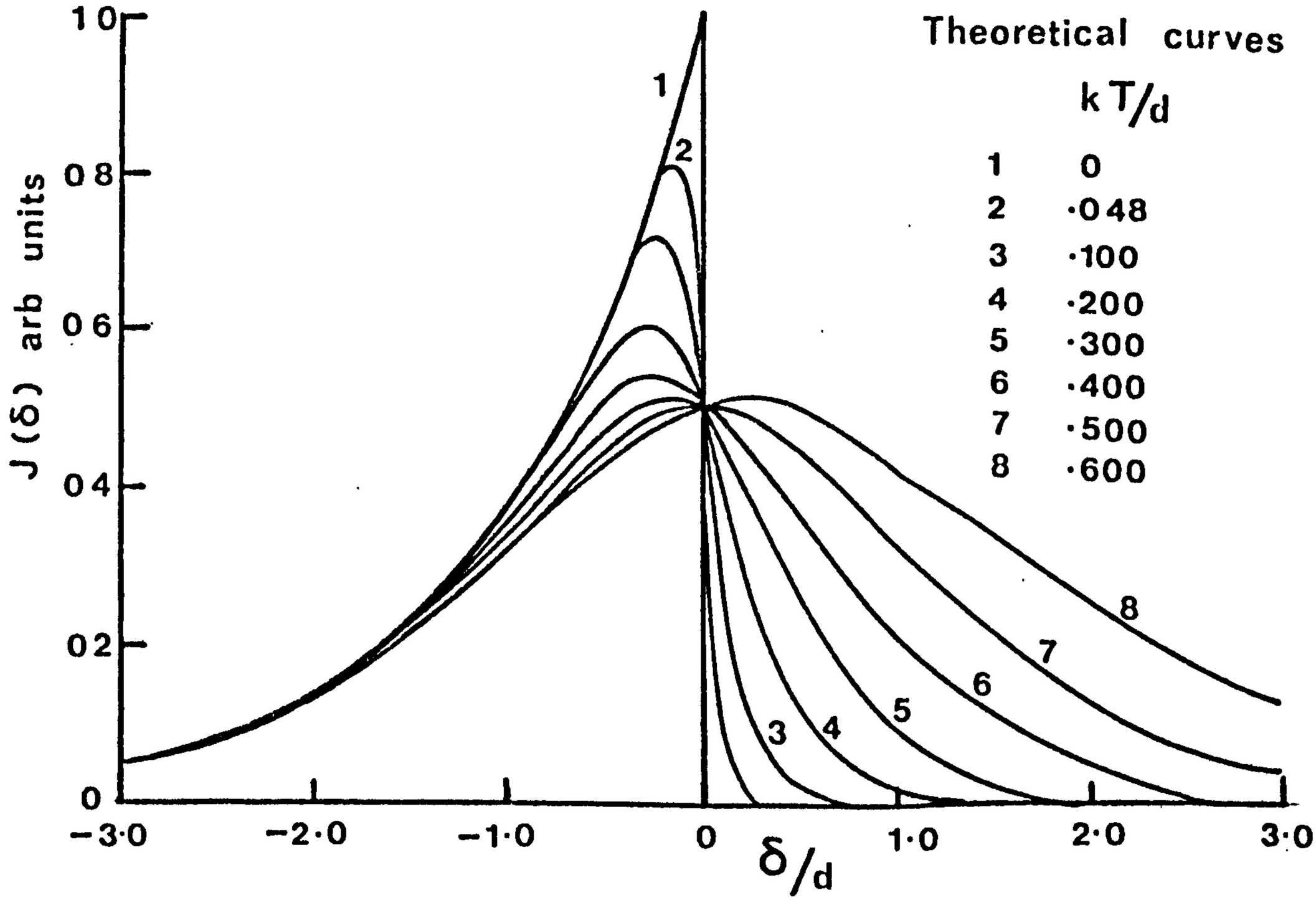

Fig. 6.2 Theoretical total energy distribution plots for various values of ($\delta_{/d}$) (134).

$$(TED)_{FWHM} = 0.693\, d\,, \tag{6.5}$$

$$d = 9.76 \times 10^{-9}\, E\, \phi^{-\frac{1}{2}}\ \ t(y)^{-\frac{1}{2}} \tag{6.6}$$

where $t(y)$ is given by eqn. (6.3). For typical applied fields, ($2 - 5 \times 10^7$ V/cm), this ranges between 0.063 eV and 0.155 eV. At relatively low current densities, measured values of 0.14 eV - 0.22 eV in close agreement with the theory have been reported (130 - 132). At high current densities, the Boersch effect (114) is known to play an important role in broadening the energy distribution. Recently, Cumming and Smith (132) have measured the energy spread from W(111) to be 3.2 eV at 2 mA emission current.

In the thermally assisted field emission mode (TF), the energy spread is usually higher than either for cold field emission or thermionic emission. Veneklasen et al (133) have assumed an energy spread of 2.5 eV at 100 μA emission and1200 K. Such high values in this mode can be explained as follows. Following Swanson and Crouser (134), the total energy distribution $J(\delta)$ assuming a free-electron model is given by

$$J(\delta) = J\ \frac{e^{\delta/d}}{d(1 + \exp^{\delta/kT})} \tag{6.7}$$

where δ is the electron energy relative to the Fermi level, J is given by (6.2) and d is given by (6.6). Eqn. (6.7) breaks down for $kT > 1$ and is regarded as unreliable for $kT > 0.7$. Figure 6.2 shows $J(\delta)$ as a function of δ/d for various values of kT/d (134). At low temperatures ($\frac{kT}{d} << 1.$) the energy distribution is narrow, as most emitted electrons are a result of "cold" field emission. As the temperature is raised, the potential "barrier" will be depressed below the vacuum level allowing more electrons to be emitted thermionically. This condition occurs at $^{kT}/d = 0.5$, which for W, assuming $E = 4.10^7$ V/cm and $\phi = 4.5$ eV, corresponds to a temperature of ~ 1400 K. The FWHM in this case will be about 3 - 4 eV. As

the temperature is raised further, the majority of electrons will be thermionically emitted and the energy distribution will be narrow again.

6.3 PRACTICAL ASPECTS OF OPERATING FIELD EMITTERS IN PROBE FORMING SYSTEMS

Although field emitters have been successfully used in conventional SEM's as well as the Scanning Transmission Microscope (STEM) their use in higher probe current instruments (> 1×10^{-9} A) is not successful. This has been due to the fact that in the latter case, the emission current, I_e, is at least an order of magnitude higher than in the STEM which normally uses I_e of about 1 - 2 μA. As a consequence of this, a noisier emission results which is believed to be due to ion bombardment of the emitting area by ions resulting from electron bombardment of the anodes (135). Another reason for the noisy emission, is the vacuum conditions near the emitter. Tsong and Muller (136) note that the pressure near the emitter is at least x10 worse than the system base pressure because of residual gas polarization effects. This figure is compared with van Oostrom's (131) suggestion of a pressure of 1×10^{-14} torr for a 10% decay in emission current in 1000 hrs, and the more commonly used system's pressure of no better than 1×10^{-10} torr.

For a thoroughly outgassed first anode, a pressure of 1×10^{-10} torr and I_e less than 10 μA, an emission stability of the order of 5 -10% is achieved. For higher pressure and poorly degassed anodes, a higher level of instability will result.

The work described in the next section is aimed at establishing operational conditions for a stable emission (to within 5%), from a W(310) emitter used in the present SAM.

6.3.1 Cleaning of the Emitter

After flashing the field emitter to desorb contaminants, a monolayer of adsorbed gas builds up in a few minutes, causing the emission to drop to less than 25% of its original value (i.e. after flashing). Depending on the pressure conditions and the total emission current, an emission stable to within 10% is obtained for 10 - 40 minutes. This period is called the useful operating life, UOL, Figure 6.3 illustrates the UOL as defined here. At the end of the UOL, the noise level increases as a result of gas adsorption on the emitter resulting in a change in the work function of the different planes and hence causing a variation in the emitted current in addition to ion bombardment of the emitting area. Unless the emitter is re-flashed, a vacuum arc is initiated with the subsequent destruction of the emitter. However, repeated flashing of the emitter tends to increase its radius, requiring a higher voltage, V_e, to be applied in order to obtain the same current. This puts a further constraint on the use of the emitter in a fixed lens geometry as is the case for the Butler lens (137). According to Barbour et al (138), in the absence of an applied field, the emitter radius increases as,

$$\left(\frac{dr}{dt}\right)_o = A \exp \frac{-Q}{kT} \tag{6.8}$$

$$A = \frac{1.25\ \gamma\ \sigma_o\ D_o\ \alpha}{Ao\ k\ T\ r^3} \tag{6.9}$$

where γ is the surface tension, σ_o is volume per atom, A_o is the atom surface area, D_o is the diffusivity constant, Q the activation energy for surface diffusion, r is the emitter radius, and T is the temperature. In the presence of an applied field, E, the dulling rate will be (138),

$$\left(\frac{dr}{dt}\right)_E \simeq \left(1 - \frac{r\,E^2}{8\pi\,r}\right)\left(\frac{dr}{dt}\right)_o \tag{6.10}$$

Equation (6.10) shows that $\frac{dr}{dt}$ can be controlled by the applied field. In

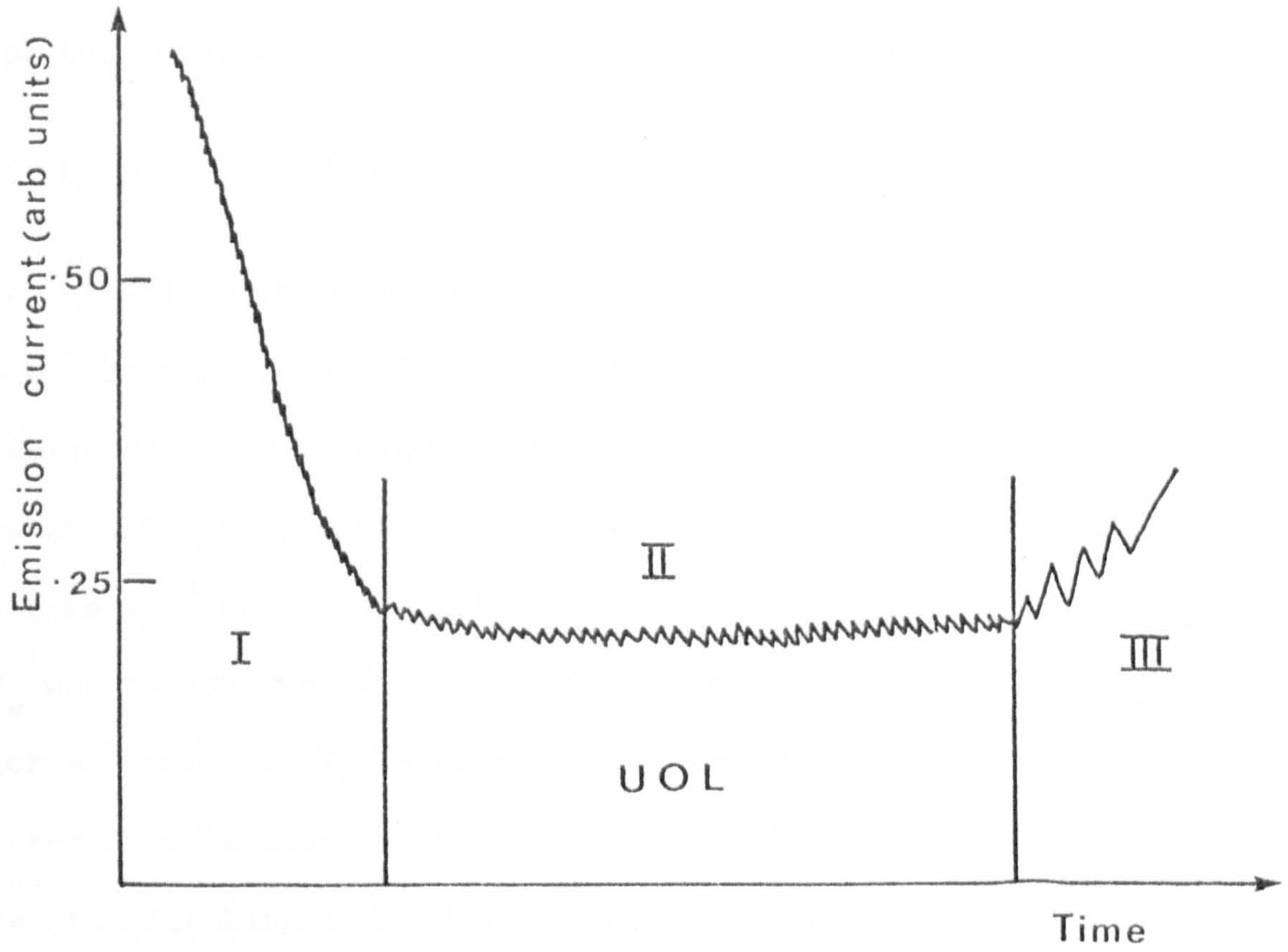

Fig. 6.3 The definition of useful life time (UOL). (I) depicts the decrease in current as adsorption builds up, (II) depicts the UOL, (III) shows the effect of ion bombardment to emission stability.

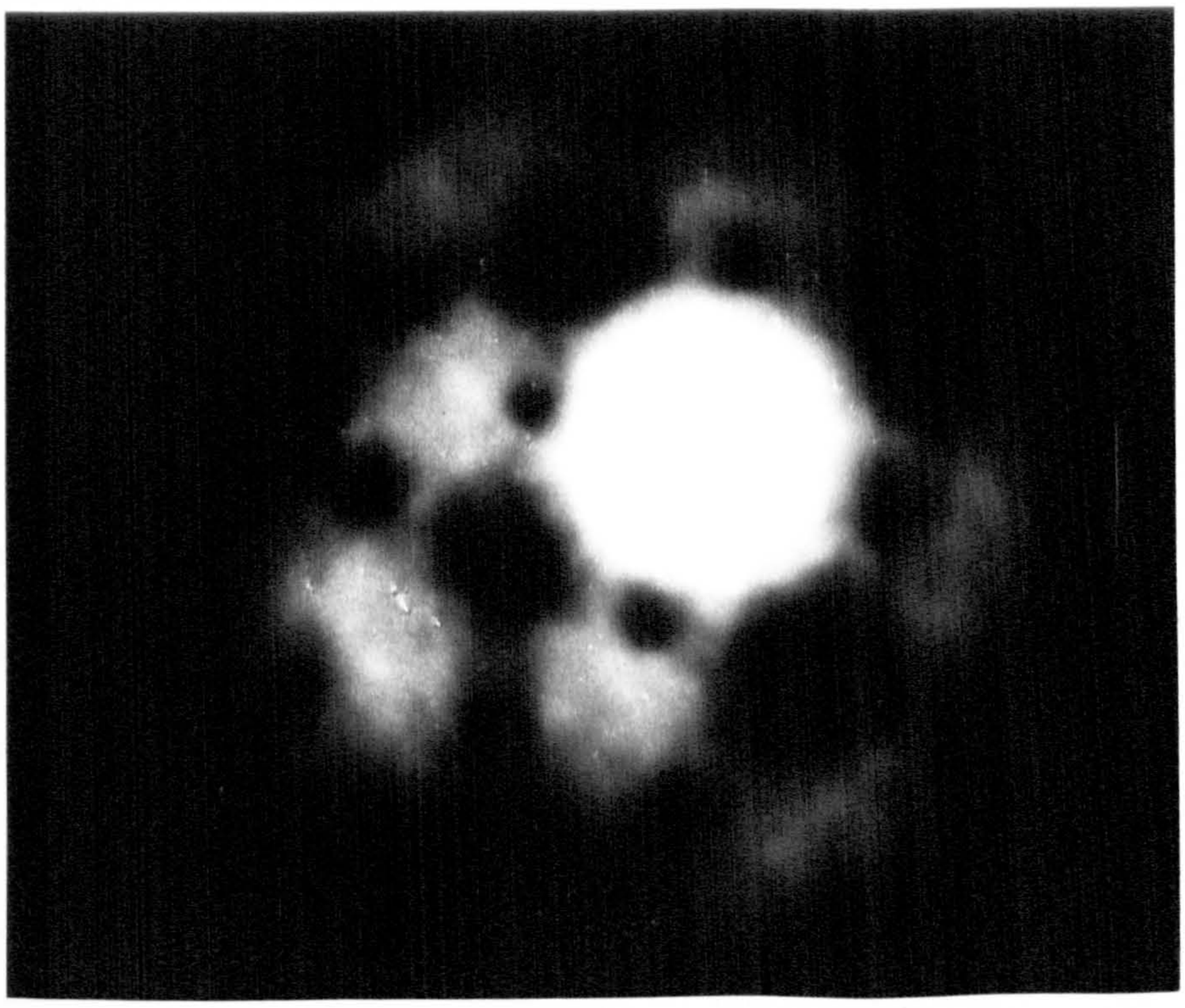

Fig. 6.4 Field emission pattern from clean W(310), V_e = 3.0 eV and I_e = 5 μA.

the case of tungsten, for $\frac{dr}{dt} = o$, the required field will be

$$E = 8.1 \times 10^4 \, r^{-\frac{1}{2}} \quad V/cm \tag{6.11}$$

In order to establish the value of this field, the following empirical procedure has been adopted. First, the emitter is flahsed to obtain a clean emission as shown in Figure 6.4. The cleanliness condition can be further established by plotting the dependence of the emission current I_e on the voltage V_e, known as the Fowler-Nordheim plots (120). The extract voltage V_e needed for 1 - 10 μA emission current is then noted. A reverse voltage corresponding to V_e is applied for subsequent flashing of the emitter. For a new emitter or an emitter that has been exposed to the atmosphere, the flashing temperature should be about 2100 - 2200 K. This ensures that most contaminants are desorbed. A temperature of about 1500 K - 1700 K can then be applied for subsequent cleaning. This is because in UHV, the principal contaminant will be CO, which can be desorbed at about 1500 K. Of the emitters investigated by the author, a change in V_e of up to ± 25% during flashing, has retained the tip radius to within 10% (as can be judged from V_e giving the same I_e value).

6.3.2 The Effect of the Rate of Degassing The Anodes On Current Stability

The following experiment was designed to establish the effect of cleanliness of the anode on the emission stability. An auxiliary vacuum system was used as a field emission microscope (FEM) in this experiment. Two tantalum, Ta, plates, 3 x 4 cms, and of thickness 125 μm were used as the first anode. These were mounted on a manipulator to allow either of them to be positioned 2 cms in front of the emitter. Each anode had an aperture in the middle which subtended an angle at the emitter of 1×10^{-1} rad. Provision for heating one of the plates to a temperature of about 1000^{o} K was made. The phosphor screen of the FEM in front of this set up

was used to collect the emitted electrons. Fluctuations in the intensity of the pattern on the screen were detected by using a photomultiplier. The output signal (noise) was collected as a noise voltage and displayed on an x t recorder at different frequencies as shown in Figure 6.5. The system was baked to 200^{o} C and one of the Ta anodes was heated in situ to ~ 1000^{o} K for 3 hours at the end of the bake-out. All measurements were taken at a base pressure of about 5×10^{-10} torr unless otherwise stated. The emission current was normally kept below 10 μA to reduce outgassing of the phosphor screen. The tip was first flashed to establish the clean W(310) pattern. The outgassed anode was then positioned in front of the emitter and the intensity fluctuations recorded at different frequencies. The average of two measurements was taken at each frequency with flashing of the emitter at the end of each set of measurements to restore the clean W(310) condition. The un-heated Ta anode was then positioned in front of the emitter and the above measurements repeated. A small pressure rise of $1 - 2 \times 10^{-10}$ torr was noticed in this case.

Figure 6.6 shows the results obtained. It is clear from the Figure that the noise level is less for the heated anode. It should also be noted that the higher noise level is at low frequencies (< 20 Hz). This is consistent with the assumption that the low frequency noise is mainly due to ion bombardment of the emitting area (135). In addition observation of the whole pattern with the anode removed at the end of each experiment has shown a greater fluctuation of the emission from the unheated anode. The highest emission fluctuation came from the most intense spots suggesting that most bombardment is on the emitting area. This is in agreement with results obtained by Swann and Smith (135). The above results suggest that a high number of these ions are generated as a result of electron-stimulated desorption (ESD) from the anode surface. As a result of ESD, neutrals are released from the anode and subsequently ionised by the

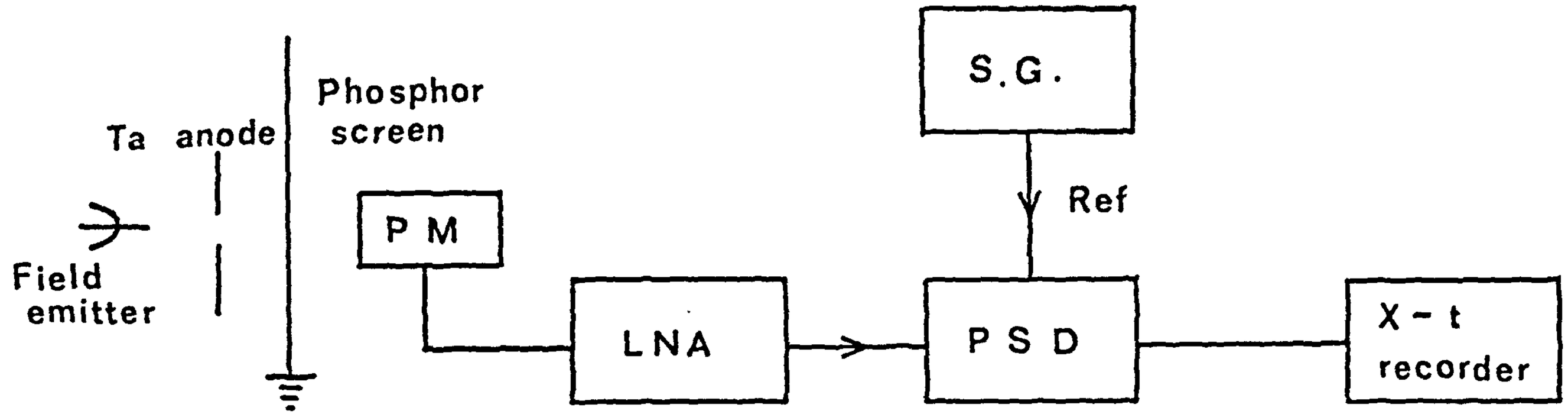

Fig. 6.5 Schematic of the experimental set up to measure the noise level from field emitters.

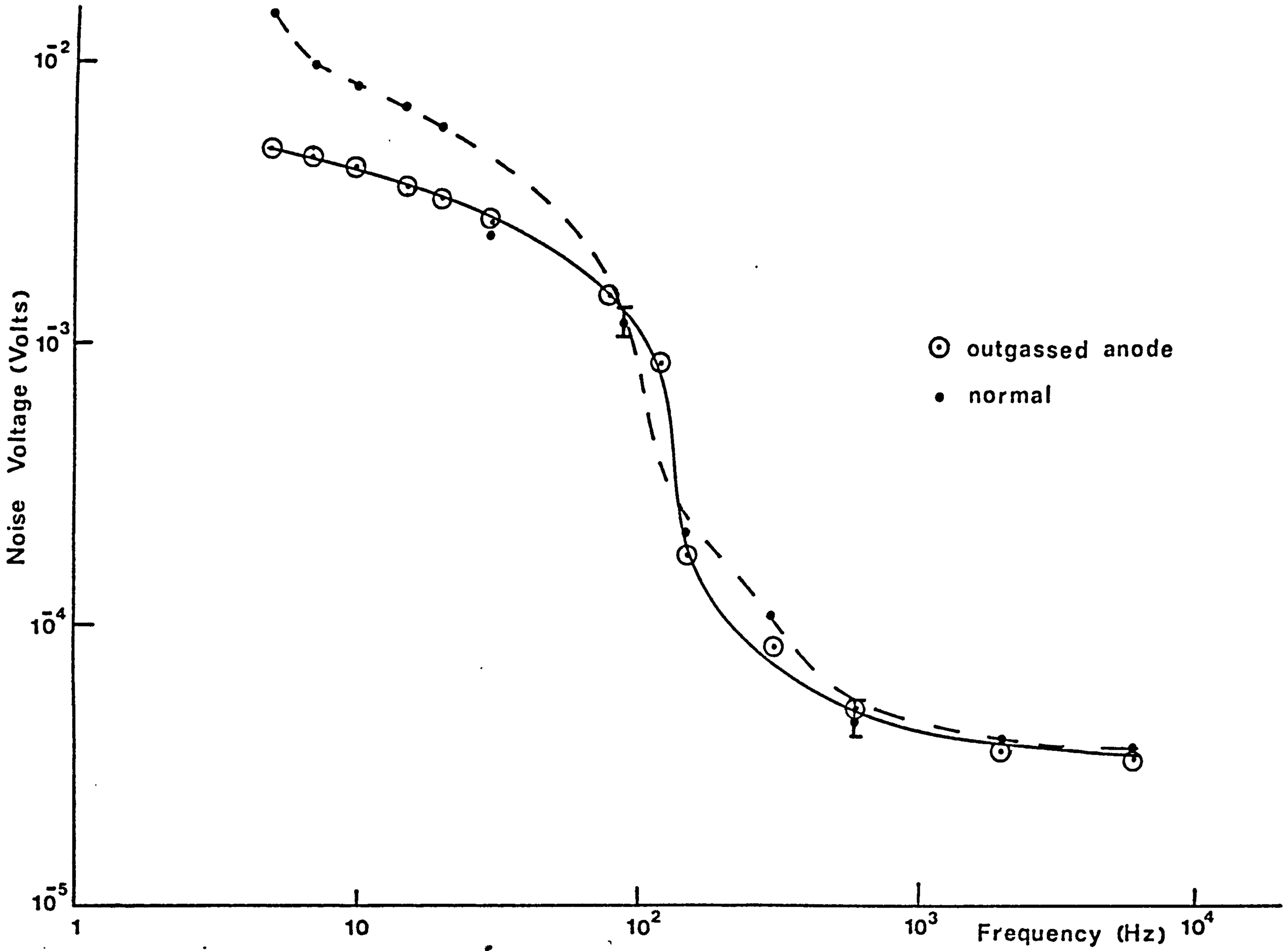

Fig. 6.6 Noise voltage (volts) versus frequency (Hz) from a normal and an outgassed anode.

primary electron beam.

It is clear from these results that a thorough out-gassing of the first anode is essential for emission stability. This requirement can be achieved easier by using a thinned first anode and indirect heating. Preliminary tests with a 150 μm thoriated tungsten filament and a similar anode thickness to that used in the above experiment has yielded comparable anode temperatures (i.e. 800 - 1000^{o}K, using few mA emissions from the filament).

Several authors (135, 139) have indicated that the rate of degassing from the anode plays an important role in the stability of the emission current. In the first SAM apparatus, a longer UOL, and a more stable emission have been observed after several hours of continuous emission of between 10 - 30 μA. This represents an indirect way to degas the first anode.

6.3.3 The Effect of Pressure On Emission Stability

Fluctuations in the intensity of the total emission pattern were used for measuring the pressure effects on the emission stability using the above set up. At higher pressures, the noise level increases and the UOL cycle is shorter. Figure 6.7 shows the variation of emission noise at two different base pressures. The pattern was masked allowing only fluctuation in a 6 mm spot to be detected. Figure 6.8 shows the variation in the emission pattern with time at the start and end of a UOL, at a pressure of 5×10^{-9} torr. The emission current drops to about 1.2 μA from 5 μA in about 25 minutes when the diffuse pattern of Figure 6.8b is obtained. At pressures of about 1×10^{-10} torr, this transition takes a longer time (up to one hour depending on the cleanliness of the anode).

It is concluded from the above results that proper degassing of the anode is essential for emission stability. Careful design of the

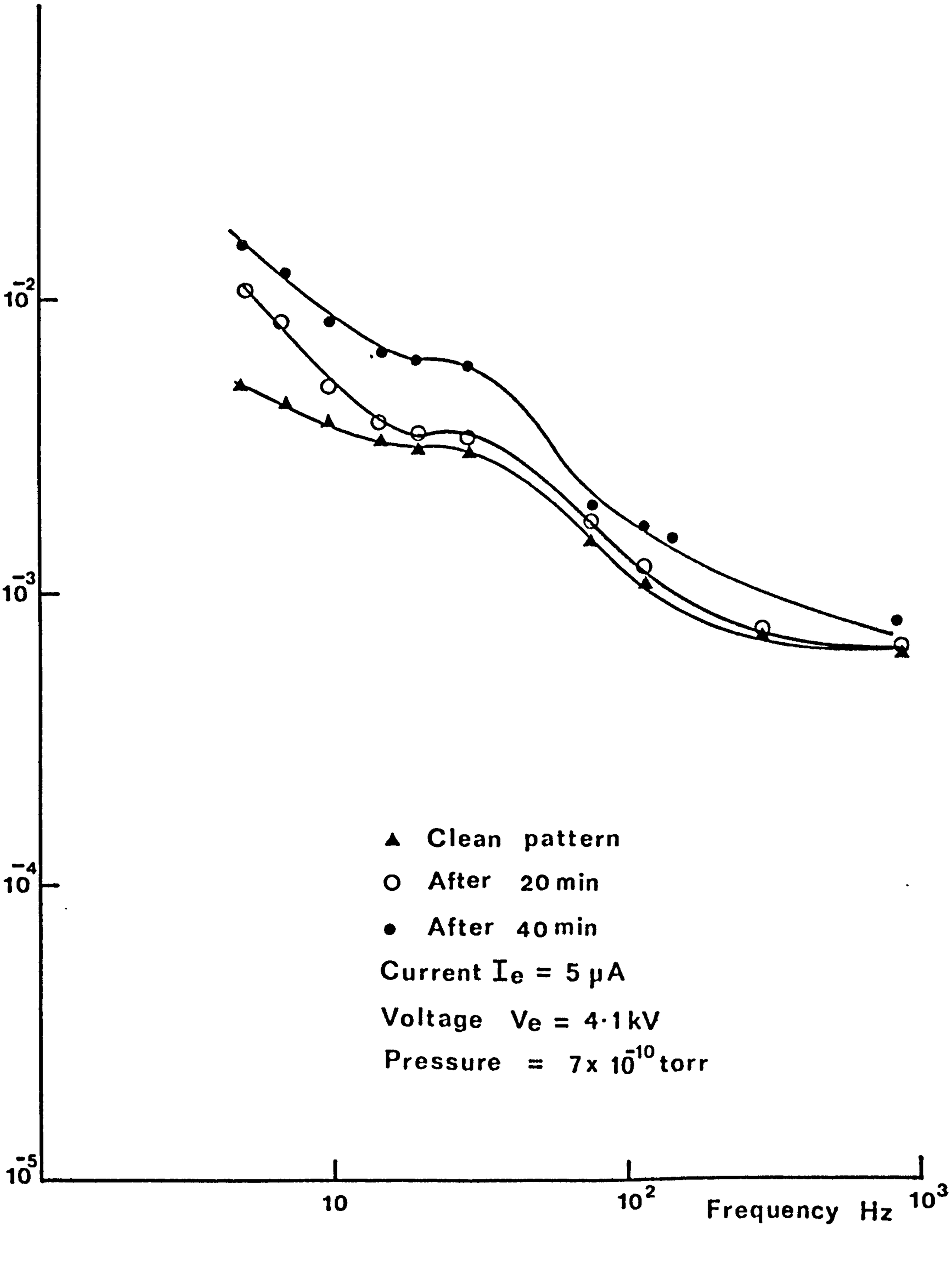

Fig. 6.7 The effect of pressure on emission stability.

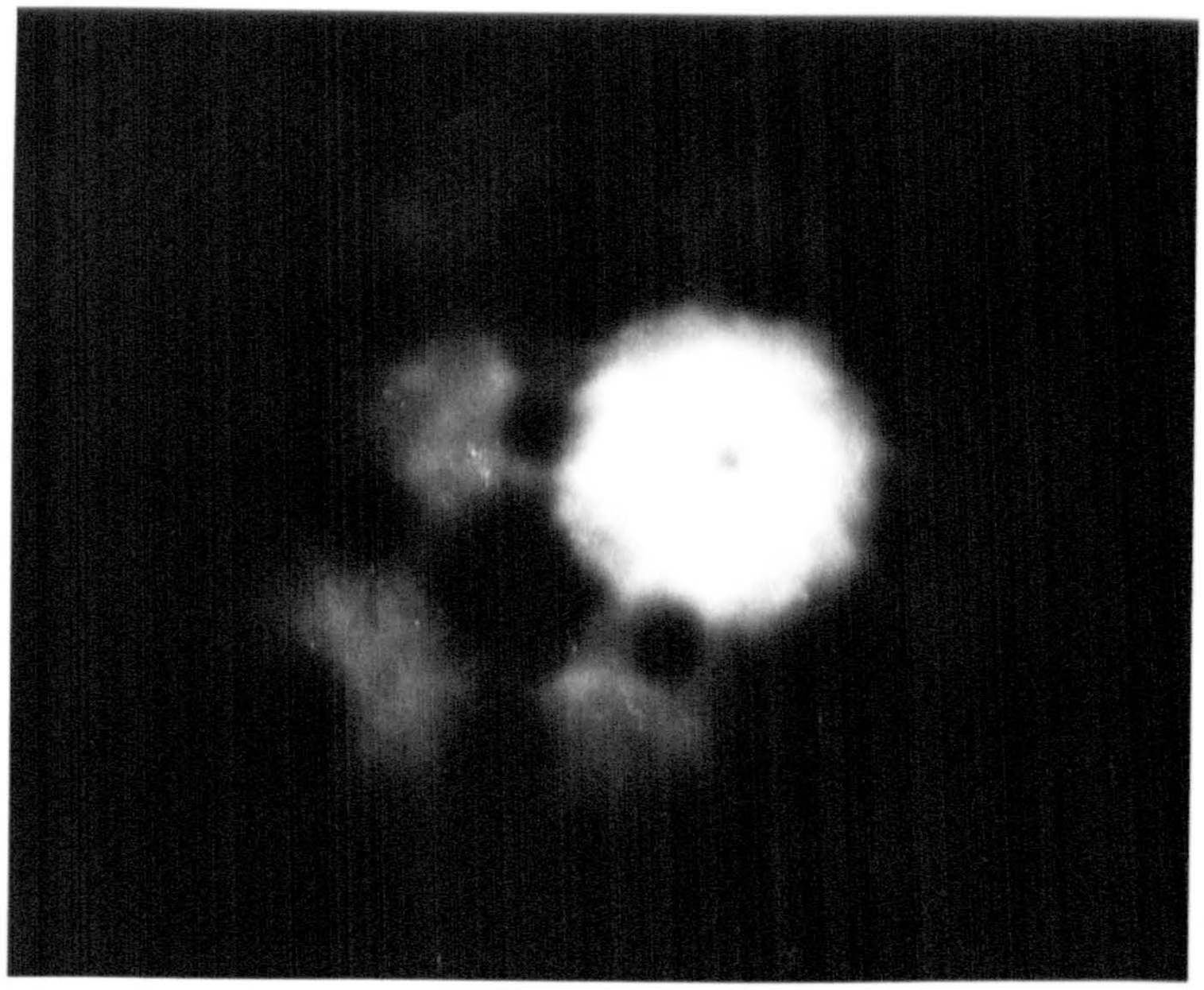

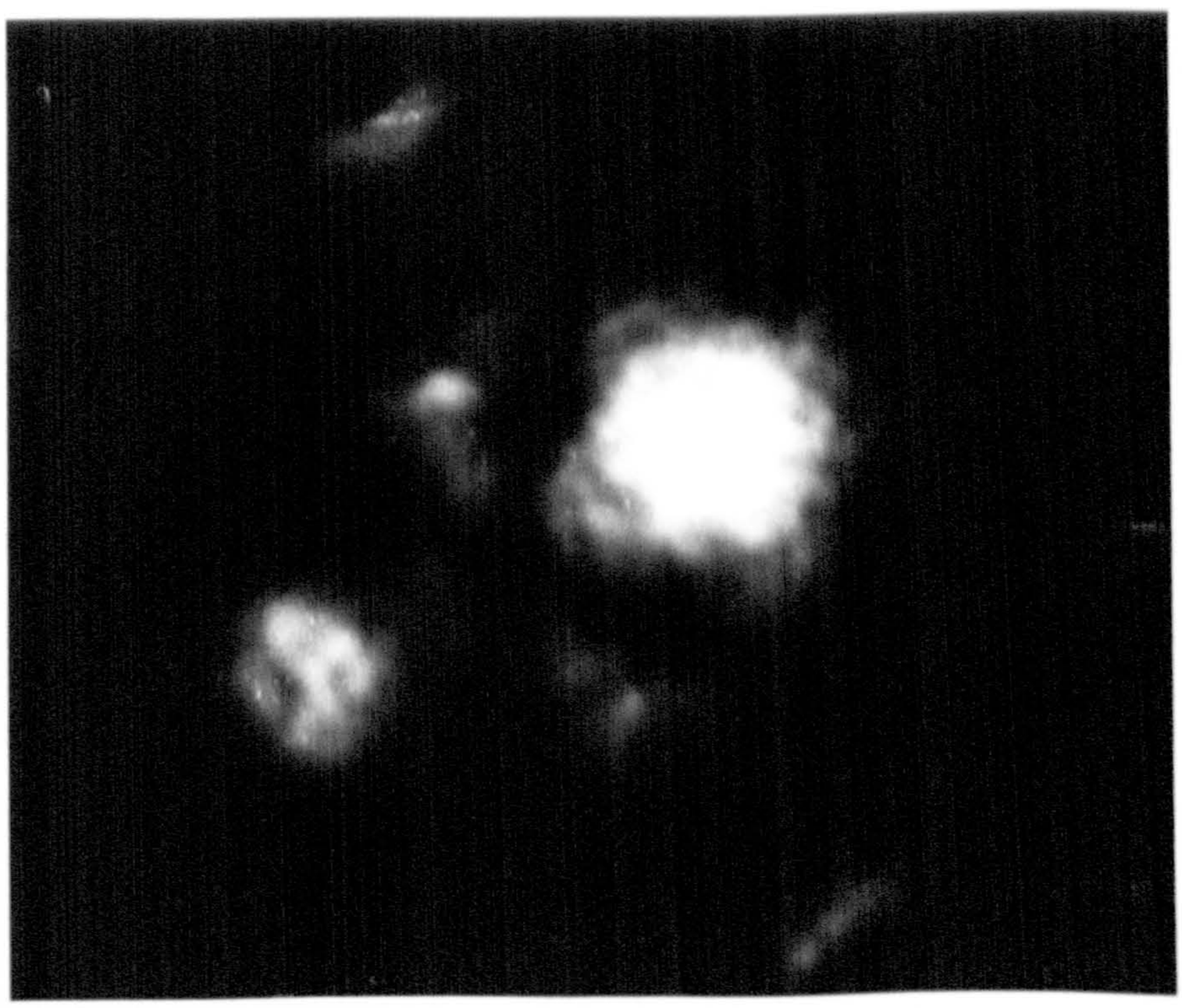

Fig. 6.8 The variation in emission pattern (stability) with time at a pressure of 5×10^{-9} Torr (a) at the start and (b) end of a UOL. Note the grainy diffused pattern in (b) believed to be due to ion bombardment of the emitter tip.

anode and the choice of a particular emitter to confine angular emission (see later) should be considered. An improved pumping speed around the emitter should be provided with a base pressure of better than 1×10^{-10} torr for a longer UOL.

6.3.4 The Build-up of W(310)

To reduce the effects of the high angle of emission from W(310), and further reduce V_e, Crewe et al (72) have used a built-up W(310) emitter. The build-up process can be understood from eqn. (6.10) as follows. For low applied field values, $E < (\frac{8 \pi \gamma}{r})^{\frac{1}{2}}$ surface tension forces predominate causing dulling of the emitter with time due to migration of atoms away from the tip (140). For intermediate values, a balance between the surface tension and the electrostatic forces is avhieved, as shown by eqn. (6.11). If the applied field is allowed to exceed the value $E > (\frac{8 \pi \gamma}{r})^{\frac{1}{2}}$, electrostatic forces predominate. Because of the low probability of nucleating new atom layers in certain crystallographic directions, the tip can not be grown in length. Instead, the emitter builds up into a polyhedral shape with the tip surface consisting of large plane facets separated by sharp edges and corners (140). Figure 6.9 is a micrograph showing this effect. Tamaki et al (128) have measured the W(310) protrusion to be about 2 - 3 nm diameter and 1 nm in height.

This technique has been applied in the present study. A small reduction in angular emission and up to 40 - 50% reduction in V_e were obtained. However, the author's experience with the built-up W(310) suggests a noisy emission current with time. The reason in this case is that the small protrusion produced in the build up process is subjected to a greater density of ion bombardment than in the case of no build up. In addition, the rate of reproducing one spot from the W(310) built-up emitter was low. This agrees well with Tamaki et al's observation that

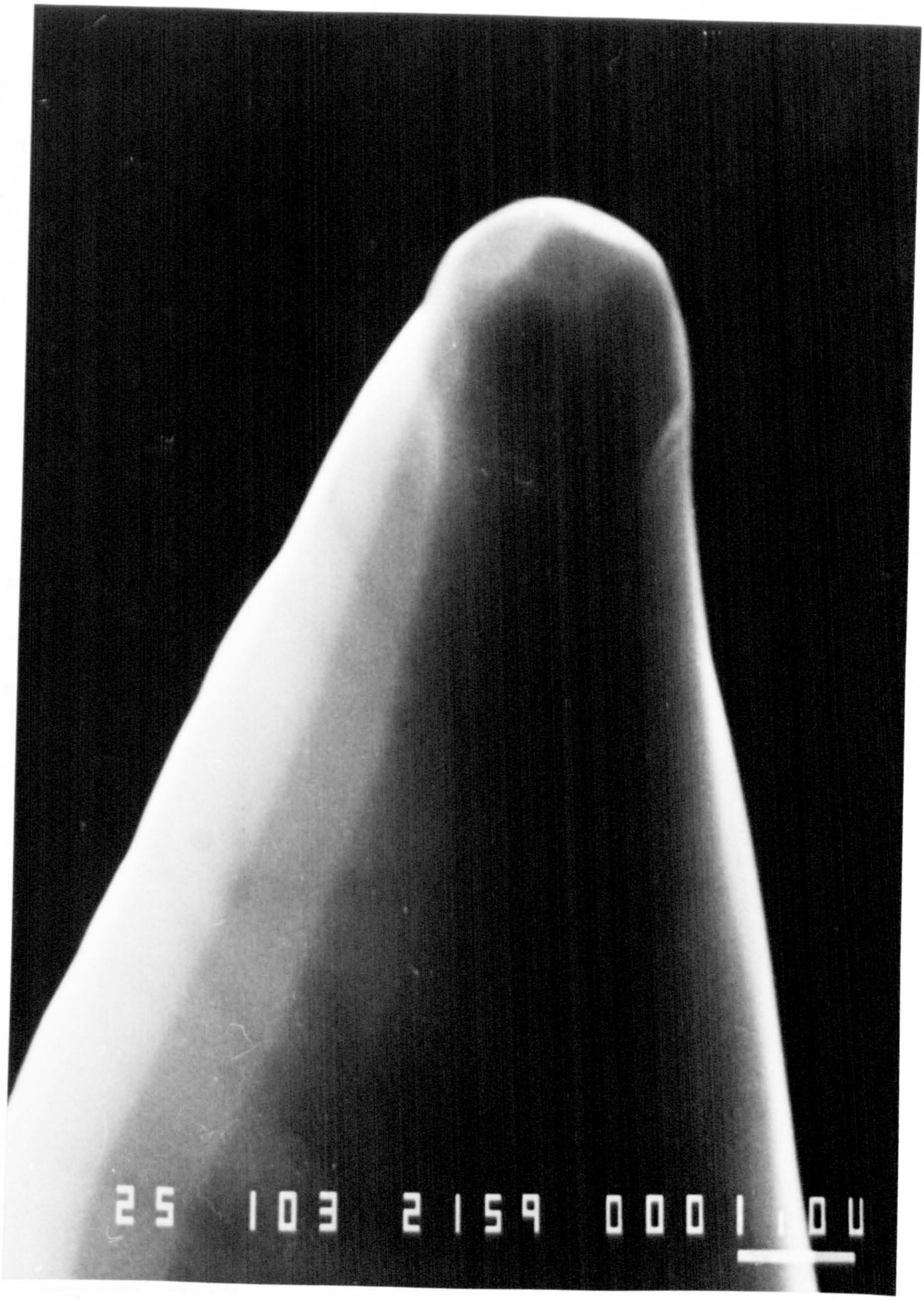

Fig. 6.9 SEM micrograph of a Zr/O/W(100) built up emitter, showing the polyhedral shape of the emitter tip (courtesy of D . Tuggle).

the built-up spot is realised in a short time (< 10 secs). Subsequent heating encourages protrusions from the other (310) planes to grow, and hence increase the effects associated with ESD.

6.4 GENERAL REMARKS ON THE W(310) FIELD EMITTER

The W(310) emitter has been the most commonly used electron source in field emission probes since its introduction by Crewe et al (72) in 1967. The choice of this orientation was first based on its low work function as can be seen from Table 6.2. Subsequent measurements of emission noise from several orientations showed the W(310) to have the lowest noise level (132, 141).

Plane	w.f.	
	Swanson and Crouser	Dyke and Dolan
100	4.5	4.71
110	5.2 - 5.47	5.7 - 5.99
111	4.45 - 4.55	4.39
211	4.7 - 4.9	4.35
012	—	4.34
122	—	4.65 - 4.88
310	4.16 - 4.34	4.31

Table 6.2 Work function of the various planes of W

Despite the above useful properties of W(310) with respect to other orientations, its use as an electron source in high probe current systems is not advantageous for several reasons. Firstly, the cone angle of emission from each spot from this emission pattern is high (0.9 - 1 rad),

while only a fraction from the axial spot is used in the probe, of the order of 10^{-2} - 10^{-3} rad. Secondly, the emission current comes from the four (310) directions, namely (310), (30$\bar{1}$), (3$\bar{1}$0) and (301) as can be seen from Figure 6.10 (also compare with the clean W(310) pattern of Figure 6.4). This means a high rate of ESD and hence ion damage of the emitting area as shown earlier. Thirdly, a higher number of W(310) emitters are destroyed in vacuum arcs than are W(100) for example. According to Veneklasen (142), dislocations in the material, W, move in the direction of the applied field along the (100) plane. For the W(310) oriented emitter, the (100) plane is surrounded by the four (310) planes. Hence, the movement of dislocations in the (100) direction can cause the release of impurities trapped in the dislocation and the initiation of a vacuum arc that destroys the emitter. Finally, in the fixed geometry (i.e. the Butler lens) a sharp emitter (< 50 nm radius) with low extract voltage V_e is required. This is not particularly advantageous over blunter emitters except for the low V_e value. Sharp emitters are less able to withstand micro-discharges. In addition the smallest source size is not obtained with the smallest emitter radius (126).

6.5 ANGULAR CONFINEMENT OF THE ELECTRON EMISSION FROM W(100) IN THE TF MODE

The build-up mechanism described above for W(310) can in fact be applied to any other orientation and material. However, the angular separation of the built-up directions is what favours one orientation over another. For W(310), this is ~ 30^{o}, while for the W(100) it is 90^{o}, hence causing the field to be higher in only one direction - that from which the emission comes. Swanson and Crouser (134) have used this technique to confine emission from W(100) to be within 0.1 - 0.3 rad, with a reduction

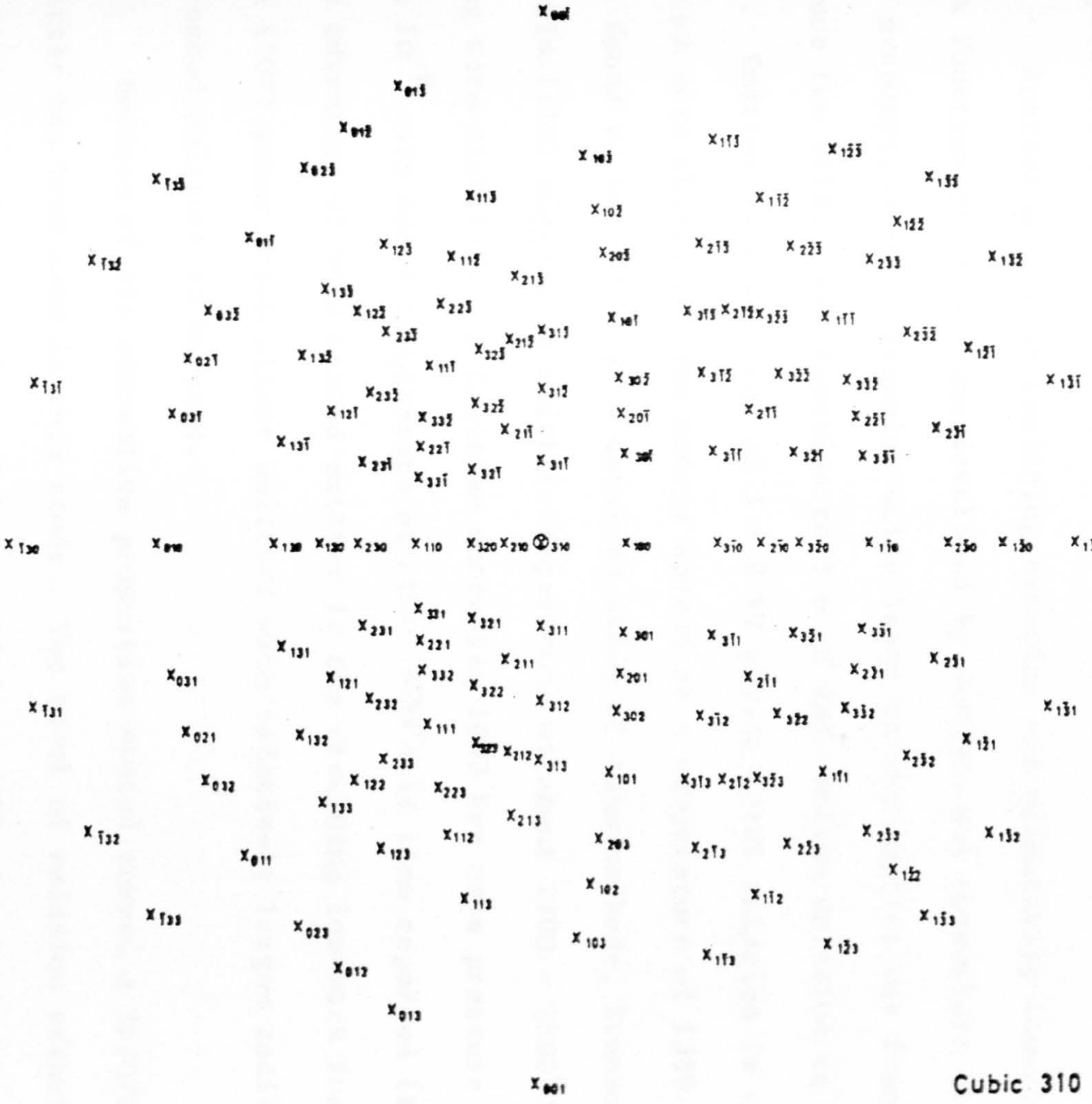

Fig. 6.10 Orthographic projection of a hemispherical tungsten emitter surface with (310) plane on the axis.

in V_e of up to 50%. Veneklasen and Siegel (143) have reported an empirical method for building up W(100) in the presence of Oxygen. At 10 μA emission current, V_e ranges between 3.5 - 5.5 kV, giving angular current density of 130 μA/str and confining the emission to 0.12 - 0.2 rad. The emitter is used in the TF mode for emission stability. The energy distribution was found to increase with both emission current and temperature. For 15 μA emission current, the FWHM of the energy distribution was 0.5 eV for a temperature of 1100^{o} K.

Another method of confining emission and selectively lowering the work function of W(100) was developed by Swanson and co-workers (134,139). The evaporation of a zirconium-oxide layer on the emitter was found to reduce the W(100) work function to 2.6 eV and confine emission to 0.1 - 0.2 rad. Emitter voltages, Ve, of 3 - 8 kV giving total emission in excess of 100 μA were obtained. The energy spread at a temperature of 1350 - 1450 K was found to be 1 eV. In a detailed study of this cathode, Swanson and Martin (139) suggest an emitter temperature of about 1700 - 1800^{o} K for long term stability. A lifetime exceeding 1000 hrs at a pressure of 2×10^{-8} torr and a temperature of 1350 - 1450^{o}K is also reported (139). One advantage of this coated emitter is the resulting low work function of the (100) plane which allows emitters with relatively larger radii than uncoated emitters to be used.

Because of its attractive properties stated above, a Zr/O/W(100) emitter has been used in this study. The level of emission stability in comparison with W(310) is much better giving a UOL of practically tens of hours. Preliminary experiments confirm the forward peaked nature of the emission. Cold field emission from this emitter was found to have the same disadvantages as the W(310). Great care should be exercised for the activation of this emitter, and under no circumstances should the emission be allowed to exceed few tens of μA in the first 5 - 10 minutes.

The following procedure for activating a Zr/O/W(100) emitter in the TF mode is recommended and was found by the author to minimise cathode destruction due to excessive emitted current. In addition, the tip shape was maintained, as can be seen from the I_e - V_e relation, over a period of several thousands hours of operation.

First, a "reverse" voltage of between 1.5 - 2 kV is applied to the emitter (no emission is possible in this mode). The emitter is then flashed to a temperature of about 1700 - 1750^{o} K for a period of 5 - 10 secs to desorp the loosely bound contaminants. The emitter's voltage is again reversed to the normal field emission mode, V_e, of about 1.5 - 2 kV, and its temperature is slowly raised to about 1000 - 1200^{o} K over a period of up to 15 - 30 minutes. At the end of this period, the emission current, I_e, rises to about 20 - 30 μA. It is recommended that I_e should not exceed this value at the early stages of activation in order to reduce likely emitted current initiated arcs. This mechanism (139) is responsible for the destruction of the emitter. The temperature is further raised to about 1600 - 1700^{o} K in the course of the next 15 minutes, and the emitter is left at this temperature for a further 2 hrs. At the end of this period, an emission current of about 100 - 300 μA should be obtained and the emitter is ready for use. Figure 6.11 shows the current-time dependence of a Zr/O/W(100) emitter. Although the high operating temperature (1600 - 1800^{o} K) was recommended by Swanson and Martin (120), for long term stability, it was found that one can reduce the temperature to about 1300 - 1400^{o} K and have a stable emission, to within 10%, for several hours. This low temperature has, in addition, allowed retention of the emitter's shape as can be estimated from its I_e - V_e characteristics. Furthermore, the reduction in temperature does not grossly reduce the beam current. In any case, the latter can always be increased with slight increase in V_e, due to the low work function of the emitter.

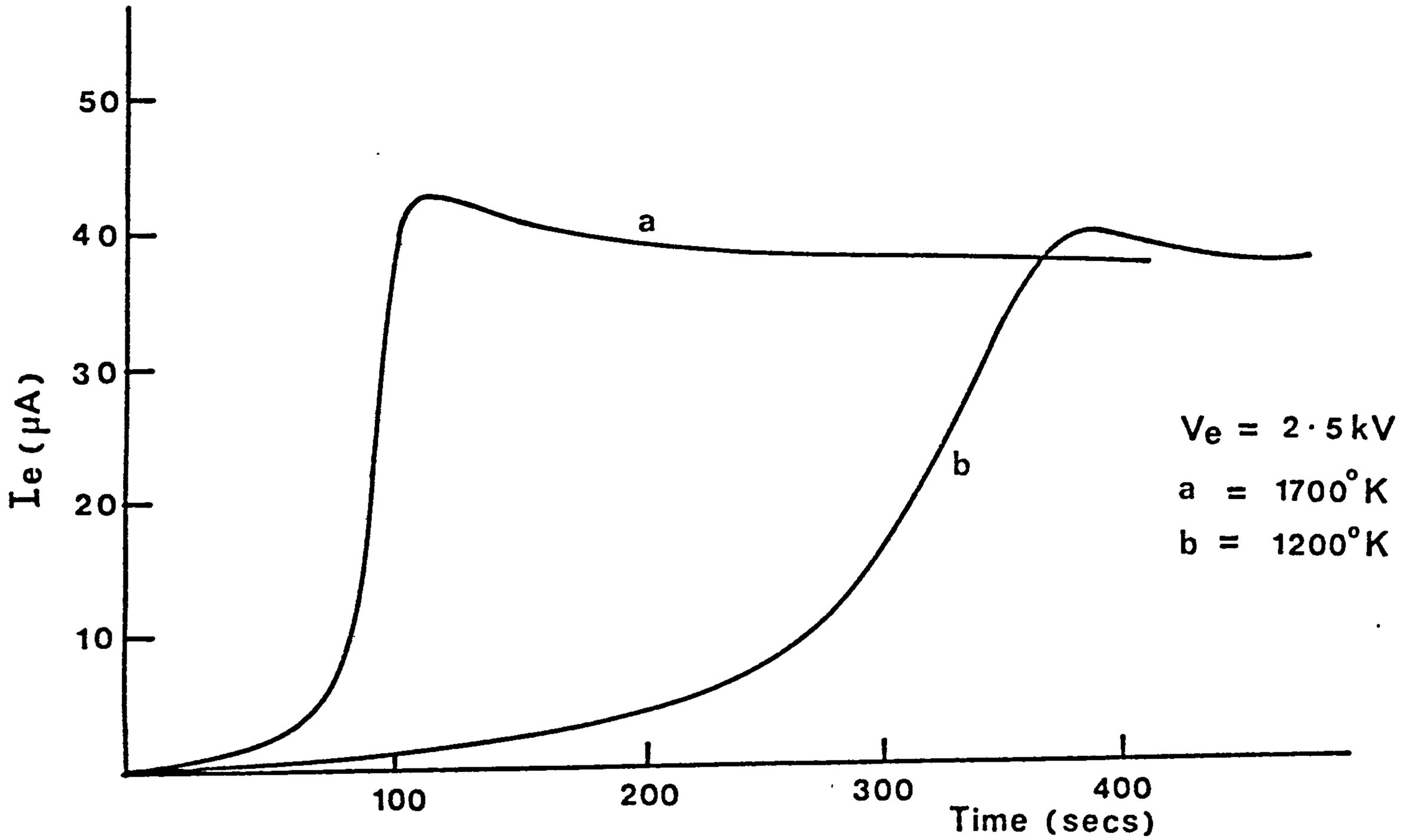

Fig. 6.11 The relation between emission current and time from a Zr/O/W(100).

	W(310)	Built-up W(100) (143)	Zr/O/W(100) Swanson (139)
emission angle (rad)	0.8 - 1 rad	.12 - .2	.12 - .2
$\frac{dI}{d\Omega}$ (Sr) (I = 10 μA/Sr	10 μA/Sr	130 μA/Sr	100 μA/Sr
Δv	.2 eV	.4 - .5 eV	.7 - .8 eV
operating temperature	300 K	1200 K	1200 - 1500 K
emission noise at 10^{-9} torr	5 - 10%	10%	10%
useful operating time	∿ 30 mins	> 10 hours	> 10 hours
emitter radius	< 100 nm	> 500 nm	> 500 nm
wf	4.3 eV	4.5 eV	2.6 eV
V_e	1 - 2 kV	4 - 6 kV	2 - 4 kV

Table 6.3 A comparison between the characteristics of three different emitters (assuming 10 μA total emission).

A comparison between the performance of the emitters investigated here, and the built-up W(100) is given in Table 6.3. The advantage of the built-up W(100) over the W(310) and to a lesser extent the Zr/O/W(100) is shown. In particular, the built-up W(100) has better stability than W(310) and yet a narrower energy spread than the equally stable Zr/O/W(100). In addition it has the highest brightness. The Zr/O/W(100) on the other hand can be operated at a lower V_e in comparison to built-up W(100) of the same emitter radius due to its low work function.

However, the choice of a particular crystal orientation in addition to its mode operation will depend largely on the kind of application of the electron probe. In cases like the scanning transmission microscope (STEM) where a beam current of 10^{-10}A is sufficient, W(310) in the cold mode will be advantageous to use. For high probe currents (i.e. > 10^{-9}A) either Zr/O/W(100) or built up W(100) in the TF mode should be used.

CHAPTER 7

THEORETICAL CHARACTERISTICS OF PROBE FORMING SYSTEMS

7.1 THE REQUIRED PROBE CHARACTERISTICS

The feasibility of a high spatial resolution scanning Auger microscope for surface analysis has been demonstrated in Chapters 3 and 5. The incorporation of a high resolution electron energy analyser has also been shown. The probe characteristics of such a system can be summarised as follows:

a - A small probe size, < 50 nm, for high spatial resolution.

b - A beam current of more than 1×10^{-9} A for fast Auger imaging, i.e. less than 500 secs.

c - A large working distance to allow access to the electron energy analyser.

d - A high precision specimen stage to be accessed for other techniques;

e - A U.H.V. environment for the specimen.

It has also been demonstrated, in Chapter 6, that field electron emitters are the best electron sources to meet the above requirements (a, b).

In the following sections we will review the electron optics of probe forming systems, analyse an electrostatic lens used in field emission probe systems, and finally compare some of the widely used electrostatic lenses.

7.2 DEFINITIONS AND NOTATIONS

The purpose of this section is to acquaint the reader with the notations and relationships of electron optics as used here. For more

detailed discussion on topics of the optics of charged particles and its analogy with geometrical optics, the reader is referred to standard texts, e.g. Grivet (144), and El kareh and El kareh (145).

Throughout, and for simplicity, we distinguish between the object space where the electron source is, and the image space of the lens. In this notation, a subscript o refers to terms in object space, and a subscript i refers to terms in image space. The Helmholtz-Lagrange relation between the magnification M, the potentials and beam angles on object and *image sides of the lens* V_o, V_i, α_o, α_i respectively will be written as

$$\alpha_o = M\left[\frac{V_i}{V_o}\right]^{\frac{1}{2}} \alpha_i \qquad (7.1)$$

Ideally, the action of an electron lens is the faithful point to point imaging of a small object. However, the performance of a real lens deviates from the ideal one due to two kinds of aberrations. The first is mechanical and is due to imperfections in the lens shape. The second is electronic and is a function of the charge and speed of the particles. Astigmatism, ellipticity and coma are examples of the first type, while chromatic and space charge are examples of the second type. Spherical aberration, on the other hand, depends upon the form of the lens and its convergence. It should be noted that the primary aberrations in a carefully constructed lens are usually spherical and chromatic.

The spherical aberration causes the off-axis electrons in object space of α_o to be focussed more strongly at the image plane than those close to the axis. The diameter of the circle of least confusion on the image plane due to spherical aberration is given by,

$$d_{si} = \tfrac{1}{2} C_{si} \alpha_i^3 \qquad (7.2a)$$

where C_{si} is the spherical aberration coefficient and α_i is the semi-

angle of divergence, both referred to image space. The equivalent expression in object space is:

$$d_{so} = \frac{1}{2} C_{so} \alpha_o^3 \qquad (7.2b)$$

where C_{so} and α_o are the equivalent of C_{si} and α_i in object space. For any lens, d_{si} and d_{so} are related by the lens magnification, M such that

$$d_{si} = Mdso \qquad (7.2c)$$

The coefficients C_{si} and C_{so} are related by the H.L. formula (7.1). Using (7.2b) and (7.1) in (7.2c), one gets

$$C_{si} = M^4 \left[\frac{V_i}{V_o}\right]^{3/2} C_{so} \; . \qquad (7.2d)$$

The chromatic aberration causes electrons leaving the object point with different energies eV and e(V + ΔV) to be focussed on the image plane into a spot of diameter

$$d_{ci} = 2 C_{ci} \alpha_i \frac{\Delta V}{V_i} \qquad (7.3a)$$

where C_{ci} is the chromatic aberration coefficient of the lens in image space. Similarly, this can be expressed in object space as

$$d_{co} = 2 C_{co} \alpha_o \frac{\Delta V}{V_o} \qquad (7.3b)$$

where C_{co} is the same as C_{ci} but in object space. Again, d_{ci} and d_{co} are related by M,

$$d_{ci} = M\, dco \qquad (7.3c)$$

and in the same way C_{ci} and C_{co} are related by

$$C_{ci} = M^2 C_{co} \left[\frac{V_i}{V_o}\right]^{3/2} \qquad (7.3d)$$

Equations (7.2) and (7.3) suggest that one can minimise the effects of the aberrations by choosing a priori small angles α. Although this is true as regarding spherical and chromatic aberrations, the limiting aperture of the system has two other effects. First, upon passing through the aperture, the electron beam will be diffracted. For circular apertures, the diffraction pattern will consist of a bright central spot, called the Airy disc, surrounded by fainter rings. Considering small angles, and adopting the Rayleigh criterion for resolving power, the diameter of the disc of least confusion caused by electron diffraction is given by

$$d_d = 0.61 \frac{\lambda}{\alpha_i} \tag{7.4a}$$

where λ is the electron's wave length and is equal to

$$\lambda = \frac{1.25}{V_i^{\frac{1}{2}}} \text{ nm} \tag{7.4b}$$

Secondly, the limiting aperture of the system will determine the beam current. For a field emitter of angular current density $\frac{dIe}{d\Omega}$, the beam current is usually given by

$$I_b = \pi \alpha_o^2 \frac{dIe}{d\Omega} \tag{7.5}$$

7.3 THE PROBE SIZE

The diameter of the focussed spot is usually calculated by combining the effects of the lens aberrations, the diffraction, and the emitting source size. It is conventional to assume, for the beam diameters considered here, namely few tens of nm's, that the aberrations are independent. Therefore, the final probe diameter can be obtained by adding these contributions in quadrature such that

$$d = \left\{M^2 dg^2 + d_{ci}^2 + dsi^2 + d_d^2\right\}^{\frac{1}{2}} \qquad (7.6)$$

where d is the final probe diameter, dg is the source diameter, and d_d, d_{ci} and d_{si} are as defined earlier. For higher resolution, d_s and d_d will not be independent and a wave optical treatment will be needed (146).

Equation (7.6) represents the general form of the factors contributing to the final spot diameter. It should be mentioned however that different authors have assigned different widths to these contributions. The discrepancy arises from the assumptions made about which diameter is involved (e.g. FWHM, half power points, standard deviation, etc.) and the subsequent approximation that follows. Smith (147) defines the probe diameter as that containing 80% of the beam current assuming a Gaussian distribution for the current density. Crewe et al (72) used the FWHM of the current distribution as the probe diameter. A further discrepancy involves the chromatic aberration as it depends on the chosen value of energy spread ΔV . Brores (112) used the $FW\frac{1}{e}M$ of the energy distribution, while Crewe et al (72) quote a value of 0.2 eV without defining what it measures.

Finally, the relationship between the theoretical and the experimental probe diameter will be considered. It is conventional for probes, in the region of few nm diameters, to scan the beam across a sharp edge and examine the resulting wave form. Smith (147) has measured the beam diameter to be between 17.5% and 82.5% of the maximum signal, which is equivalent to 80% of the beam current. Recently, Venables and Janssen (148), again assuming a Gaussian distribution, have defined the beam diameter to be the FWHM of the distribution. This is equal to 1.4 (20 - 80%) of the edge resolution. More stringent definitions have been adopted by Todd et al (149) who measure the beam diameter between 10% and 90% of the edge resolution test. Cleaver and Smith (76) have used a different

approach by measuring the distance between the points where the extrapolated maximum gradient intersects 0% and 100% of the final signal.

7.4 ELECTRON LENSES FOR FIELD EMISSION PROBES

The incorporation of field electron emitters in micro-probes has necessitated the use of different lens shapes from those found in conventional electron probes. One of the simplest lens types is the two element lens introduced by Butler (137), and later used by Crewe et al (72). The lens shape, shown in Figure 7.1, was designed to give a small change in the potential on either side of the electrode apertures. By doing so, the action of the apertures as lenses with large aberrations is greatly reduced (150). It is found that such a shape has, in addition, a particularly small spherical aberration contribution. For an 8 cms working distance, using this lens, Crewe reported a spot diameter of about 20 nm with a beam current in the range of 10^{-11} - 10^{-10} A using a W(310) built-up emitter. A similar lens to this, with a 12 cms working distance (HB200 SEM, V.G. Microscopes Ltd., U.K.) has been used in this study and will be compared later with different lens shapes.

Munro (151) has compared the Butler lens with a number of simplified two element shapes, and concluded that the asymmetric lens of Figure 7.2 has better aberration coefficients than the Butler lens. In addition, the Munro lens is much easier to construct.

Kuroda et al (152) have used a symmetric three element lens system similar in shape to the Butler lens. The advantage of a three element lens is the ability continuously to change the energy of the electron beam, via the central anode, without changing the working distance (153). A spot diameter of about 100 nm with a beam current of up to 1×10^{-8} A was indicated, and experimental results within a factor of 2 in the case of

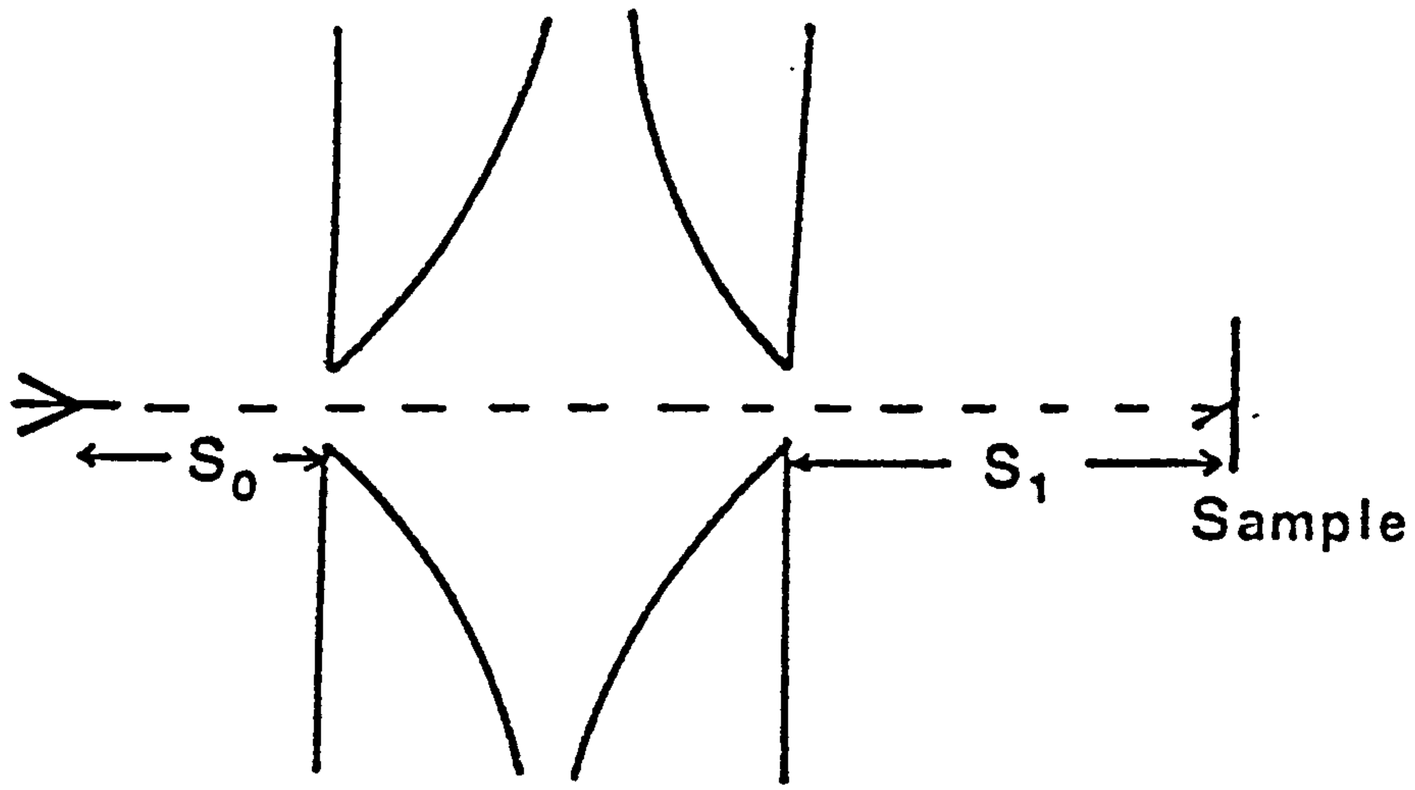

Fig. 7.1 The Butler lens.

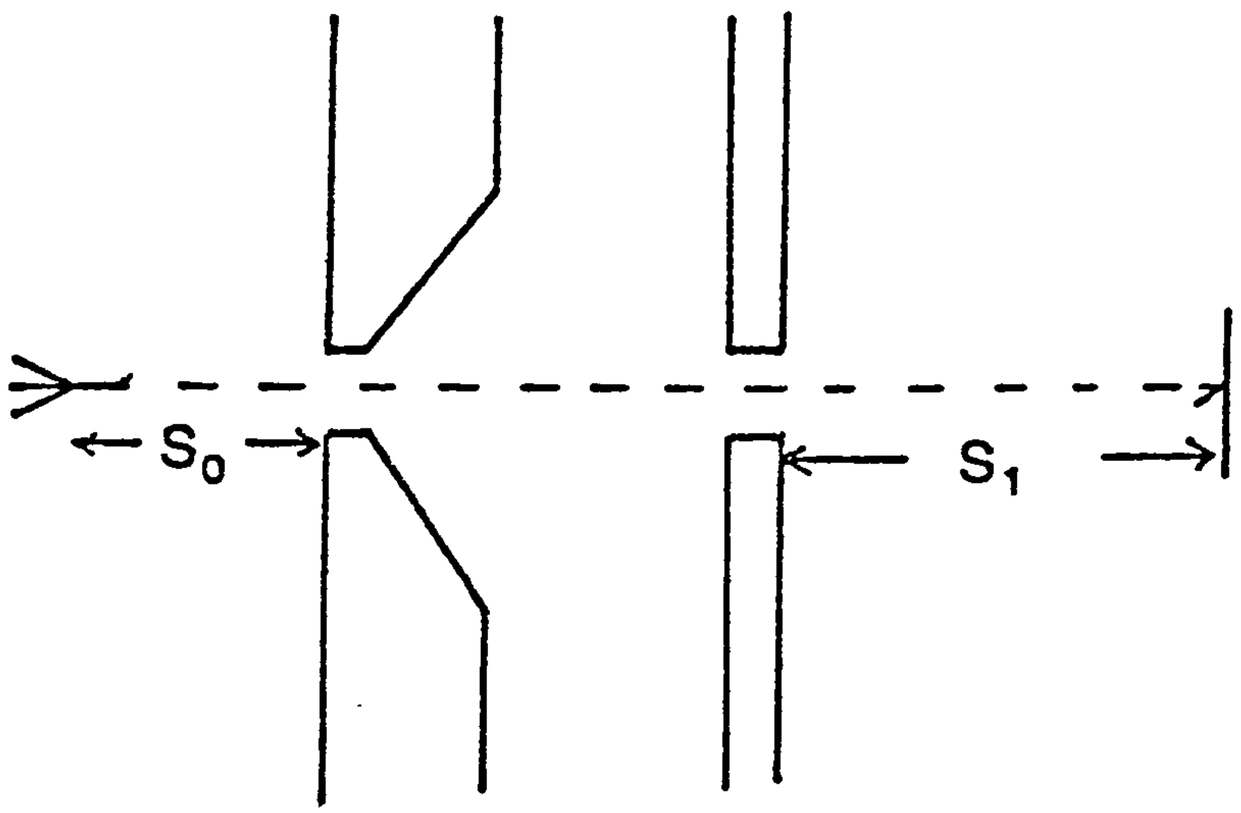

Fig. 7.2 The lens of Munro.

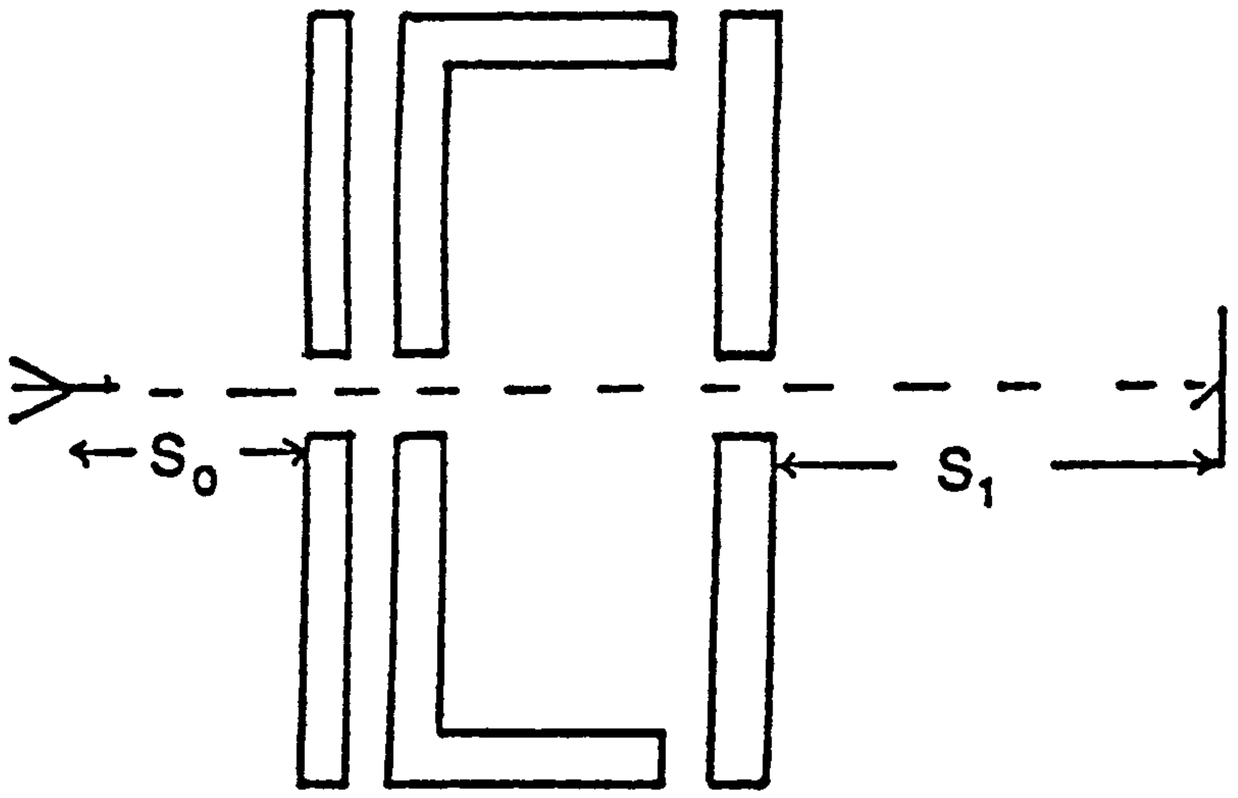

Fig. 7.3 The lens of Orloff and Swanson.

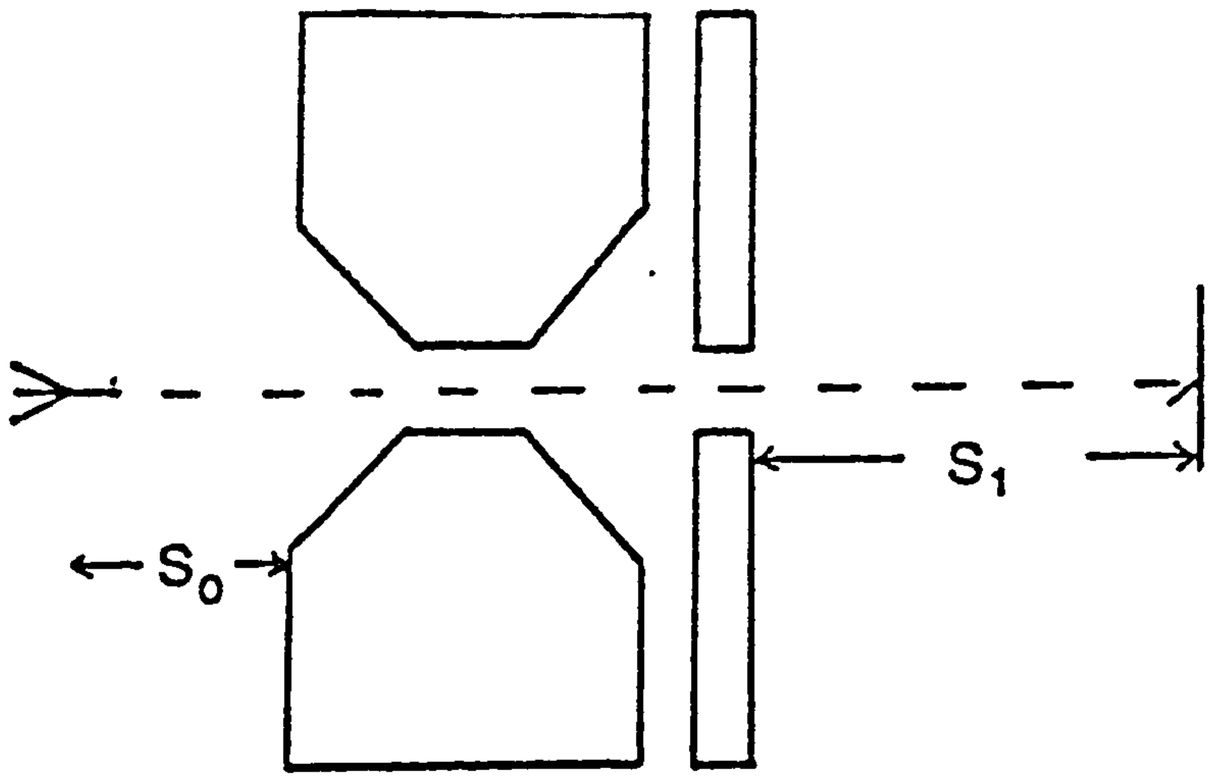

Fig. 7.4 Modified Munro lens.

beam current were obtained (154).

Riddle (139) has studied a number of electrostatic einzel lenses for use in a field emission probe system. The emphasis of his analysis was specifically for a reduced spherical aberration. It was found, as suggested by Seeliger (156), that asymmetric lenses, where the bulk of the central electrode is nearer to the first, have a small spherical aberration. Figure 7.3 shows a schematic of such a lens which was found to have favourably low spherical and chromatic aberrations. Orloff and Swanson (157) have studied the electron optical characteristics of this lens when used in the "zoom" mode, i.e. variable energy and magnification for a fixed image distance. They indicate a spot of about 50 nm with a beam current of up to 1×10^{-8} A at 30 kV, using a 5 kV emitter with $I_e = 1$ m A/str.

The addition of a magnetic lens (or lenses) to any of the above lenses can improve both beam current and spot diameter. For the system proposed by Kuroda, the magnetic lens would operate in the optimum magnification conditions given by the three element lens. A spot diameter of about 10 nm at the same beam current of 1×10^{-8} A should be expected in this case (158). For the Butler lens a similar improvement has been obtained (159).

Cleaver and Smith (70) have used a simpler three element lens system, with the first electrode acting as a Wehnelt. With two magnetic objective and condenser lenses, a spot diameter of about 10 nm and a beam current of 1×10^{-9} A were obtained. Several other systems giving comparable results, but all using auxiliary magnetic lenses have been reported (e.g. (148)).

The addition of magnetic lenses, although favourable for improving spot size and current, as has been shown above, is not particularly suitable for application in the present study. Firstly, the residual magnetic

fields from the added lenses, even with careful shielding, would almost certainly affect the resolution of the Auger spectrometer. For high energy resolution, the analysed electrons need to be decelerated to about 1 eV. Secondly, for a UHV system, as in SAM, the magnetic lens would have to be carefully designed to be bakeable. Alternatively it can be made demountable and hence placing a further constraint on the final geometry. Even in this latter case, the residual field can not be completely shielded. Based on these points, the choice of an all-electrostatic probe forming system was favoured.

The two element lens, in addition to its simplicity in construction and operation has the advantage of a low energy focus (usually a few hundred volts). This gives the operator a larger field of view, beneficial in locating an area of interest, and extra possibilities of application, such as electron energy loss spectroscopy (EELS). The work by Munro is not specifically informative about the properties of this lens when used in a SAM, i.e. the variation of the spot size with beam current at low and high energies, and the dependence of the aberrations on the inter-anode separation for various R values. For this reason the decision was then made to study the optical properties of this lens for a beam voltage in the range .1 - 60 kV, and an emitter voltage, V_e of up to 5 kV. A comparison between this lens and the existing Butler lens will be made along with the three element lens by Orloff and Swanson (157).

7.5 METHOD OF CALCULATION

The electron optical parameters of the lenses studied here were computed with two programs provided by Munro (158). The programs are written in Fortran to be used on the IBM 370 computer. Slight modifications were necessary for transferring them to the University of York main-

frame computer, DEC 10.

The first program uses the finite element method with boundary conditions determined by the lens geometry to calculate the axial potential distribution V(z) of the lens. The second program is then used to compute the electron trajectories r(z), using V(z) values and numerically solving the paraxial ray equation of the lens,

$$r'' + \frac{V'r'}{2V} + \frac{V''r}{4V} = o \qquad (7.7)$$

where primes denote differentiation with respect to z. This program is also used to compute the spherical and chromatic aberration coefficients C_s and C_c referred to object space (or image space using formulae (7.2d) and (7.3d)) by numerical integration of the following expressions (144),

$$C_s = \frac{1}{16\sqrt{V_o}} \int_{z_o}^{z_i} \left(\left\{ \frac{5}{4}\left[\frac{V''}{V}\right]^2 + \frac{5}{24}\left[\frac{V'}{V}\right]^4 \right\} r_o^4 + \frac{14}{3}\left[\frac{V'}{V}\right]^3 r_o' r_o^3 - \frac{3}{2}\left[\frac{V'}{V}\right]^2 r_o'^2 r_o^2 \right) \sqrt{V}\, dz \,, \qquad (7.8)$$

and

$$C_c = \sqrt{V_o} \int_{z_o}^{z_i} \left\{ \frac{1}{2}\frac{V'}{V} r_o' + \frac{1}{4}\frac{V''}{V} r_o \right\} \frac{r_o}{\sqrt{V}}\, dz \qquad (7.9)$$

where $r_o(z) = o$ and $r_o'(z) = 1$ are the initial conditions, and $V_o = V(z_o)$, i.e. the potential on the object side. For more details on the finite element method, the reader is referred to (159). A third program was written by the author to compute the beam diameter and current using the resulting C_s and C_c from the above program and formulae (7.5) and (7.6). The accuracy of the calculation was checked by running the test examples provided. In this case exactly the same results were obtained. In addition, the lens of Crewe (72) was also analysed and good agreement (to within 5%) was obtained. This limit is set by the error in reading

numbers out of a published graph.

7.6 RESULTS

The electron optical characteristics of the lens shown in Figure 7.2 were calculated for the voltage range $.1 < R < 60$ where $R = V_i/V_o$. The inter-anode spacing was varied from 4 to 16 mm for this lens and at a working distance of 80 mm. Figures 7.5a - d show the results obtained. The dimensions of the lens are shown in Figure 7.2. It should be noted that all the lens parameters scale with its length except the magnification, M. The 4 mm inter-anode spacing forms a strong focussing lens giving the best results in terms of aberration coefficients at a fixed R. However, the practical disadvantage of such narrow anode gaps is the likelihood of electrical arcs between the anodes.

A small reduction in the aberration coefficients of between 10 - 15% was achieved by changing the shape of the first electrode near the emitter as shown in Figure 7.4. Such a small improvement should not be considered as it introduces further complications. In particular, it introduces a lower pumping speed around the emitter and a restriction on the physical size of the outgassing facilities of the first anode. Further, the overall magnification of the lens is smaller than that due to Munro. This improves the beam diameter at the expense of a lower beam current.

Figure 7.6 compares the beam diameter, at a fixed beam current, for three different lenses, shown in Figures (7.1), (7.2) and (7.4), as a function of voltage ratio R. The beam current was chosen to be 5×10^{-9} A using I_e = 100 μA/str, an energy spread of 0.3 eV, and V_e = 2 kV. The inter-anode distance of the V.G. lens is 12 mm, while for the other two it is 8 mm. At a voltage ratio R = 10, it can be easily seen that the Munro lens gives an improvement of about 40% on the beam diameter with respect to the

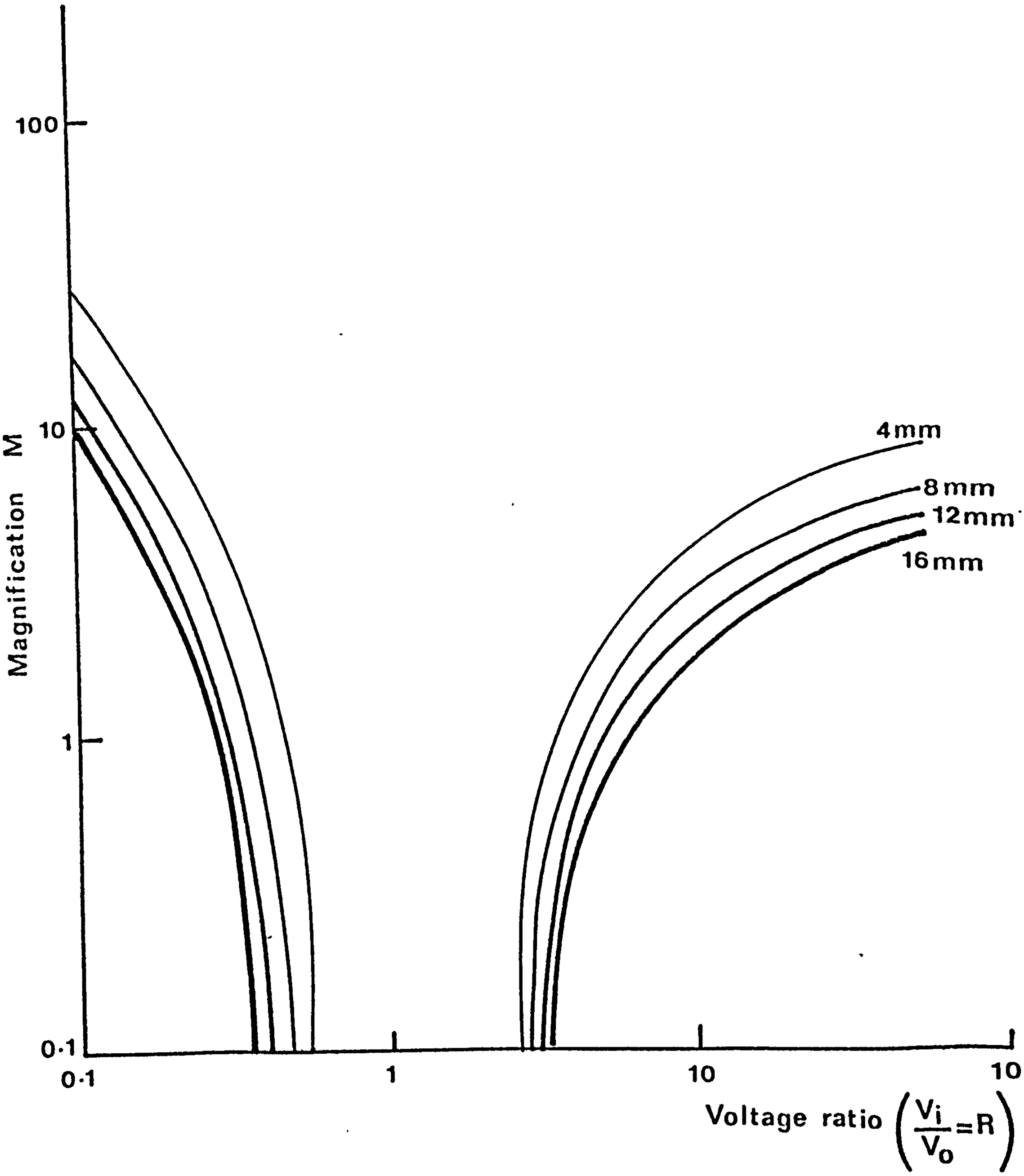

Fig. 7.5 The electron optical characteristics of lens of Fig. 7.2 for a range of anode spacing, 4 - 16 mm. (a) Magnification, M, (b) emitter first anode distance, S_o, (c) chromatic aberation, C_c and (d) spherical aberration C_S versus voltage ratio, R.

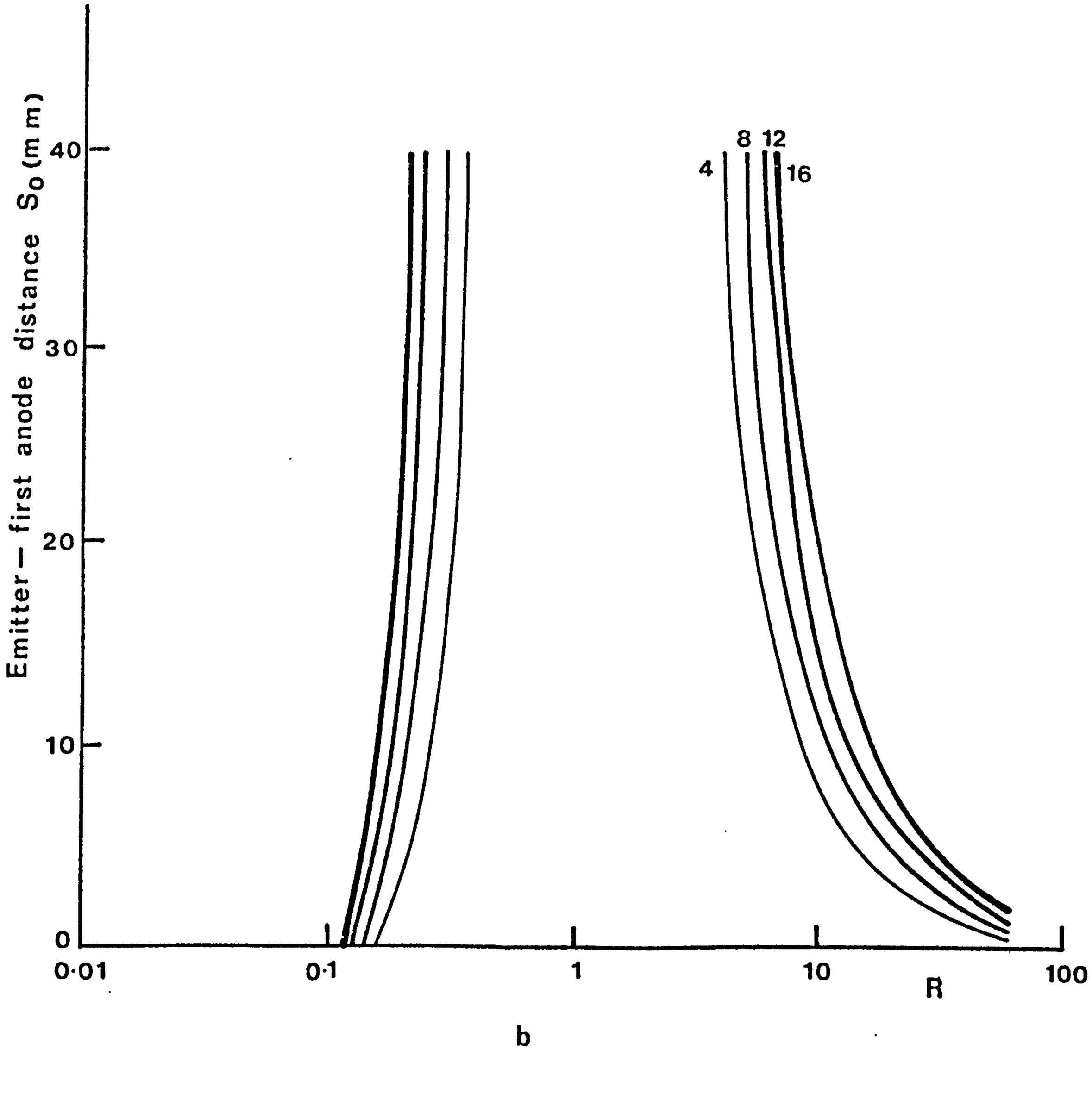
Emitter – first anode distance S_o (m m)
40
30
20
10
0
0·01
0·1
1
10
100
R
4
8
12
16

b

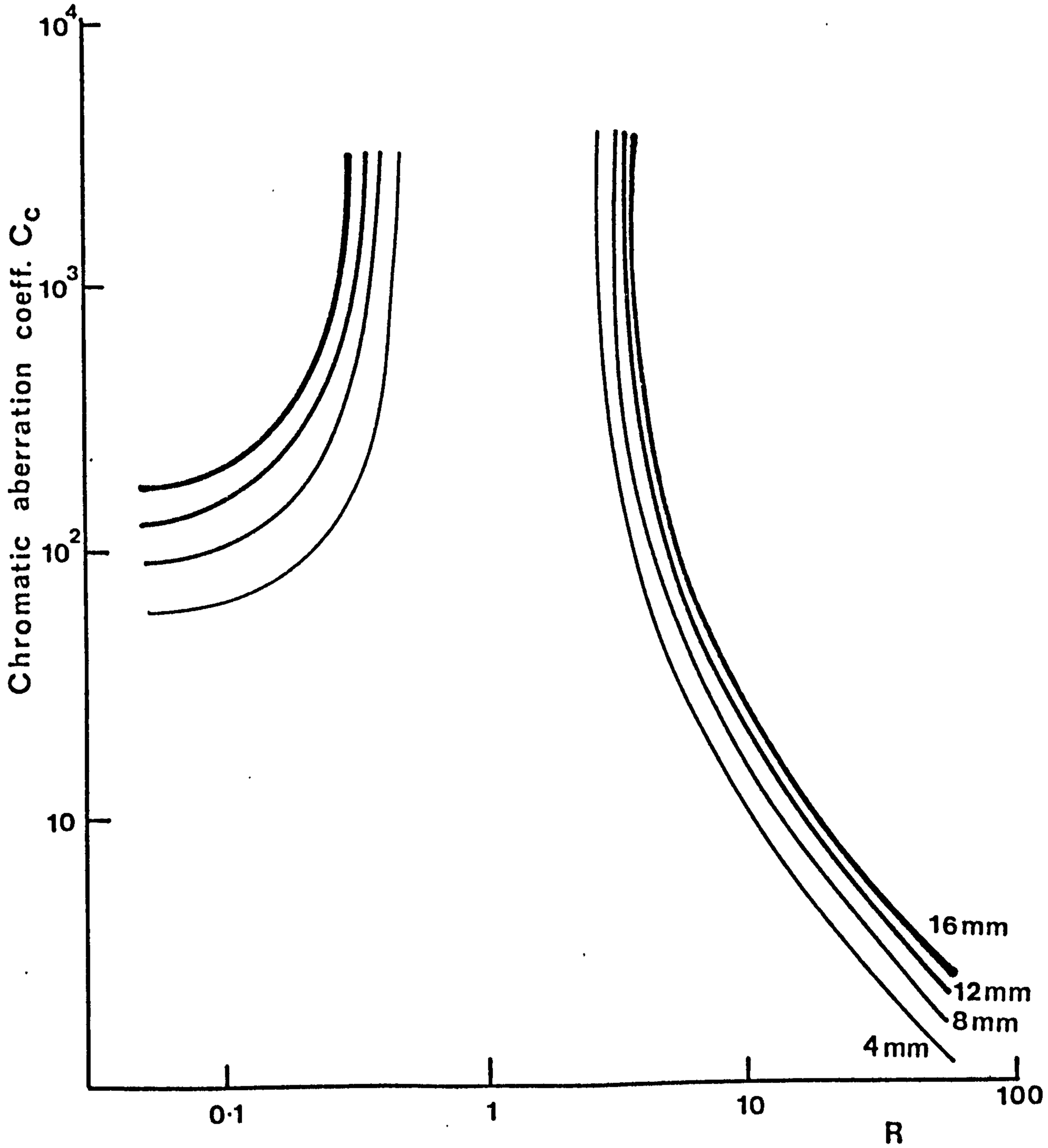
Chromatic aberration coeff. C_c
10^4
10^3
10^2
10
0·1
1
10
100
R
16mm
12mm
8mm
4mm

C

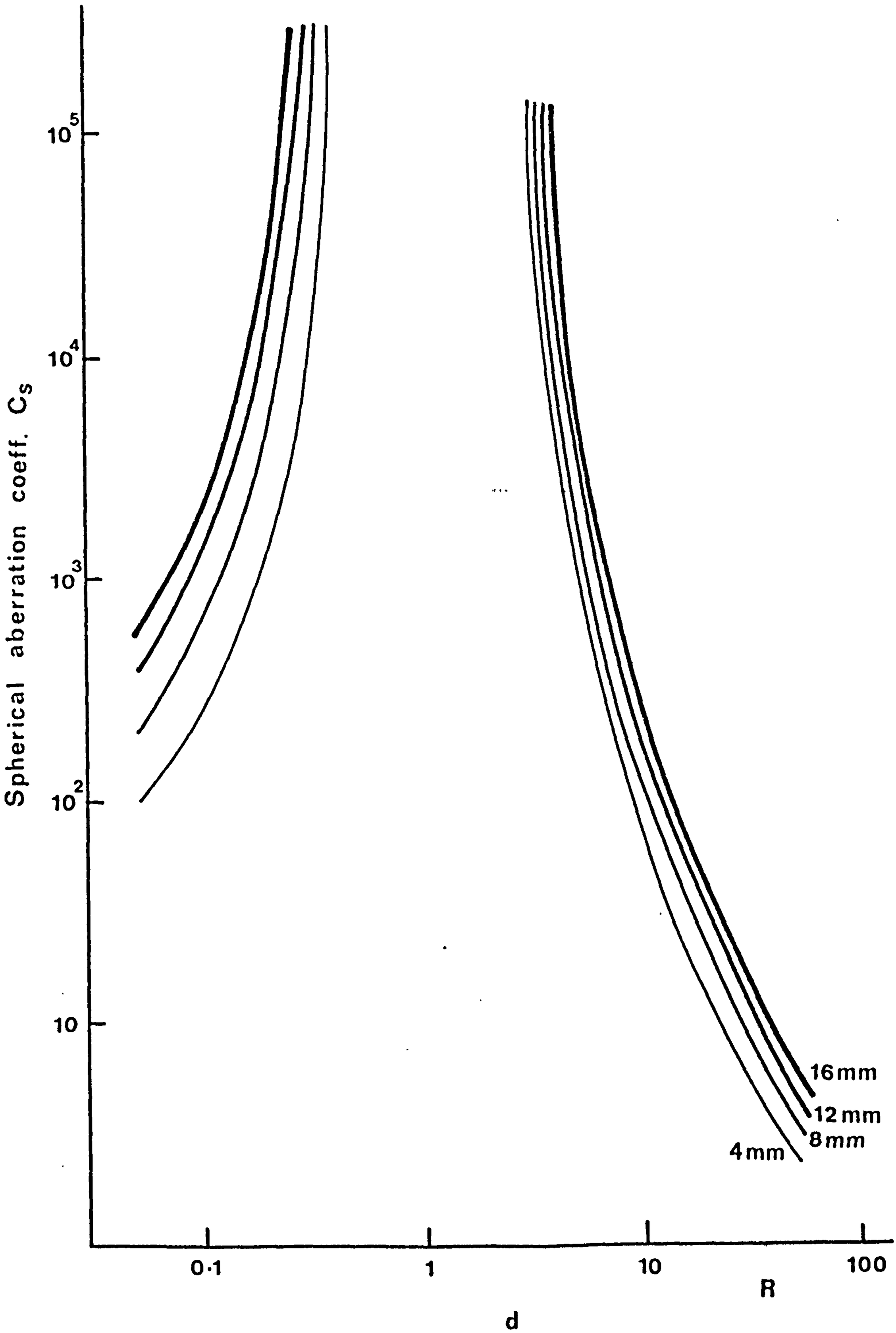
Spherical aberration coeff. C_S
10^5
10^4
10^3
10^2
10
16mm
12mm
8mm
4mm
0·1
1
10
100
R
d

V.G. lens and about 10% of the lens of Figure 7.4, namely 38 nm spot diameter with 5×10^{-9} A at 20 kV beam energy.

It is instructive to compare the results obtained here for the two element lens of Munro, referred to as the M lens, with the three element lens of Orloff and Swanson, referred to as the OS-lens. Figure 7.7 shows the relation between the spot diameter as a function of beam current for the two systems at 30 kV beams. The following data were used, V_e = 5 kV, ΔV = 2 eV, $I_e = 1 \times 10^{-3}$ A/str, and a working distance of 50 mm was assumed for the OS lens; and V_e = 3 kV, R = 10, ΔV = 0.3 eV and a working distance of 80 mm was assumed for the M-lens. It is clearly seen from the Figure that the M-lens is superior at low beam currents of up to 1×10^{-8} A. In this region, the beam diameter is controlled by the contribution of d_c. For higher beam currents a bigger aperture will be needed and as a result d_s will dominate. The OS-lens on the other hand is superior at higher beam currents. In addition, for lower primary energies, the OS-lens is advantageous, due to the use of the central electrode. For a 10 keV beam, a spot diameter of about 100 nm and 1×10^{-8} A should be expected. For the same energy and beam current, the M-lens will give a spot diameter of more than 15 times that of the OS-lens.

7.7 CHOICE OF THE LENS

From the above comparison, it can be seen that a two element lens of the type suggested by Munro looks attractive to be used in a SAM. Beam currents of the order of 1×10^{-8} A in a spot of diameter 40 nm should be expected, which is comparable to a three element lens system. In addition, this lens is easier in construction and operation than a three element lens, and does not require special machining as does the Butler lens.

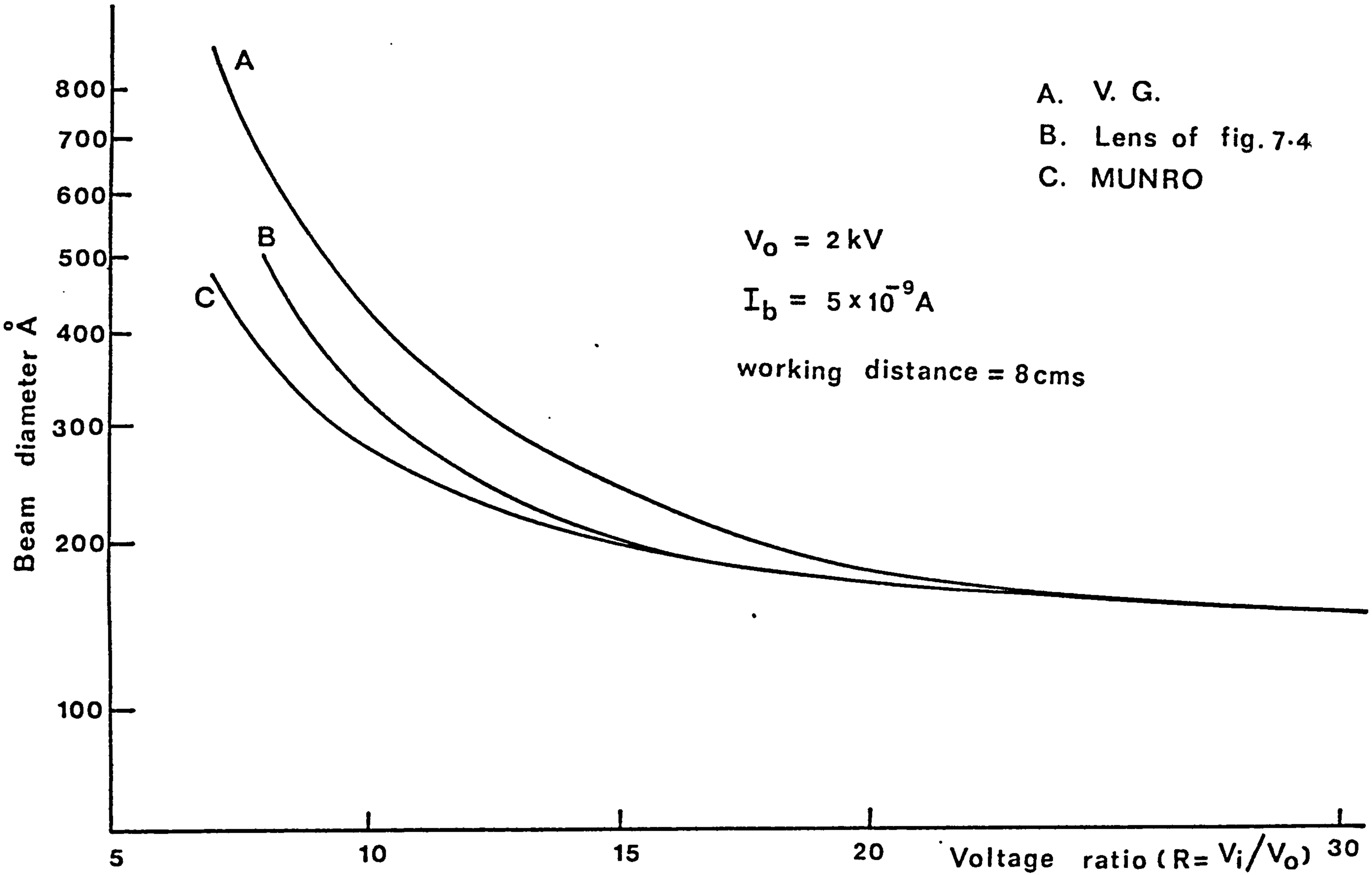

A. V. G.
B. Lens of fig. 7.4
C. MUNRO

V_o = 2 kV

$I_b = 5 \times 10^{-9}$ A

working distance = 8 cms

Fig. 7.6 Comparison of probe diameters for the lenses of Fig. 7.1, 7.2 and 7.4 in the case of iso-beam current of 5 nA.

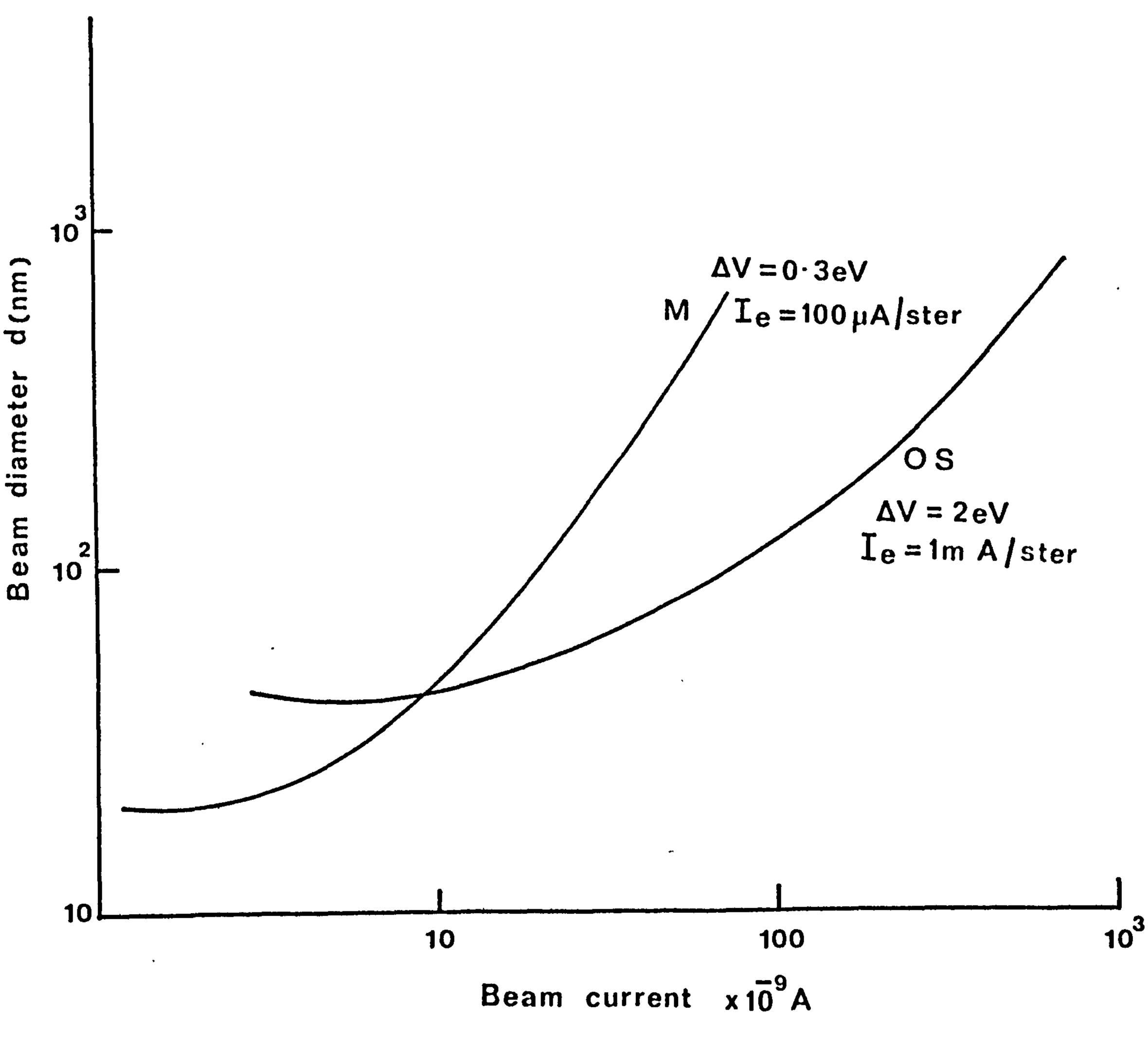

Fig. 7.7 Comparison of the probe diameter versus probe current for the lens of Munro (M), and the lens of Orloff and Swanson (O-S).

Furthermore, the low energy focus of this lens should prove beneficial in extending the range of the system's application, to e.g. EELS, in addition to its larger field of view which aids in locating an area of interest on the sample. Finally, if the emitter's separation from the first anode can be made to vary in situ, then one should be able to extend the range of primary energies used for a fixed emitter voltage. In this case, a lower beam current will result, at small R values, but this can be offset by a slight increase in V_e.

Based on the above comparison, it was decided to re-construct the electron optical column, using a two element lens, as that shown in Figure 7.2. If a stigmator/deflector similar to that used by Rang (160) is added, the electron column will be all electrostatic and thus compatible with the requirements of a high spatial, and high energy resolution SAM.

Figure 7.8 is a schematic of the geometrical arrangement of the new design electron column. The large working distance is provided to allow for an isolating valve between the electron column and the specimen. This is beneficial in the case of admitting reactive gases to the system that may alter the emitter work function.

The variation of beam diameter as a function of convergence angle is depicted in Figure 7.9. A focussing ratio R of 7 : 1 is assumed for two emitters with different energy spread and source diameter.

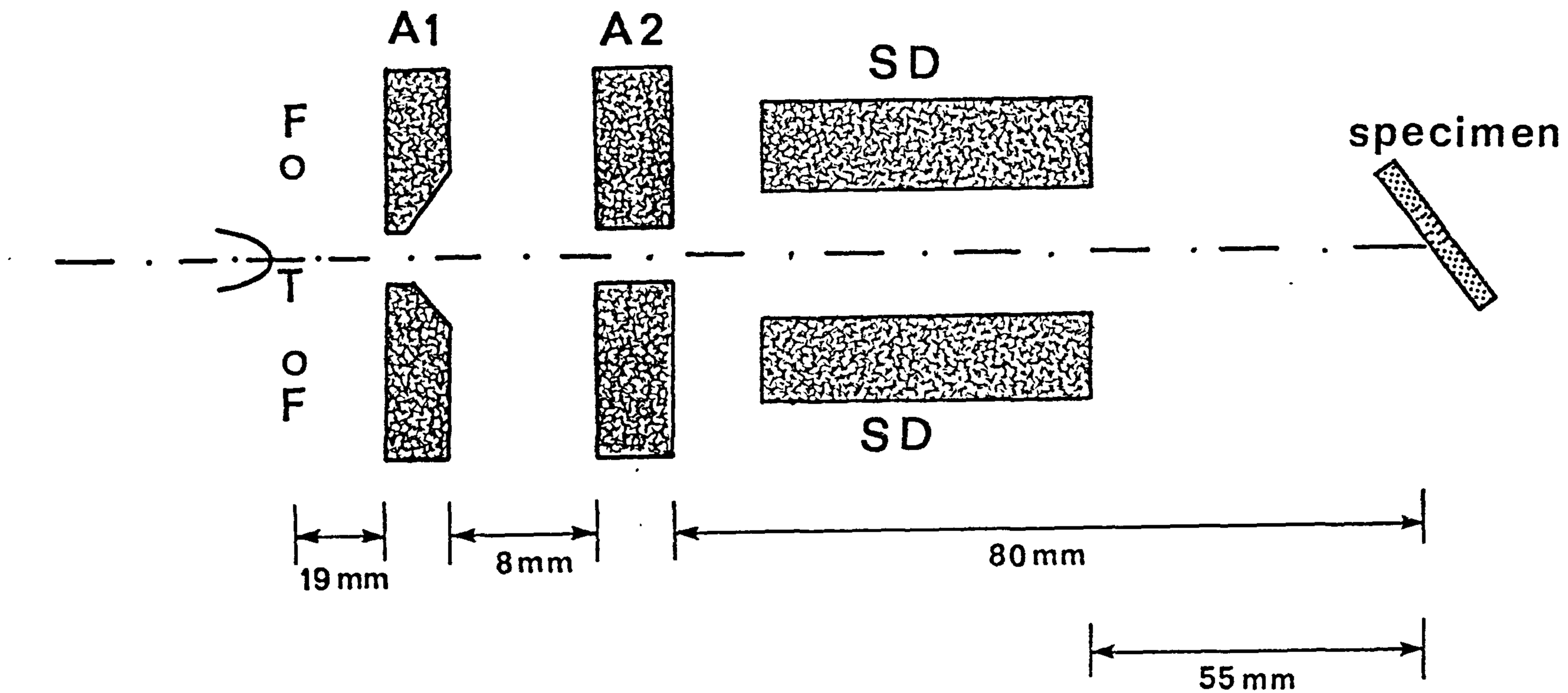

Fig. 7.8 A schematic of the electron column to be built. (T) the electron emitter, (F) the degassing filament, A_1 and A_2 anodes, and SD is the stigmator/deflector.

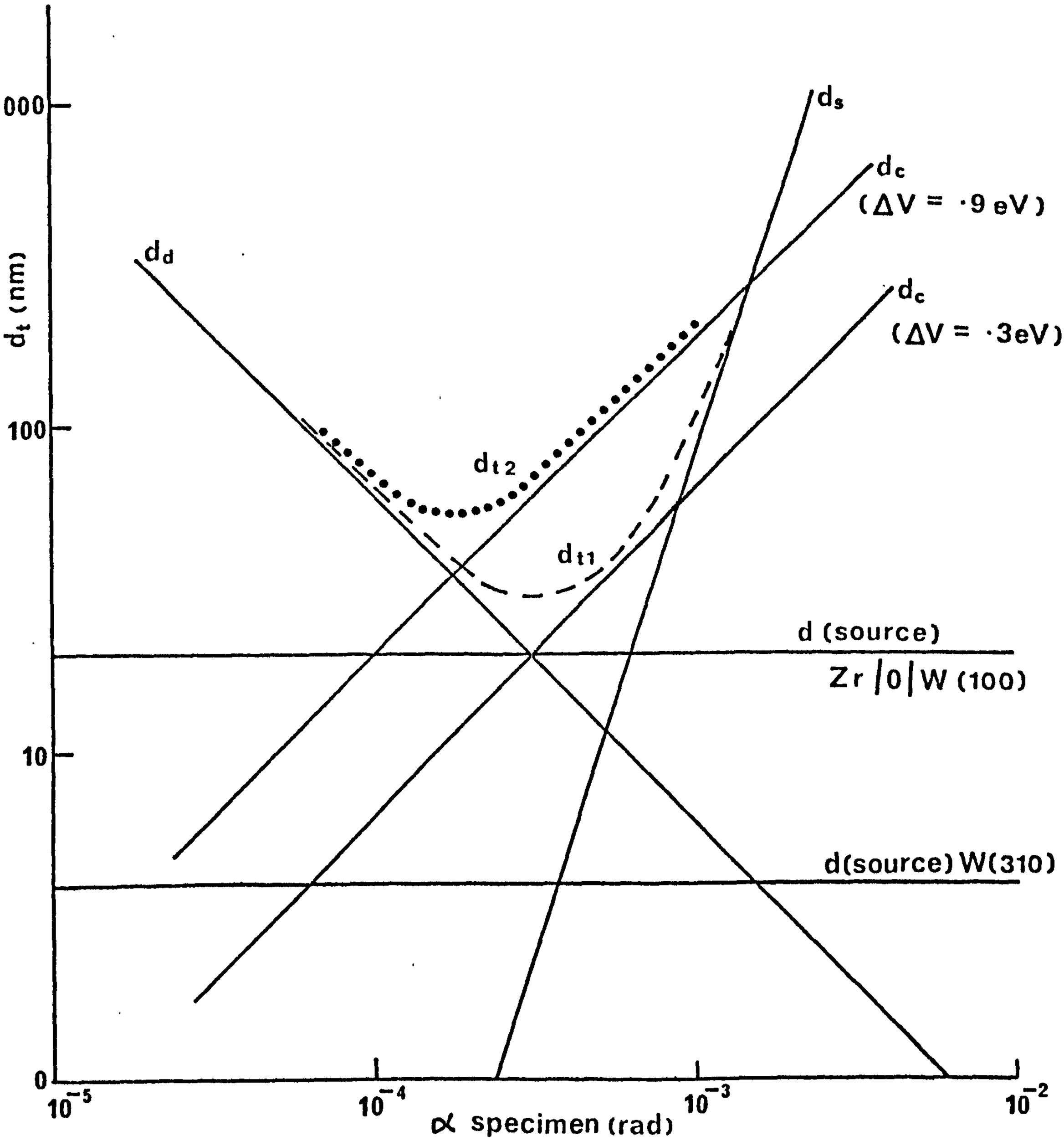

Fig. 7.9 The variation of beam diameter as a function of convergence angle at a focussing ratio of 7 : 1 for two emitters, W(310) and Zr/O/W(100).

CHAPTER 8

DESIGN AND CONSTRUCTION OF THE ELECTRON OPTICAL COLUMN

8.1 INTRODUCTION

From the work presented in the preceding chapters, the possibility of high spatial and high energy resolution SAM have been demonstrated. In Chapter 7, a comparison between electrostatic lenses used in a field emission probe forming systems was made. It was found that a simple two element electrostatic lens of the type suggested by Munro is comparable in performance to three element lens systems in the beam energy range of 20 - 30 kV. Such a lens should focus 1×10^{-8} A into a 40 nm spot diameter, using a W (310) field emitter in the cold emission mode with a total emission current of about 30 μA.

Due to limitations of the vacuum system described in Chapter 3, and in view of the results obtained for the electron optical characteristics of the simplified two element lens system, it was decided to re-design both the vacuum system and the electron optical column. The latter would be an all electrostatic system using the above lens with a stigmator/deflector of the type described by Rang (160). In addition to the high resolution spectrometer the rebuilt instrument would feature a high precision manipulator, a RHEED camera, a saddle-field ion gun for specimen surface cleaning, a low energy (2 kV) thermionic electron gun (LEG 31, V.G. Scientific Ltd.) for standard Auger spectroscopy, and a mass spectrometer (Anavac 2, V.G. micro mass, U.K.). Only the field emission gun is to be operated manually, the remainder of the system could be operated either manually or via a Hewlett-Packard system 9845B desk top computer. This is to replace the DMC (described in Chapter 3) and would be linked with the University's main frame computer (DEC 10 system) for further image process-

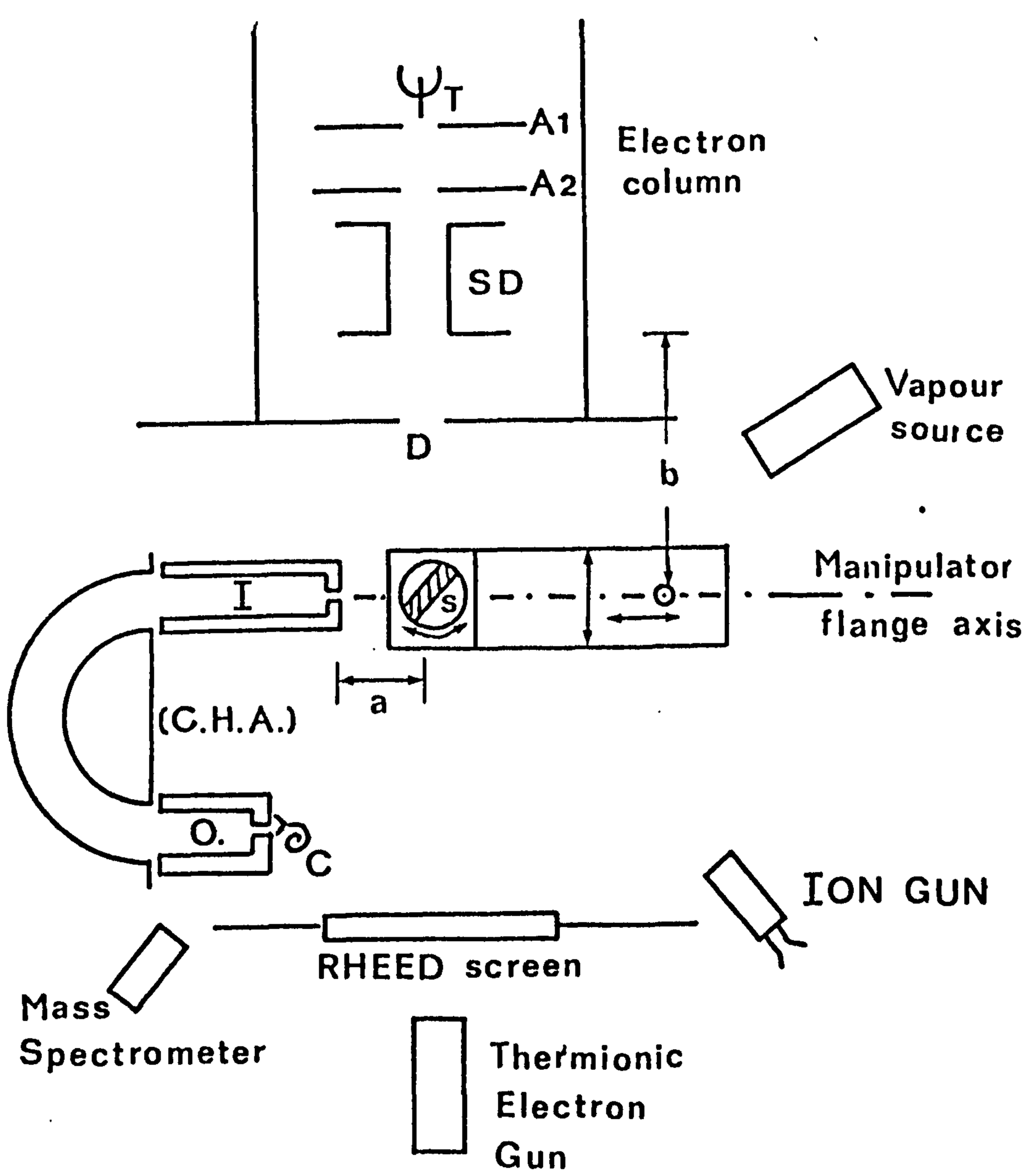

Fig. 8.1 The arrangement of the vacuum components of the second instrument.

Fig. 8.2 A photograph of the experimental set up of the second instrument.

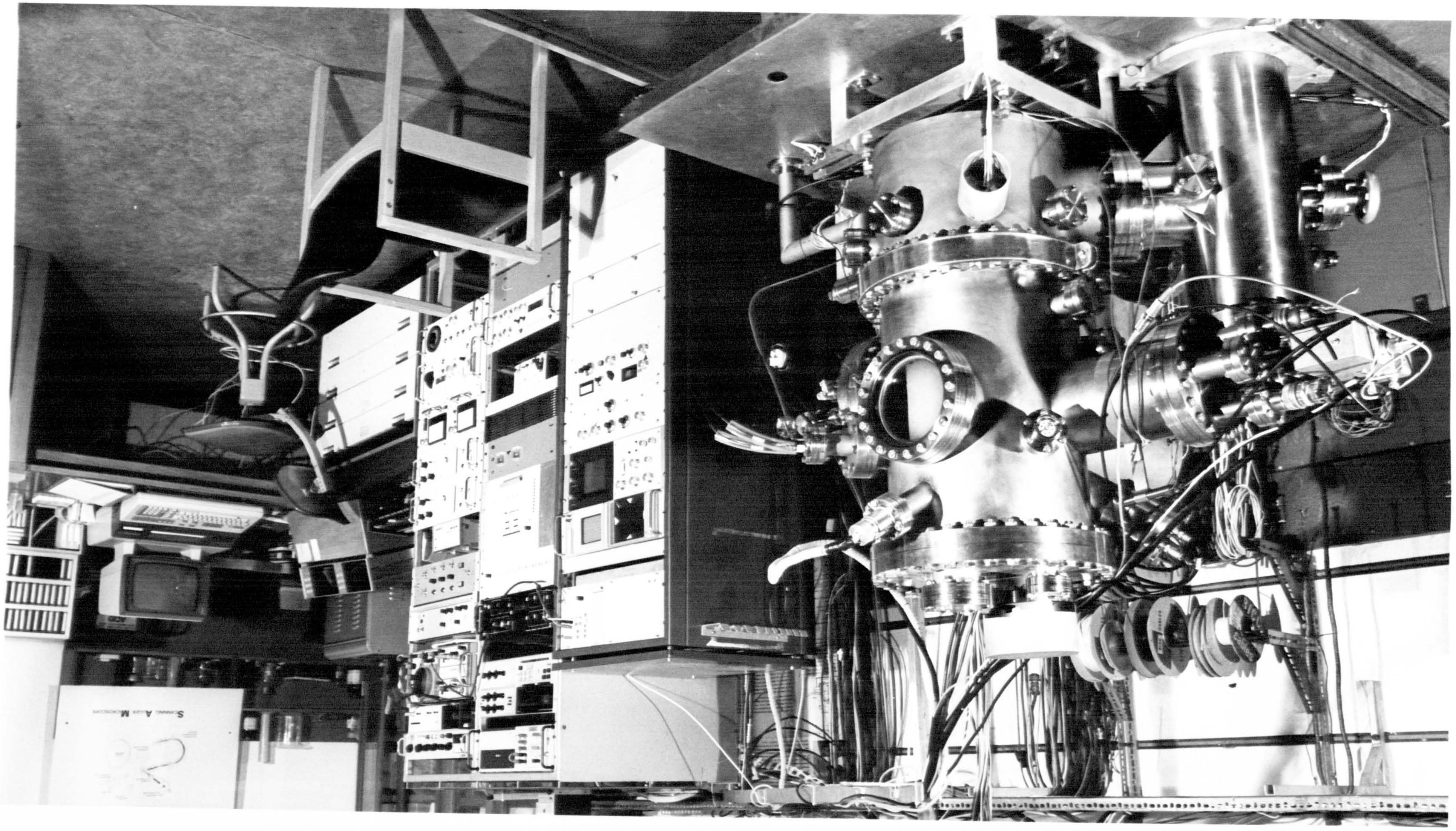

ing. Figure 8.1 depicts the arrangement of the vacuum components of the rebuilt instrument and a photograph is shown in Figure 8.2.

The present chapter is devoted to the description of the design and construction of the electron optical column, designed and built by the author. The justifications for the choice of particular materials in the construction of the various parts of the column (e.g. anode material, insulators, etc.) are presented. In some cases, experimental tests had to be carried out before the final choice was made.

8.2 THE VACUUM SYSTEM

For a stable emission from cold field emitters, and in particular for a long UOL, it is necessary to maintain a pressure $\lesssim 1 \times 10^{-10}$ torr in the emitter region. Similar pressure requirements at the sample position are necessary for surface physics experiments. At 10^{-10} torr, and assuming unity sticking coefficient, a monolayer would form in approximately 15 hrs (161). This should be a reasonable time for the examination of a chosen sample immediately after cleaning.

To maintain such a pressure in the emitter region, the electron optical column is differentially pumped from the main system. 1 mm diameter aperture isolates the two chambers. The former is pumped by a 60ℓ/sec ion pump (Varian Ltd.) through a 12.5 cms diameter aperture and is supplemented by a titanium sublimation pump (TSP) evaporating onto ~ 3200 cm^2 of a service well below the emitter. A sorption-forepump combination is used initially to evacuate the system. After baking at 170^{o} C for 24 hrs (a limit set by the channeltron used in the CHA), a nude Bayard-Alpert ionisation gauge (VIG 10, V.G. Scientific) below the emitter measures a pressure of ~ 5×10^{-11} torr. A gate valve with a viton seal is provided to isolate the gun chambers during admission of gases.

The system is made of stainless steel throughout. However, because of the stringent conditions of low magnetic fields, a 1 mm thick internal mu-metal shield is provided for the specimen chamber. In addition, the earth's field is cancelled with the use of three pairs of Helmholtz coils. These give a field at the specimen of less than 10^{-7} Tesla.

The main system is pumped with a 600ℓ/sec diffusion pump (E04-Edwards, Ltd.) filled with polyphenyl ether (Santovac 5 fluid) and supplemented with a 200ℓ/sec cold trap (V.G. Scientific) and a TSP evaporating onto 6000 cm^2 of a service well below the specimen. With the same bake-out described above, the system pressure is usually ~ 1×10^{-10} torr.

8.3 ELECTRICAL BREAKDOWN

There are two major electrical breakdown mechanisms in electron guns. The first is associated with breakdown along the surface of the high voltage insulators, while the second occurs in the inter anode spacing. In both cases flashover from the first anode to ground occurs leading to the destruction of the emitter in the following way. As a result of the discharge, the potential of the first anode is rapidly brought to ground potential by the low impedance spark. In this case the emitter will be subjected to a field determined by the potential of the first anode which is usually several times that of V_e. Consequently the emitter will be destroyed by the excessive emission current drawn. Such a mechanism has been reported by several authors and has caused emitter failure in their instrument (168). Figure 8.3 shows an emitter destroyed by this mechanism.

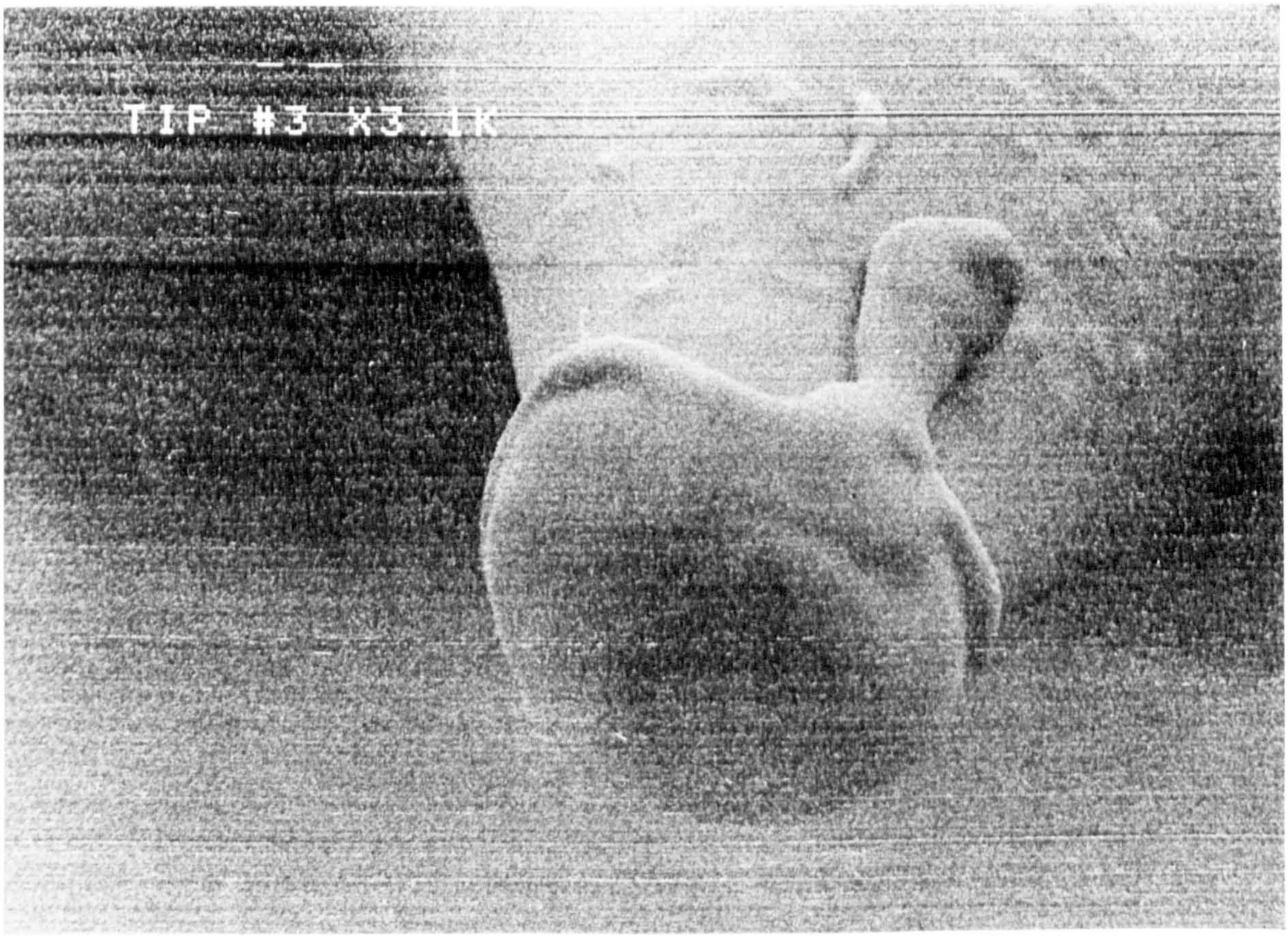

Fig. 8.3 SEM micrograph of an emitter destroyed in a vacuum arc.

8.3.1 The High Voltage Feedthrough and Emitter Mount

Figure 8.4 shows a schematic of the feedthrough and emitter mount and Figure 8.5 is a photograph of it. Normally three high voltage leads through the vacuum wall are sufficient for the electron gun. These are the first anode feedthrough at a potential of $(V_i - V_e)$, and two of a potential V_e for the field emitter's filament, to enable in situ heating. Two additional feedthroughs at a potential V_e have been incorporated for the first anode cleaning filament. These are rated at V_e because during operation this filament can be either at V_e or $(V_i - V_e)$.

The first anode high voltage insulator is made of a cylinder of Pyrex glass 5 cm long and 7.5 cm in diameter which is joined to Kovar cylinders at both ends. The length of the glass is based on the work of Shanon et al. (162) who found the first flashover gradient for a 2.5 cms pyrex cylinder to occur at 10 kV/cms. Thus, the gun can be operated safely up to 50 kV before the first flashover occurs. Preliminary tests of this feedthrough have been carried out up to 45 kV with no signs of breakdown. This is higher than the requirements of the gun design (the microscope power supply is only 30 kV output) but necessary for two reasons. Firstly to test the theoretical assumption on the electrical resistivity of pyrex, and secondly, to round off any sharp edges on the high voltage components.

Four feedthroughs rated at 7 kV (Smith Industries) are used for the emitter and first anode outgassing filaments. These were first mounted on a flat stainless steel plate 8 cms in diameter, at equi-distance from the centre. The plate was then joined to the Kovar metal at one end of the glass cylinder. This assembly then carries a potential $(V_i - V_e)$. The connection to the first anode is made via a spiral spring attached to the plate (see Figure 8.5). The spring is made of inconel wire of 1.5 mm diameter with a ball shaped end at the connection to the first anode. The

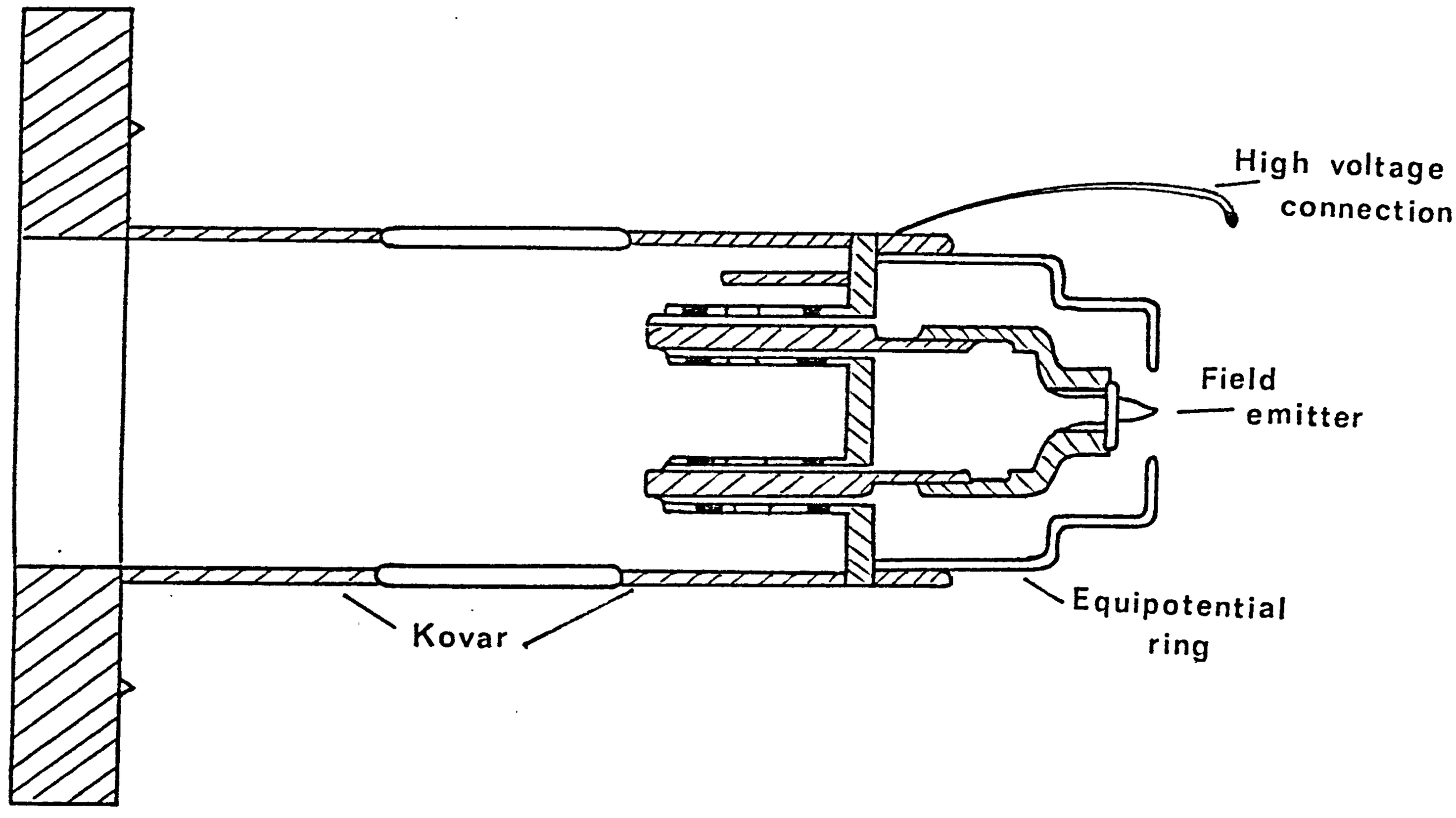

Fig. 8.4 Schematic of the high voltage feedthrough.

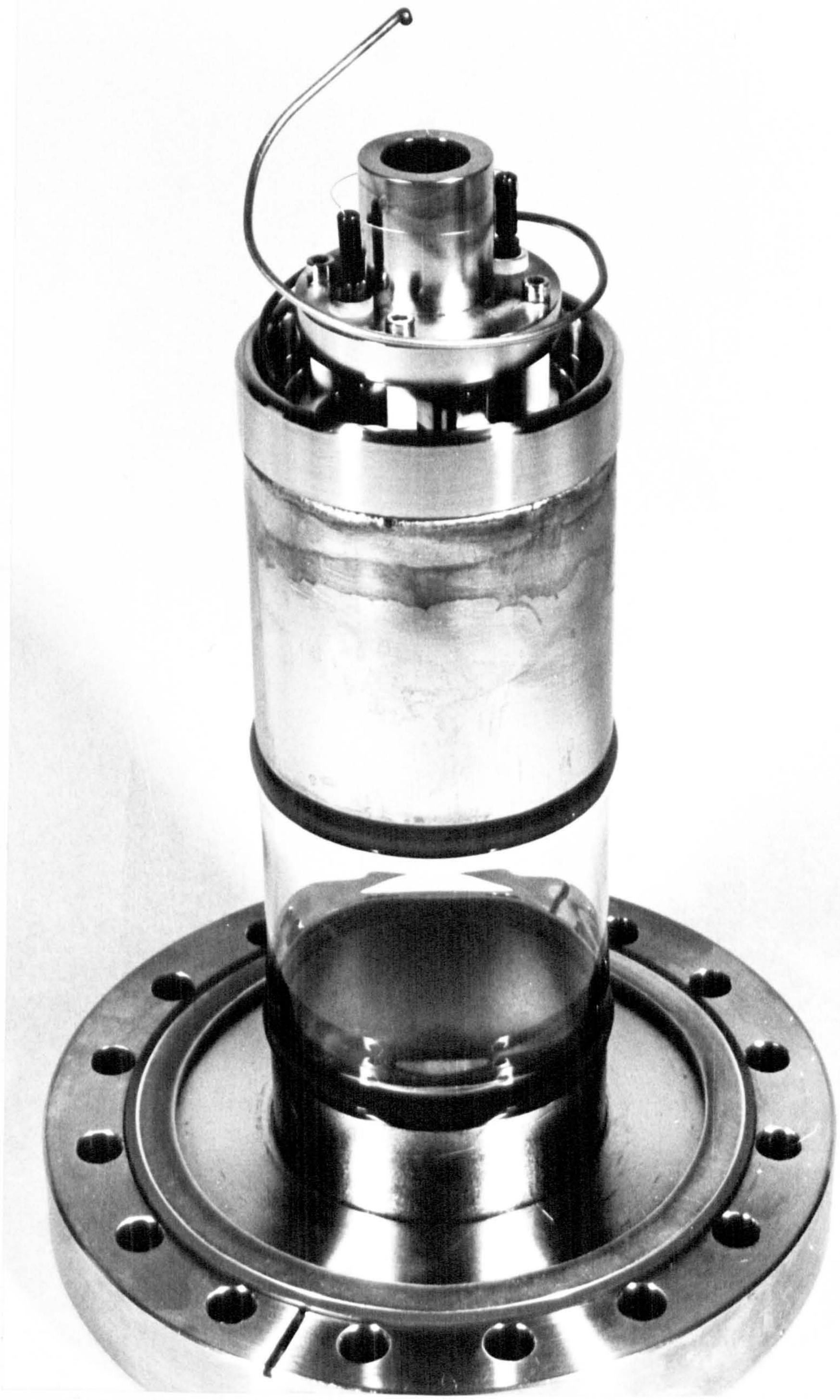

Fig. 8.5 Photograph of the high voltage feedthrough.

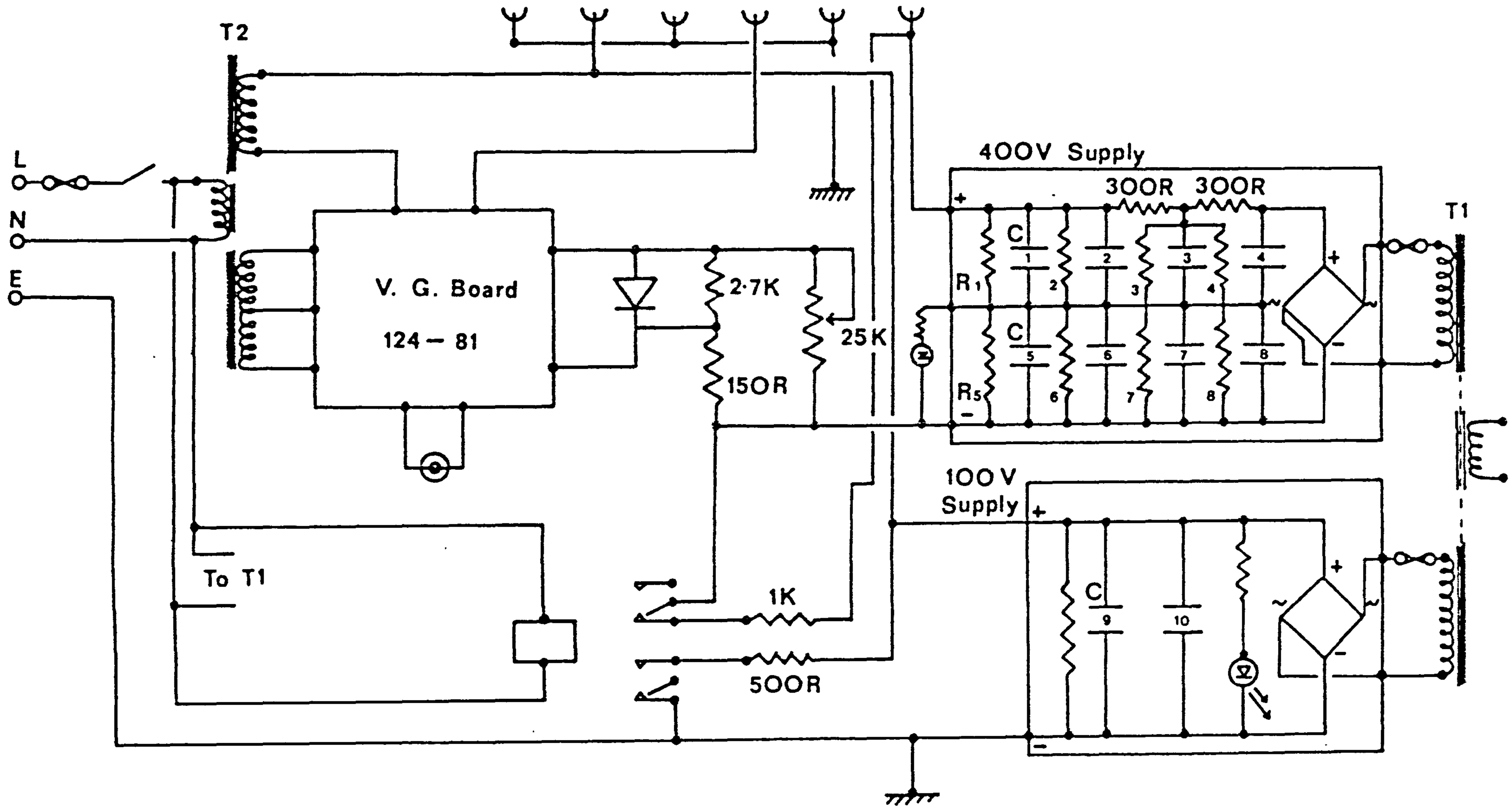

Fig. 8.6 Circuit diagram of the power supply for the first anode degassing filament.

other side of the glass cylinder is joined to a 150 mm stainless steel metal flange. The faces of the flange and plate are parallel to better than 5×10^{-3} radians (1 in 185 mm). The emitter mount is central to within 1.0 mm of the optical axis. The outgassing filament is made of a 150 μm tungsten wire to a circular shape that surrounds the emitter. Electrons from the filament bombard the first anode with an energy of 400 eV. During outgassing, the potential of the surroundings of the first anode are negatively biased to prevent electron bombardment of the anode's insulators. Electron bombardment causes dissociation of CO and so deposition of C on the surfaces of the insulators. Such an effect has been detected during development and has led to insulator breakdown through tracking. Figure 8.6 depicts the circuit diagram of the filament power supply which is a modified version of a standard ionisation gauge controller (IGP3, V.G. Scientific) to allow for the negative biasing.

The feedthrough is mounted on a bellows assembly as can be seen from Figure 8.7. This enables translation of the emitter in the x - y plane of ± 3.0 mm for alignment purposes. The bellows are also used for altering the emitter to first anode spacing externally, hence allowing a focussing ratio R over the range $7 < R < 12$ to be achieved. In addition it is used for aligning the emitter with respect to the column's optical axis by changing the length of the four supporting pillars between the emitter mounting flange and the second anode (see Figure 8.7).

A highly polished shield ring is mounted internally on the first anode. This ring is used for locating the high voltage spiral spring which is attached to the high voltage feedthrough. It also ensures that the emitter is in an equipotential enclosure, even at the maximum separation between the emitter and first anode. This precaution is essential since the field strength of the emitter would increase dramatically if it came out of the enclosure with the subsequent damage caused to the emitter as a

Fig. 8.7 Photograph of the electron column's vacuum chamber showing the emitter carrying flange and the bellows used for emitter translation in (x,y) plane and external change in emitter - first anode spacing.

result of the large emission current drawn.

Another source of discharges in high voltage instruments that can be troublesome, is the high voltage cable, and in particular air gaps near the conductors where the field is a maximum. The design criteria for the cable are the exclusion of air gaps while at the same time ensuring that it is readily disconnected from the gun (e.g. during bake-out). This is achieved via a push fit mechanism between brass cylinders located in a PTFE plug. The cylinders are vertically cut at one end to allow for a good fit with the feedthrough pins. The choice of this simple arrangement was based on the fact that the feedthrough pins are inside an equipotential region at high voltage. The plug was found to operate satisfactorily up to 45 kV. However, above 25 kV, signs of corona discharge begin, particularly in a humid atmosphere.

8.3.2 The Electrode Material

The absence of a charge-carrying medium in high vacuum should offer ideal insulation between electrodes. In fact, if the field emission phenomena is considered alone, a strength of about 10^7 volts/cm should be obtained. In reality, vacuum gaps do not, unfortunately, show a simple $\frac{V}{d}$ dependence, where d is the inter electrode spacing. Bennet et al. (163) have found that field emission processes are the primary initiating mechanisms of electrical breakdown for electrodes of high tensile strength. A similar observation has been found in this study which shows that a discharge is always preceded by a field emission current presumably emanating from microscopic protrusions on the electrode surface. Besides the electrode material, several other factors are known to control the electrical breakdown strength of vacuum gaps. These have been reviewed by Bolin et al. (164) and in summary are:

1 - Electrode material is important in general, but the anode material is

more important than that of the cathode. An approximate ranking of some known materials in order of increasing breakdown strength is C, Be, Pb, Aℓ, Cu, Ni, Fe, SS, Ti, Ta, Mo, W .

2 - Surface cleanliness is more important than surface finish.

3 - Electrode geometry (shape and size) is important. A decrease in breakdown voltage is obtained with an increased electrode area, while for spherical electrodes increased curvature increases the breakdown voltage.

4 - The dependance of the breakdown on electrode spacing is linear for gaps < 5.0 mm. A less rapid increase is obtained with larger gaps.

5 - Improved performance of vacuum gaps is achieved by dielectric coating of the cathode surface to inhibit field emission.

6 - Breakdown depends on pressure conditions being constant at below 10^{-5} torr and rises to a maximum at 10^{-2} torr. This effect can be used for blunting emitting protrusions from the cathode leading to an improved ultimate breakdown voltage.

7 - Conditioning of the electrodes (such as that described in (6)) improves the breakdown strength.

In addition to the electrode material being of a high tensile strength, gas desorption should also be taken into consideration and particularly that of the first anode. Achard et al. (165) studied the gas desorption of some of the above listed materials, namely SS, Ti, Inconel, and Cu. Their results show that SS has a comparable outgassing rate to Ti and lower than the others under electron bombardment of 1.4 keV electrons. Hansen and Lauer (166) found that fields of up to 10^5 V/cm can be sustained with SS electrodes and with careful cleaning fields of 1.5 - 2 x 10^5 V/cm are possible. Since the smallest vacuum gap in the present lens is 8 mm

with a maximum voltage of 30 kV, corresponding to a field of < 40 kV/cm, it follows that SS should be a suitable material to use. In addition it is the easiest to obtain and machine of any of the higher breakdown strength materials listed above. It was then decided that Immac 5 (SS) should be used for the construction of all electrode and emitter mount components. Immac 5 is a non-magnetic material and has been extensively used at our laboratories in the construction of electron energy analysers and electron lenses.

Two methods of surface finish of the electrodes have been used depending upon the position of the particular electrode. All surfaces that are subjected to electron bombardment have been carefully machined and then gently electropolished to remove burrs left from machining. It was found that longer periods of electropolishing produced rougher topographical surfaces than shorter periods, when examined under the SEM. All other surfaces of the electrodes have been mechanically polished. The electropolishing solution was as follows:

Sulphuric acid	15%	by volume
Phosphoric acid	63%	" "
Water	22%	" "
Voltage	7 volt	
Current density	~ 2.5 - 4 A	depending on surface area to give a minimum of 500 A/m^2
Time	~ 3 - 5 minutes.	

This treatment was followed by inspection under a high power optical microscope (i.e. magnification of X200 - X500) and was repeated with rough surfaces. The mechanical polishing on the other hand consisted of turning the surface on a lathe to speeds of 2000 rpm and using successively finer grades of ScC papers.

All the edges have been rounded to a minimum radius of 3 mm and vacuum gaps kept to a minimum of 8 mm which is the inter-anode spacing. A

Fig. 8.8 Photograph of the electron lens with the equipotential shield cap.

stainless steel cylinder surrounding the electrodes and mechanically polished from the inside was found necessary to reduce breakdown between the first anode and the inside of the vacuum wall.

8.3.3 The Inter-anode Insulator

The purpose of this insulator is to support and insulate the first anode from the second anode which is at ground potential. Several solid insulating materials have been used in high voltage instruments. The important points to be observed in the design of this insulator have been reviewed by Bolin et al. (164) and are as follows:

1 - It is the surface condition and not the bulk properties that control the breakdown strength.

2 - Surface discharges usually originate at the negative junction of metal, insulator and vacuum. At this junction the surface of the insulator is charged by electrons that are field emitted at the junction due to imperfect contact.

3 - Shaping of insulator and cathode-insulator junction helps to raise breakdown strength.

4 - An improvement of the breakdown strength by a factor of two to five can be achieved by conditioning, a process whereby the insulating materials are exposed to fields somewhat higher than their normal operating fields.

5 - Alumina and Pyrex 7070 have been quoted as the most suitable materials for use in UHV. Both have shown a voltage breakdown gradient of about 90 kV/cm after conditioning.

Although pyrex 7070 has a high value of breakdown strength, the shapes suggested for such a condition are difficult to use with cylindrical insulators. In addition, Shannon et al. (162) have found the first flash-over gradient to occur at 10 kV/cm, which is not high enough for this application. A further complication in the design, if pyrex is chosen, will be the method of joining it to the SS anodes.

Alumina on the other hand has been the most widely used insulator in

electron guns, with its first flashover gradient occuring between 15 - 20 kV/cm (162). The first flashover gradient is defined as the voltage required to cause a breakdown over the surface of the insulator. Normally this takes place at a lower voltage than in a straightforward vacuum gap. However, this insulator has been mostly glued to the metal when used (70, 168). A disadvantage of this arrangement is the lower bake-out temperature of ~ 120° C set by the glue which makes it also unattractive to use in this study.

A material recently introduced that has not been used, to the author's knowledge, as a high voltage insulator, is machinable glass ceramic (Dow corning Ltd.). The manufacturer has given the following properties for the insulator.

Volume resistivity = 10^{14} ohm - cm at room temperature

Dielectric strength = 10^{4} volts/cm

Thermal expansion = $10^{-5}/C^{o}$ up to 600° C

Maximum usable temperature = 1000° C

A preliminary test sample in the shape of a cylinder 3 cms long and 1 cm diameter was tapped on both ends with M3 taps. When the holding bolts were screwed in position, the inner length was reduced to about 2 cms. The first flashover was detected at ~ 20 kV at a pressure of about 1 x 10^{-7} torr. Further conditioning increased this value to 40 kV, which is quite adequate for the intended application. Different electrode shapes and contacts with the metal have improved the situation further as will be shown later. One of the advantages of this insulator compared to other known materials is its ease of machining which made its use attractive in this study. Machinable glass ceramic is similar to stainless steel in this regard.

In the light of the above discussed properties of machinable glass ceramic, the decision was made to use this material as the inter-anode

insulator in preference to other established materials used in electron probes. The final design comprised four rods 3 cms in length and 1 cm diameter. The choice of rods rather than the usual single large diameter cylinder was to allow a higher pumping speed between the anodes and the use of less material.

As mentioned previously the metal-insulator and vacuum contact point at the negative side of the electrode is the most important junction (167). Imperfect contact gives rise to field emitted electrons that attack the insulator. Both damage of the insulator end at the negative junction and tracking along its surface have been observed during development. This was finally improved by placing an annealed oxygen-free copper washer at each joint for more perfect contact. To reduce the tracking along the surface even further, the rods were shaped with grooves near the negative end.

Kofoid (167) has found that field emission effects at the negative metal junction can be reduced by placing the insulator in an area of reduced field. This is usually done by placing the insulator in a groove in the metal. In addition, he found that the angle between the metal and insulator plays an important role in the breakdown mechanism and suggests an inclination of about 60^{o} of the metal with respect to insulator as the best arrangement. These points were taken into consideration in the final design. A polished shield cap has been fitted on top of the first anode as can be seen in Figure 8.8 which insures the low value and uniformity of the field around the insulator.

8.4 THE DEFINING APERTURE

The choice of the size of the defining aperture (called henceforth the aperture) in an SEM column is based normally on the smallest possible

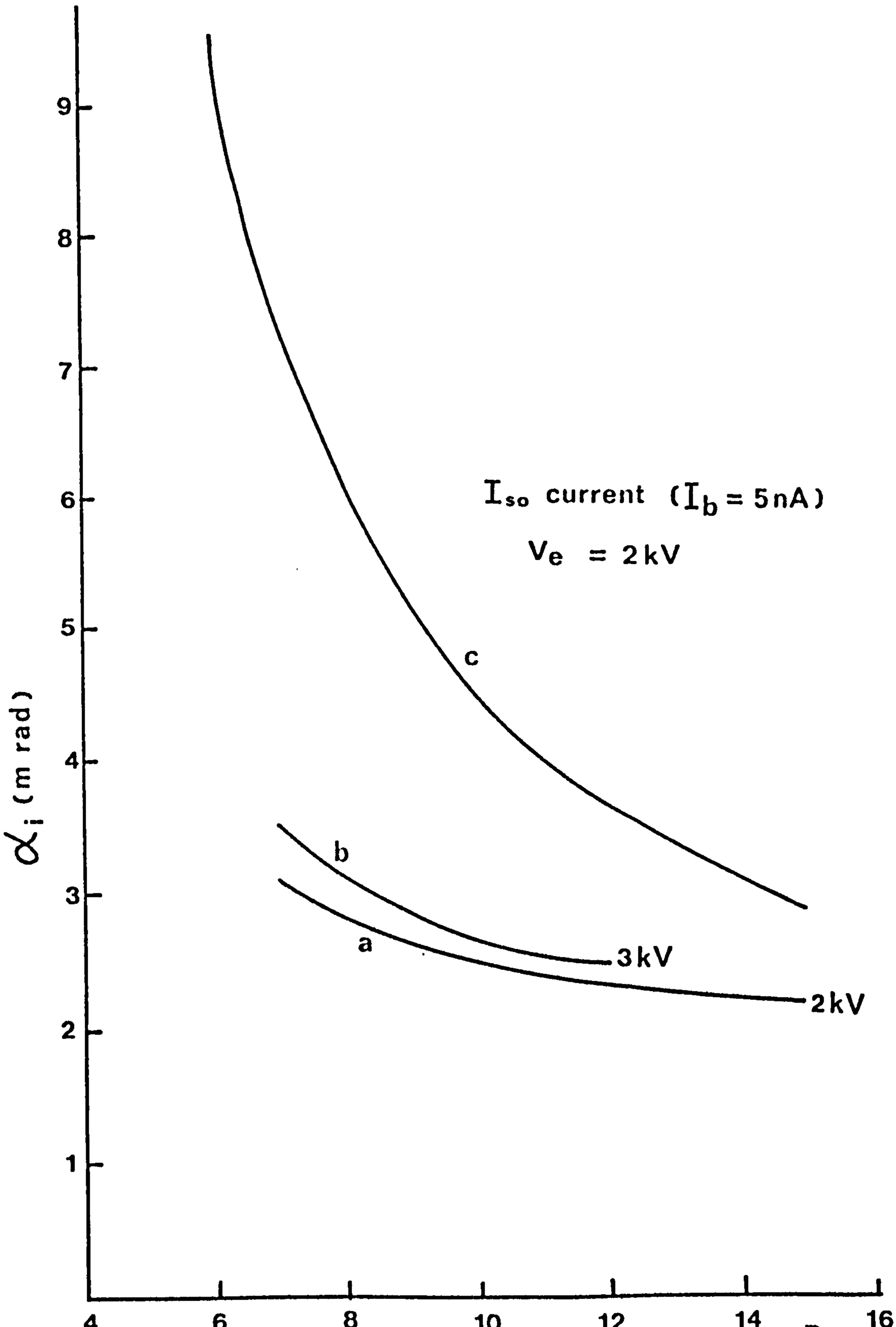

Fig. 8.9 The relation between the image space half angle, α_i as a function of R for (a) V_e = 2 kV, (b) V_e = 3 kV, (c) for a beam current of 5 nA.

spot size. For the present gun, this is controlled by the emitter voltage V_e and the acceleration ratio R. In Figure 8.9 graphs (a) and (b) give the value of the image space half angle α_i (i.e. giving the smallest spot size) as a function of R for two V_e values 2 kV and 3 kV respectively. At R = 12 the optimum aperture is 35 μm in diameter for V_e = 2 kV and is 50 μm for R = 7.

In SAM the requirement of high beam current is equally as important as small spot size, as stated earlier. In Figure 8.9 graph (c) is an iso-current of 5 nA value for a total emission of 100 μA/str and V_e = 2 kV. The required aperture size at R = 7 is 110 μm and is 60 μm in diameter for R = 12. The corresponding change in beam diameter in this case will be from 33 to 60 nm for R = 12 and 7 respectively. For an intermediate value of R = 9 an optimum aperture of 80 μm will result in a spot of about 42 nm. Although a set of different apertures would be advantageous in controlling beam diameter and current, the mechanical drive to incorporate it would be complicated for two reasons. The first is the shape of the vacuum system, while the second is the accuracy with which the aperture should be positioned with respect to the optical axis.

The decision was to choose a near optimum pre-centred aperture with a hole size that allows a beam current of about 5 nA at the smallest usable R value, i.e. 7. The corresponding change in beam diameter for this aperture with respect to R is plotted in Figure 8.10 for two possible emitters, namely cold W(310) and TF Zr/O/W(100). The difference between the two emitters is in the value of the energy spread which contributes to chromatic aberration. Over the possible R values of 7 to 12, the beam diameter in this case would be increased by about 2.5X with a corresponding increase in current by a factor of X4.

Theoretically, the aperture can be placed anywhere along the path of the electron beam. Crewe et al. (72) have found it suitable to place it at

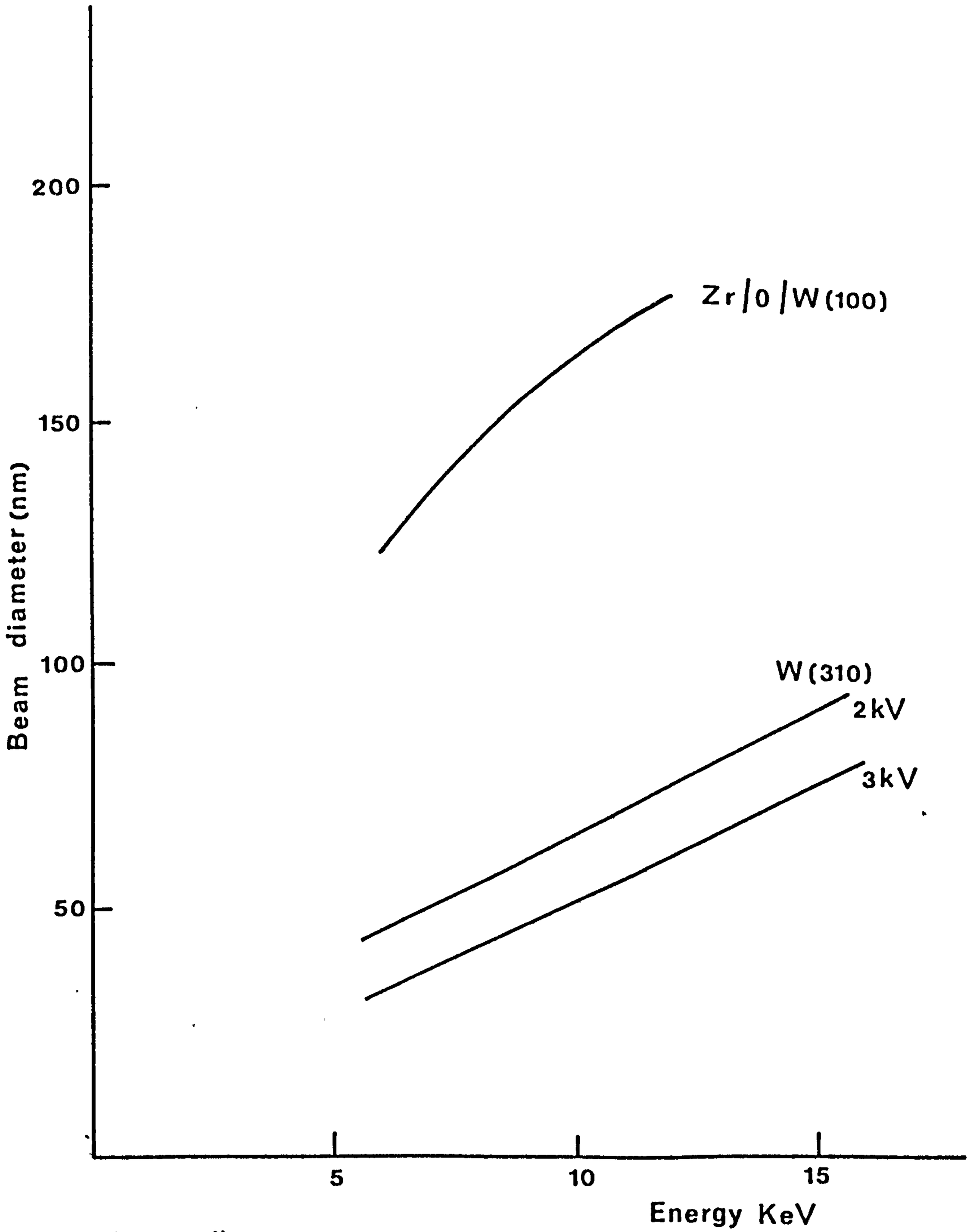

Fig. 8.10 The change in probe diameter with respect to R for an aperture of 75 μm radius placed at the first anode in the case of W(310) (a,b) and Zr/O/W(310) (c) field emitters.
($\alpha_i \approx 7 \times 10^{-4}$ rad.)

the back of the second anode. In the preliminary design, a similar arrangement was adopted. However, in order to improve the stability of the electron emission by reducing ESD from the first anode, its aperture was enlarged to 3 mm in diameter. This was based on the computer analysis of the lens which showed less than a five percent increase in aberration coefficient with the large aperture. This arrangement created an interesting problem. For R = 10, the first anode aperture subtends an angle of 1.25×10^{-1} radians at the emitter, allowing a sizable fraction of the emitted electrons to pass through and impinge on the second anode. As a result of this process, some of the secondary electrons generated at the second anode reach the high voltage insulator and cause a slow build-up of charge. After operation of about 20 - 40 minutes, depending on I_e, a voltage breakdown occurs with the subsequent destruction of the emitter. This has been observed several times with a damaged field emitter used in the thermal mode. The solution of this problem was to move the aperture to the first anode, hence reducing the number of electrons impinging on the second anode. Janssen and Venables (109) and Craven (168) have detected a halo of low intensity electrons that extended to about 5 μm around the electron beam spot and identified it to be secondaries generated at the first anode. They reduced this effect to an undetectable level by placing a smaller aperture at the first anode.

In the first design, 100 μm Molybdenum apertures, 3 mm outer diameter (Agar Aids) were used. The aperture was placed in a holder by a push fit mechanism and held in position by a stainless steel split ring. The centre of the aperture could be positioned on the optical axis of the gun with an accuracy of about 10 μm, as will be described later.

Because of the breakdown problems discussed above caused by the aperture being at the second anode, a different aperture both in size and dimension had to be used in the final design. This was made in the depart-

mental workshop from Molybdenum foil of 200 μm thickness, and 4.0 cms in outer diameter. The hole was spark-eroded. Several apertures of different sizes had to be made and the best rounded hole, 150 μm diameter was selected by examination under an optical microscope. This hole size will shift the optimum operating condition to R = 8. The aperture is held in place between two split inconel rings, which is necessary for two reasons. First since the aperture is a near push fit, this can lead to gas being trapped between it and the first anode. This is poor UHV practice and also may lead to a gas discharge. Secondly, since the aperture will be under constant electron bombardment during operation, a thorough out-gassing will be necessary. This method of support and the 200 μm thickness of the aperture provided good thermal isolation for the aperture, allowing it to reach much higher temperatures during the out-gassing operation. In an auxiliary vacuum chamber, a temperature in excess of 700^{o} C was obtained using a similar arrangement.

8.5 THE CONSTRUCTION AND ASSEMBLY OF THE GUN

8.5.1 Estimates of Accuracy In Construction

Imperfections in machining and assembling of the various parts of the gun can often lead to deviation from the ideal situation with regard to probe size and current. These are usually in the form of misalignment of the axes of the anodes called eccentricity, the misorientation or tilt of one of the anodes with respect to each other, ellipticity and corrugation of the anodes' apertures. Figure 8.11 is a schematic illustrating these faults. Ellipticity and corrugation of the anode apertures cause astigmatism, and eccentricity and tilt cause both coma and astigmatism. With the aid of a stigmator, small values of astigmatism can be corrected,

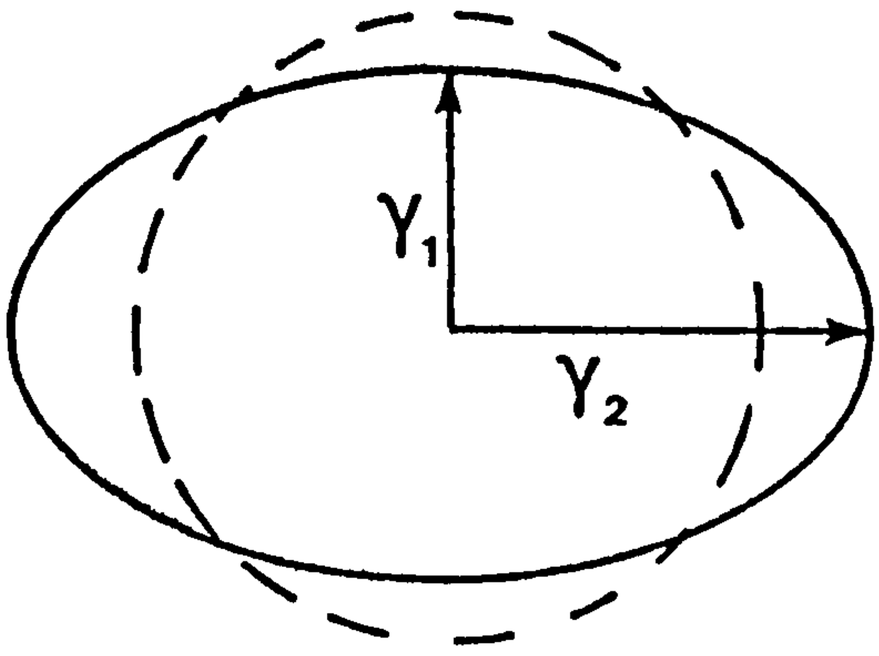

$\delta_{ell} = \gamma_2 - \gamma_1$

a Ellipticity

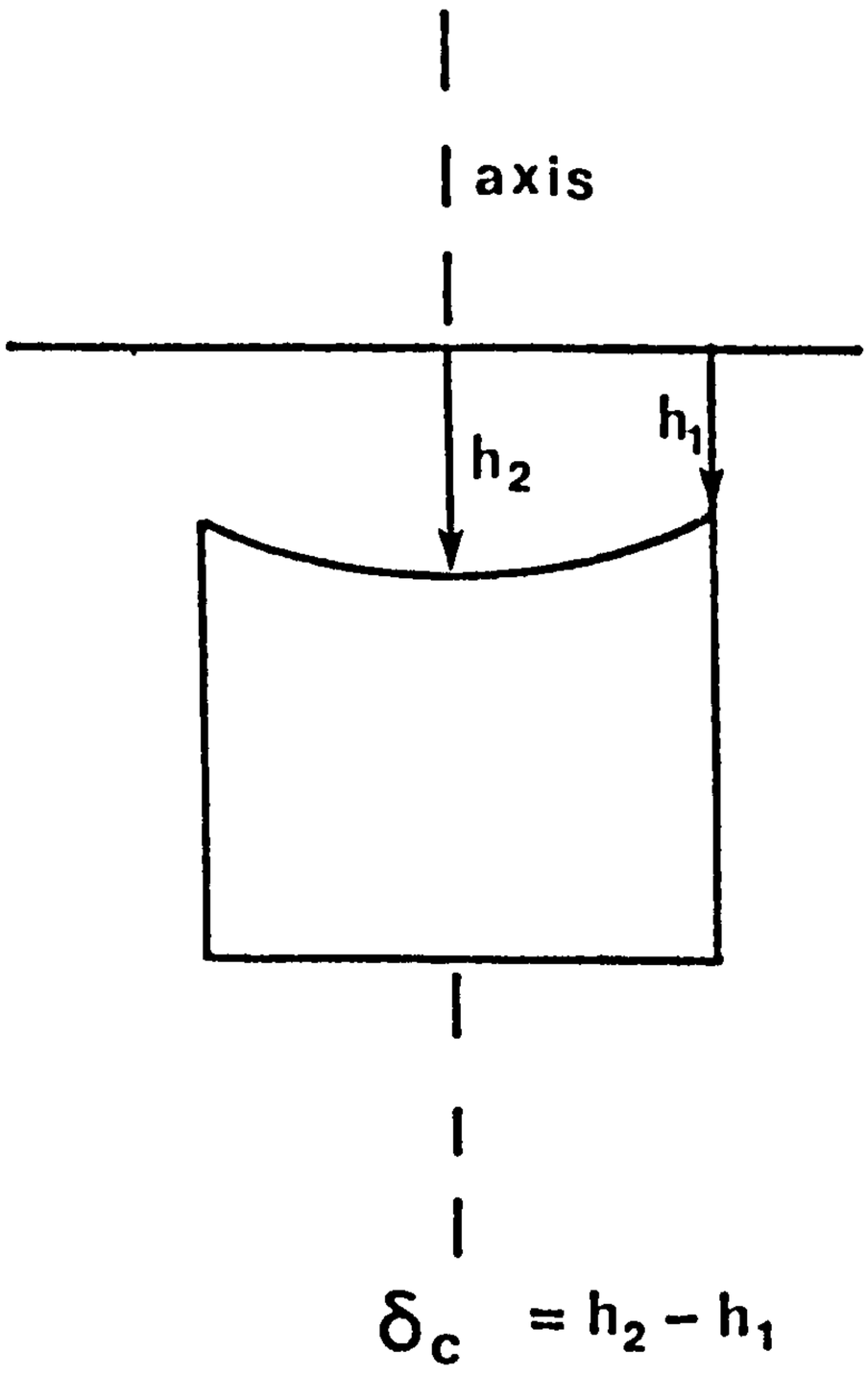

$\delta_c = h_2 - h_1$

b Corrugation

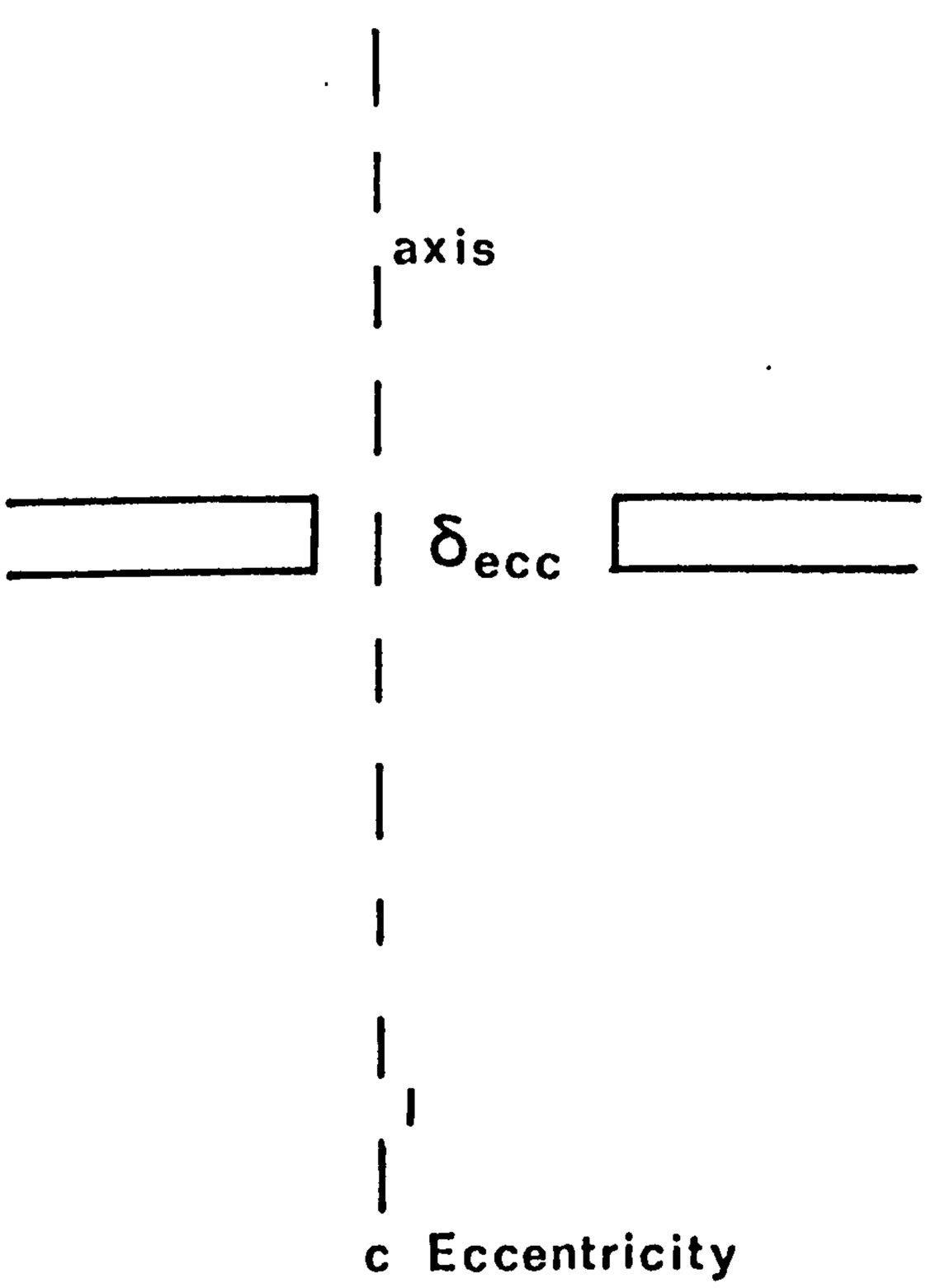

c Eccentricity

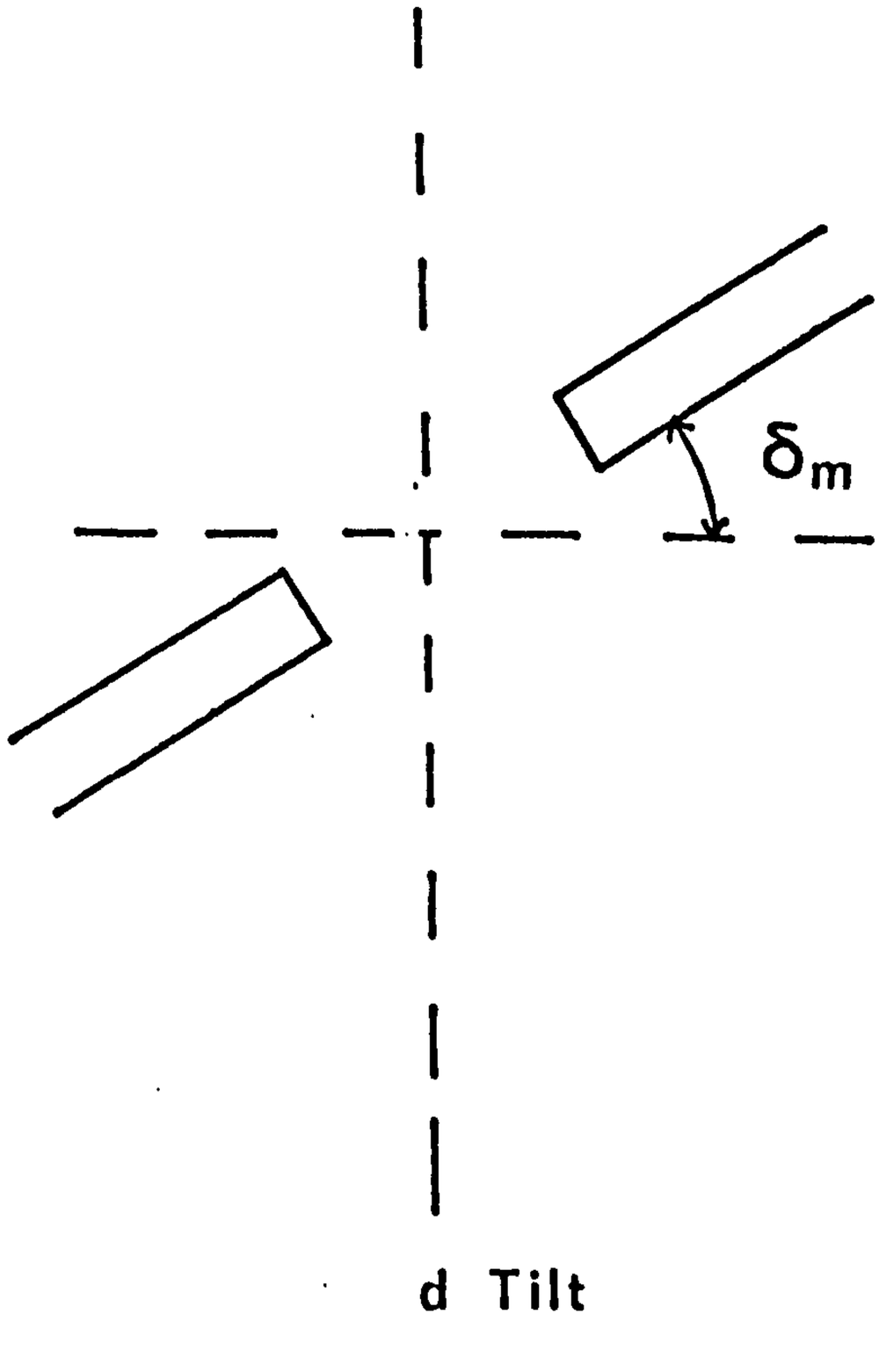

d Tilt

Fig. 8.11 The definition of (a) Ellepticity, (b) Corrugation, (c) Eccentricity, (d) Tilt.

while coma can not be corrected. Therefore the limits within which the tolerances in construction and assembly will not grossly deviate from the calculations should be set.

The effects of these faults on electron lens characteristics have been studied, in the general case, by Bertein (169) for the electrostatic lens, and by Sturrock (170) for the magnetic lens. Bertein calculates the effect of a displacement $\delta_i (i = x,y)$ of one of the electrodes by assuming that an axial ray would pass through the strongest part of the lens a distance δ_i from the centre in one plane and through the centre in a perpendicular plane. For a lens of focal length f, the spot size will be increased by an astigmatic term of the order of $C_{Si} \frac{\delta_i^2}{f} \alpha_i$. In addition, the circles of least confusion on the gaussian plane due to spherical aberration will be separated by $C_{Si} \frac{\delta_i^2}{f}$. Thus, the spot size will not be increased providing that $\frac{\delta_i}{f} << \alpha_i$ (i.e. $\frac{\delta_i}{f}$ << aperture radius). A similar argument would apply for a tilt of δ_α by one of the electrodes. For ellipticity of the electrode, an astigmatic length $Z_a \sim \delta_{ell}$ will be introduced by assuming that the ellipticity of the electrode $(\delta_{ell}/(r_{max} + r_{min}))$ is the same as that of the field at the centre.

Craven (168) has compared estimates of the accuracy in the construction of electrostatic lenses for the case of magnetic lenses treated by Archard (171) under similar conditions (i.e. the focus is formed just inside the lens field when the focal lengths of the projector and objective start to differ). The obtained results were applied to the two element lens used with an optimum aperture. He found that in order to obtain the theoretical beam diameter (of the order of 10 nm in his case) the tolerances for the eccentricity and tilt ought to be about 8 μm and 2×10^{-4} radians respectively. However, values of the order of 40 - 60 μm for the former or about $1 - 4 \times 10^{-3}$ radians for the latter would increase the beam diameter by about 100%. These estimates do not take into account the

contribution of chromatic aberration and Craven suggests a factor of X2 to be added in his case. Recently, Kuroda et al. (172) have estimated using numerical methods the effect of eccentricity for the two and three element electrostatic lenses. Their results agree well with those by Craven. For an optimum aperture they found that a displacement of the anodes by <100 μm will be acceptable in the two element lens. In particular, for R = 11, a 10 μm displacement will add <1% to the spot diameter and 50 μm will add about 20%. For a lower value of R = 8, a 10 μm displacement will add even less than 0.5% to spot diameter. More stringent conditions have been found in the three element case, particularly between the first and second electrodes. Based on Craven estimates, if a system is operated in the chromatic aberration condition, as with TF emitters, a higher value could be tolerated.

For ellipticity and corrugation, Craven has found that a 0.5 μm disturbance does not give any increase in spot diameter and argues that even a higher value can be accepted on the assumption that this will introduce only astigmatism which can be corrected with a stigmator.

The angular and spatial alignment of the emitter with respect to the optical axis of the gun have also been estimated by Craven for different focussing ratios R between 4.5 - 13. For negligible contribution to the spot diameter, the emitter should be placed on the optical axis to within 29 and 7 μm for focussing ratio between 4.5 - 13. The angular alignment of the emitter for negligible contribution should be within 10^{-2} rad of the optical axis, provided the emitter is spatially aligned. These figures were based on the results of Wiesner and Everhart (126) who found that the virtual spot size contribution is $< 5000\ \alpha_o$ MÅ.

The emitters used in this study have been supplied by FEI Corporation McMinville, Oregon, U.S.A.. They are usually spot welded to a hair pin and are perpendicular to the mounting ceramic disc with an accuracy of about 10^{-3} rad.

8.5.2 The Construction and Assembly of the Anodes

To achieve the accuracy estimated above, stringent machining accuracy was required. This was in the range ± 2.5 µm which is the accuracy of the machining tools in the Departmental workshop. Figure 8.12 shows a photograph of the assembled anodes. A circular plate 98 mm in diameter and 4 mm thickness is used as the second anode. Six 8 mm pumping holes were drilled on a Pitch Circle Diameter (PCD) of 7 4 mm. The plate has a 3 cm hole in the centre in which the second anode aperture holder is located. On the inner side facing the first anode, four recesses 12 mm in diameter and 1 mm in depth are machined for locating the high voltage ceramic insulators. On the other side tapped holes for locating the aperture holder and the stigmator assembly were made. A cross-sectional diagram of the first anode is shown in Figure 8.13. The simple geometry of the first anode relaxes the condition of both ellipticity and corrugation in comparison with the shape used by Crewe et al. (72). No checks were made of the final design for these two faults. Four similar recesses to those in the second anode were machined on the inner side. The annealed oxygen-free copper washers were first placed in the recess and the ceramic insulators were then located on them. The latter is held in place via a 3 mm diameter stainless steel bolt. Although it is possible to argue that the use of stainless steel bolts directly in contact with the ceramic will negate the action of the washers this is not entirely correct. In this particular application, it is the end of the bolts inside the ceramic that gives rise to field electron emission. This is supported by inspection of the inside of the tapped ceramic which has revealed signs of damage. However, as this is inside the ceramic, its effects should be minimal compared to damage caused in the absence of a washer. Possibly the damage in this region can be reduced by using a soft material (or ceramic paste) that would improve contact between the stainless steel bolt and the ceramic.

Fig. 8.12 The assembled anodes.

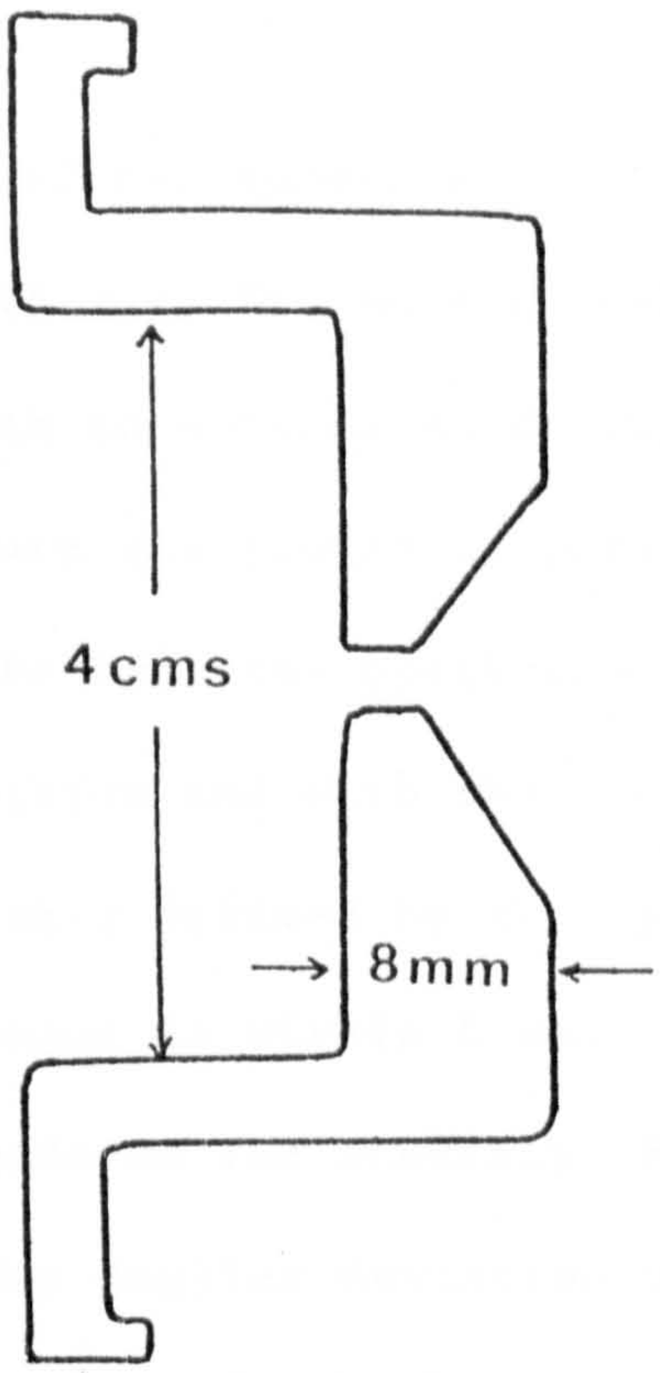

Fig. 8.13 Cross-sectional diagram of the first anode.

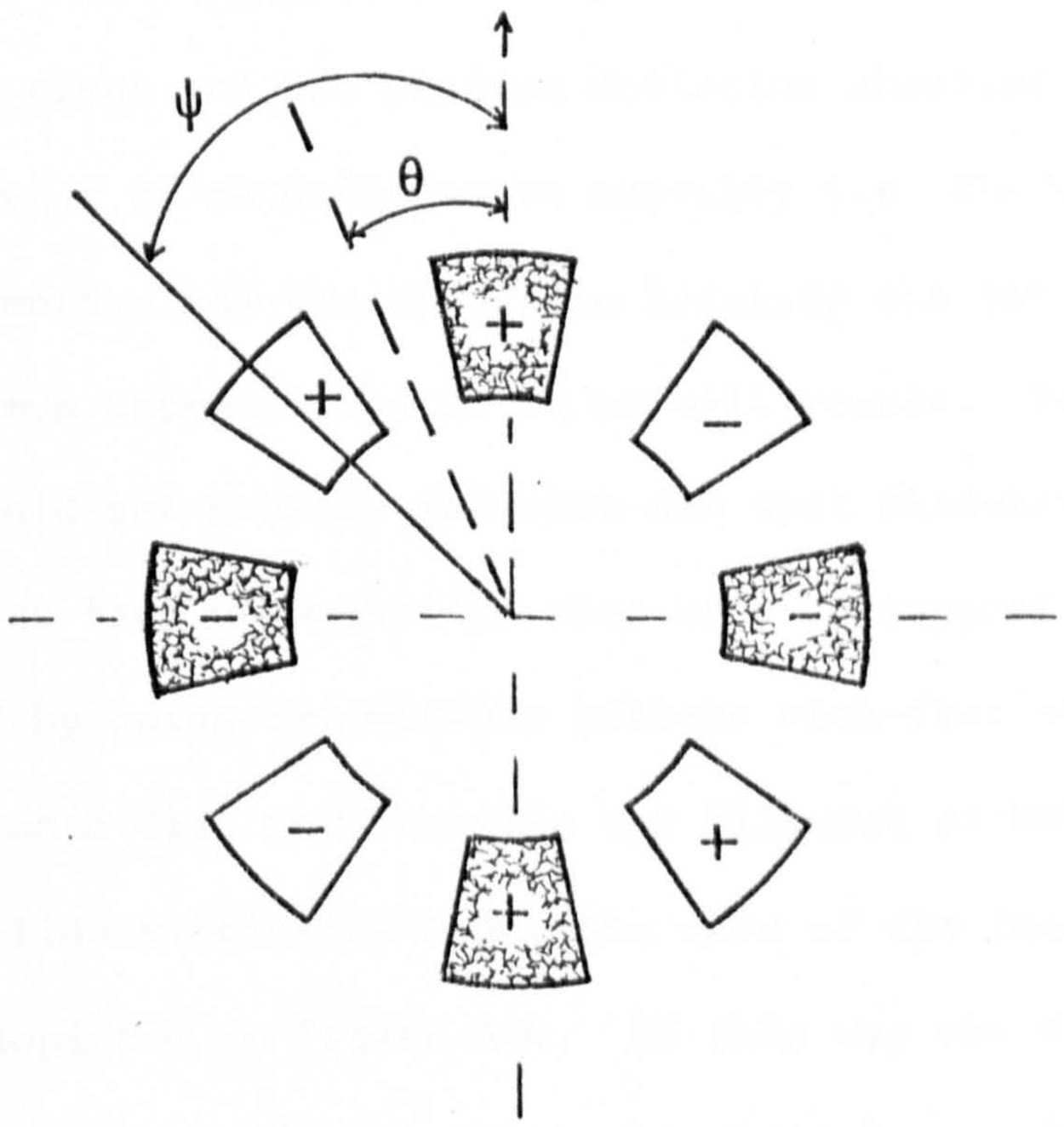

Fig. 8.14 Schematic of the Octopole stigmator/deflector.

The final alignment of the anodes was achieved with the aid of a precision milling machine (Aciera F1, Aciera fabrique de machines, Le Locle, Suisse) equipped with an optical microscope of magnification X 100. Firstly the defining aperture was placed in position at the first anode and its centre considered to form the optic axis. The second anode aperture is then placed in position and with the aid of four 12 BA screws is positioned on the optical axis defined by the aperture of the first anode. The accuracy of this alignment is within 5 μm. It should be mentioned that this measurement depends on the accuracy of the vertical motion of the milling machine, and any angular deviation of this will accordingly shift the defined optical axis. To check against any errors introduced in this way, the assembled anodes were rotated through 180^{o} around a vertical axis and the centre of the second anode's aperture noted. This is considered to form the optical axis of the assembled anodes. A de-assembling procedure then follows, and the position of the first anode's centre is checked against the defined optical axis. This experiment was repeated several times and the maximum deviation observed was approximately 10 μm. In the event of an unfortunate assembly i.e. the errors introduced by the vertical motion and the errors in locating the two anodes are additive, a maximum eccentricity of 16 μm will result. From previous discussion this should not grossly increase the spot diameter.

The emitter feed throughs are also used to support the emitter. This is achieved by using two movable pillars with flat stepped ends for locating the ceramic disc that carries the filament assembly. The pillars are allowed to slide vertically along the side of the feedthrough. This arrangement is depicted in Figure 8.4. In this way the distance of the emitter from the first anode can change by about 8 mm. This facility is used for different emitter lengths as well as changing the focussing ratio. Split copper cylinders are attached to the pillars and are used for making

the contact with the emitter pins.

The degassing filament for the first anode is mounted on a cylinder that is placed around the emitter. The filament is made of 150 μm tungsten wire and can be at either emitter of first anode potential during operation. The cylinder carrying this filament is mounted on the emitter manipulator in a push fit mechanism and it serves to keep an equipotential around the emitter.

Normal UHV cleaning procedures have been used. However, in the final assembly, and when replacing an emitter great care is exercised to exclude any dust, or any loosely adsorbed particles from the gun components. A noticable reduction in vacuum discharges has been obtained in this way.

8.6 THE STIGMATOR AND SCAN SYSTEM

8.6.1 The Stigmator

Electrostatic and magnetic stigmators have been used for the correction of ellipticity astigmatism. The ease in the construction of magnetic stigmators and its electronics has favoured their use with the rapid development of magnetic electron lenses. However, in UHV systems, with a requirement for baking, magnetic stigmators are a disadvantage. In addition, for the present instrument with a high energy resolution spectrometer, the residual magnetic fields are likely to degrade the performance of the analyser. Such difficulties have favoured the use of an electrostatic type.

In its simplest forms the stigmator consists of four plates at right angles to each other with opposite pairs having the same potential. Such a system can be considered as a "weak" quadrupole lens. Since the

line foci of this simple system are not always parallel to those produced by the astigmatism of the lens, correct orientation of the stigmator will be necessary. Haine (173) has allowed for mechanical adjustment in his system. However, by adding a second quadrupole rotated by Ψ with respect to the first, Rang (160) was able to control both direction and amount of compensating astigmatism independently.

The idea of the system is to produce two astigmatic components A and B at right angles to each other and that can rotate in a plane normal to the electron path. A and B act to cancel the lens astigmatism by elongating the electron spot in one direction and contracting it in another. The rotation of the correcting fields is achieved by connecting the two quadrupoles to the output of a sine - cosine potentiometer which has a voltage of the form

$$V_A = \frac{V}{\sin 2\Psi} \sin 2\,(\Psi - \theta)$$

$$V_B = \frac{V}{\sin 2\Psi} \sin 2\,\theta \qquad (8.1)$$

where Ψ and θ are as defined in Figure 8.14. Rang has arranged the voltages on the plates to be obtained via a mechanical system that controls both its magnitude and sign. The latter is set to be 90^{o} out of phase for neighbouring plates.

Bertein (158) has suggested a different configuration system consisting of six elements, with an applied potential of the form

$$V_k = V \cos\,(\theta - 2\frac{k\pi}{3}) \qquad (8.2)$$

where k is the number of the elements (from 0 to 5). The resulting astigmatism is proportional to V and one of the line foci makes an angle $\frac{\theta}{2}$ with respect to the zeroth element.

A preliminary test system based on the Bertein idea was built for use with the first instrument. A photograph of this system is shown in

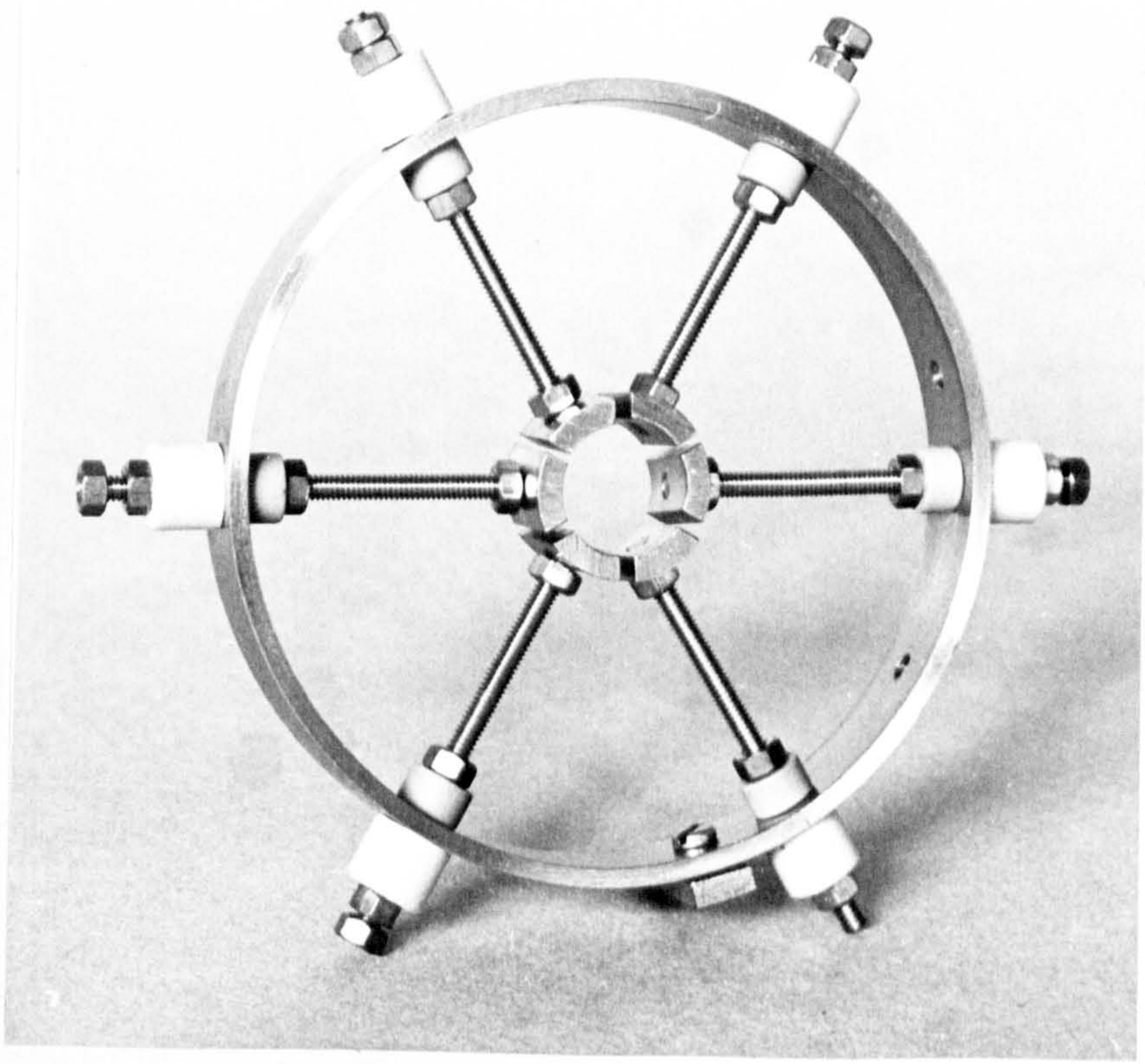

Fig. 8.15 Photograph of the Hexpole stigmator/deflector.

Fig. 8.16 Photograph of the Octopole stigmator/deflector.

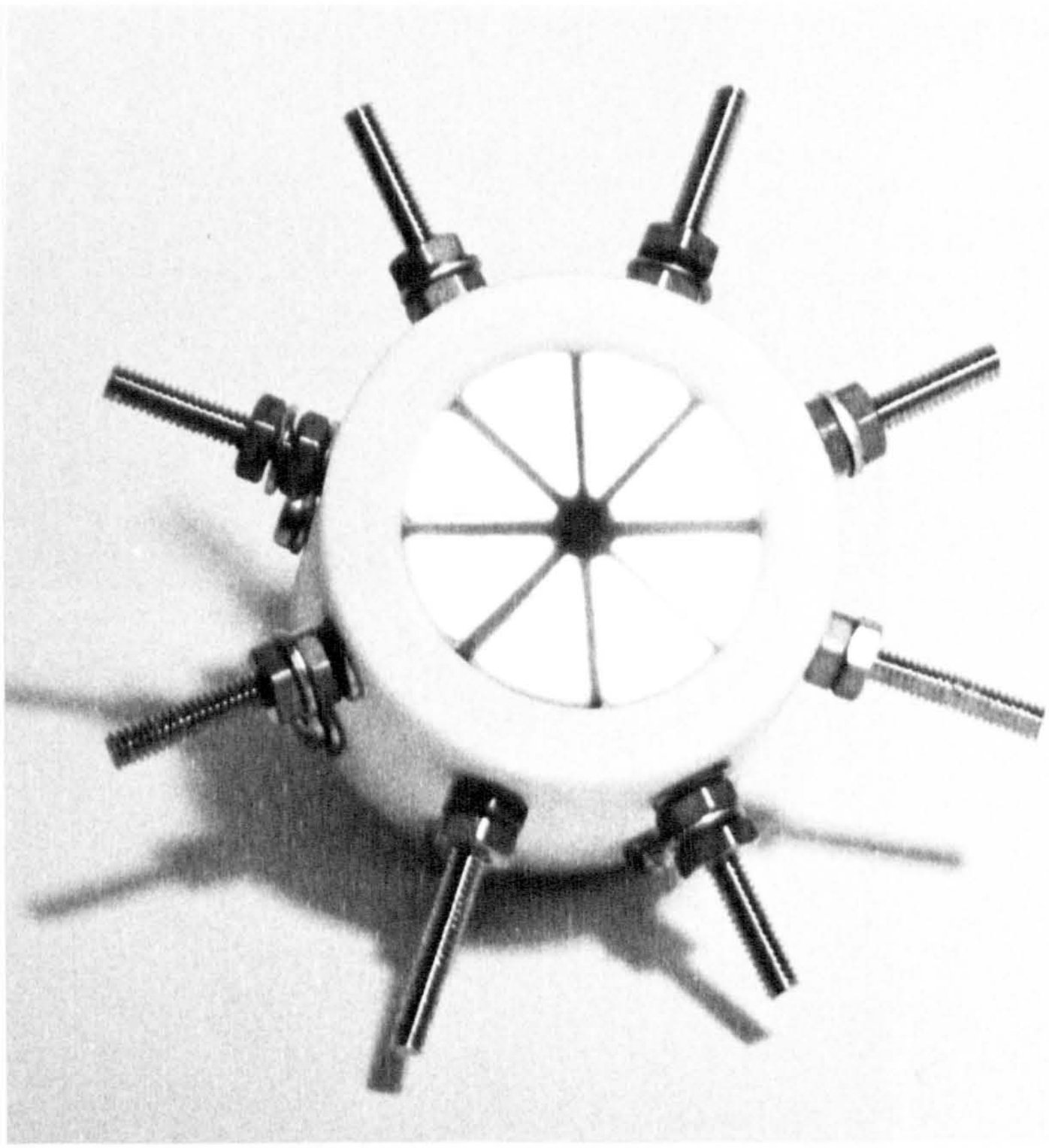

Figure 8.15. The plates were arranged at 5 mm from the axis and were 1 cm in length. The system was comparable in performance with an eight pole magnetic stigmator, which was part of the first instrument. Potentials of up to 20 - 25 volts were the maximum needed for the correction of astigmatism of few μm in length which compares favourably with Bertein's prediction of 100 volts for the correction of a 10 μm astigmatism.

The final design is based on the octopole system described above and was chosen due to its symmetry when used as a deflector as well. Figure 8.16 shows the assembled system which consists of 8 immac 5 stainless steel plates, 2 cms in length arranged at 1.5 mm from the axis and held together via a machinable glass ceramic cylinder. The ceramic cylinder is also used for isolating the plates from the mounting stainless steel cylinder at the back of the second anode. Fibre glass covered copper wires are used for the electrical connection to the elements. The wires are enclosed in an earthed copper shielding and are brought to a standard eight pin Varian feedthrough at the vacuum wall.

The voltage requirements of this system are much less than the six element test system due to the closer distance with respect to the axis, and amount to a few volts only, taken from the scan power supply via a resistor chain. The controls consist of two potentiometers connected to the power supply for magnitude and angle of the correcting field. One of the two quadrupoles is connected to the "sine" output of a sine-cosine potentiometer and the other, which is displaced through 45^{o}, depends on the "cosine" output. A linear potentiometer controls the magnitude of the correcting voltage. A multi-core double coaxial cable connects the feedthrough to the power supply via an eight pin plug (Amphenol Ltd.). The circuit diagram of the stigmator supply is shown in Figure 8.18 as a part of the scanning system.

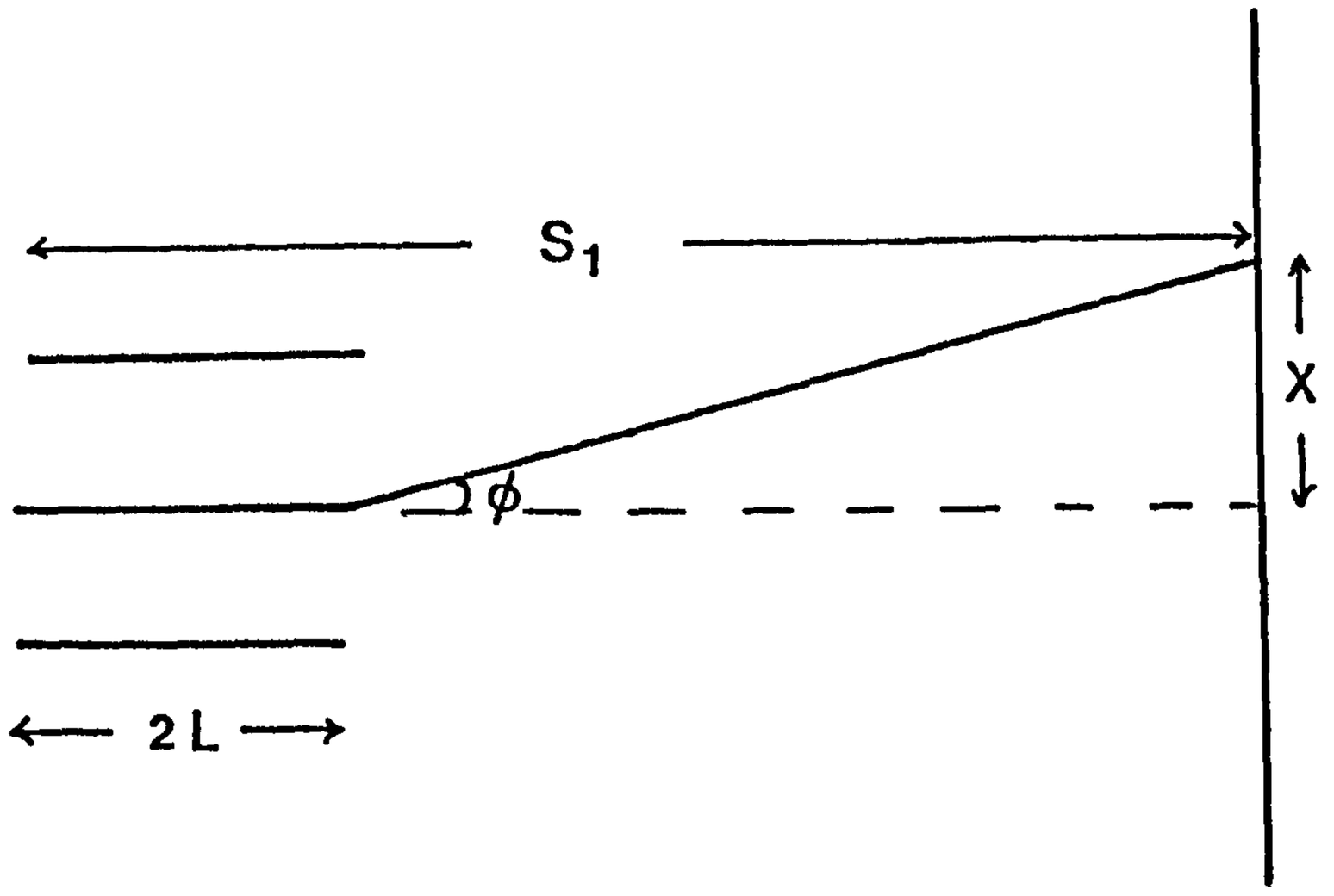

Fig. 8.17 The definition of the deflection angle Ø.

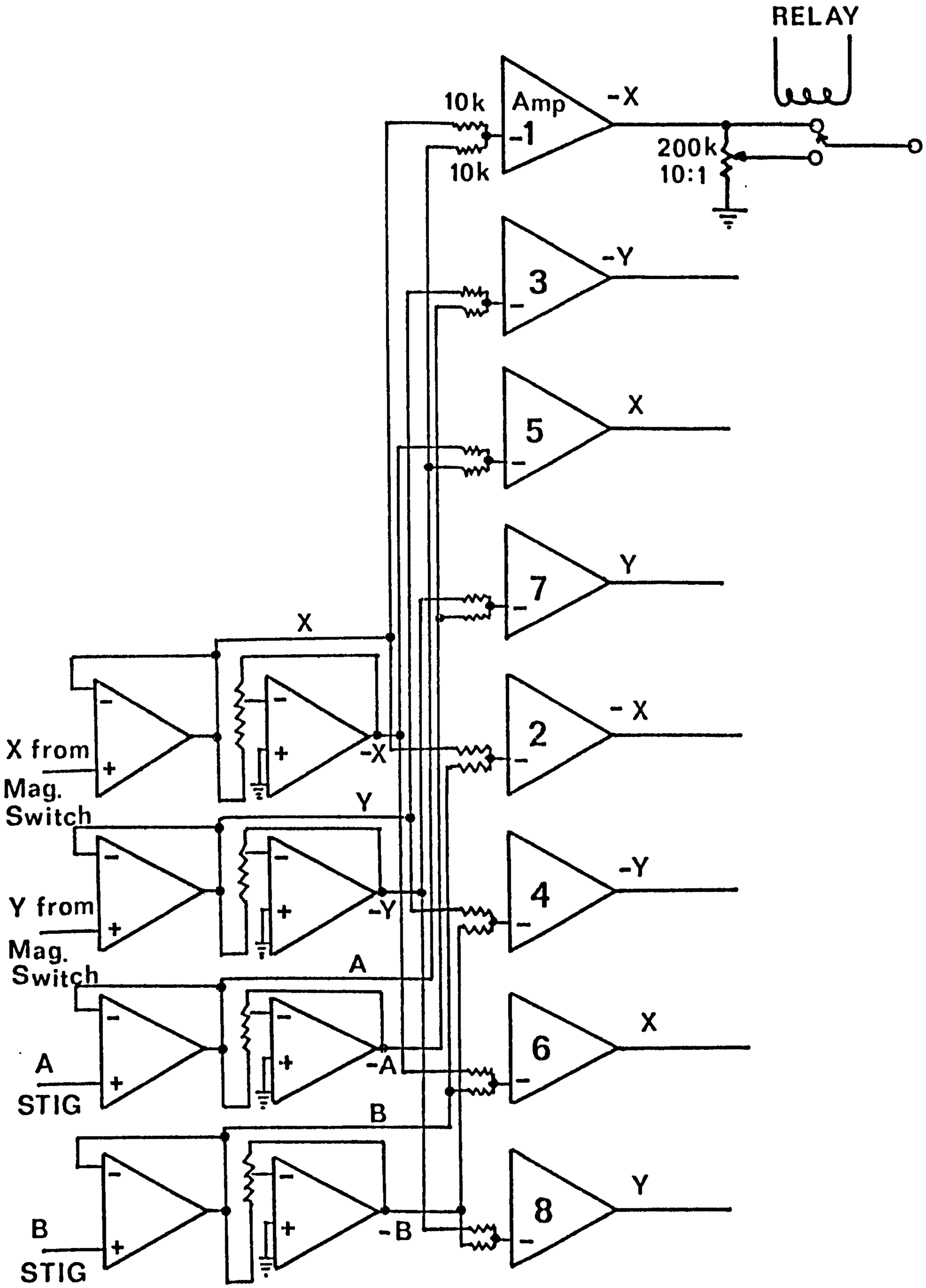

Fig. 8.18 Circuit diagram of the scan generator power supply.

8.6.2 The Scanning System

For high resolution (i.e. high magnification) microscopy, the electron beam would need to be deflected through small angles about the centre of the deflection system. A large field of view (i.e. scanning larger areas) is important for two reasons. The first is to aid the operator in searching for interesting features on the sample, and secondly to simplify calibration of the magnification. The deflection angle ϕ is defined in Figure 8.17 and is given by

$$\phi = \frac{X}{S_1 - L} \tag{8.3}$$

where $2X$ is the width of the scanned line, S_1 is the working distance and $2L$ is the length of the deflection plates.

Both magnetic and electrostatic systems have been used in the SEM, with the former being the most widely used for the same reasons as magnetic stigmators. For the magnetic system, the relation between the number of turns n and current i of the deflecting coil for a deflection angle ϕ in radians of a beam voltage V_i, is given by (85)

$$\phi = 0.75\ ni\ V_i^{-\frac{1}{2}} \tag{8.4}$$

In the electrostatic system, if voltages $\pm V$ are applied to parallel plates of length $2L$ and separation $2y$, the angular deflection ϕ in radians for a beam voltage V_i is given by (85)

$$\phi = \frac{L\,V}{Y\,V_i} \tag{8.5}$$

The octopole stigmator described above can also be used as a scanning system, if one considers each opposite four plates as a pair of parallel plates. In this case, the deflecting voltages will be superimposed on the astigmatism correcting voltages. A field of view of about 3 mm was chosen at beam energy of 30 kV. The required voltages for this condition are

about ± 130 volts. Figure 8.18 shows the circuit diagram for the scan generator power supply used. It consists of 8 amplifiers fed from the ± 130 volts rails from a standard 130 volts power supply unit. A front panel multipole switch is connected to a resistor chain for defining the required voltages at a certain magnification, and the same cable used for the stigmator is used also for scanning. The magnification ranges from X 50 to X 250 k in ten steps. A residual AC component of about 2 mv was detected at the output. This will amount to degredation of about 3 - 4 nm in the resolution.

8.7 THE SEM DETECTOR

Several secondary electron detector schemes have been reported in the literature (e.g. Channel multipliers, Hughes (174), Griffithet al (175); solid-state detectors at positive potential, Gonzales (176) and Crewe et al. (72); scintillator-photomultiplier systems, Everhart and Thornley (177)). The first instrument incorporated a similar arrangement described in section 3.2.3, to that described by Everhart and Thornley. This system was satisfactorily used for displaying images at TV rates with a beam current of the order of 2 - 5 x 10^{-10} A. It was decided to use this arrangement again in the new instrument for the following reasons. It gives a better signal to noise ratio in comparison with the above schemes at low beam currents (41). Several photomultipliers similar to the one used were in use in the Department and therefore replacements were easily available within the Department in case of failure as well as for routine tests. Finally, the scintillator consists of a (P1 type) phosphor screen, 4 cms in diameter with a 3 mm metal film on the edge for electrical contact. The author has made several of these screens.

The scintillator screen was made of pyrex glass in comparison with

the widely used plastic (177) for two reasons. Firstly, it can withstand the bake-out temperature of the instrument and secondly the degradation rate is negligible compared with the plastic (178). The disadvantage of glass is that its luminous efficiency is about half that for the plastic. However, this can be compensated for in part by increasing the scintillator voltage. The latter has a maximum value of 12 kV.

An 80% transparent metal grid in front of the scintillator having a variable voltage in the range −100 to +200 volts provides a collection field for either the secondary or backscattered electrons emitted by the specimen. The output of the detector is used directly to form an analog SEM image, or to be routed to a 0.0 - 1 M Hz voltage controlled oscillator (described in Chapter 3) to provide a count proportional to the total secondary electron yield. This is used to form a digital SEM image and normalisation of spectra against beam current fluctuations. With the new scanning system described above, the fastest display time per frame is about ¼ sec.

8.8 THE SPECIMEN STAGE

The specimen manipulator is a purpose built UHV manipulator designed by P.V. Head of the Cavendish Laboratory, Cambridge, and built in the Departmental main workshops at York. The design is indicated in Figure 8.19. Three orthogonal translations of the specimen are provided by bevel and slide motions. The vertical translation is provided by a rotary motion operating a vertical lead screw providing ± 50 mm. Linear motions provide translation in the horizontal plane of about ± 8 mm. The sample can be rotated about the vertical axis to control the angle of incidence of the electron beam or to rotate the sample for different experiments (e.g. standard AES from a thermionic 2 kV electron source, ion bombardment, evaporation, etc.). The azimuthal orientation of the sample is provided

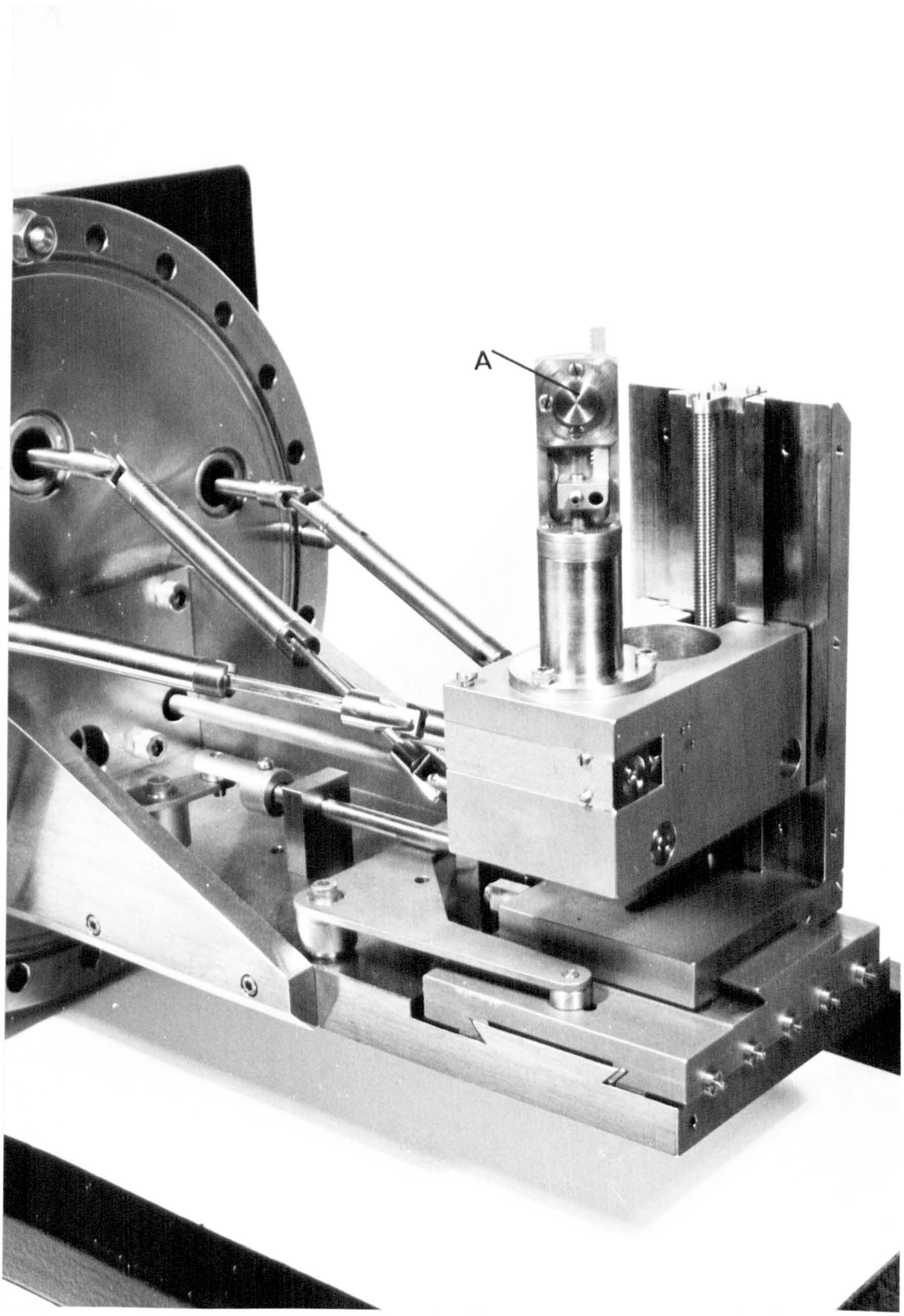

Fig. 8.19 Photograph of the specimen stage.

by a rack and pinion that rotates the sample about its surface normal. Six different specimens can be mounted on a stainless steel holder at the top of the post A in Figure 8.19. The specimens range in size and the largest possible on the present holder is 6 x 8 mm. Provision for heating the sample has also been included. Immac 5 stainless steel and phosphor bronze have been used in the fabrication of the bevels and slides. A thin film of molybdenum disulphide (Dow corning Inc.) is used for the lubrication of the slides and other moving parts of the stage. This material has been proved to be compatible with UHV. The manipulator has been designed to have a stage stability of a few tens of Angstroms. This has not been checked experimentally.

8.9 VIBRATION

To achieve resolution of about 30 - 40 nm, with an electron gun magnification of ~ X 2, the emitter, lens, and specimen must stay fixed relative to each other to better than this value. As a precaution all construction was made as solid as possible to make the natural frequency of vibration high. In addition, the whole apparatus rests on plates supported by car tyre inner tubes for vibration isolation from the floor. Furthermore the electrical connections and cables to the various parts of the apparatus have been arranged to drop vertically downwards to give as little effect on vibration as possible.

8.10 STRAY MAGNETIC FIELDS AND SHIELDING

A.C. and D.C. magnetic fields can be troublesome in high resolution SAM. A large D.C. field would seriously interfere with the analysis of low energy electrons by the spectrometer, whereas stray A.C. fields would

degrade the microscope resolution. Large Helmholz coils were built to surround the instrument and cancel the Earth's magnetic field in the vicinity of the electron gun and spectrometer. The large size of the coils is only to provide convenient access to the instrument. The ion pump is enclosed in a 6 mm thick mild steel case to reduce the residual field due to the ion pump magnet. In addition, care was taken to degauss all the bolts and the nuts as well as tools used in assembling the column and specimen.

The A.C. fields are more difficult to identify and to reduce to a tolerable level. Magnetic fields of the order of 5×10^{-8} Tesla will deflect 30 keV electrons 1 μm approximately in a distance of 8 cm.

In order to reduce the effect of A.C. fields, considerable care was taken to shield the instrument through the provision of mu-metal shields. The specimen chamber was provided with a 2 mm thick mu-metal inner shield manufactured by Telcon Ltd.. The spectrometer was also enclosed in a second shield within the vacuum chamber. The windows, manipulator and the top of the specimen chamber which have several ports were each fitted with external removable mu-metal shields.

In the original design, the gun chamber was designed to have an inner and an outer shield. It was intended that the inner shield would mate with the specimen chamber inner shield. However, the inner gun shield, which consisted of a tube 9 cm in diameter, 25 cm long and end caps to enclose both anodes and the stigmator/scanner system could not be used. Firstly, because it deformed during the annealing process (by Telcon Ltd.) and secondly it had sharp edges which broke down at approximately 15 kV. Several attempts were made to remove the sharp edges without affecting the magnetic properties of the mu-metal. Chemical etching with different acids as well as light mechanical polishing were used. These however were not successful and the shield had to be removed. The outer shield was de-

signed and made in the Departmental workshop and annealed by Telcon Ltd.. The D.C. field on the axis of this shield when mounted was less than 3×10^{-6} Tesla, and a similar figure was obtained at the sample position, giving a shielding factor of about 100. No further attempt was made to shield the rest of the instrument electrical units, e.g. power supplies, CRT, etc. as these were the same as used with the first instrument.

8.11 THE ELECTRON GUN POWER SUPPLY

The analysis of electron lenses in Chapter 7 and the choice of the lens design were influenced by the availability of the power supply unit provided with the first instrument. The unit was supplied by V.G. Microscopes Ltd. and successfully used to produce an electron beam of about 40 nm diameter. Minor modifications to the system have been made at York to allow different emitter modes to be used, namely reverse bias during emitter cleaning and T.F. operation of emitters (see Chapter 6).

Figure 8.20 illustrates the principle of operation of the electron gun, where the 5 kV supply is used to extract electrons from the emitter V_e, and the 30 kV, V_i supply is used to accelerate and focus the electron beam. A block diagram of the supply is shown in Figure 8.21. The dark solid lines illustrate the different supply units, V_e, V_i, and the emitter heater. The latter is a constant voltage supply delivering either pulses or continuous current that is variable from 0.5 - 3.0 A. The pulses are of 2 secs duration. The dashed lines illustrate the isolated parts of the supply. Both the heater and V_e units are isolated to 30 kV. The isolation is achieved by enclosing the units in equipotential metal casings that are held at a potential of $-V_i$ with respect to ground. The metal boxes are enclosed in a perspex box which in turn is supported by 5 cm long perspex rods inside a larger earthed box. The front panel control to this

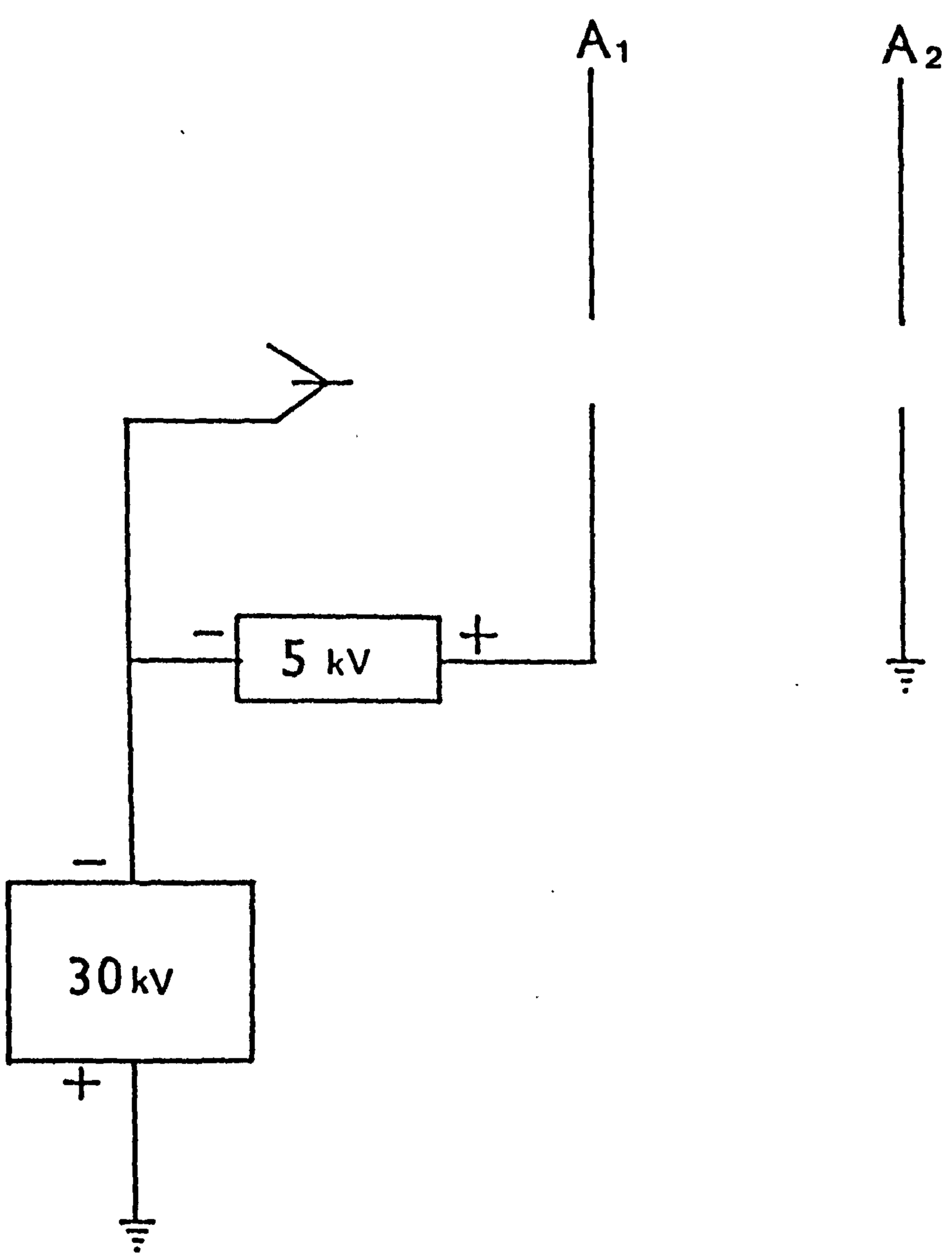

Fig. 8.20 The principle of operation of the electron gun.

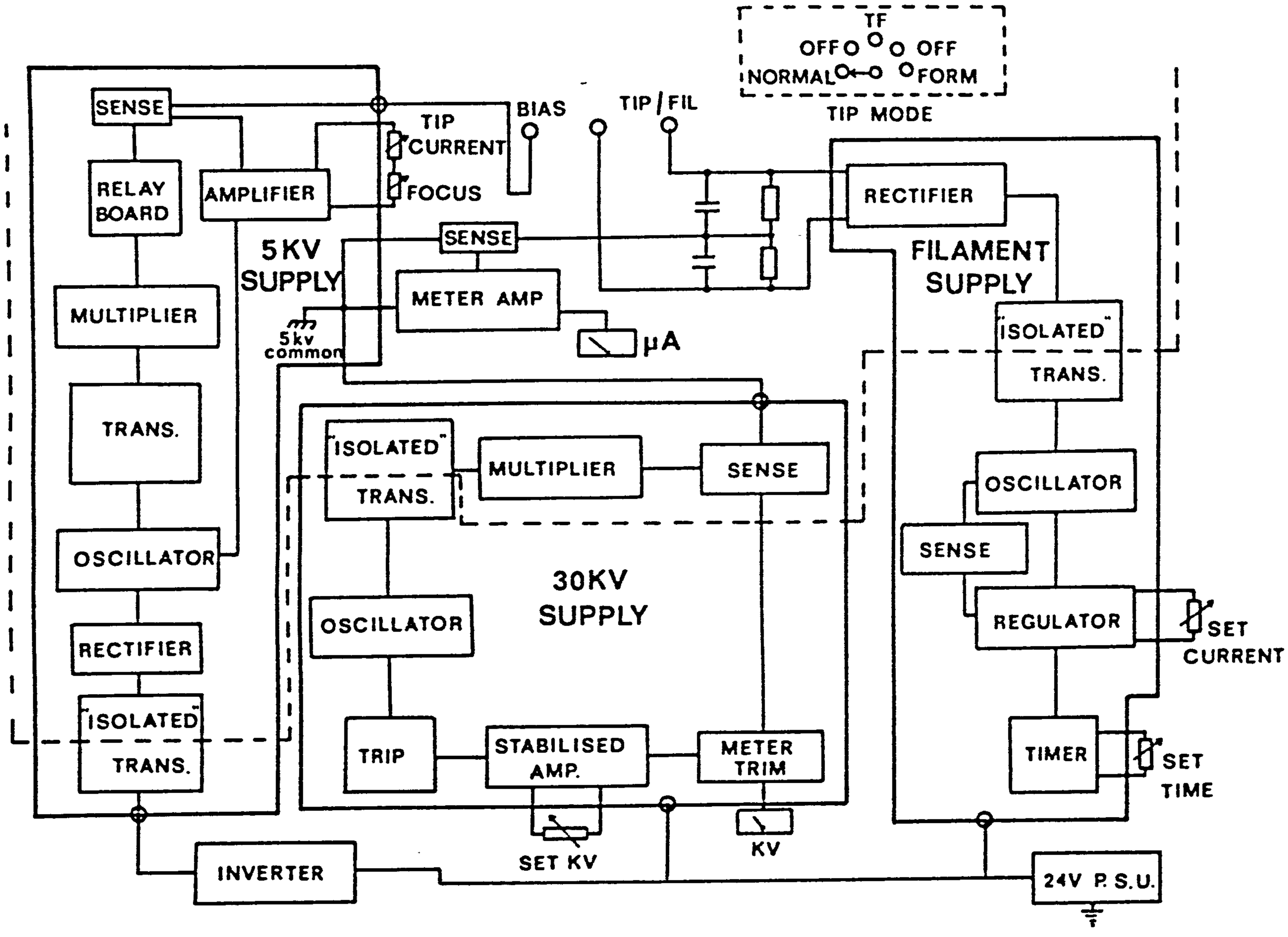

Fig. 8.21 Block diagram of the electron gun power supply.

isolated box being made via 10 cms long perspex rods. The air gap between the earthed box and the high voltage units is used as the insulating medium. The power supply has been tested to a potential of 30 kV in the first instrument without any flashovers.

The requirements of the V_e and V_i supply units with particular reference to stability, drift and ripple on the output should be such that changes in the electron energy at the emitter or either of the two anodes produces negligible shift in the image position. For electrostatic lenses, values of the order of 10^{-4} - 10^{-3} V_i cause little change in image position (179), (i.e. the V_i supply should be capable of being set to better than this value). In addition, the peak to peak ripple and the drift over the period of a photograph should be less than this value. For high quality images i.e. 256 x 256 pixels with 100 m sec dwell time, the collection time can be of the order of 1 - 2 hrs. For the V_e supply, stability, drift and ripples should be less than the energy spread of the emitted electrons. This is because of the contribution to the chromatic aberration, as discussed in Chapter 7. In the case of field emitters operated in the cold mode, values of about 0.2 - 0.3 eV are representative of the energy spread while larger values of about 0.5 - 1.0 eV have been measured in the case of T.F. mode.

The characteristics of the various units of the supply have been quoted by the manufacturer (V.G. Microscopes Ltd.) as follows: for the V_i supply

Output voltage	0.1 - 30.0 kV continuous via 10 turn helipot.
Output current	100 μA
Output voltage polarity	negative
output ripple	1 part in 10^5

The extract supply V_e has the following specification

Output current	100 μA
Output voltage	0.1 - 5 kV
Fine voltage control	80 volts across 3 turn helipot for fine tuning of the focussing via V_e.
Output ripple	6 parts in 10^5

After the modification at York, the following additional facilities are available from the V_e unit,

T.F. operation	0.5 - 3.0 Amp at 5 kV
Output current	300 μA
Output voltage	0.1 - 5.0 kV in either polarity.

Recent tests of these supplies have shown a deterioration in terms of output ripple. In particular, the V_i supply has shown a 3.5 volts p-p, 100 Hz ripple that is locked to the mains, in addition to a different ripple of ~103 Hz that is out of phase with the first and of a lesser p-p, value of ~2 volts approximately. This value is higher than the manufacturer's specification. However, for electrostatic lenses the p-p ripple and drift of the high voltage supply can be as high as one part in a thousand (125).

The V_e supply on the other hand has been under constant repair for the last two years. In particular, the isolated transformer had proved to be the most deficient part in this unit. The p-p ripple and drift of this supply are within the limits specified earlier, and are much less than the energy spread of the emitted electrons.

Due to the age of this unit and its faults, it was decided to use it in its present form and eventually to design a new power supply which includes the modifications added in York.

CHAPTER 9

THE PERFORMANCE OF THE INSTRUMENT

9.1 INTRODUCTION

This chapter is concerned with the evaluation of the various parts of the instrument. These are, the vacuum system, the field electron emitters used with respect to stability and beam current, the electron optical characteristics of the column and finally the use of the instrument for the production of Auger point analysis, Auger line scanning and Auger imaging.

9.2 THE VACUUM SYSTEM

It was stated in Chapter 8 that a base pressure of about 2×10^{-10} torr at both the emitter and specimen regions is an essential condition for the operation of the instrument. The first is due to the use of a field emitter as the electron source. It was shown in Chapter 6 that emission instability of more than 10% is obtained as a result of operating the emitter at a pressure of higher than 5×10^{-10} torr. The second is concerned with the specimen cleanliness (see Chapter 3).

In the present geometry, it is difficult to measure the pressure directly at the emitter region because of the high voltages used and the conditions for the gun components (see discussion in Chapter 8). Instead two precautions were taken to ensure an accurate measurement of the pressure in this region. The first is the provision of high speed pumping routes between the emitter region and the pump. The second is positioning the ionization gauge (VIG 10, V.G. Scientific, U.K.) about 15 cms from the emitter. This was found reliable for the measurement of a pressure rise

of about 5×10^{-12} - 1×10^{-11} torr due either to cleaning the emitter or in the case of outgassing of the first anode, when compared to similar conditions for an emitter used in an auxiliary vacuum system (Chapter 6).

In the specimen chamber, no restrictions are encountered.

A rotary pump (EDM 12, Edwards High Vacuum, U.K.) is used to pump the whole system to a pressure of about 5×10^{-3} torr in the course of about 5 - 10 minutes. The specimen chamber is then pumped with the diffusion pump to a pressure of about 5×10^{-7} torr and the gun chamber with the ion pump to a pressure of $\sim 10^{-6}$ in the course of 1 hr. Upon baking the system to a temperature of about 170^{o} C for 24 hrs, a pressure in the region of $1 - 3 \times 10^{-10}$ torr is obtained in both chambers. Further pumping with the TSP (by depositing a monolayer of Ti every 6 hrs) can improve the pressure considerably over the period of a few days and a pressure of $5 - 7 \times 10^{-11}$ torr was detected in both chambers in this case. The differential aperture used allows a pressure gradient of about 10^{-2} torr to be maintained between the two chambers.

During operation and with a total emission current of 15 - 20 μA the pressure in the gun rises to about $2 - 6 \times 10^{-10}$ torr depending on the outgassing rate of the first anode. It was found that a minimum outgassing period of 4 hrs with a dose of electrons ~7 mA at 400 eV is essential to keep the pressure in the emitter region below 2×10^{-10} torr for a total emission of 15 μA from W(310). After exposure to the atmosphere, the desorption rate of the first anode returns to its initial high value unless the above treatment is repeated.

9.3 THE ELECTRON EMITTER

9.3.1 W(310) Emitters

Two different emitter orientations and modes of operation have been used in the instrument, namely W(310) and Zr/O/W(100) in the cold and TF modes. The operation of the W(310) in the TF mode was not successful and the emission stability was lower than the cold mode by at least a factor of 2 - 3. No attempt to pursue investigation of this emitter in the TF mode was made in view of the success in using Zr/O/W(100) emitters.

The emitters used were obtained from FEI Co., Oregon, U.S.A. with a radius specified to be about 30 ± 10 nm, to ensure a small V_e value. The processing of the emitter is in the D.C. mode which reduces V_e for a given emitter radius in comparison with A.C. processing (Chapter 6). This is depicted in Figure 9.1. The activation of a new emitter or one that has been introduced to the atmosphere is done following the procedure outlined in Chapter 6.

The FEM has been used initially as a test chamber for establishing the operational conditions of new emitters. However, observation of the pressure rise in the vacuum tank during cleaning and the value of the cleaning current were found to be reliable guides for the activation of emitters in the column. This is done in three stages. Firstly, low current pulses of about 1.5 A for 1 sec each are used to drive loosely bound contaminants off the emitter. The current is then increased slowly to observe the largest pressure rise which is usually $\sim 5 - 10 \times 10^{-10}$ torr. It is recommended that this stage is achieved over several cleaning pulses to reduce the risk of emitter damage. The final stage shows a decrease in the pressure rise to $\lesssim 1 \times 10^{-11}$ torr with current pulses of about 2.1 Amps corresponding to temperatures of the order of 2200^{o} K. This stage is also accompanied by a change in the pattern leading to an intense axial emission. For an out-

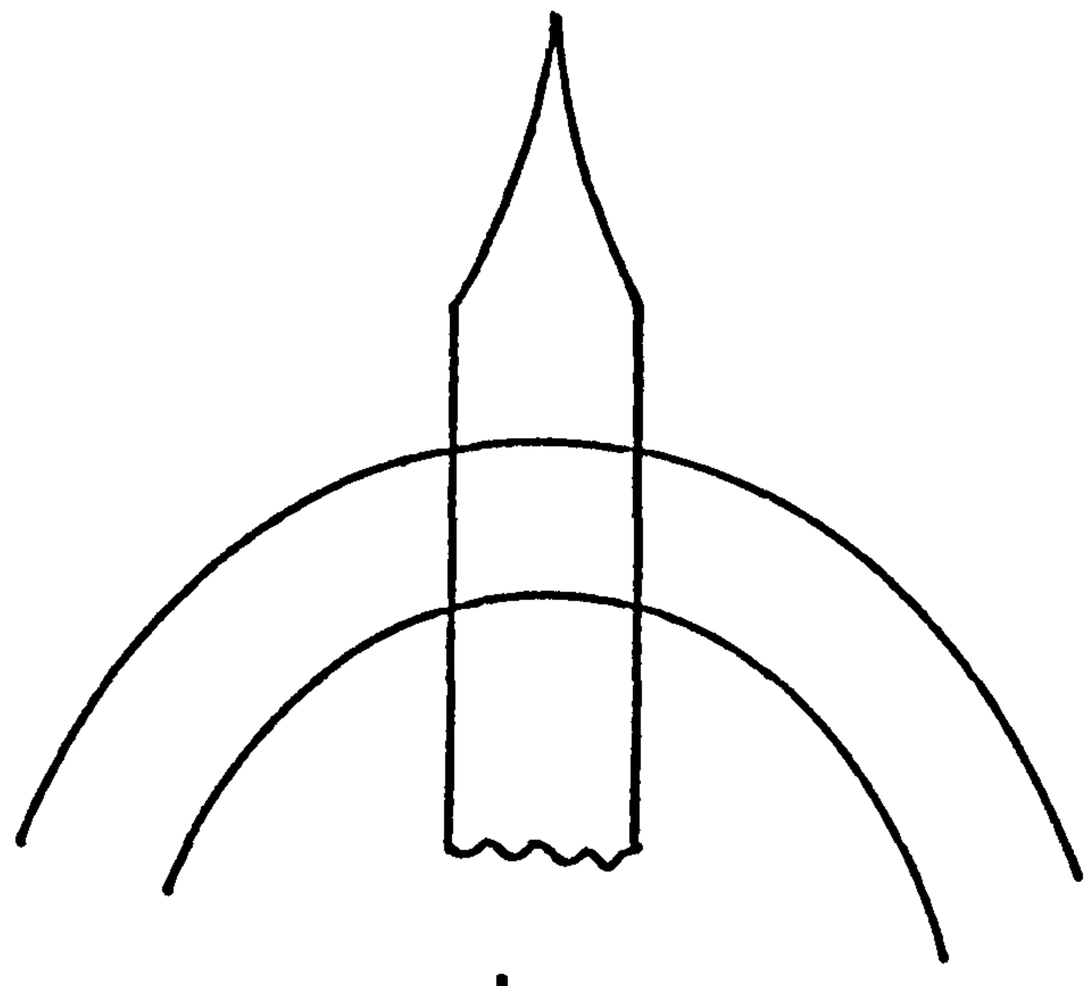

d.c.

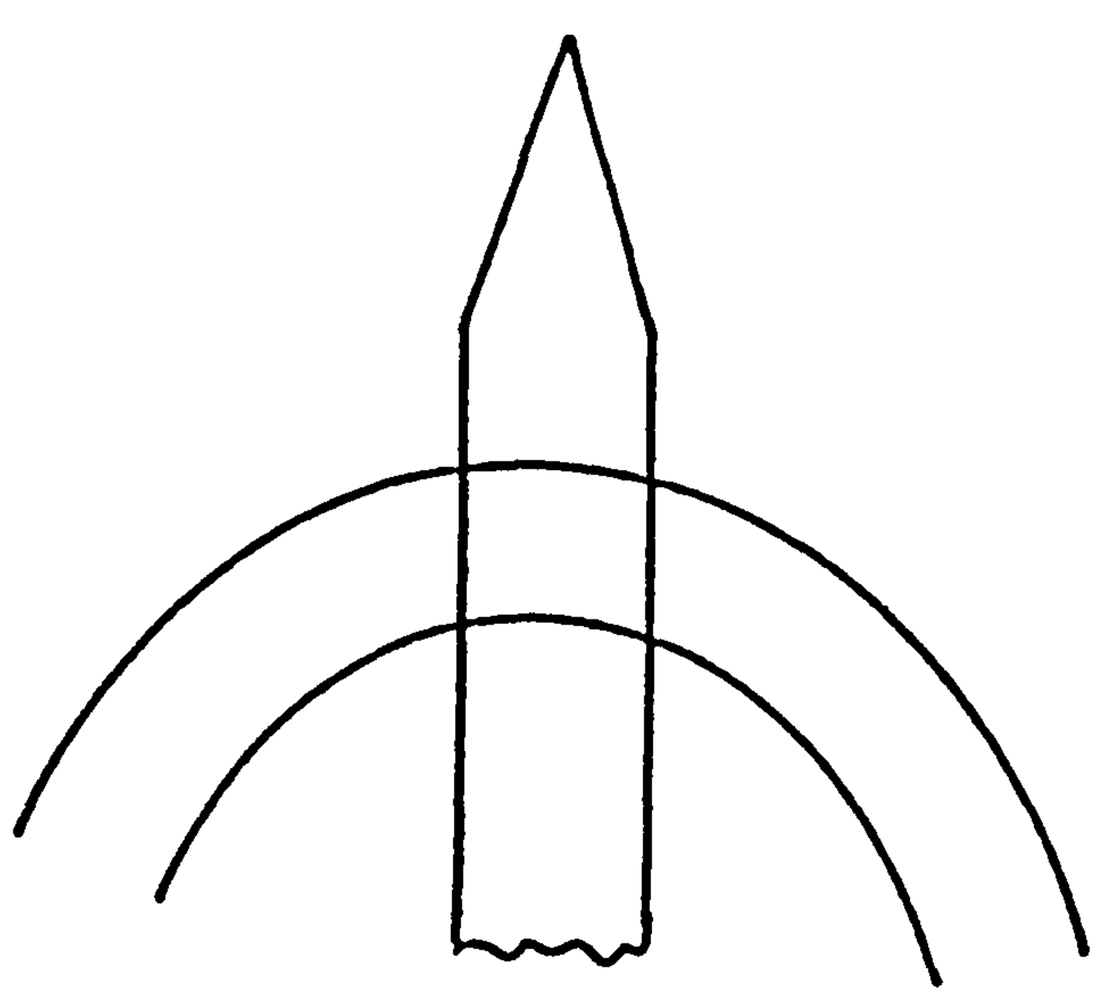

a.c.

Fig. 9.1 Schematic of emitter profile for (a) d.c. processing and (b) a.c. processing.

gassed first anode, and a total emission current of about 15 - 20 μA, the pressure rise in the system is about 7 - 10 x 10^{-11} torr. All the cleaning is carried out with reverse fields. Since the emission stability depends on the total emitted current, the latter is always kept below 20 - 30 μA. UOL cycles of between 30 - 60 minutes have been achieved. This time allowed the recording of two Auger images, but was still considered inconvenient as cleaning of the emitter was necessary to restore emission stability and beam current. In situ build up of the W(310) plane was found to give similar emission noise to that from clean W(310). At high values of total emission this mode could be considered disadvantageous in terms of energy spread due to the Boersch effect.

A major disadvantage of this emitter is its sensitivity to micro-discharges resulting from mechanical vibration of the instrument. e.g. movements of sample holder and during alignment of the column. See also discussion in Chapter 6 concerning the operation of W(310) emitters for more details. As a result, emitter life varied, depending upon when the accident destroyed it.

An observation by the author in support of the theory concerning the movement of dislocations to the emitting area in stress field due to $\vec{E}$ has been seen with W(310). It was found that in some cases emitters from one batch are destroyed during operation after a relatively short time of use with no apparent outside cause e.g. mechanical vibration. In some other cases the life of emitters from a different batch was much longer, giving up to 8 months of continuous daily use of the apparatus. This can only be explained by the above theory.

Measurement of the beam current has shown a similar behaviour to total emission. After flashing the emitter, and for total emission of about 20 μA, the beam current can be as high as ~ 4 nA. At the end of a UOL, the emission drops to about 10 μA, but the beam current can be as low

as 7 - 8 x 10^{-10} A as illustrated in Figure 6.3. The reason for this decay is given in Chapter 6.

9.3.2 Zr/O/W(100)

This emitter is obtained from the same supplier. Information from the manufacturer showed that emitter radii < 100 nm can be obtained. In this case, a low V_e value of between 1 - 2 kV can be used allowing a favourably high focussing ratio, R to be used. However, inspection of the emitters in the SEM showed that the radii are normally between 300 - 1000 nm. This was later explained by the manufacturer to be due to the process of Zr deposition which is done at high temperatures that inevitably blunt the emitter. The consequence of this is a lower R value.

Cold field emission from Zr/O/W(100) exhibits the same problems as W(310). In addition, after a few minutes of operation the central spot (due to emission from the (100) plane) gradually loses intensity and at the same time the four surrounding (310) planes start to emit. Such a pattern is not usable in electron probes.

In the TF mode, the emitter has shown remarkable emission stability of about ± 5% with UOL of practically tens of hours. The procedure outlined in Chapter 6 for the activation of the emitter has been used in the microscope and found reliable. Depending on the emitter radius, V_e values of 1.5 - 3 kV have been used.

For a total emission of ~ 20 - 50 μA, the beam current is normally between 5 - 10 nA. On some occasions, up to 100 nA of beam current was obtained under the same geometrical arrangements by slightly increasing the extract voltage V_e. Figure 9.2 shows the behaviour of the beam current with time. It should be mentioned that in the first hour of operation a slight increase in the beam current of about 30% will be obtained for a processed emitter. The stability shown in Figure 9.2 is obtained over UOL

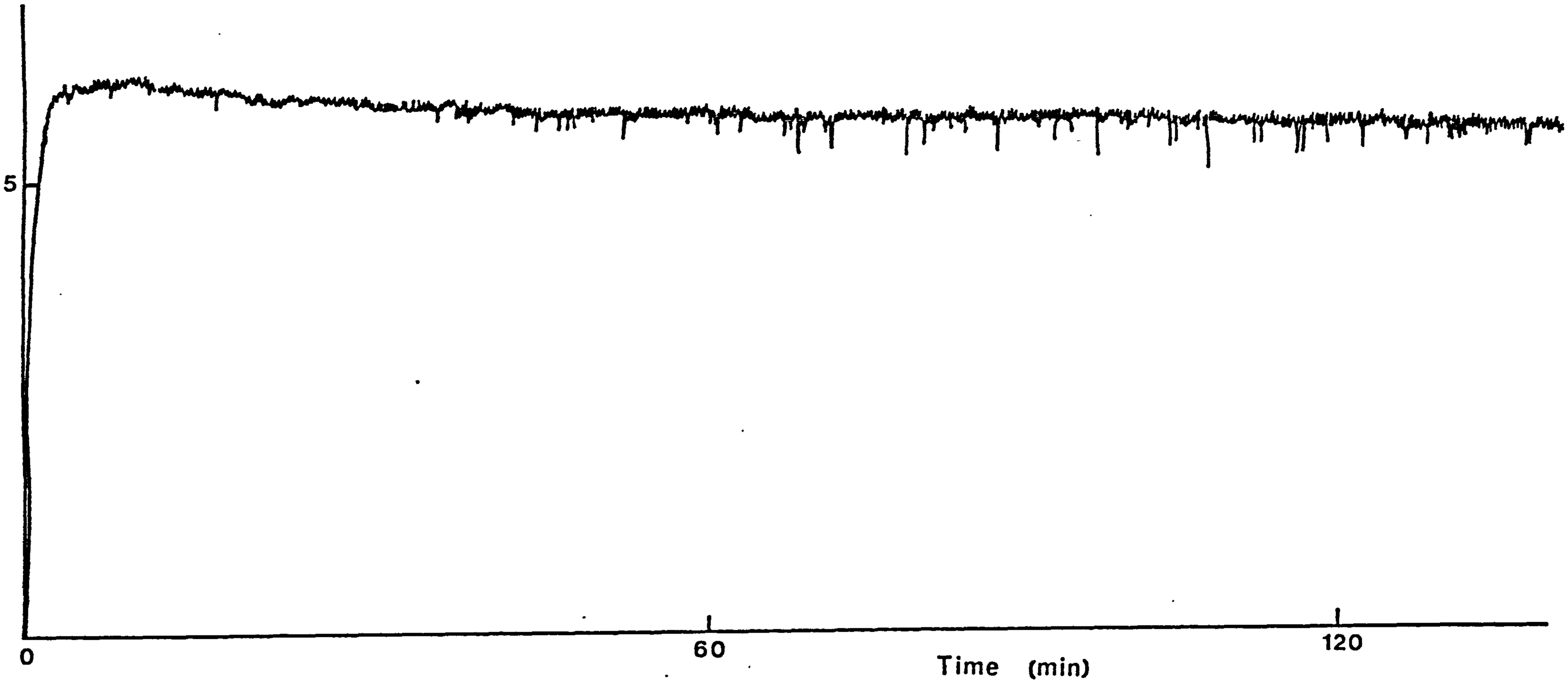

Fig. 9.2 Beam current versus time from a Zr/O/W(100) emitter.

of up to 10 hrs of operation. Longer periods of few hundred hours have been obtained by Swanson and Martin (139), but this was not tested in the present work. The lack of a similar experiment has made direct comparison with published data difficult at this stage. However, Swanson and Martin (139) have operated a similar emitter in an FEM but with a slightly higher flicker noise (of up to ~10% of the total emission current) due to the high pressure used, namely 10^{-8} torr. With an aperture subtending a 27 m rad total angle at the emitter they obtained a beam current of about 10^{-7} A which compares well with the value obtained in this work at similar temperatures (i.e. 1600 - 1700^{o} K).

No difficulty with microdischarges of the kind discussed with W(310) has been experienced. This is mainly due to the larger emitter radii used in addition to thermal cleaning of the emitting area at this temperature.

It was found that the relatively high value of emission current in this mode aids in outgassing the first anode, particularly during the early stages of operation. The emission stability was further improved by strictly operating the emitter at pressures < 5×10^{-10} torr.

9.4 THE ELECTRON OPTICAL COLUMN

9.4.1 The Application of the High Voltage

The high voltage insulators have been designed to withstand a voltage of up to 50 kV, and were tested to 45 kV with no signs of flashovers.. The application of the 45 kV was done to test the design figure, although the maximum applicable voltage of the electron column is only 30 kV set by the present power supply. After the activation of an emitter and the establishment of a stable emission, the high voltage V_i is then applied to obtain a focussed electron beam. V_i is increased slowly to prevent any

flashovers.

If the system has been at atmosphere for any reason, a high voltage test is applied before any attempt to use the instrument is made. In this case the system is connected differently where the emitter is at the same potential as the surrounding components, and hence preventing field emission, but the whole assembly is at a high voltage (~ 30 kV) with respect to the ground potential. The purpose of this test is to ensure that the high voltage region is free from any sharp edges that may be introduced during the changing of either an emitter or the first anode degassing filament, in addition to any loosely adsorbed particles. A 50 kV power supply (Brandenberg Ltd.) is used in this experiment and the voltage is increased at a rate of several kV per minute up to 30 kV. All the discharges that occur in this test have been preceeded by an exponential increase in current suggesting field emission type of discharge.

9.4.2 The Alignment of the Emitter

The final alignment of the emitter with the optical axis of the column, defined by the anode apertures, is done in two stages. A first order alignment is achieved first at low magnification using the low V_i focus. This is done by scanning the emitter in the x - y plane until the beam is totally cut off by the defining aperture, and the middle point of this plane is considered as a first order alignment. In the second part a high voltage image at X1k - X2k is used to minimise the image shift with a small change in focus. Care should be taken of the confusion with astigmatism that may arise in this test if a higher magnification condition is used. Usually any sharp feature on the sample (e.g. a cross bar of a standard electron microscope grid) can be used for this test.

The alignment mechanism used consists of driving the emitter on the bellows assembly using four M4 bolts. It was planned to change these bolts

with four standard bakeable micrometers at a later stage. However, they have proved satisfactory so far and an emitter shift of a few microns is usually obtained, judged by measurement of a sharp feature in the image. The angular alignment of the emitter is provided via four adjustable posts between the flange carrying the emitter and the plane of the first anode. This facility has not been needed yet, which confirms both the manufacturer's accuracy of mounting the emitter on the hair pin as well as the construction of the mounting mechanism. Many cycles of baking the system to ~ 170° C have not altered the above alignment over the period of two years.

Residual astigmatism can be corrected after the completion of the alignment, using a similar feature on the sample. It was found that minor tuning of the emitter alignment may be needed after correcting for astigmatism.

9.4.3 The Correction of Astigmatism

The careful assembly of the elements of the column, in addition to minimising the risk of microdischarges, ensures as well the minimum amount of astigmatism due to insulating materials on the electron path. In the present study, an He jet has been used after the final assembly of the elements to clean the apertures, the inter-anode spacing, and the stigmator elements which are the most likely sources of astigmatism. With this procedure, the astigmatism in the instrument has been found to be only a few microns and can be easily corrected. Figure 9.3 is a series of images depicting the action of the stigmator. For reasons that will become clear later, the full power of the stigmator has not been used yet, but it is hoped that a value of few nm should be obtained.

No provision has been allowed for aligning the stigmator with the optical axis of the column. However, this has not introduced gross

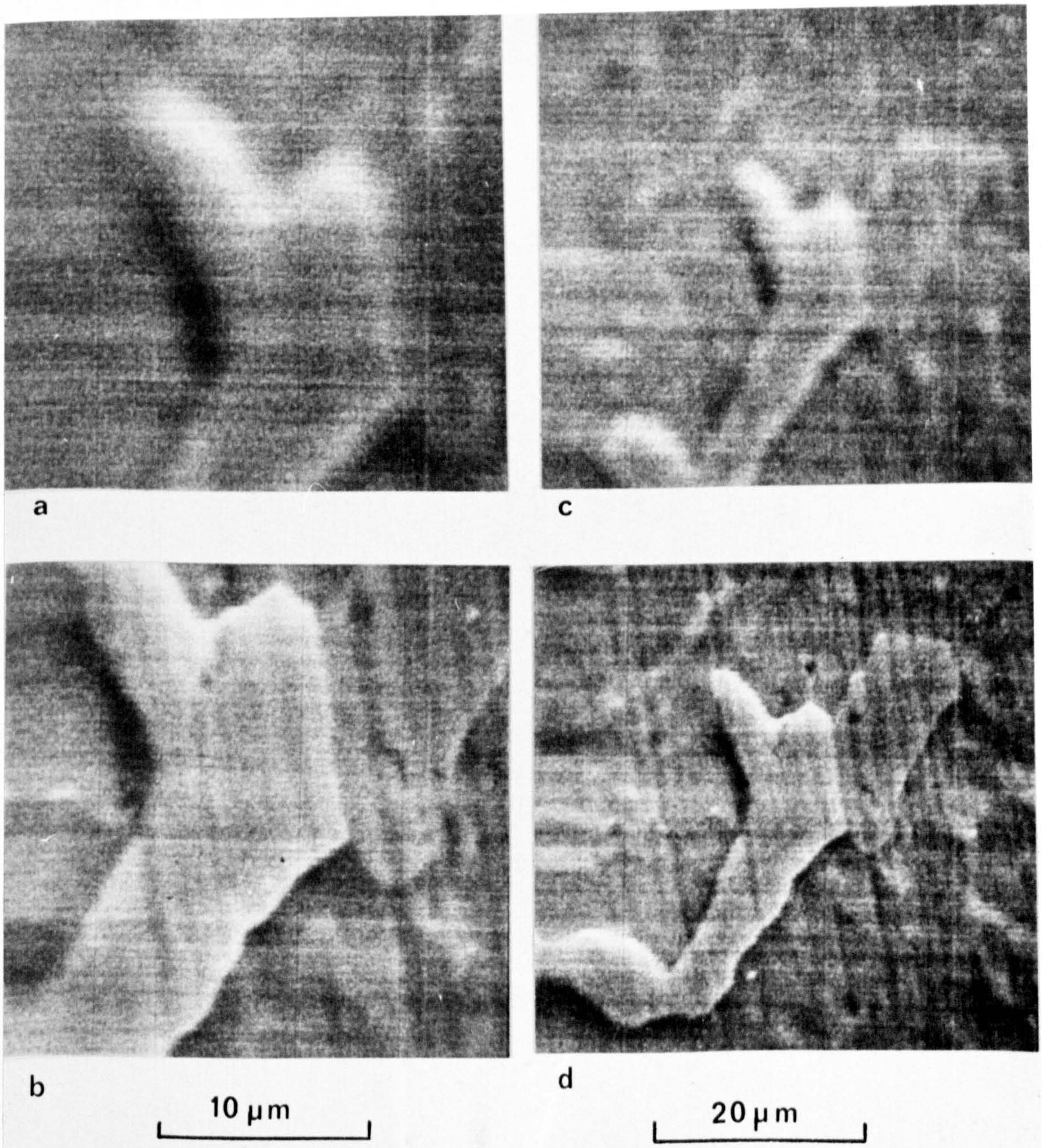

Fig 9.3: Scanning electron micrographs of an Aluminium sample showing the correction of astigmatism using the octopole system. (a) and (c) uncorrected, (b) and (d) corrected and focussed. $E_p \sim 23.2$ keV, $I_b \sim 8$nA.

aberration as can be seen from the performance of the column.

9.4.4 The Magnification and Field of View

At any given accelerating voltage V_i, there are 10 fixed magnification settings and one variable to about 5 X. Table 9.1 gives the values of these settings for a V_i = 17.3 kV which varies between X 50 - X 250 k. These values are for a specimen distance (w.d.) of 80 ± 1. mm and R ≅ 7. The specimen manipulator has a lateral movement of about ± 8 mm which can vary the above listed values by up to ± 10%. Normally, the specimen is set at the intersection of the electron beam with the axis of the input lens of the CHA giving a w.d. of ~ 80.0 ± 0.5 mm, by maximising the number of analysed electrons at a certain energy by the CHA. Different objects have been used to calibrate the magnification which included a standard 50 μm hole (Agar Aids Molybdenum aperture) used for the Faraday cup, and microscope grids of 100 and 200 lines/inch spacings. In addition, several other objects have also been examined in a different SEM (Cambridge Steroscan 600) and agreement to within 5% has been obtained. At high scanning speeds (approaching TV rates), the scan amplifiers introduce some distortion to the image. However, for computer controlled rasters of 0.25 secs/frame no distortion is introduced.

The magnification settings are only correct for a given V_i. Due to the variation of both V_e, and R, different V_i will be always encountered. This however, should not change the magnification ratios given above, but a scaling factor should be employed for the specific V_i used. Figure 9.4 shows the dependence of the magnification on V_i at one setting. The dependence is linear and with the range of V_i values to be used (12 kV < V_i < 25 kV), a scaling factor of $2(keV)^{-1}$ results.

At low V_i values, the above magnification settings will be reduced. Table 9.1 gives also the corresponding magnification values in this case,

Position	Magnification			
	High Ep		Low Ep	
	Min	Max	Min	Max
1	X 50	X 250	1	5
2	125	625	3	15
3	250	1250	6	30
4	500	2.5k	12	60
5	1250	6.25k	30	150
6	2.5k	12.5k	60	300
7	5k	25k	120	600
8	12.5k	62.5k	300	1500
9	25k	125k	600	3000
10	50k	250k	1200	6000

Table 9.1 Microscope magnification at a specimen distance of 8 cms and final energy of 17.5 keV and R ≃ 7.

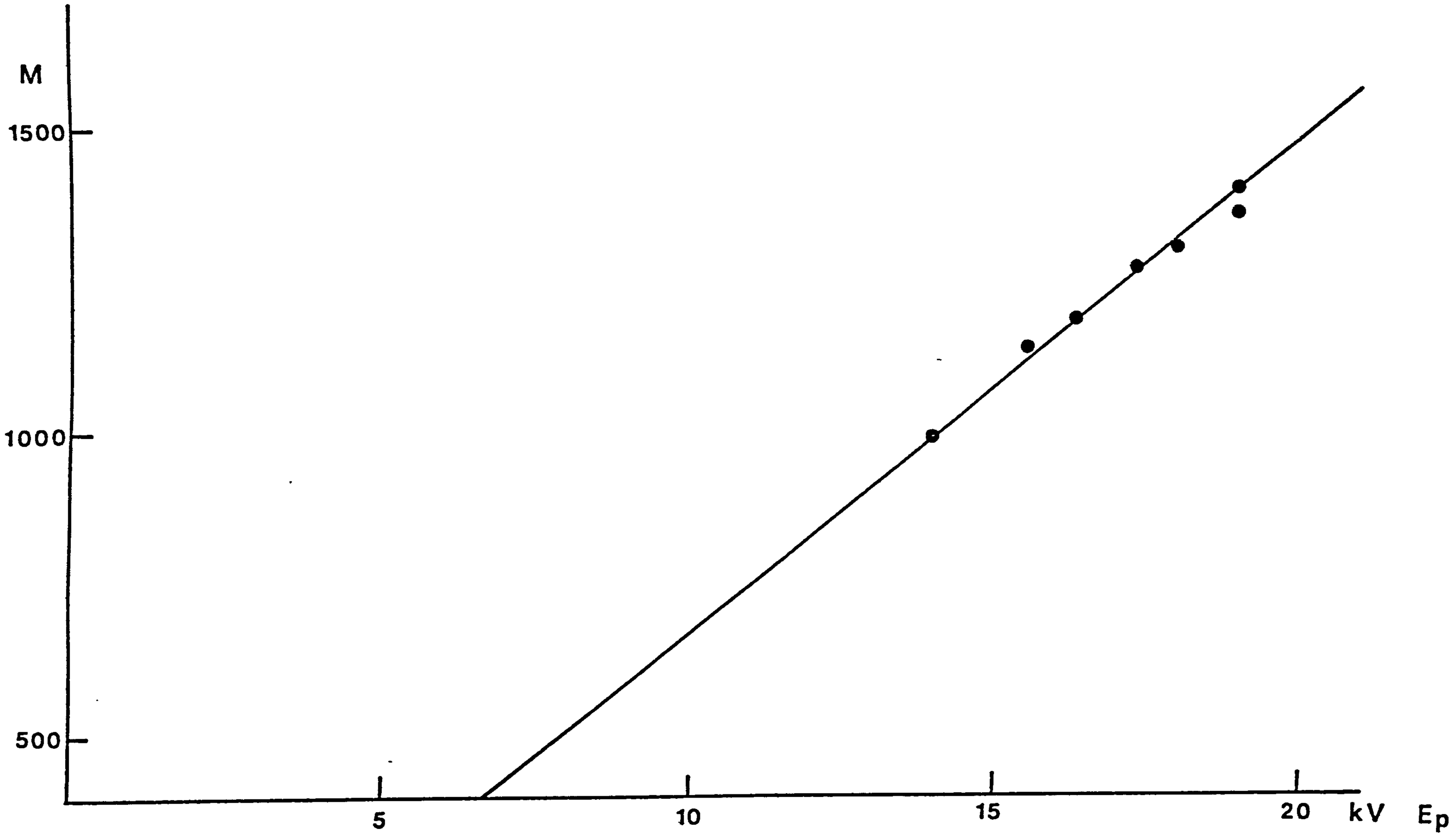

Fig. 9.4 The dependence of the magnification, M on the primary energy at one setting for high V_i values.

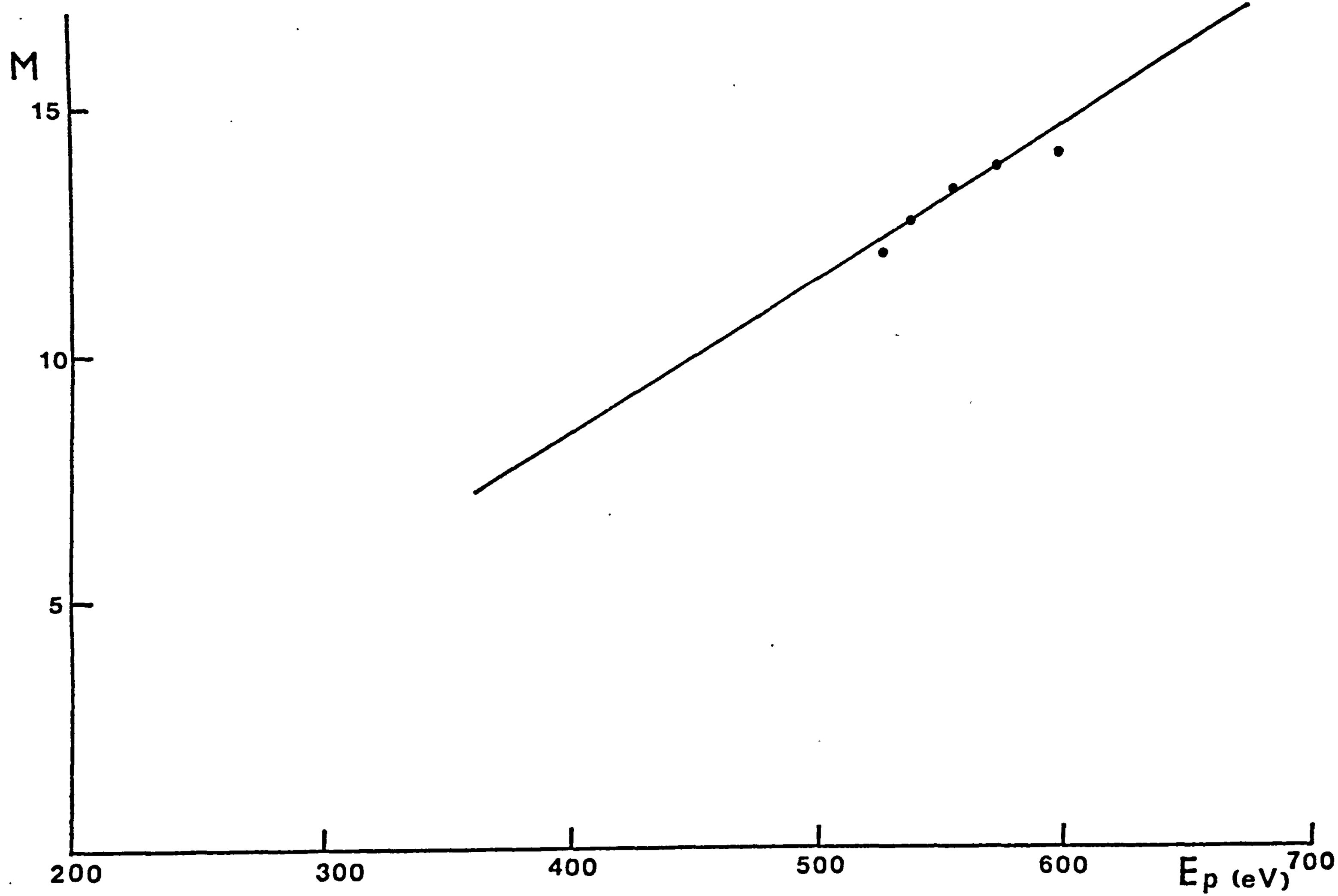

Fig. 9.5 The dependence of the magnification M on the primary energy at one setting for low V_i values.

and Figure 9.5 depicts the dependence of Mon V_i at low V_i and a fixed setting.

The design figure for the field of view at 30 kV is ~ 3 mm. It should be mentioned that the field of view also depends on the value of V_i. Figure 9.6 shows this dependance for several V_i values at R = 7. At low magnification the expected large field of view is not obtained because of the interception of electrons by the system's differential pumping aperture. Nevertheless, a maximum field of view of about 5 mm diameter at V_i = 13.8 kV is obtained.

9.4.5 The Focussing Ratio and Beam Current

One of the properties of this column is the provision of a variable focussing ratio, R (between 7 - 12) at a fixed working distance. This is achieved externally via the mounting bellows, and internally via the emitter holder. Measurements of the distance from the first anode aperture plane to the emitter, S_1 can be made with an accuracy of ± 1 mm. The choice of a high R value is determined by the sharpness of the emitter (i.e. low V_e value). The column has been operated over the entire range of R values of the design and good agreement with the theory has been obtained. Figure 9.7 is a theory/experiment comparison of S_1 vs R.

The high R value was used when the column first produced a focussed electron beam. Stray magnetic fields and inadequate shielding of the test chamber has made the accuracy of measuring the beam current uncertain by a factor of ~ 2 - 3. Instability of the high voltage power supply and the risk of discharges have lately prevented the use of higher R values than 9. Figure 9.8 shows the expected and measured beam current as a function of R, for the two different emitters used. In the case of Zr/O/W(100), the theoretical predictions were based on Swanson and Martin's measurements (139). However, a direct comparison is rather difficult as their emitters were

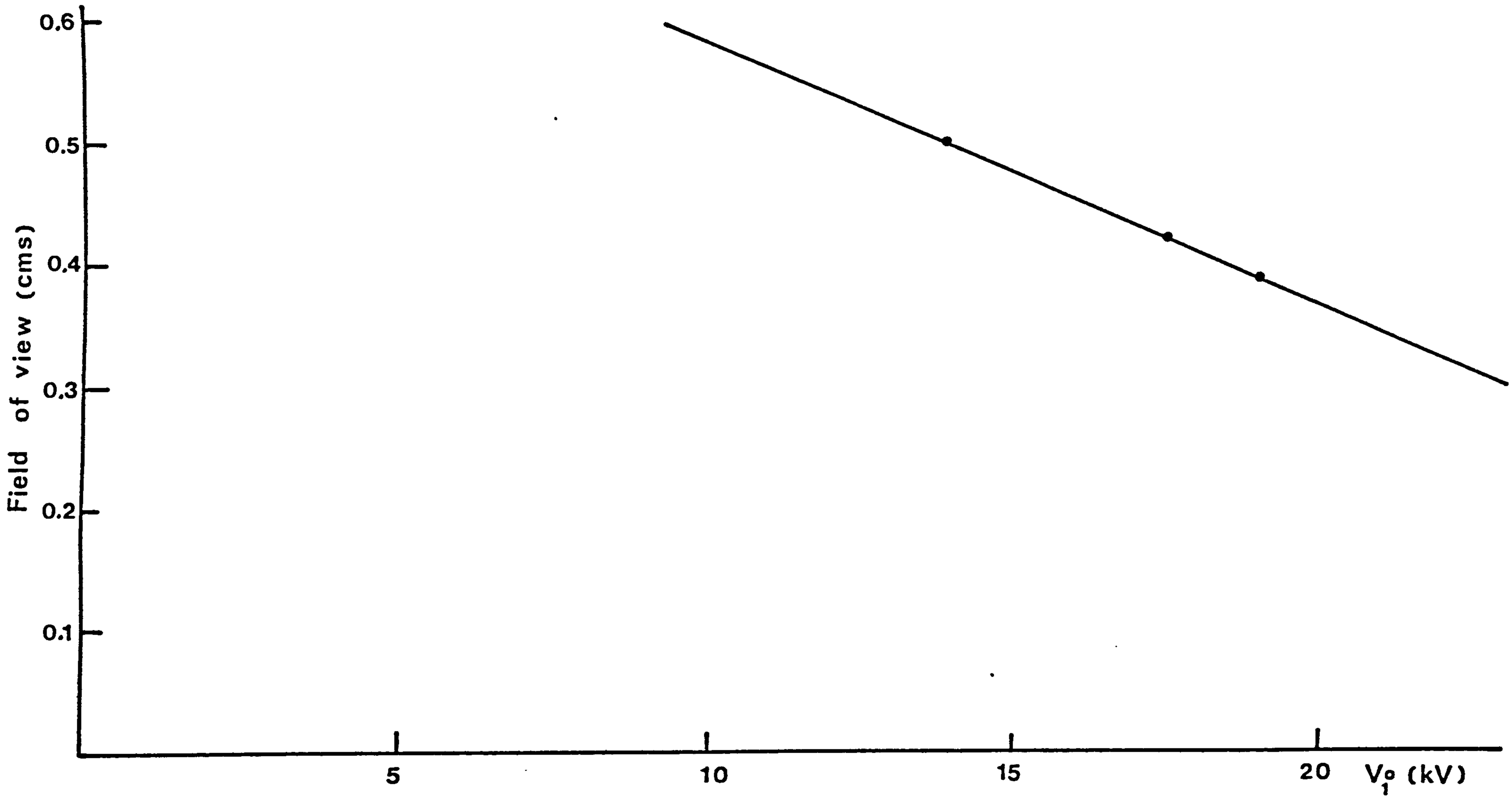

Fig. 9.6 The dependence of the field of view on the primary energy for R = 7.

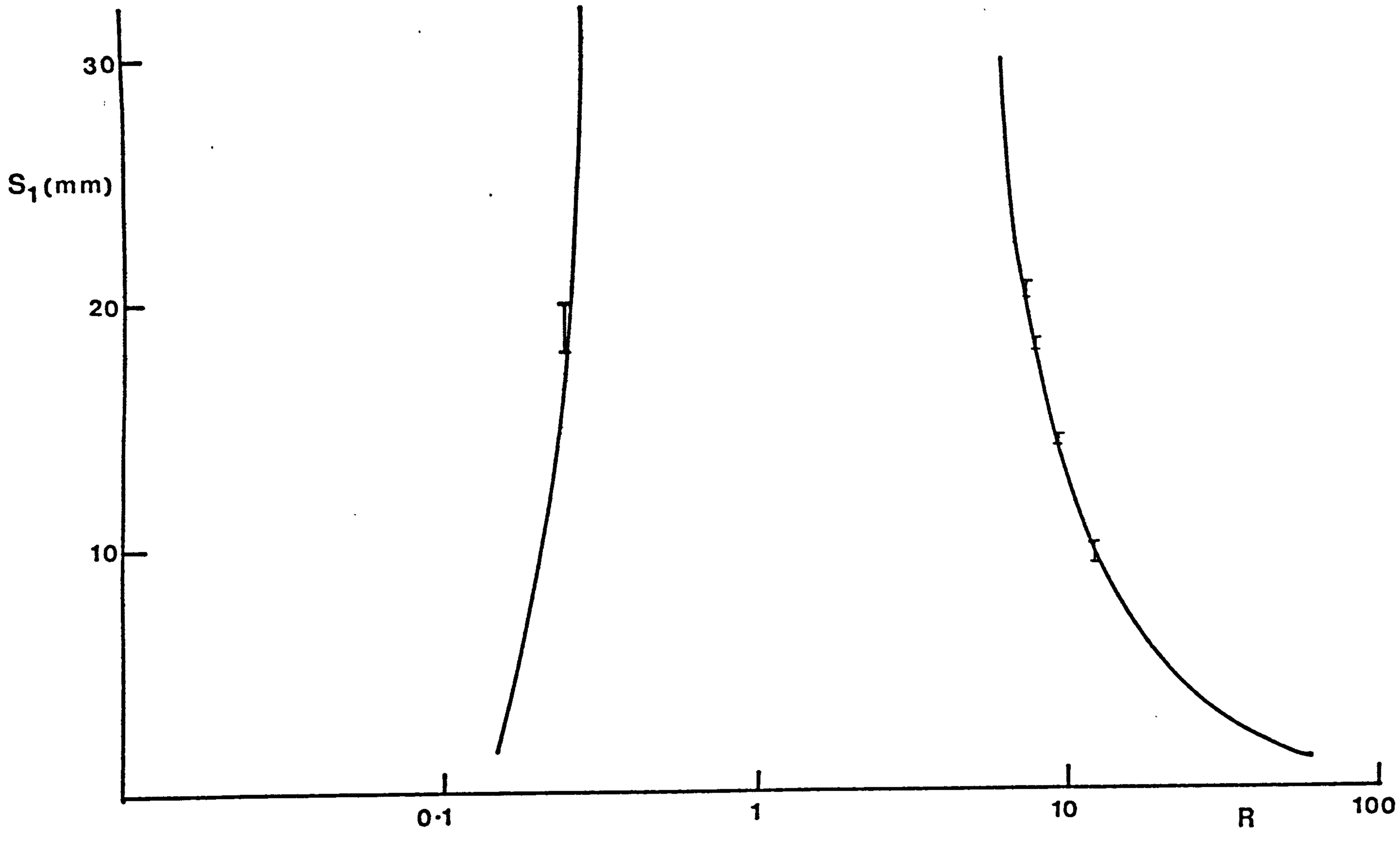

Fig. 9.7 Theory/experiment comparison of S_1 versus R.

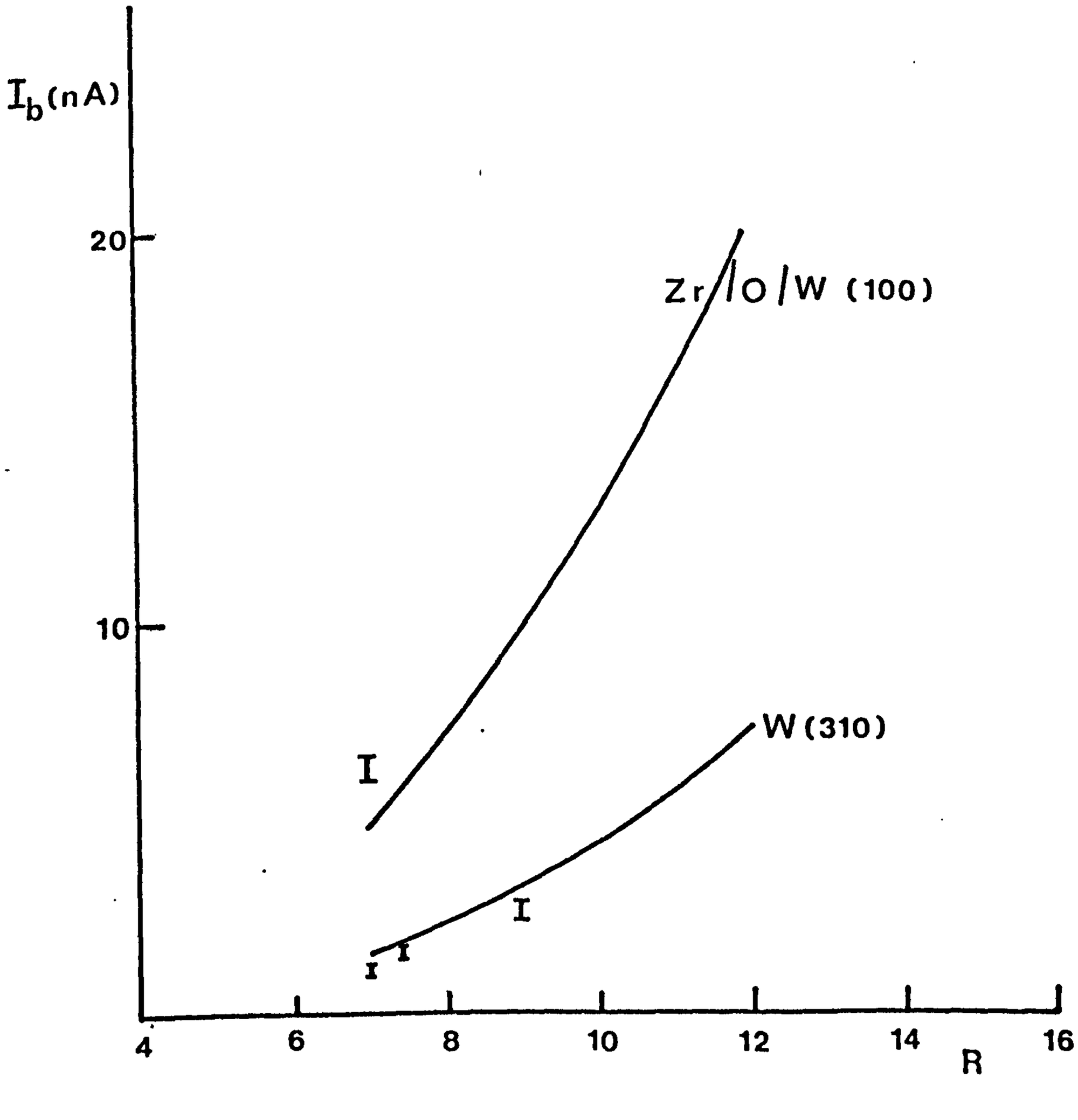

Fig. 9.8 Expected and measured beam current from W(310) and Zr/O/W(100) emitters.

larger in diameter and operated at a higher temperature than is used here. It was found in the present study that a large proportion of the recorded I_e is due to thermal emission. By reducing the emitter's temperature by about 300 - 400° K, to about 1000 - 1100° K, a drop in I_e from ~100 μA to 10 - 15 μA is obtained accompanied with a relatively small reduction in beam current of ~10%. Such a reduction in temperature usually causes a noisier emission and is not favourable. On the other hand, increasing V_e by about 10 - 15% has always resulted in an increase in beam current by a factor of ~2 - 3 but with a small increase in I_e of less than 15%. It was found that operating temperatures of about 1500° K have resulted in the best compromise between the emitter's stability and a reduction of the emitter dulling rate as observed by V_e, in addition to a low emission current that should improve the energy spread. Beam current of about 5 - 10 nA is routinely obtained with $V_e \simeq 2 - 2.5$ kV and Ep ≈ 15 - 20 kV at the above temperature.

9.4.6 Resolution

In transmission electron microscopy, the examination of a micrograph of a carbon film that contains a wide range of spatial frequencies is a standard method for determining resolution. Such a technique is not applicable in the SEM for the lack of an equivalent specimen, although a first order estimate of the resolution can still be obtained from micrographs of high contrast specimens.

The widely accepted method for measuring the resolution in the SEM has been developed at the Engineering laboratories, Cambridge University. It consists of sweeping the electron beam perpendicularly across an opaque edge and monitoring the transmitted current. Smith (147) has assumed the transverse distribution of the current density to be a Gaussian function and considered the electron beam diameter as that within which 80% of the

current is obtained. Several other definitions for the beam diameter have been adopted by various authors (148, 180).

The accuracy of this method depends on the sharpness of the edge used and on any contaminants on it (such as polymerized oil) which affects the shape of the ends of the profile giving erroneously larger diameters. Another likely source of error that can arise in this method is if a scintillator is used to monitor the secondary electron signal on sweeping the edge. In this case, scattered electrons at the edge can increase the rise time of the signal giving apparently larger beam diameters. By reducing the scintillator collection angle, Cleaver (180) has reduced the measured beam diameter in his system by a factor of ~50% .

The above method has been used for measuring the beam diameter in the present work. Figure 9.9a is a typical scan across the edge of 50 μm aperture of the Faraday cup giving the signal rise of the collected electrons. The collector of the Faraday cup was biased with -30 volts to prevent the detection of scattered electrons from the edge of the aperture. Measurement of 10% - 90% of the maximum rise in the signal ranged between 220 - 300 nm. At low V_i, a similar measurement gives a beam diameter of about 4.6 μm.

The above edge profiles (Figure 9.9) are taken with a Zr/O/W(100) emitter. During the early stages of development where the W(310) emitter was used, features of about 100 nm could be resolved, but no edge profiles were recorded.

With the use of the Zr/O/W(100) emitter additional components to the system have been added e.g. heating power supplies, fans to cool the electronics. The effects of these on resolution will be discussed later.

The aperture of the system is 150 μm in diameter and for R = 7 this gives $\alpha_o = 3.75 \times 10^{-3}$ radians. In this geometry the theoretical beam diameter should be about 140 nm (see Figure 7.9). Figure 9.9a shows a

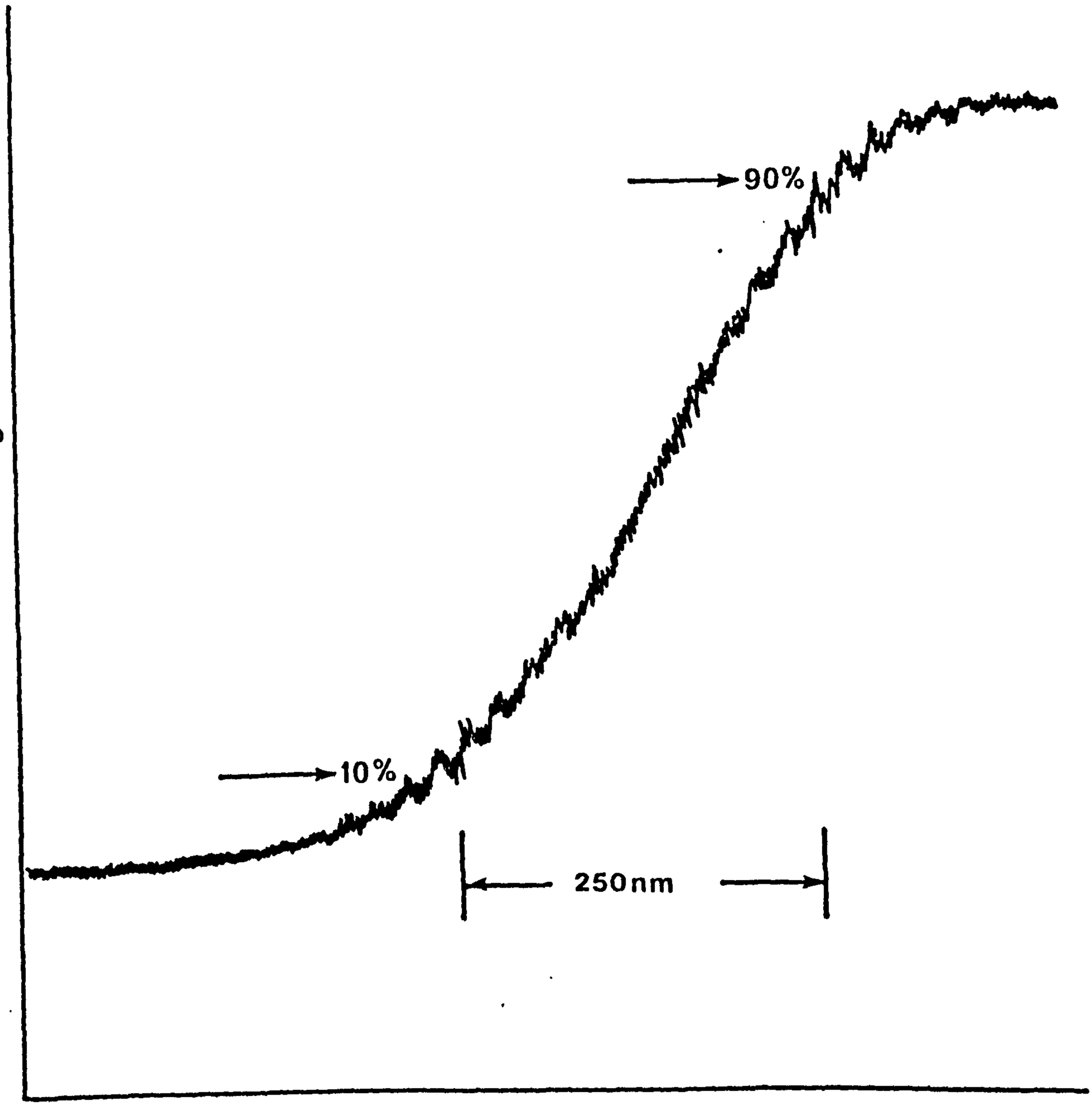

Fig. 9.9a Beam current versus beam displacement plot as the beam traversed a sharp edge. (a) Ep = 17.5 keV. (b) Ep ≅ 580 eV.

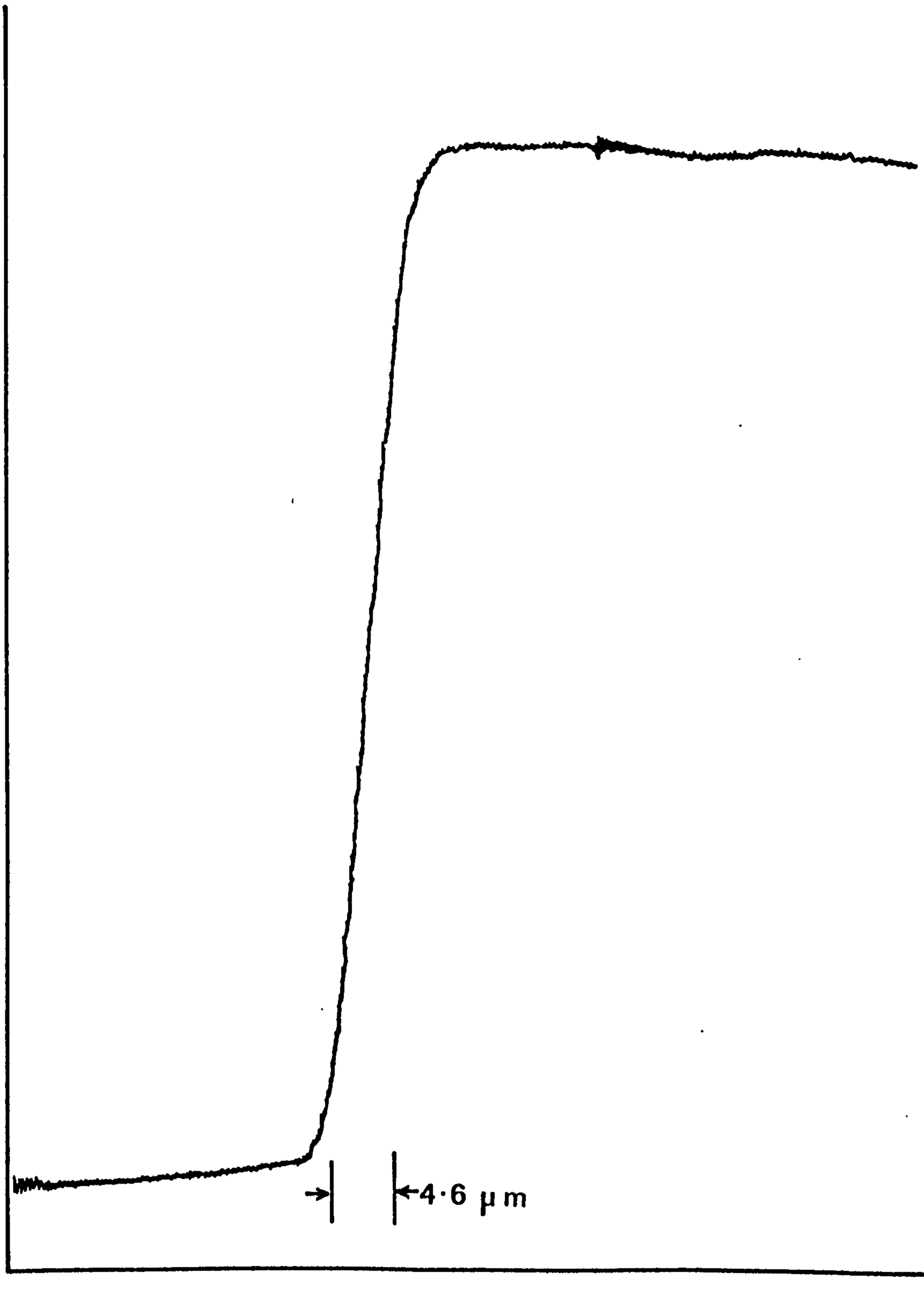

Fig 9·9b

beam diameter which is approximately a factor of 2 X the theoretical prediction. At low V_i, and the same above conditions, the theoretical beam diameter is about 4 μm.

At high magnification (> x 20k), careful inspection of the SEM micrographs reveals the presence of vibration and/or A.C. interference smearing off fine details. The amplitude of this interference is about 200 - 250 nm with a frequency of about 104 Hz. The latter was measured using a signal generator fed to a loud speaker. It was found that the amplitude of the interference signal increased either as the loud speaker was directed towards the main vacuum system, or with an increase of the signal volume. This test does not necessarily imply that the interference is of a directly mechanical character. The effects of this signal on a sharp edge are shown in Figure 9.10.

The most likely sources of this signal can be classified into two groups, mechanical or electrical in origin. The probable electrical sources are, the A.C. fields of the laboratory mains system, A.C. fields from power transformers of the various components, or interference from the TF heating supply (which was not designed for TF operation). The mechanical sources on the other hand include vibration of the whole instrument by the action of the boiling of the oil from the diffusion pump or boiling of the liquid nitrogen used in the cold trap, in addition to the system's ventilation and the action of the fans used for cooling the system's massive electronics.

The investigation of the above sources has shown, as can be judged from the quality of the image obtained, that the resulting interference is probably a combination of some of the above listed sources. Unfortunately one can not totally exclude all such sources in one test as these are essential for the production of a SEM image.

It was possible however to show that some of these sources are more

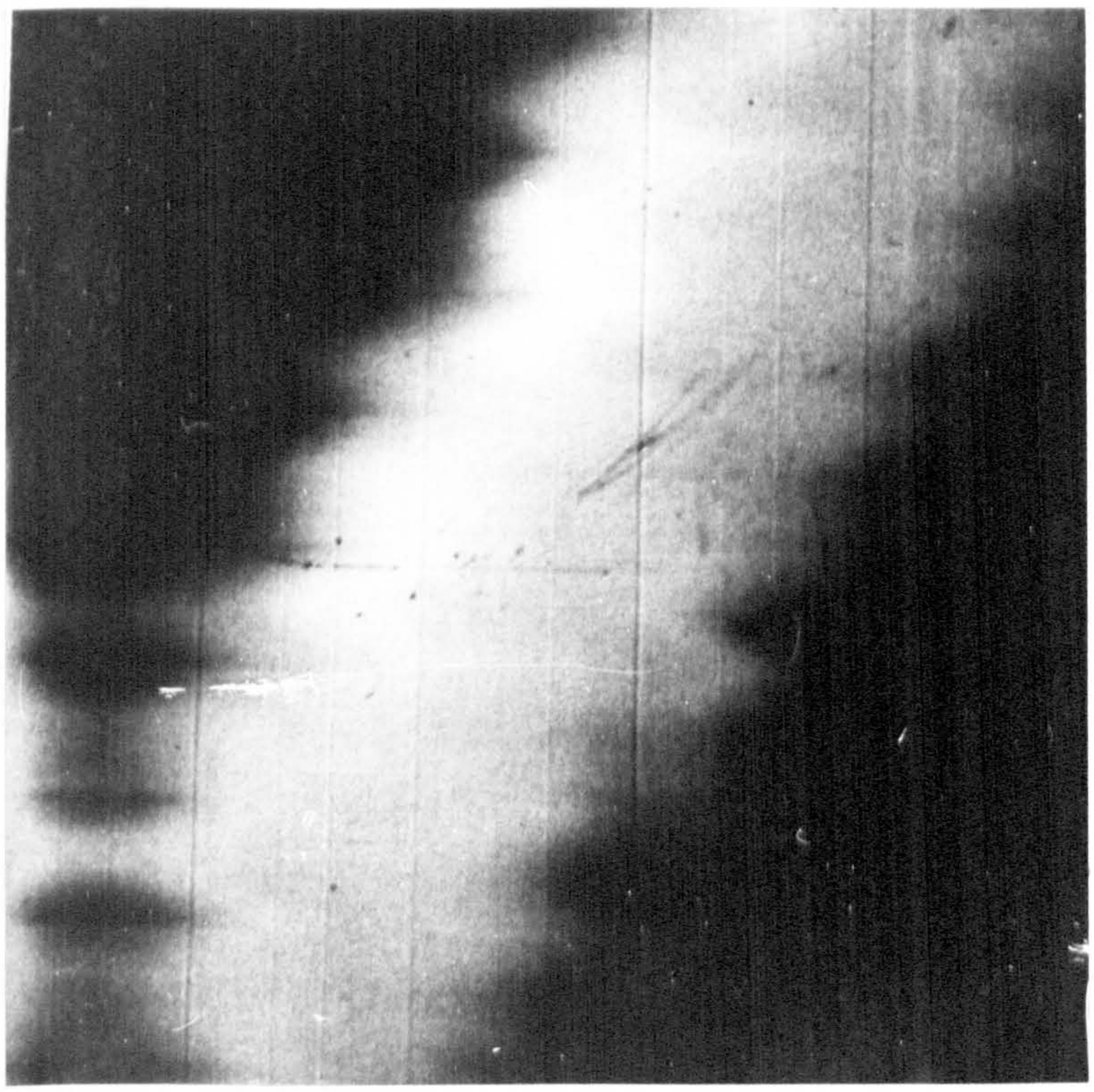

Fig. 9.10 Effects of vibration on edge sharpness.

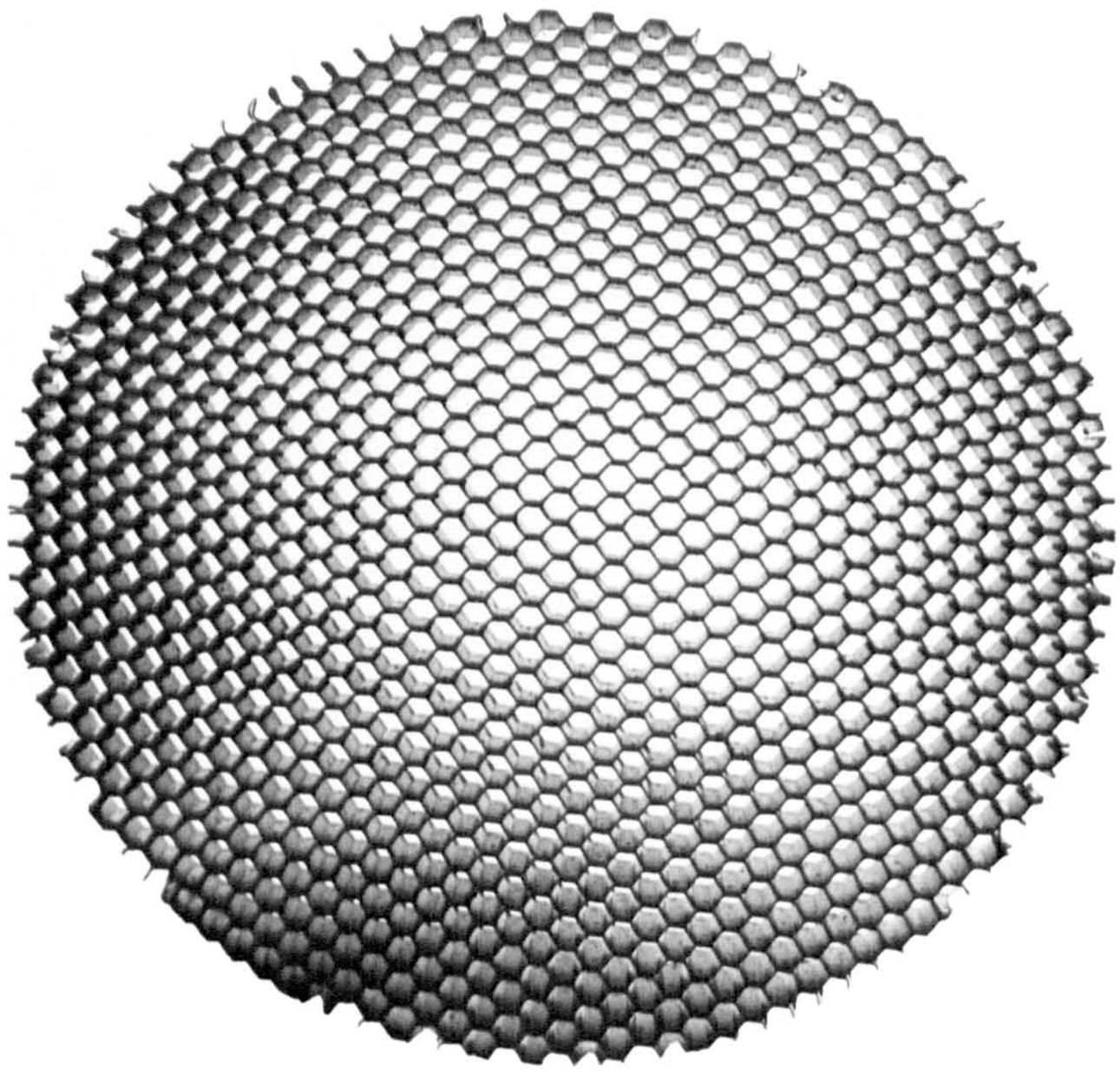

Fig. 9.11 Photograph of the honeycomb stainless steel cells used for reducing the vibration in a diffusion pump.

significant than others. For example, the TF supply shows a ripple on the output of about 2 - 3 mV p-p, and both the V_e and V_o supplies show ripples within the design figure. The analyser and scanner-stigmator supply showed a significant contribution to the interfering signal. This was reduced by about 20% upon enclosing these supplies in an earthed shield.

An investigation of the mechanical vibration has revealed three main sources of interference, namely transmitted vibration from the floor due to natural vibration of the building, vibration of the instrument due to the action of the boiling oil in the diffusion pump and finally interference from the laboratory cooling system which consists of several fans mounted on the electronics console and an air conditioner. On the other hand the vibration of the system due to the boiling action of the liquid nitrogen was removed completely by stopping using the trap. The cost of this is a higher partial pressure of hydrocarbons on the vacuum system, but no apparant deterioration in the total pressure of the system.

The first kind had also been encountered in the first instrument and compensated for by raising the whole vacuum system on car inner tyres. The second source is an inherent problem of diffusion pumps when used in electron microscopes. Bubbles formed in the boiling oil that can grow in diameter up to the pump's throat, i.e. 10 cm in the present pump, explode upon reaching the vacuum. This gives rise to a mechanical vibration of the system and can be easily seen on the microscope CRT and correlated with the sound of the explosion.

Several schemes have been devised to reduce this effect to a tolerable level, and range in complexity with the particular application of the instrument. The manufacturer (Edwards, High Vacuum Ltd.) have suggested reducing the power to the pump heaters to stop the oil from boiling, or reducing the oil in the pump by about 35%. In both cases, a reduction in the pumping speed results. The latter method was used earlier in the

present work, but later abandoned due to the inefficient pumping. Another way of overcoming this problem is by de-coupling the pump from the system. This is achieved by using bellows between the pump and the main vacuum system.

A different solution presently under investigation by the author, is to control the size of the bubbles by confining them in small diameter cells immersed in the oil. Preliminary results show that this method does not reduce the pumping speed while reducing the noise impact of the explosion of the bubbles. Figure 9.11 shows the small diameter cells used, which are made of stainless steel in the shape of a honeycomb and supplied by Burnley Engineering Products Ltd., U.K..

A thorough investigation of the effects of the cooling system was carried out using a laser doppler vibrometer (System 55X - Disa Ltd., U.K.). It was found that this source vibrates the system via two routes. The first is through the cables connecting the vacuum system to the electronics console where all the fans are mounted. The second is the air in the laboratory acting on the vacuum system both to vibrate and resonate in a drum like action. In addition, it was found that the specimen manipulator has a smaller and different frequency of vibration from that of the main vacuum system, perhaps due to its solid construction.

Two main low frequencies of oscillation, 50, 100 Hz, in addition to a small 20 k Hz signal were measured. When the vibrometer was directed toward the laboratory wall only the 50 Hz and 20 kHz signals were found, but the former with an amplitude of about 25% of that found on the system. By switching off the various fans, identification of the individual sources responsible for each frequency was as follows. The 100 Hz signal originated from the fans on the system's magnetic field coils power supply while the 50 Hz originated from the fans of the system computer interfacing supply and the air conditioner.

A reduction of these sources to a tolerable level is sought in the following ways. The first is to couple the specimen stage to the main vacuum system to force them to have the same frequency of oscillation. The second is a re-arrangement of the fans and cables connected to the system as well as adding weights to the chamber to make it more stable and re-routing the cold air stream generated by the air conditioner. Finally the solution of the diffusion pump vibration currently under investigation should be included.

The effect of the A.C. fields in the laboratory on the electron beam has also been investigated. This was found to be of the order of 10^{-5} Tesla. The use of the mu-metal shield around the gun chamber has reduced this by about an order of magnitude. However, since this shield is used externally a deterioration of its performance with time will be obtained as a result of dismantling. In the present geometry it is difficult to have the original internal shield but perhaps a modified version will improve the shielding further.

A slight improvement has been obtained by the addition of mu-metal shields over the various ports of the system.

9.5 THE SPECIMEN MANIPULATOR

The specimen manipulator has been in use for a period of over 2 years with very little difficulty in terms of the movement of the different motions and rotations. However, as regarding stability of the stage, it was found that due to the long shafts used for the different drives, an amount of energy is stored due to the action of winding the drive. Upon selection of a feature on the screen, the energy stored acts to wind the drive further in the same direction. This is estimated to be of the order of one micron over a period of 20 minutes. One way to minimise this effect

is to re-wind the drive slightly after choosing a feature and hence releasing the stored energy. Alternatively, increasing the diameter of the driving rods to make them more rigid and less "springy" when wound should help minimise the stored energy that causes the drift. This modification is under way at the moment.

9.6 THE USE OF THE COLUMN IN THE AUGER MODE

9.6.1 Point Spectra

The column is not intended for high quality standard AES, where for this purpose a 2 keV thermionic gun (LEG 31, V.G. Ltd.) is used. However, point spectra from the column are important for two reasons. Firstly it can be used for fast chemical identification of a chosen feature in an SEM micrograph at high resolution. Secondly, it forms the basis for either Auger line or frame scans.

Figure 9.12 shows point spectra revealing a number of different energy Auger peaks. This clearly demonstrates that the electron beam is sufficient for generating a usable Auger signal. At low Auger energies, the beam current and/or the spectrometer window had to be reduced to stop saturation of the electron chaneltron of the CHA. Analysis by point spectra can be done anywhere on the sample by digitally positioning the electron beam on the required place.

9.6.2 Auger Line Scanning

Figure 9.13 shows a digital 128 x 128 point scan analogue intensity SEM of a region of a plasma etched test sample supplied by British Telecom Research Lab. with a 0.14 μm point resolution. The sample consisted of approximately 1 μm thick Aℓ with 2% S_i metallisation on an $S_i O_2$ substrate.

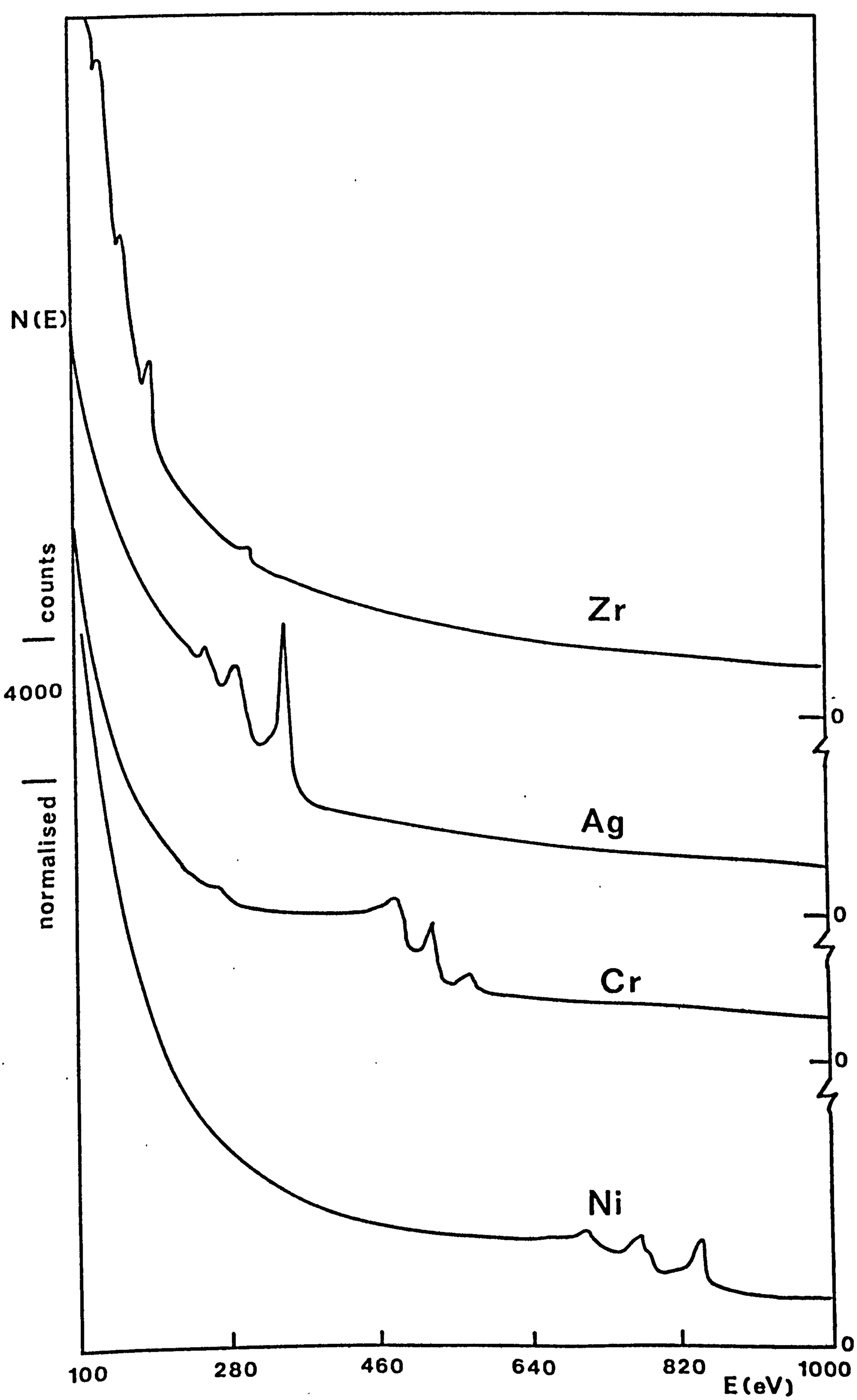

Fig. 9.12 Point spectra of different energy Auger peaks.
I_b = 1 - 3 x 10^{-9} A. Ep = 15 - 20 keV.

Spectra from points a and b of Figure 9.13 show the Aℓ, LVV and Si, L_{23} VV Auger peaks respectively (Figure 9.14). By modulating the spectrometer at 1 k Hz between 63 and 70 eV for Aℓ and 73 and 85 eV for $S_i O_2$, while scanning the electron beam at a rate of 200 m sec per spatial point, the line scans of Figure 9.15 were obtained. To normalise against fluctuations in beam current and the effects of sample surface topography, clearly visible in Figure 9.13, the Auger signal proportional to the peak height was divided by the digitised SEM signal at each line scan point. A more effective normalisation technique is to divide the Auger signal by a ratio count extracted from the N(E) spectrum, namely $(N_1 - N_2)/(N_1 + N_2)$ where N_1 is the electron count at the Auger peak in the spectrum and N_2 is at some energy just above the peak.

9.6.3 The Auger Imaging

The first Auger images produced were of the same sample area shown in Figure 9.13 by using the same analyser energy modulation described above. Figure 9.16 shows Z (intensity) modulated Aℓ and $S_i O_2$ Auger images using the SEM signal for normalisation. Each 16 grey level image of 128 x 128 pixels, with a dwelltime of 20 m sec per pixel, was collected in 7.5 minutes, 25% of this time being for computer processing.

The bright areas shown in the SEM picture (9.13) were identified by point Auger analyses as S_i particles, probably residues from the plasma etching process. They appear in the Aℓ Auger map (Figure 9.16a) as they shadow part of the metallisation from the analyser but because their effective Auger peak position changed as the particles charged during scanning they are absent from the Si Auger map (Figure 9.16b).

Figure 9.17 is a low magnification SEM image of a different microcircuit sample, showing Aℓ contact pads. The figure shows three different levels that were identified by AES as Aℓ, $S_i O_2$ and S_i from points a, b,

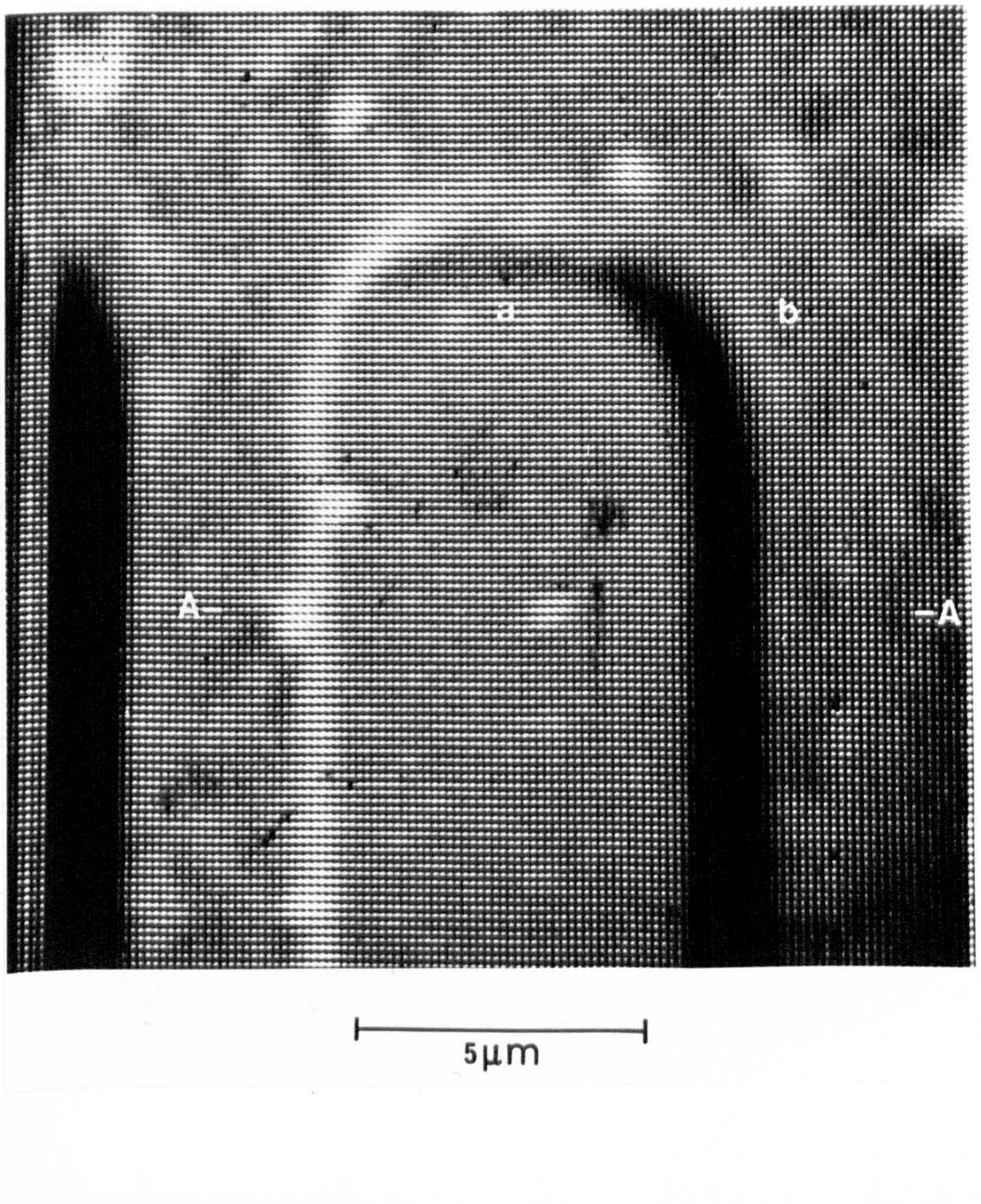

Fig. 9.13 A digitally scanned SEM image of 128 x 128 pixels of a region of a plasma etched test sample showing a 0.14 µm point resolution. $I_b = 5 \times 10^{-10}$ A and Ep = 11.2 keV.

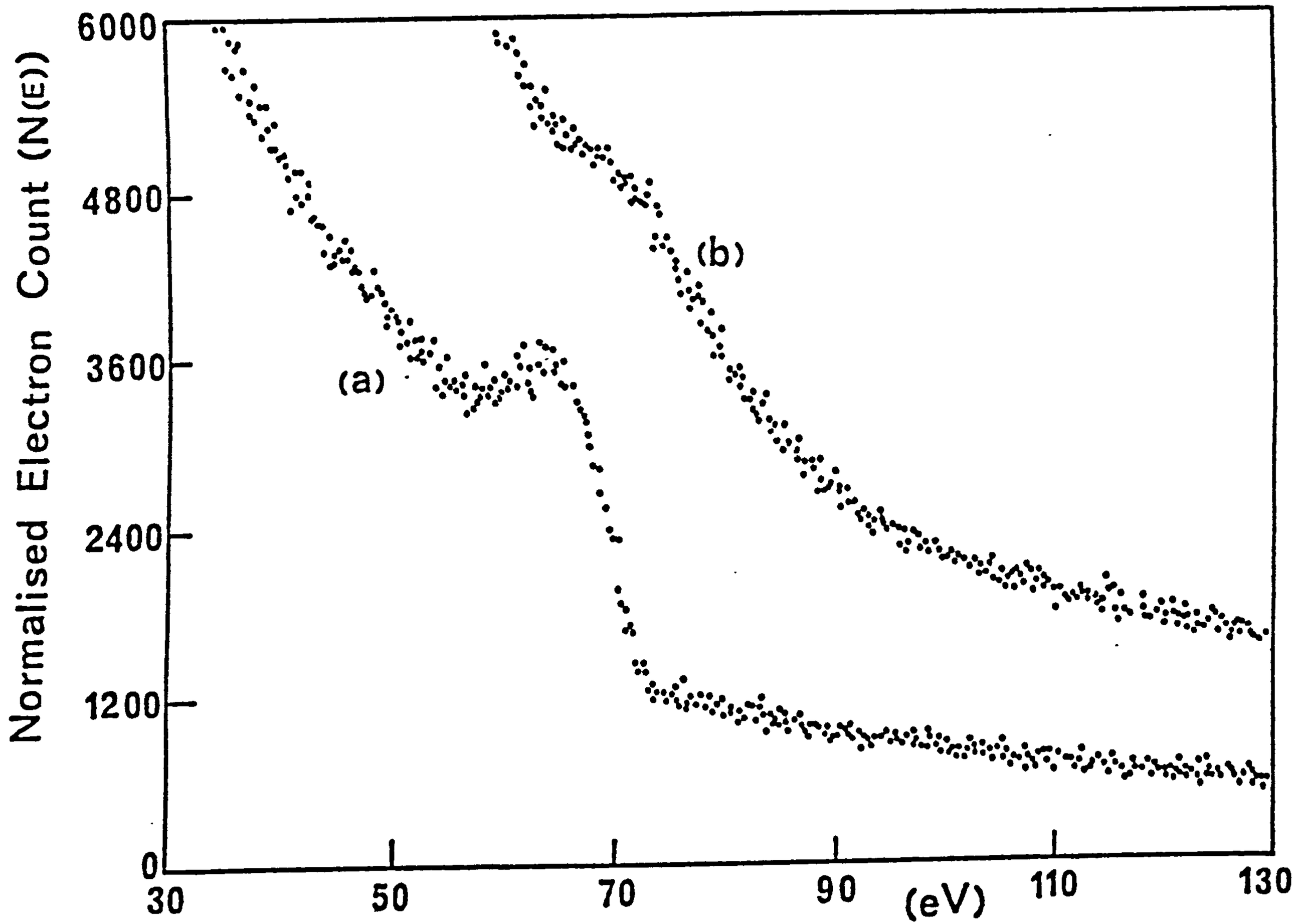

Fig. 9.14 Auger spectra from points (a) and (b) of Fig. 9.13, taken with an analyser constant pass energy of 50 eV, $I_b = 4 \times 10^{-10}$ A, $E_p = 15.2$ keV.

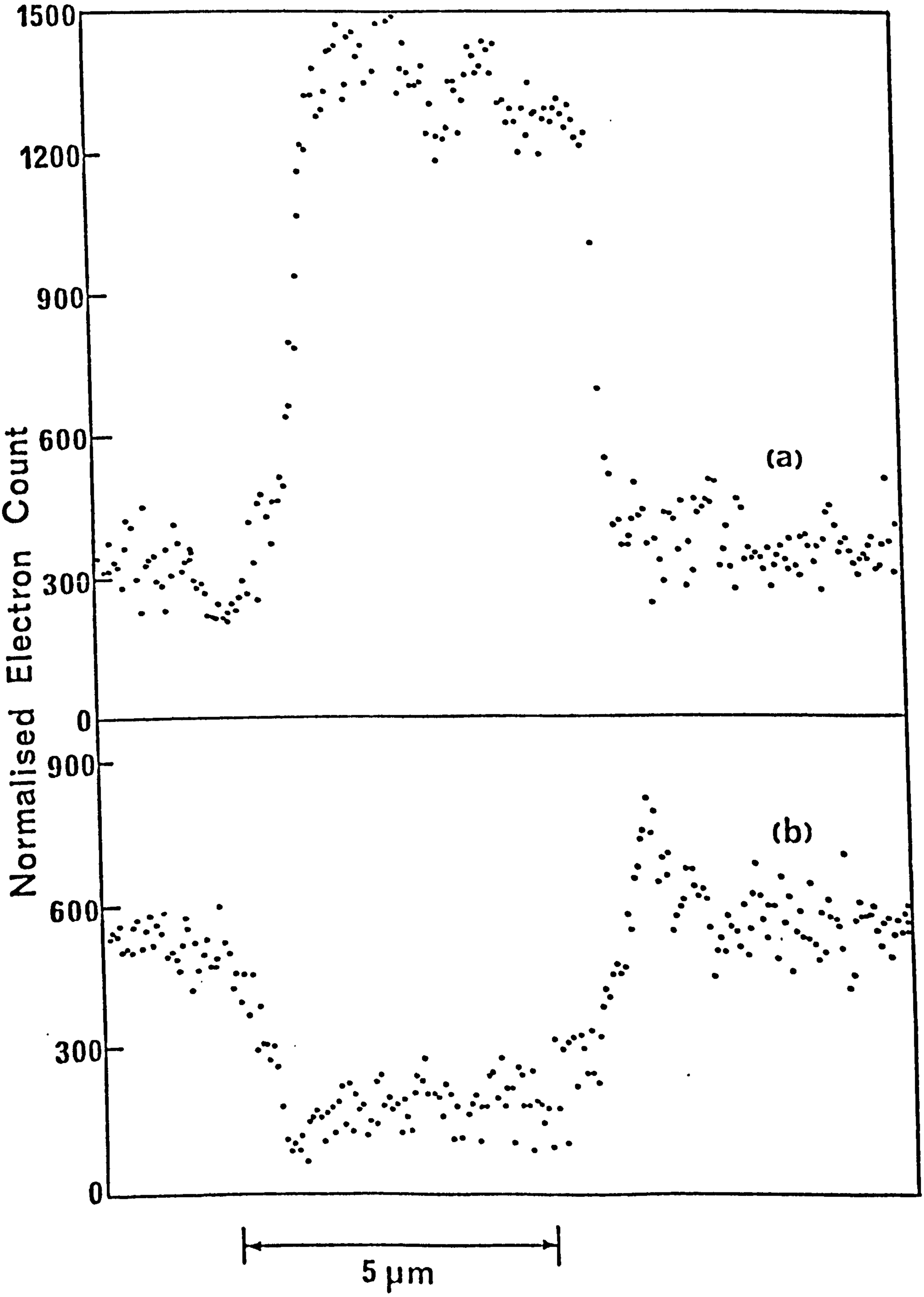

Fig. 9.15 Normalized (SEM) Auger line scans across the line A - A of Fig. 9.13. (a) The Aℓ peak at 63 eV and (b) the Si peak at 73 eV as shown in the spectra of Fig. 9.14.

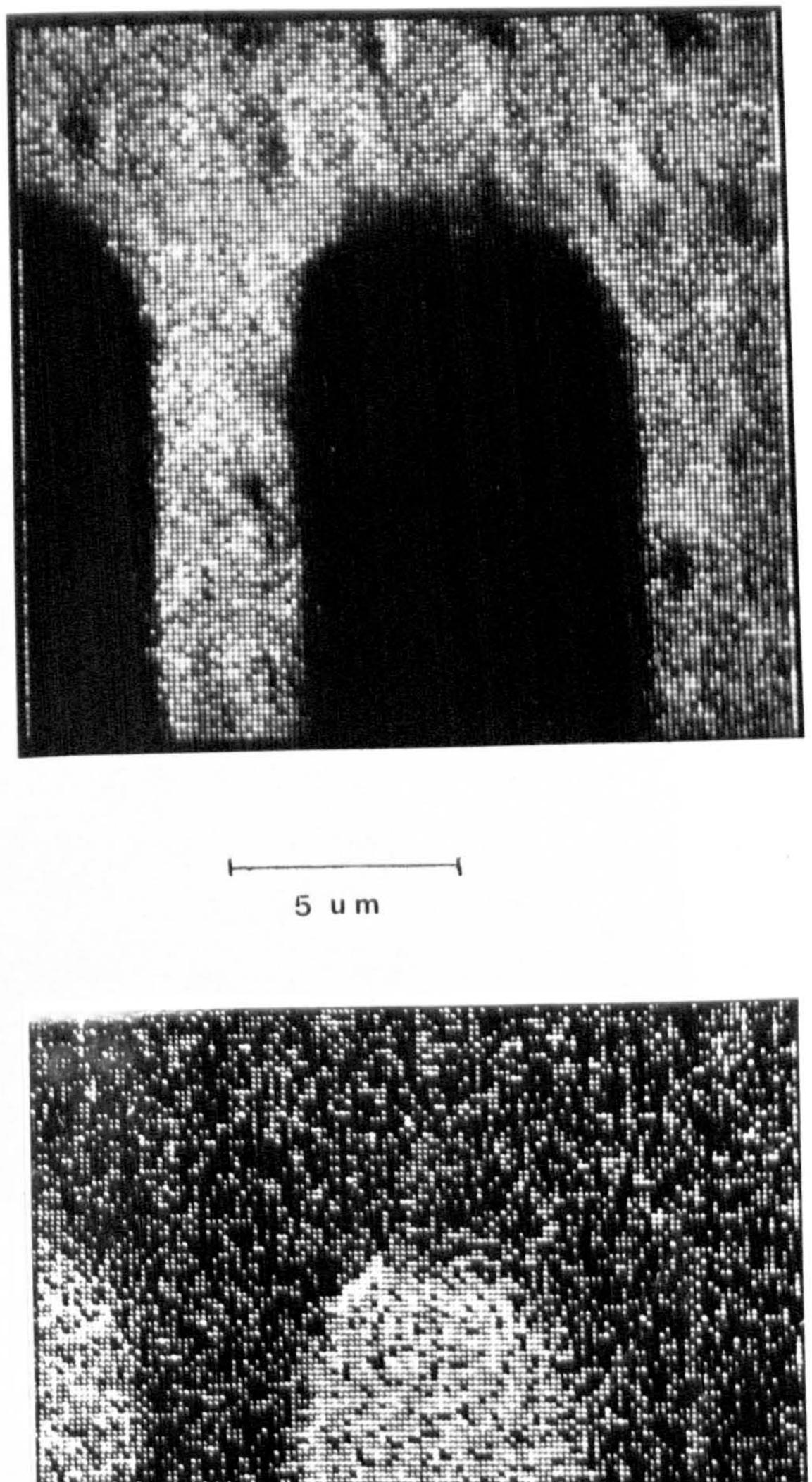

Fig. 9.16 Z (intensity) modulated Aℓ and SiO_2 Auger images of feature shown in Fig. 9.13. 128 x 128 pixels, 20 m sec per pixel. Frame scan time is 7.5 mins.
(a) I_b = 1 nA, Ep = 12.1 keV.
(b) $I_b = 5 - 10 \times 10^{-10}$ A, Ep = 15.8 keV.

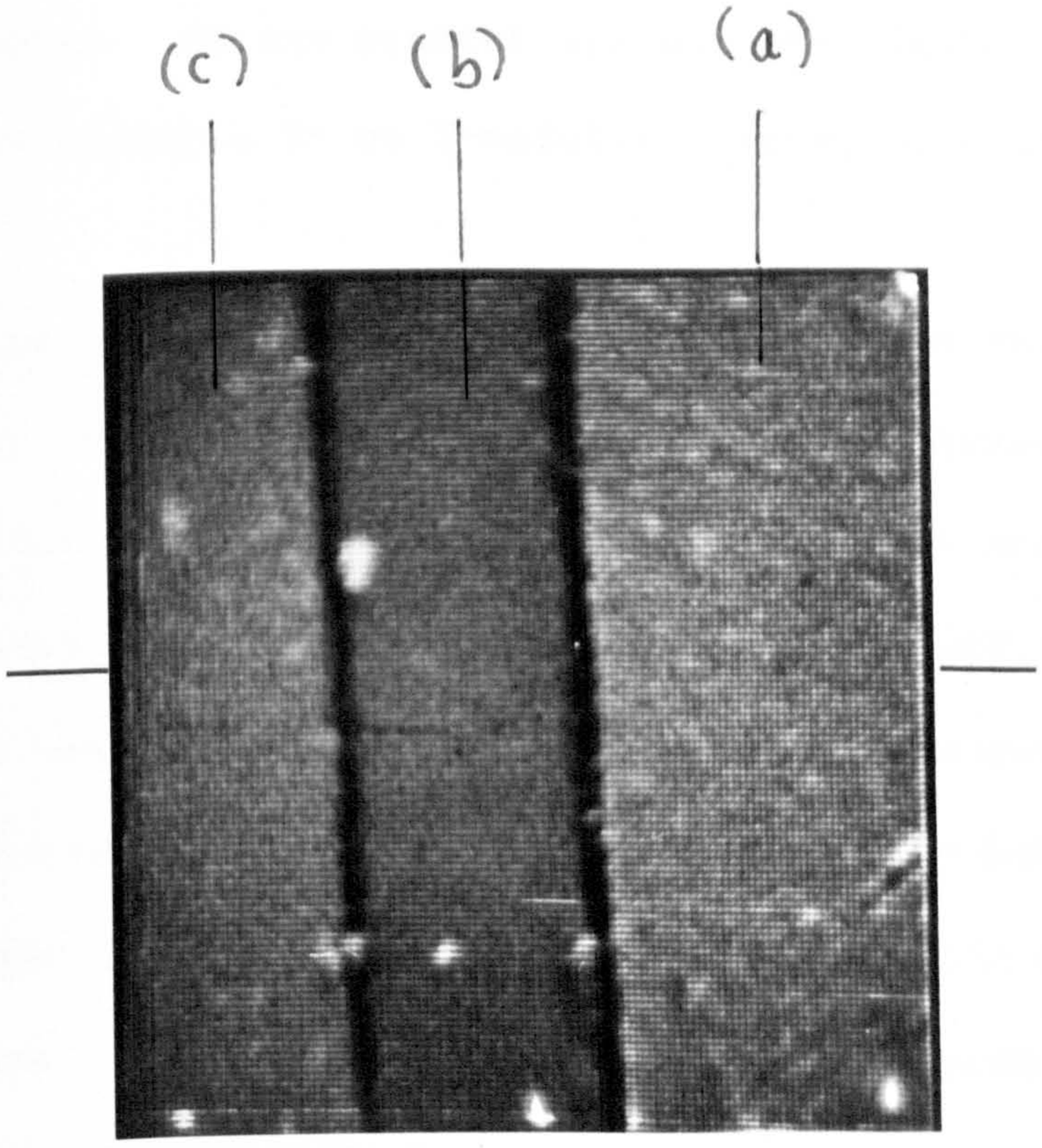

Fig. 9.17 SEM of a microcircuit sample. Ep = 15 keV.

and c respectively. Figure 9.18 shows Auger line scanning across a horizontal line in Figure 9.17 using the different Auger peaks. Due to the overlapping of these energies, the signal level in each line scan has shown three instead of two levels, as the case would be for well separated energies. Auger mapping of this area is shown in Figure 9.19. In both line scans and images, the $(N_1 - N_2)/(N_1 + N_2)$ normalisation was used.

Another way of presenting an Auger image is the "Y-modulation" such as that shown in Figure 9.20. This image can be printed or displayed on the computer screen and is normally used as a guide for the quality of the collected image. In the present system, any digital image can be re-displayed in either a Z- or Y-modulated form, once it has been stored on tape.

The performance of the electron column has shown a probe current of the order of $10^{-8} - 10^{-7}$ into a spot 200 - 300 nm diameter, with probe current stability of about 2 - 3%/hr. Although the measured beam diameter is roughly twice the theoretical calculation of 140 nm, the latter was based on an energy spread ΔV of about 0.9 eV. However, if recent estimates of ΔV are taken into consideration, i.e. $\Delta V \sim 1.5 - 2$ eV, the beam diameter will be controlled by the contribution of chromatic aberration yielding a spot diameter of about 250 - 300 nm in good agreement with the experimental measurements.

Finally, the capability of the column to deliver a beam current in excess of 10^{-7} A with a stability of 2 - 3%/hr offers additional areas of application of the electron column such as electron beam lithography. In addition, this is an improvement on the current state of commercially available field emission probes.

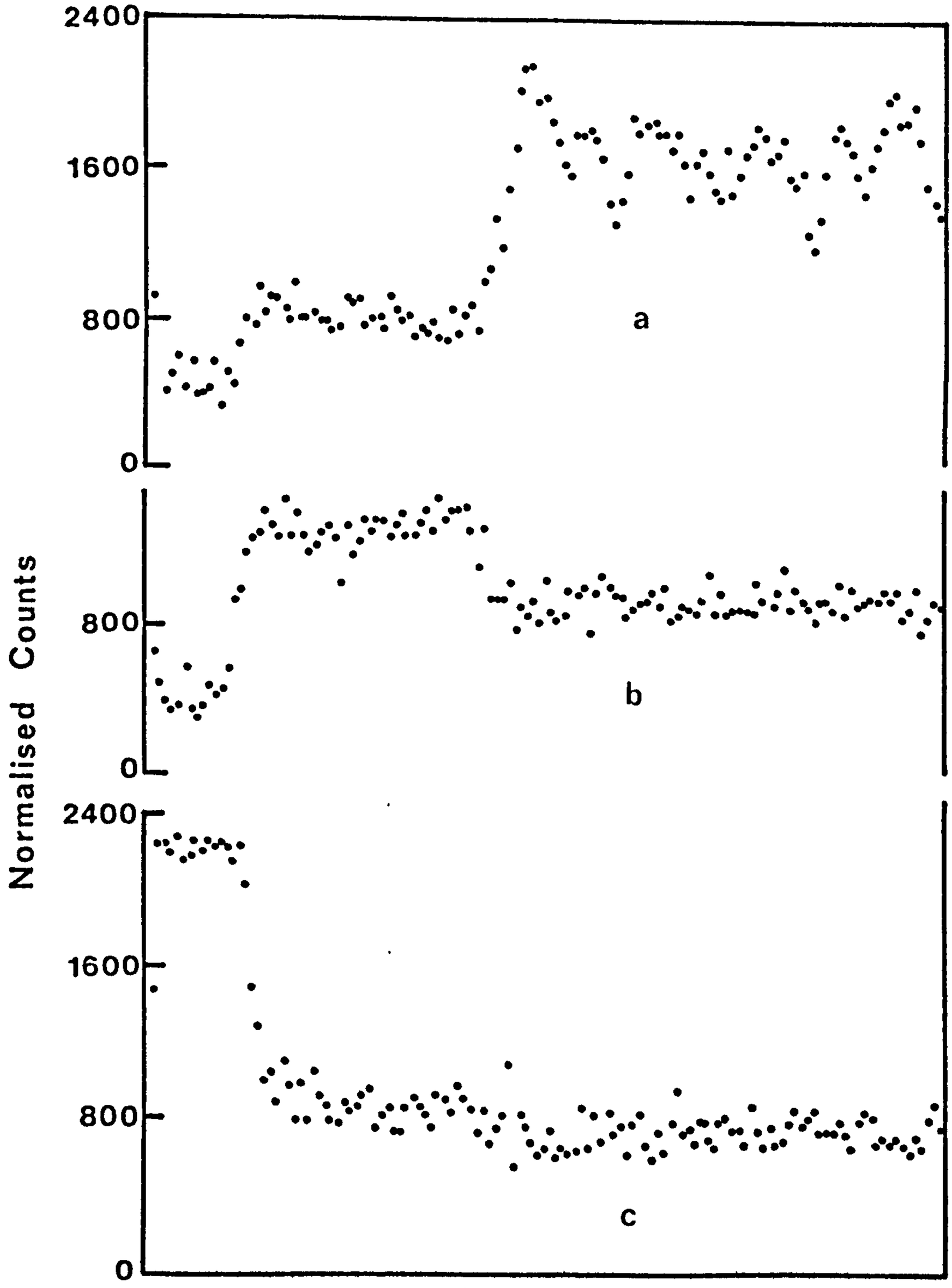

Fig. 9.18 Auger line scans across the line A - A of Fig. 9.17. 50 eV analyser pass energy, normalized with $(N_1 - N_2)/(N_1 + N_2)$. (a) Aℓ (63 eV). (b) SiO_2 (73 eV). (c) Si (90 eV).
Ep = 15.2 keV, I_b = 1.5 nA.

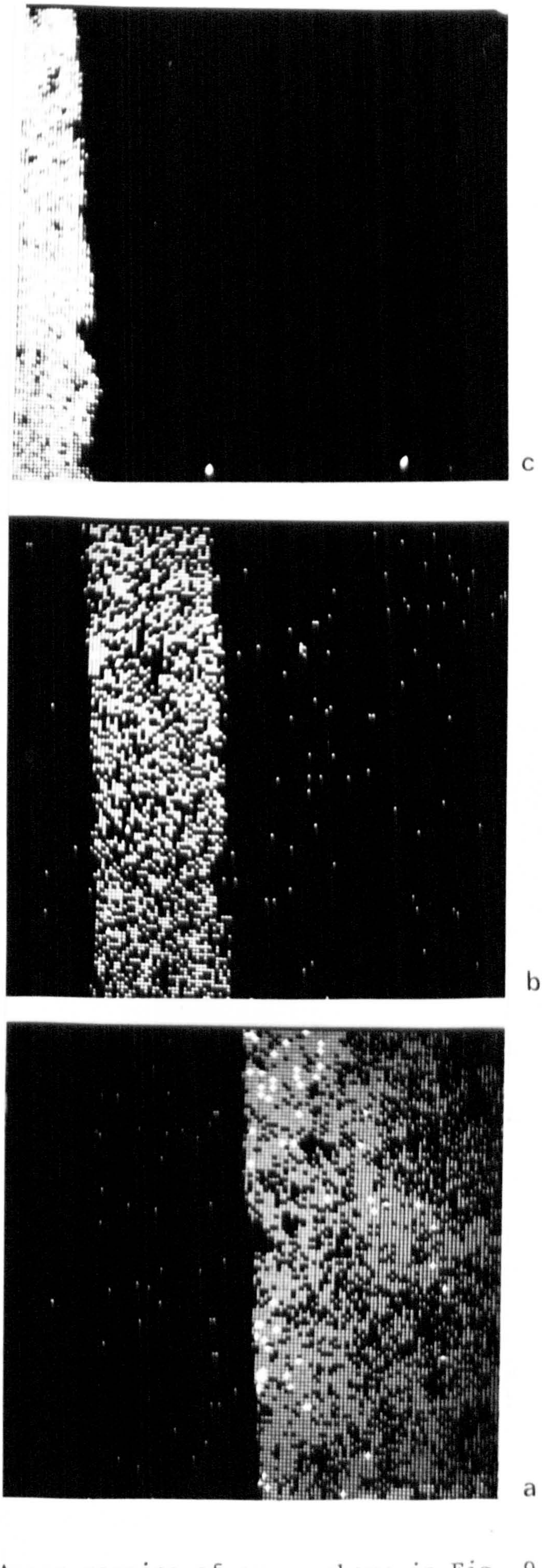

Fig. 9.19 Auger mapping of areas shown in Fig. 9.17. (a) Aℓ (b) SiO_2 and (c) Si. Ep = 15.2 keV. I_b = 1.5 nA.

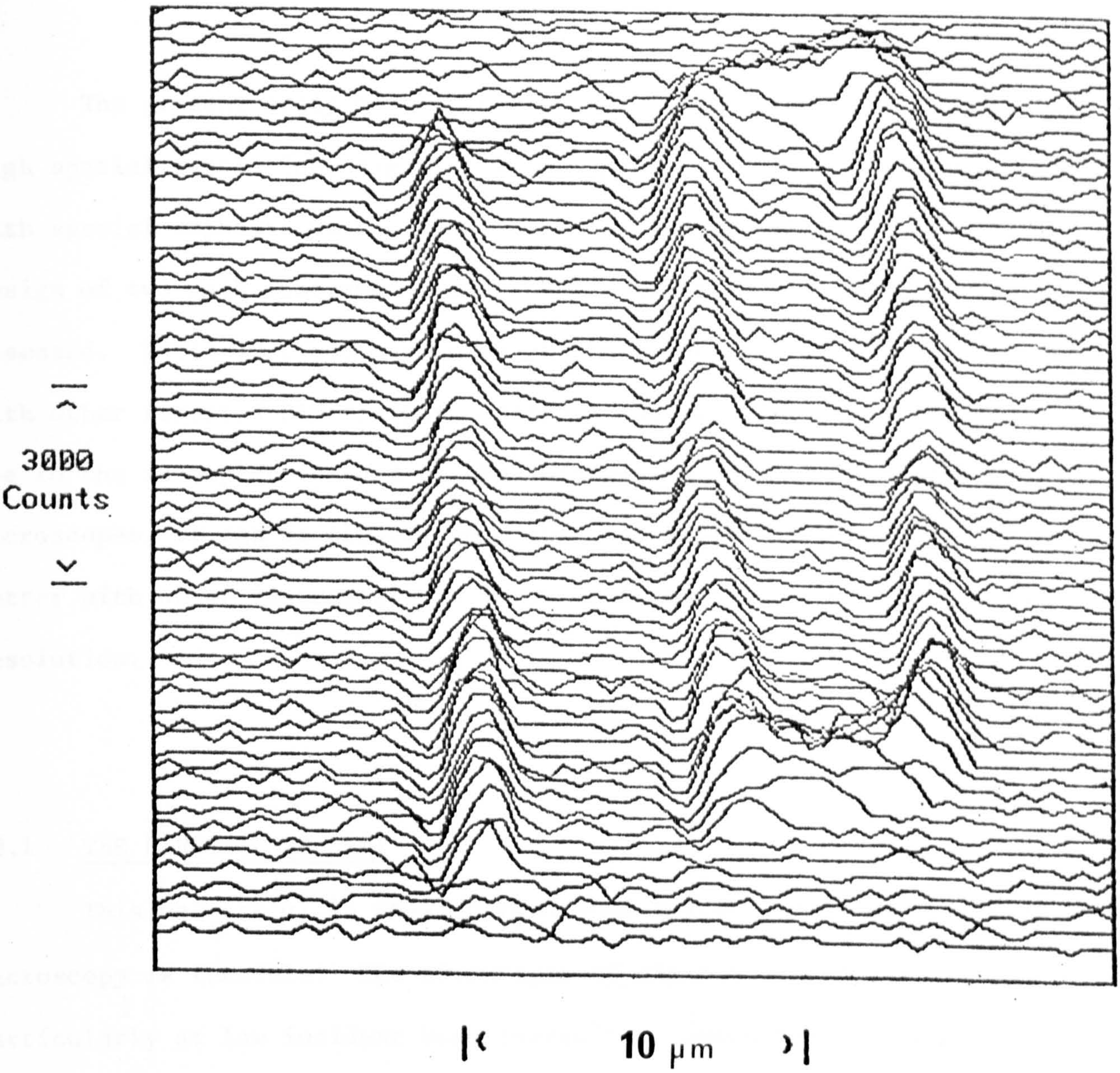

Fig. 9.20 Y modulated Auger image of Aℓ on SiO_2 substrate.

CHAPTER 10

CONCLUSION AND SUGGESTIONS FOR FUTURE WORK

The present study has dealt with the design of a high energy and high spatial resolution, digital, scanning Auger electron microscope (SAM) with special emphasis on the spatial resolution of the technique. The design of two such instruments under UHV conditions have been presented and assessed. Table 10.1 compares some of the properties of these instruments with other reported SAM designs. Although direct comparison is difficult due to the incomplete nature of the information available for the various microscopes, it can be clearly seen that the second instrument compares better with other instruments in terms of frame scan times and spatial resolution.

10.1 THE FIRST INSTRUMENT

This was useful in showing that high spatial and high energy Auger microscopy is feasible. The advantages of digital collection of data particularly at low incident beam current was demonstrated. Auger maps of calcium and sulphur on titanium are given. These are 128 x 128 pixel images with a frame scan time of the order of 28 minutes and a spatial resolution of 100 nm.

The main difficulties with this instrument were the inflexibility to perform in situ complementary experiments essential in surface science (e.g. ion sputtering, thin film deposition, etc.) due to the small size of the vacuum tank. Furthermore, the stability of the specimen stage was inadequate for high resolution microscopy in addition to the lack of sample rotation. But by far the most serious disadvantage of this instrument was

Author	S.R. nm	I_{beam} (A)	Energy Analyser	Electron Source	Signal Processing	F.S.T. 128 x 128 pixel images (mins)
McDonald et al.(80)	5000	2.5×10^{-8}	CMA	T	Analogue	102*
Ishida et al. (83)	700	8×10^{-8}	CMA	T	Analogue	15
Venables et al. (68)	30	2×10^{-8}	CMA	F.E.	Analogue	8.5*
1st instrument	100	5×10^{-9}	CHA	F.E.	Digital	2 8
Le Gressus et al. 198			CMA	T	Analogue	
Veneklasen et al.(133)	40	2.5×10^{-9}	CMA	F.E.	Digital	—
2nd instrument	100	6×10^{-9}	CHA	F.E.	Digital	6

*100 x 100 pixel Auger images

Table 10.1 A comparison of the useful properties of some reported SAM instruments featuring submicron resolution, S.R. (spatial resolution), T (thermal), F.E. (field emitter), F.S.T. (frame scan time).

the performance of the electron optical column in terms of a low and unstable beam current accompanied by a high rate of emitter failure.

10.2 THE SECOND INSTRUMENT

A second instrument was built to avoid some of the above difficulties. This instrument is now operating and comprises a new all electrostatic field emission column, a multiport chamber that carries an additional thermionic gun for standard Auger spectroscopy, a mass spectrometer, a saddle-field ion gun for specimen surface cleaning, a fluorescent screen and window for use with the field emission column and sample as a RHEED camera, an evaporation source, gas admittance facilities, in addition to the electron spectrometer, the secondary electron detector and the specimen stage. The latter is a purpose built, UHV, high stability stage (better than 10 nm) and provides three orthogonal translations in addition to rotation around the azimuth and normal to the specimen surface.

A dedicated desk top computer (HP 9845B) is used for controlling the experiment and processing of data. The computer replaces the purpose built (DMC) described in Chapter 3. Computer control in SAM is necessary for the following reasons. First a particular experiment in SAM is usually complex and requires many adjustments in setting up. In this case computer control allows the operator to concentrate on the experiment rather than on setting it up. Secondly, in order to maximize the signal to noise ratio of the Auger data, particularly at low beam currents as is the case for high resolution SAM, it is necessary to count the collected electrons individually (62). The resulting digital data is conveniently read into a computer for subsequent processing, as demonstrated in the first instrument. Finally, instrumental development in conventional Auger spectroscopy and SAM has come to the point where data processing is necessary (182, 183).

The interfacing of the computer with the instrument is achieved with a set of transistor-transistor logic (TTL) boards designed at York. All the software for control of the experiment, and data collection, storage and subsequent processing had been developed at York (184, 185). Data transfer to a faster computer and more lengthy processing operations for improving the quality of the Auger maps are underway.

Aℓ and SiO_2 Auger images of 128 x 128 pixel with frame scan times of the order of 6 - 8 minutes have been obtained. Representative spectra from a number of samples of different atomic numbers and Auger transitions are presented to demonstrate both the efficiency of collection and the adequacy of beam current.

10.3 THE FIELD EMISSION COLUMN

An all-electrostatic field emission column consisting of a two element lens and an eight pole stigmator/deflector has been described. The lens is based on the type suggested by Butler (137). However, modelling the electron trajectories showed no need for hyperbolically shaped anode surfaces as suggested by Butler. Theoretical estimates of the probe diameter are in the range 40 - 140 nm depending on the emitter and focussing ratio used. The column working distance is 55 mm. External and internal adjustment allow a focussing ratio over the range 7 - 12 to be achieved for an emitter of 2.5 kV extract voltage.

An investigation of the use of field emitters in high current (1 - 100 nA) probes has been carried out. The procedure for emitter processing established in an auxiliary test chamber have been used directly in the final design. Both cold W(310) and thermally assisted Zr/O/W(100) emitters have been used. UOL of tens of hours with an emission stability of 2 - 3%/hr has been achieved from the latter. In addition the

low work function of this emitter allows larger radii to be used at comparable V_e which is advantageous in withstanding microdischarges. However, the disdavantage of this emitter is its large energy spread (~ 0.9 eV) in comparison with cold W(310) (~ 0.2 - 0.3 eV). This has the effect of increasing the electron beam diameter through chromatic aberration. Experimental electron beam profiles within a factor 2 of the theoretical estimate have been obtained. An electron beam current of about 5 - 10 nA in good agreement with theoretical estimates is obtained. Higher beam currents of the order of 10^{-7} Amp have also been achieved in the present column by slightly increasing the extract voltage V_e by about 15 - 20%.

10.4 THE AUGER ELECTRON ENERGY ANALYSER

A concentric hemispherical analyser (CHA) accessed by electron lenses at the entrance plane of the hemispheres is used for energy analysis of the emitted electrons. It operates at a working distance of 10 mm. Six different energy modes (constant energy window or constant resolving power) can be achieved via the control electronics without making any mechanical changes to the electron optics of the analyser assembly. The constant window modes have values of 1 eV, 3 eV and 6 eV while the constant resolving power modes have the values 170, 290 and 630.

In the present geometry, the CHA collects only 1.7% of 2π steradians as opposed to the 10% which can be collected by a CMA. This represents theoretically a fall of a factor 2.4 in signal to noise ratio (or a corresponding increase in data acquisition time to obtain the same signal to noise ratio). However, in practice, the performance of the above described analyser is comparable in signal to noise ratio with CMAs in the same measurement bandwidth. This is probably because CMAs do not achieve shot noise limited performance in the collected current whereas CHAs do.

Another advantage of this CHA is its large depth of focus compared to a CMA. This allows low magnification conditions to be used when forming an energy selected image or line scan. In addition the tolerances required in determining the distance from the analyser to sample surface are greater for the CHA.

10.5 THE SPATIAL RESOLUTION

An investigation of the effects of backscattered electrons on the spatial resolution of SAM has been carried out using Monte Carlo techniques used with some success in EMPA and SEM. Although the model chosen is based on a simpler approach than other more realistic and complicated models, comparable results have been obtained. The model was tested for the generation of Auger electrons with low incident electron energies (where the Rutherford scattering cross section is not strictly applicable) and good agreement with experimental Auger backscattering factors was obtained.

From the results obtained it was found that the spatial resolution limits in SAM are determined mainly by the incident beam diameter. For the specific case of an infinitesimally small beam, (i.e. diameter very much less than the spatial extent of backscattered electrons), broadening effects due to the latter are present but at such a low level that they are unlikely to be detected with the counting statistics normally used in SAM.

An expression for SAM edge resolution (eq. 4.18) was derived for the case of normal electron beam incidence and Auger transitions > 500 eV. This was obtained by convoluting the spatial response function due to backscattered electrons with the profile of the incident beam, assumed to be of the width of a delta function. The obtained results showed that it is the

Auger backscattering factor r that degrades the resolution of an edge but only by a factor of the order of 2 (typically $1 < r < 2$).

A preliminary study of the effects of beam incident angles and energy have shown that backscattering effects will deteriorate the resolution of SAM in the energy range 20 - 40 keV. However, in the case of oblique incidence and sharp chemical edges, two extreme possibilities for the detection of an edge are defined, namely the parallel and perpendicular modes (cf. Chapter 5). It was found that in the parallel mode the contribution of backscattered electrons is minimal. However, for the perpendicular mode two factors are responsible for the deterioration of the resolution. The first is the intersection of the electron beam with the sample surface to produce an ellipse. The effective beam diameter in this case is the major axis of the ellipse. Secondly, the spatial distribution function of Auger electrons due to backscattering is shifted away from the origin and when convoluted with the incident beam the calculated profile is broadened in comparison to the parallel mode.

A theory/experiment comparison for a silver edge on a tungsten substrate in the perpendicular mode was carried out for two beam energies of 20 and 60 keV at 50^{o} angle of incidence. The results obtained confirm that the spatial resolution in SAM is controlled by the profile of the incident beam. Furthermore, the high energy case (60 keV) showed a loss of resolution in comparison with the 20 keV case and is attributed to beam energy effects as predicted.

A different experiment to investigate the effects of oblique angle of incidence in the perpendicular and parallel modes was carried out for an Aℓ edge on SiO_2 substrate. The results obtained showed a better resolution in the parallel mode. In addition this experiment has demonstrated the advantage of being able to rotate the sample in situ around the azimuth, a unique feature of the present SAM.

10.6 FUTURE WORK

10.6.1 The Instrument

The performance of the second instrument has shown that no major modifications to the system are needed. However, there is an ample scope for several additional components that will extend the instrument's analytical power. These will be enumerated briefly below.

i. Ion gun for depth profiling

The ion beam diameter of the present gun is of the order of 1 - 2 mm on exit, but diverges to about 3 cm at the sample position. This arrangement allows specimen surface cleaning but not depth profiling. A duplicate design at a closer distance to sample would allow the latter to be achieved. For this arrangement, the existing ion gun power supply unit can be used.

ii. X-ray detector

In the present configuration, one of the signals produced by the incident electron beam is x-rays. The addition of a solid state detector of the Si (Li) type should enable qualitative EMPA analysis to be carried out. Spectra of all elements heavier than Fℓ can be collected in a few minutes at concentration levels of tenths of a percent (41). The availability of a computer should make the comparison of spectra collected from different points on the sample or with standards a relatively easy task. For the best collection efficiency it can be mounted directly above the sample using a port currently used for visual purposes.

iii. SEM detector

The addition of a chaneltron as an SEM detector is beneficial in collecting secondary electrons at a closer distance and a different angle from the present detector. The latter point is interesting for comparing the normalisation schemes used, while the first is aimed at improving the

signal collection.

iv. Backscattered electron detector

A backscattered electron image has two properties. First, high spatial resolution can be obtained by collecting low deflection backscattered electrons, or by using an energy filter. Secondly, it does not show parts of the specimen that are shielded from the collector. The use of more than one detector at different angles with respect to the incident beam would facilitate the addition and/or subtraction of images to reveal topographical contrast as well as variations in the average z of the examined surfaces (41). A suitable position for these detectors is around the input lens of the CHA.

v. Mini field emission column

The performance of the present field emission column has proved satisfactory in terms of electron beam current and energy. However, it is less advantageous in terms of resolution and continuous variance of the energy of the focussed spot. The latter property in addition to the CHA should make possible performance of angle resolved electron energy loss experiments.

Veneklasen et al. (142) have designed a mini field emission column concentric to a CMA. It has a focussed spot over the range few hundred volts to 4 kV, with a probe current of few nA. For a working distance of 3 mm, it gives a probe diameter of 40 nm at 4 keV.

The author has analysed a similar configuration shown schematically in Figure 10.1 to be used over the energy range 0.1 - 20 keV with a working distance of 10 mm. It consists of two lenses with the stigmator/defector in the middle. The function of the gun lens is to vary the system magnification and hence the beam current. The relation between the probe diameter and energy of the analysed system is depicted in Figure 10.2. A proposed position of this scheme is schematically depicted in Figure 10.3.

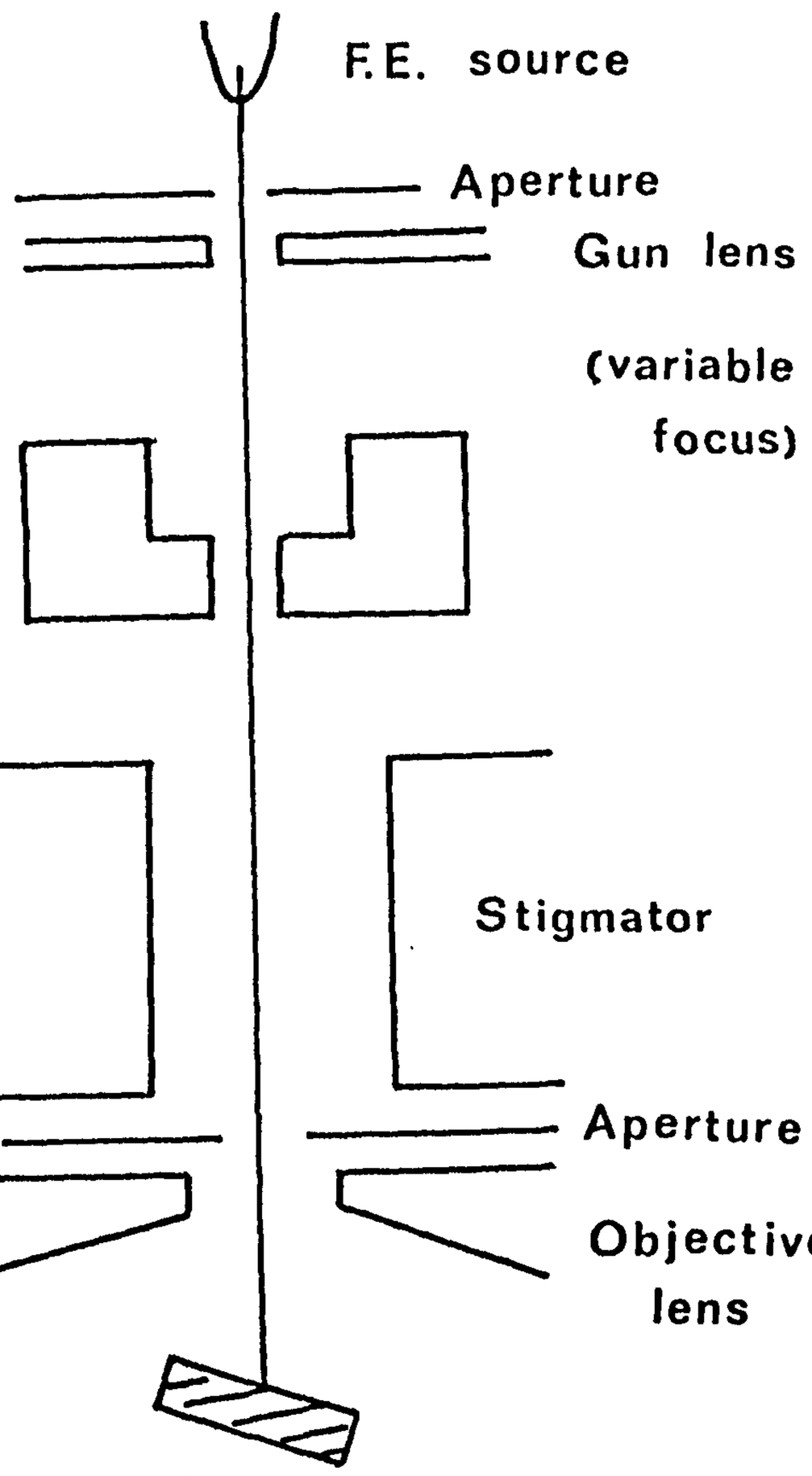

Figure 10.1 Schematic of mini field emission column.

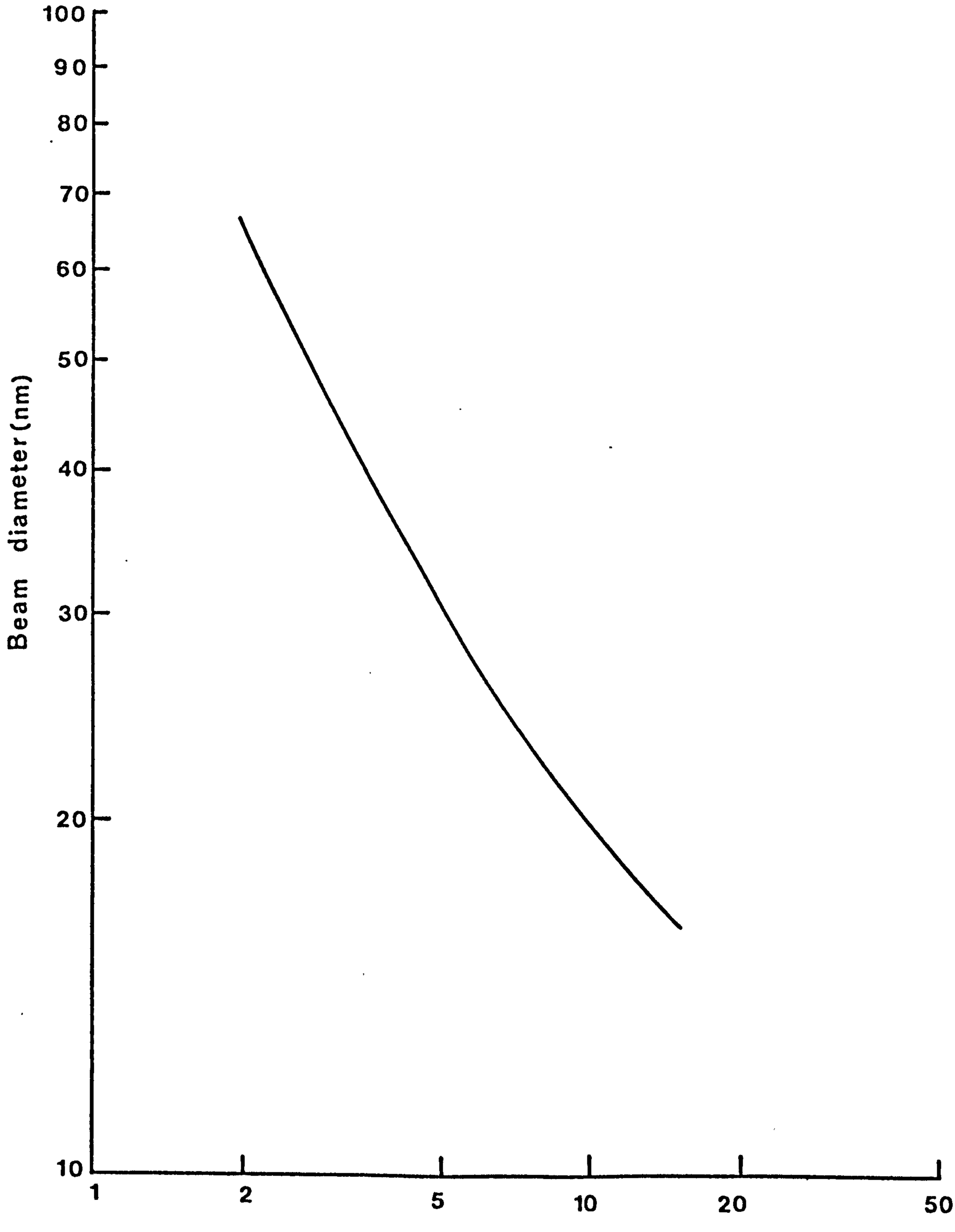

Figure 10.2 The relation between the probe diameter and primary energy of the mini field emission column of Figure 10.1 for a working distance of 10 mm. The calculation is for a source size of about 10 nm, an energy spread of 0.6 V and V_e in the range of 4 - 5 kV. At low primary energy the chromatic aberration is the dominating factor while at high primary energy it is the source size.

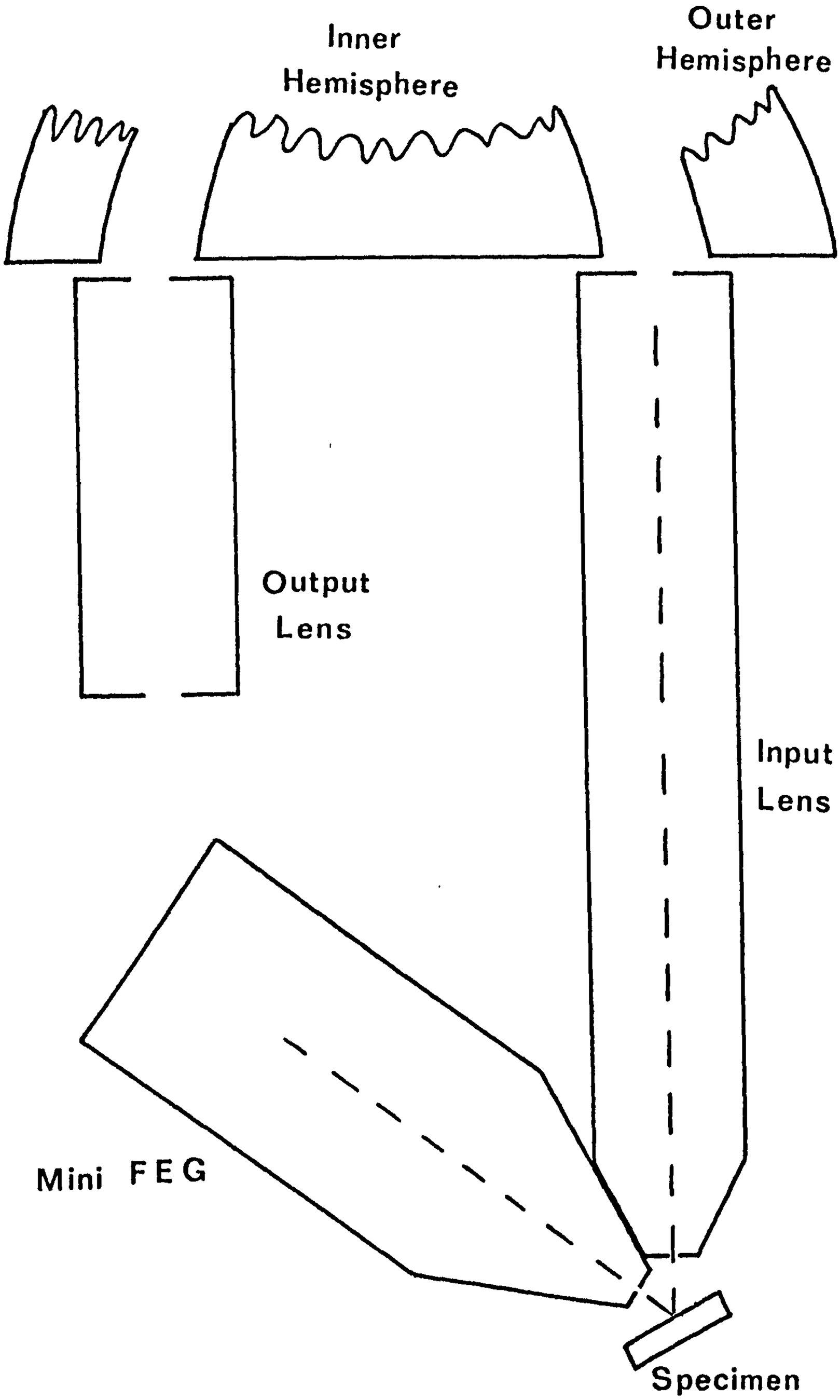

Figure 10.3 A proposed position of the mini field emission column.

This position will have the advantage of a near normal electron beam incidence compared with the present geometry. This should prove useful in terms of resolution. However, the inclusion of such a probe to the system does not imply replacing the present column which will still be useful for RHEED experiments as well as SAM with high primary energies and EPMA studies.

10.6.2 The Monte Carlo Techniques

An extension of the present Monte Carlo model to include the effects of high energy secondaries on SAM resolution is needed. Recently Shimizu et al. (105) have reported that energetic secondaries can be a significant source for low energy Auger transitions. Furthermore, a discrepancy between measured edge profiles of Aℓ and Si (LVV) with the reported theory results. A likely source for this discrepancy is the contribution of energetic secondaries.

10.6.3 Experimental Work

The instrument has been successfully used over the last two years to study several scientific and technological problems, and there remains an ample scope of investigations in different areas. However, at this stage, development of the technique in several areas should have priority.

A feature of the present instrument is the ability to perform RHEED experiments. Figure 10.4 shows the first pattern obtained from a vacuum cleaved In P (110) crystal. This image demonstrates the high resolution that can be obtained with a small probe diameter in comparison with conventional RHEED apparatus where the irradiated area is comparable with the projected area (186). A quantitative experiment to assess the present instrument against conventional RHEED instruments is needed.

Another area of research is the anisotropy of Auger emission (183,

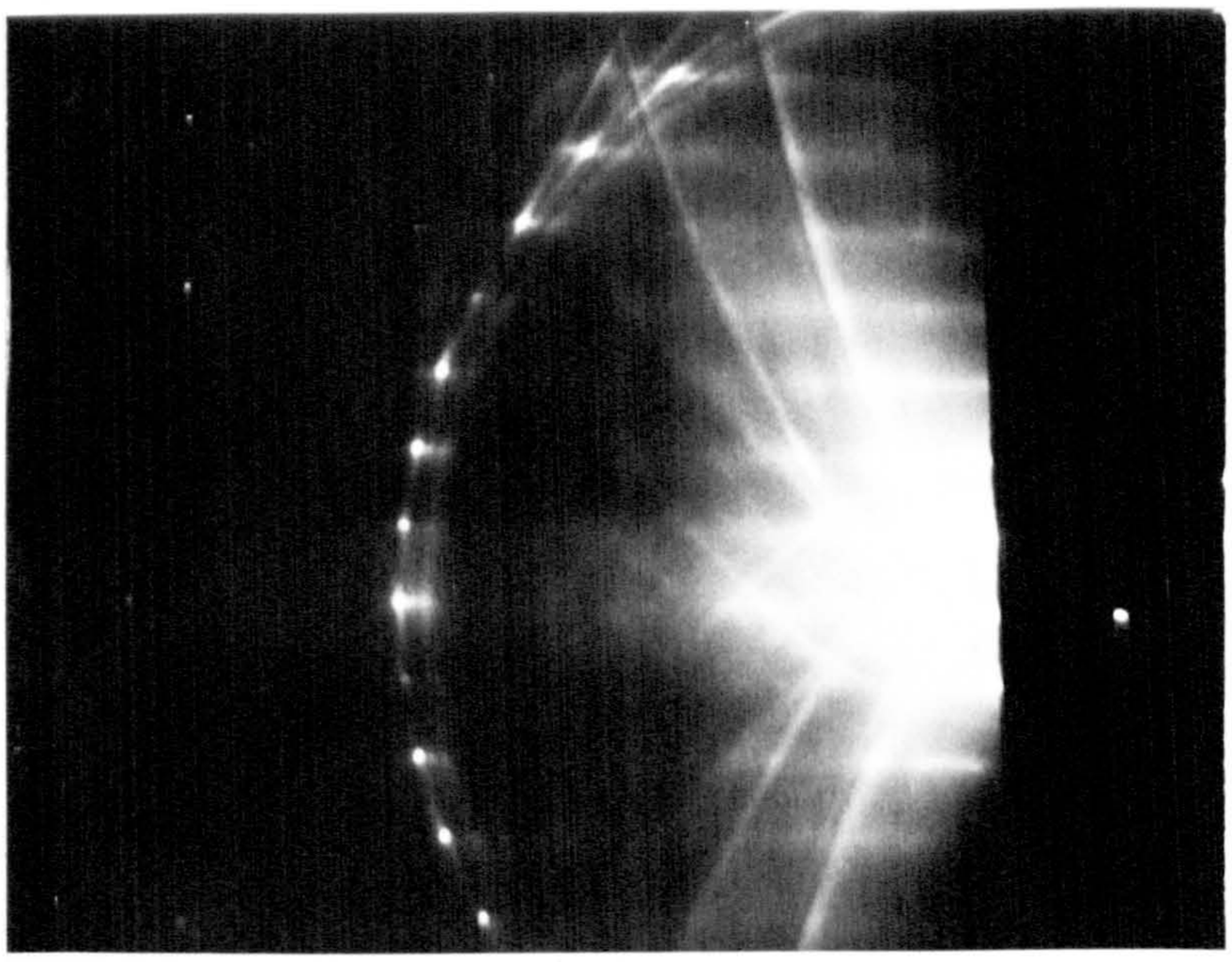

Figure 10.4 A RHEED pattern of a vacuum cleared In P (10) crystal.
E_p = 21.1 kV, I_b = 62.1 nA 2 x 2 μm area.
The spot to the right shows the specular beam(192).

187). This is another factor which may complicate quantitative information from SAM. Prutton (183) has suggested an experiment to study this effect in a SAM that has facilities to rotate the specimen in situ about its surface normal, as in the present instrument.

Finally, the effects of backscattered and high energy secondary electrons should be evaluated experimentally for a range of different Z materials. The difficulty of this experiment is the formation of a sharp chemical edge but shadowing techniques as used by Janssen and Venables should be easy to use.

REFERENCES

(1) P. Auger, J. Phys. Raduium, 6, (1925) 205.
P. Auger, Surf. Sci., 44, (1975).

(2) E.H.S. Burhop, The Auger effect and other radiationless transitions. London, Cambridge University Press (1952).

(3) D. Chattarji, The theory of Auger transitions, Academic Press (1976).

(4) J.J. Lander, Phys. Rev., 91, (1953) 1382.

(5) L.A. Harris, J. App. Phys., 39, (1968) 1419.

(6) R.E. Webber and W.T. Peria, J. App. Phys., 38, (1967) 4355.

(7) T.E. Gallon and J.A.D. Matthew, Rev. of Phys. in Tech., 3, (1972) 31.

(8) M.F. Chung and L.H. Jenkins, Surf. Sci., 22, (1970) 479.

(9) J.A.D. Matthew, J. Phys., B, (1971) 19.

(10) E. Antonides, E.C. Janse and G.A. Sawatzky, Phys. Rev. B, 15, (1977).

(11) J.A.D. Matthew and C.M. Watts, Phys. Letts., 37A, (1971) 239.

(12) H.E. Bishop and J.C. Rivère, J. App. Phys., 40, (1969) 1740.

(13) C.J. Powell, Surf. Sci., 44, (1974) 29.

(14) C.R. Brundle, Surf. Sci., 48, (1975) 99.

(15) M.P. Seah and W.A. Dench, Sur. Int. Analysis 1, (1979) 2.

(16) D.R. Penn, Phys. Rev. B, 13, (1976) 6248.

(17) C.C. Chang, Surf. Sci., 48, (1975) 9.

(18) C.R. Worthington and S.C. Tomlin, Proc. Phys. Soc. A, 69, (1956) 401.

(19) M. Gryzinski, Phys. Rev., 138A (1965) 305.

(20) C.J. Powell, Rev. Mod. Phys., 48, (1976) 33.

(21) T.E. Gallon, J. Phys. D, Appl. Phys., 5, (1972) 822.

(22) D.M. Smith, T.E. Gallon and J.A.D. Matthew, J. Phys. B, 7, (1974) 1255.

(23) J.J. Vraaking and F. Meyer, Phys. Rev. A, 9, (1974) 1932.

(24) P.M. Hall and J.M. Morabito, Surf. Sci., 83, (1979) 391.

(25) W. Reuter, in: Proc. 6th Intern. Conf. on x-ray Optics and Microanalysis, (Univ. of Tokyo Press, 1972) 121.

(26) R.L. Gerlach and A.R. Ducharme, Surf. Sci., 32, (1972) 329.

(27) D.M. Smith and T.E. Gallon, J. Phys. D, App. Phys., 7, (1974) 151.

(28) K. Sevier, Low Energy Electron Spectrometry, (1972) J. Wiley.

(29) K. Siegbahn et al., ESCA, Uppsala, Almqvist and Wiskell (1967).

(30) N.J. Taylor, Rev. Sci. Ins., 40, (1969) 792.

(31) P.W. Palmberg, G.K. Bohn and J.C. Tracy, App. Phys. Lett., 15, (1969) 254.

(32) P.J. Bassett, T.E. Gallon and M. Prutton, J. Phy. E: Sci. Inst., 5, (1972) 1008.

(33) C.J. Powell, N.E. Erickson and T.E. Madey, Elect. Spec. & Rel. Phen., 25, (1982) 87.;

(34) C. Le Gressus, SEM 82, IITRI, (1982).

(35) T.E. Gallon and J.A.D. Matthew, J. Phys. D, 5, (1972) L69.

(36) J.A.D. Matthew and M.M. El Gomati, Surf. Int. Analysis 1, (1979) 135.

(37) A. Ignative, A.V. Jones and T.N. Rhodin, Sur. Sci., 30, (1972) 573.

(38) H.E. Bishop and J.C. Rivere, J. Phys. D, 2, (1969) 1635.

(39) C.J. Powell, Surf. Sci., 4, (1980) 492.

(40) G.R. Booker, (1970), Modern diffraction and imaging techniques in material science. Amsterdam, N. Holland.

(41) O. Wells, (1974) (and ref. within), Scanning Electron Microscopy, New York, McGraw Hill.

(42) M.P. Seah and E.D. Hondros, Proc. Roy. Soc., A335, (1973) 191.

(43) A. Janssen, J.A. Venables, J.C. Hwang and R.W. Balluffi, Phil. Mag., 36, (1977) 1537.

(44) S. Ichimura, M. Shikata and R. Shimizu, Surf. Sci., 108, (1981) L393.

(45) L.A. Larson, M. Prutton and H. Poppa, J. Vac. Sci. Techn., 20, (1982) 1403 and M. Prutton (private comm.).

(46) A. Rose, Adv. Electron. 1, (1948) 131.

(47) A. Van Oostrom, Surf. Sci., 89, (1979) 615.

(48) A. Mogami and T. Sekine, Proc. 9th Int. Congr. Elect. Microscopy, Toronto, (1978).

(49) P.H. Holloway, T.E. Madey, C.T. Campbell, R. Rye and J. Houston, Surf. Sci., 88, (1979) 121.

(50) B. Joyce and J. Neave, Surf. Sci., 34, (1973) 401.

(51) J. Coad, H. Bishop and J. Rivère, Surf. Sci., 21, (1970) 253.

(52) J. Verhoven and J. Los, Surf. Sci., 83, (1979) 109.

(53) C.C. Chang, Charact. Solid Surf., (1974) Plenum, New York.

(54) S. Mroz, Surf. Sci., 102, (1981) L71.

(55) K. Roll, App. Surf. Sci., 5, (1980) 388.

(56) S. Hoffmann and A. Zalar, Thin Solid Films, 56, (1979) 337.

(57) D. Peacock, M. Prutton and R. Roberts, (1982) to be published.

(58) J.L. Hock, D. Snider, J. Kovacich and D. Lichtman, App. Surf. Sci., 10, (1982) 405.

(59) R. Browning, P.J. Bassett, M. El Gomati and M. Prutton, Proc. Roy. Soc., London, A357, (1977) 213.

(60) H. Bishop, SEM 82, IITRI, (1982).

(61) M. Prutton, J. Elect. Spec., 11, (1977) 197.

(62) G. Todd, H. Poppa, D. Moorhead and M. Bales, J. Vac. Sci. Tech., 12, (1975) 953.

(63) C. Le Gressue and D. Massignon, C.R. Acad. Sci., Paris, L286, (1975) 401.

(64) A. Mogami, Int. Thin Film Cong., Loughborough, U.K., (1978).

(65) M.P. Seah and C. Lea, SEM 73, Inst. Phys., U.K., (1973) 276.

(66) A. Janssen, C.J. Harland and J.A. Venables, Surf. Sci., 62, (1977) 277.

(67) G. Todd and H. Poppa, J. Vac. Sci. Tech., 15, (1978) 672.

(68) J.A. Venables, A.P. Janssen, C.J. Harland and B.A. Joyce, Phil. Mag., 34, (1975) 495.

(69) M. Prutton, L. Larson and H. Poppa, J. App. Phys., (1983).

(70) J.R. Cleaver and K. Smith, SEM 73, Inst. Phys., U.K., (1973) 6.

(71) P.J. Bassett, J. Phys. E, 7, (1974) 461.

(72) A.V. Crewe, J. Wall and L.M. Weller, J. App. Phys., 39, (1968) 5861.

(73) P.J. Bassett, T.E. Gallon and M. Prutton, J. Phys. E, 5, (1972) 1008.

(74) C.E. Kuyat and J.A. Simpson, Rev. Sci. Inst., 38, (1967) 103.

(75) D.W.O. Heddle, J. Phys. E, Sci. Inst., 4, (1971) 598.

(76) SAM internal report (1973) not published.

(77) R. Browning, Digital Microscope Controller (1977) not published.

(78) M. Prutton, private comm.

(79) P. Palmberg, G. Riach, R. Weber and N. MacDonald, Handbook of AES, Phys. Elect. Ind., (1972).

(80) N.C. MacDonald and J.R. Waldrop, App. Phys. Lett., 19, (1971) 315.

(81) K. Smith, private comm.

(82) A. Christou, J. App. Phys., 47, (1976) 5464.

(83) T. Ishida, M. Uchiyama, Z. Oda and H. Hashimoto, J. Vac. Sci. Tech., 13, (1976) 711.

(84) L. Schlabach, A. Seiler, F. Stucki and H.C. Siegmann, J. Less Com. Met., 73, (1980).

(85) S.J.B. Read, Electron Microprobe Analysis, Cambridge Univ. Press, (1975).

(86) O.C. Wells, A.N. Brores and C.G. Bremer, App. Phys. Lett., 353, (1973) 353.

(87) J. Cazaux, Rev. de Physique App., (1975) 263.

(88) M. Green, Proc. Phys. Soc., (London), 82, (1963) 204.

(89) H. Bishop, Proc. Phys. Soc., (London), 85, (1965) 855.

(90) R. Shimizu and K. Murata, J. App. Phys., 42, (1971) 387.

(91) E.R. Krefting and L. Reimer, Quant. Anal. with Elect. Microprobes and Sec. Ion Mass Spec., Julish, Jul. Conf. 8, (1973) 114.

(92) L. Curgenven and P. Duncumb, TI Research Lab. Report 303, (1971).

(93) R.B. Bolen and E. Lifshin, SEM 73, IITRI, (1973) 286.

(94) G. Love, M.G. Cox and V.D. Scott, J. Phys. D. (App. Phys.), 10, (1977) 7.

(95) T. Koshikawa and R. Shimizu, J. Phys. D, 7, (1974) 1303.

(96) E.H. Darlington, J. Phys. D. (App. Phys.) 8, (1975) 85.

(97) H.A. Bethe, Ann. Physik (Leipzig) 5, (1930) 325.

(98) T.S. Rao-Sahib and D.B. Wittery, J. App. Phys., (1974).

(99) F. Bloch, Zeit. Phys., 81, (1933) 363.

(100) P. Duncumb and C. Da Casa, Electron Probe Microanalysis, London, (1967).

(101) M. Lotz, Z. Physik, 232, (1970) 101.

(102) C.J. Powell, Surf. Sci., 44, (1974) 29.

(103) P. Duncumb in (94).

(104) K. Murata, SEM 73, IITRI, (1973) 268.

(105) R. Shimizu, M. Aramata, S. Ishimura, Y. Yamazaki and T. Ikuta, App. Phys. Lett., 31, (1977) 692.

(106) J. Kirshner, App. Phys., (1977) 539.

(107) J.A. Bearden and A.F. Burr, Rev. Mod. Phys., (1967) 128.

(108) A. Jablonski, Surf. and Interface anal. 1, (1979).

(109) A.P. Janssen and J. Venables, Surf. Sci., 77, (1978) 351.

(110) D. Swann and K.C.A. Smith, SEM 73, 11T, (1973).

(111) M.E. Haine and P.A. Einstein, Brit. J. App. Phys., 3, (1952) 40.

(112) A.N. Brores, 5th Int. Conf. on Ion and Laser Beam Science and Tech., Electrochemical Soc., New York, (1972) 3.

(113) A.N. Brores and H.C. Pfeiffer, Record of 11th Symposium on Electron and Laser Beam Tech., Boulder, (1971) 205.

(114) H. Boersch, Z. Physik, 139, (1954) 115.

(115) J.M. Lafferty, J. App. Phys., 22, (1951) 299.

(116) A.N. Brores, J. Phys. E. Sci. Inst. Series 2, 2, (1969) 273.

(117) H. Ahmed, Electron Microscopy Inst. Phys. Conf. Series, 14, (1972) 10.

(118) R. Shimizu, Y. Kataoka, S. Kawai and T. Tanaka, App. Phys. Lett., 27, (1975) 113.

(119) S. Zaima, et al., J. Phys. D. 13, (1980) 47.

(120) R.H. Fowler and L. Nordheim, Proc. Roy. Soc., A119, (1928) 173.

(121) R.H. Good and E. Müller, Handbuch der Physik, 21, (1956) 178.

(122) W.P. Dyke and W.W. Dolan, Adv. Electronics and Electron Phys., 8, (1956) 89.

(123) L.W. Swanson and A.E. Bell, Adv. Electronics and Electron Physics, 32, (1973) 193.

(124) C.A. Spindt, I. Brodie, L. Humphrey, E.R. Westerberg, J. App. Phys., 47, (1976) 5248.

(125) J.R. Cleaver, Ent. J. Electronics, 38, (1975) 513.

(126) J.C. Wiesner, Ph. D. Thesis, Univ. of Calif., Berkeley, (1970).

(127) L. Swanson, private comm.

(128) S. Tamaki, T. Inoue, E. Sugata and H. Kim, Jap. J. App. Physics, 15, (1976) 265.

(129) R.D. Young, Phys. Rev., 113, (1959) 110.

(130) R.D. Young and E. Müller, Phys. Rev., 113, (1959) 115.

(131) A.G. Van Oostrom, Philips Res. Rep. Supp. 11, (1966) 102.

(132) A.D. Cumming and K.C.A. Smith, Microcurrent Eng., Cambridge, (1978).

(133) L. Veneklasen, N. Yew and J. Wiesner, Int. Conf. on Ion and Laser beam Sciences and Tech., (1979) 11.

(134) L. Swanson and L.C. Crouser, J. App. Phys., 40, (1969) 4741.

(135) D. Swann and K.C.A. Smith, SEM 73, IITRI, (1973).

(136) E. Müller and T.T. Tsong, Field Ion Microscopy, Elsevier, New York, (1969).

(137) J.W. Butler, Proc. 6th Int. Conf. Electron Microscopy, (1966) Japan, 191.

(138) J.P. Barbour, F.M. Charbonnier, W.W. Dolan, W.P. Dyke, E.E. Martin and J.K. Trolan, Phys. Rev., 117, (1960) 1452.

(139) L.W. Swanson and N.A. Martin, J. App. Phys., 46, (1975) 2029.

(140) P.C. Bettler and F.M. Charbonnier, Phys. Rev., 119, (1960) 85.

(141) R. Shimizu, Y. Kataoka and H. Hashimoto, Tech. Reports, Osaka Univ., 23, (1973) 403.

(142) L. Veneklasen, private comm.

(143) L. Veneklasen and B. Siegel, J. App. Phys., 43, (1972) 1600.

(144) P. Grivet, Electron Optics, Pergamon Press, (1972).

(145) A. El Kareh and J.C. El Kareh, Electron Beams, Lenses and Optics, Academic Press, (1970).

(146) L. Frank, Optik, 41, (1974) 245.

(147) K. Smith, Ph. D. Thesis, Univ. of Cambridge, (1957).

(148) *J.A. Venables and A.P. Janssen,* Ultramicroscopy, 5, (1980) 297.

(149) G. Todd, H. Poppa and L. Veneklasen, Thin Solid Films, 57, (1979) 213.

(150) A. Crewe, Q. Rev. of Biophysics, 3, (1970) 137.

(151) E. Munro, E. Mag. 73, U.K., (1973).

(152) K. Kuroda, H. Ebisui and T. Suzuki, J. App. Phys., 45, (1974) 2338.

(153) F.H. Read, J. Sci. Inst., 3, (1970) 127.

(154) K. Kuroda and T. Suzuki, App. Phys. Lett., 25, (1974) 23.

(155) G.H.N. Riddle, J. Vac. Sci. Tech., 15, (1978) 857.

(156) R. Seeliger, Optik, 4, (1948) 258.

(157) J. Orloff and L.W. Swanson, J. App. Phys., 50, (1979) 2494.

(158) E. Munro, Cambridge Univ. Report CUEDIB - Elect. TR45, (1975).

(159) E. Munro, Image processing and computer aided design in electron optics. Ed. P.H. Hawkes, Academic Press, London, (1973).

(160) O. Rang, Optik, 5, (1949) 518.

(161) P.A. Redhead, The physical basis of ultra high vacuum, Chapman and Hall, London, (1968).

(162) J.P. Shannon, S.F. Philip and J.G. Trump, J. Vac. Sci. Tech., 2, (1965) 234.

(163) C.J. Bennette, L.W. Swanson and F.M. Charbonnier, J. App. Phys., 38, No. 2, (1967) 634.

(164) P. Bolen, F. Tse, W. Bell and M. Mulcahy, (Trans. IEEE), Insulation/circuits, (1970) 59.

(165) M. Achard, A. Calder and A. Matthewson, Vac., 29, (1979) 53.

(166) K.J. Hansen and R. Lauer, Focussing of charged particles, Ed.: A. Septier, Academic Press (1967).

(167) M.J. Kofoid, Proc. A.I.E.E. 1960, Part III, 79.

(168) A. Craven, Ph. D. Thesis, University of Cambridge, (1975).

(169) F. Bertein, Ann. de Rod. electricite, 2, (1947).

(170) P.A. Sturrock, Phil. Trans. Roy. Soc., 243A, (1951) 387.

(171) G.D. Archard, J. Sci. Inst., 30, (1953) 352.

(172) K. Kuroda, Y. Shingua and T. Suzuki, Japan. J. App. Phys., 13, (1974).

(173) M.E. Haine, J. Sci. Instrum., 31, (1954) 325.

(174) K.A. Hughes, J. App. Phys., 38, (1967) 4922.

(175) B.W. Griffith, P. Pollard and J.A. Venables, Proc. 5th Eur. Cong. Electron Microscopy, U.K., (1972).

(176) A.J. Gonzales, Electron, Ion, Laser Beam Tech., Berkeley, (1967).

(177) T.E. Everhart and R.F. Thornley, J. Sci. Inst., 37, (1960).

(178) H. Ahmed and A. George in (41).

(179) Focussing of charged particles, Ed.: A. Spetier. Academic Press, (1967).

(180) J. Cleaver, Ph. D. Thesis, Univ. of Cambridge, (1973).

(181) P.H. Holloway, Surf. Sci., 66, (1977) 479-497.

(182) H. Bishop, SEM 82, IITRI, U.S.A., (1982).

(183) M. Prutton, SEM 82, IITRI, U.S.A., (1982).

(184) R. Browning, D. Peacock and M. Prutton, EMAG 81, Cambridge (1981).

(185) M. Prutton and D. Peacock, J. A. Microscopy, 127, Pt. 1, (1982) 105 - 118.

(186) A. Chambers, private comm.

(187) D.M. Zehner, J.R. Noonan and L.H. Jenkins, Solo State Com. 18, (1976).

(188) P.H. Holloway, Surf. Sci., 66, (1977) 479.

(189) G.G. Kleinman, App. Surf. Sci., 11 - 12, (1982) 730.

(190) P.H. Holloway, J. Elec. Spec. and Rel. Phen., 7, (1975).

(191) C.C. Chang, Charact. Solid Surf., Eds.: P.F. Kane and G.G. Larrabee, Plenum, New York, (1978).

(192) D. Peacock, D. Phil. Thesis, Univ. of York, in preparation.

(193) HB 50 A, Scanning Electron Microscope, V.G. Microscopes Ltd., U.K.

(194) K. Kuroda, H. Ebisui and T. Suzuki, J. App. Phys., 46, (1975).

(195) H. Kuo and B. Siegel, Int. Conf. on Ion and Laser Beam Sciences and Tech., (1979) 5.

(196) D. Tuggle, private comm.

(197) S. Ichimura and R. Shimizu, Surf. Sci., 112, (1981) 386.

(198) C. Le Gressus, D. Massignon, A. Mogami and H. Okuzumi, SEM/11TR1 (1979).

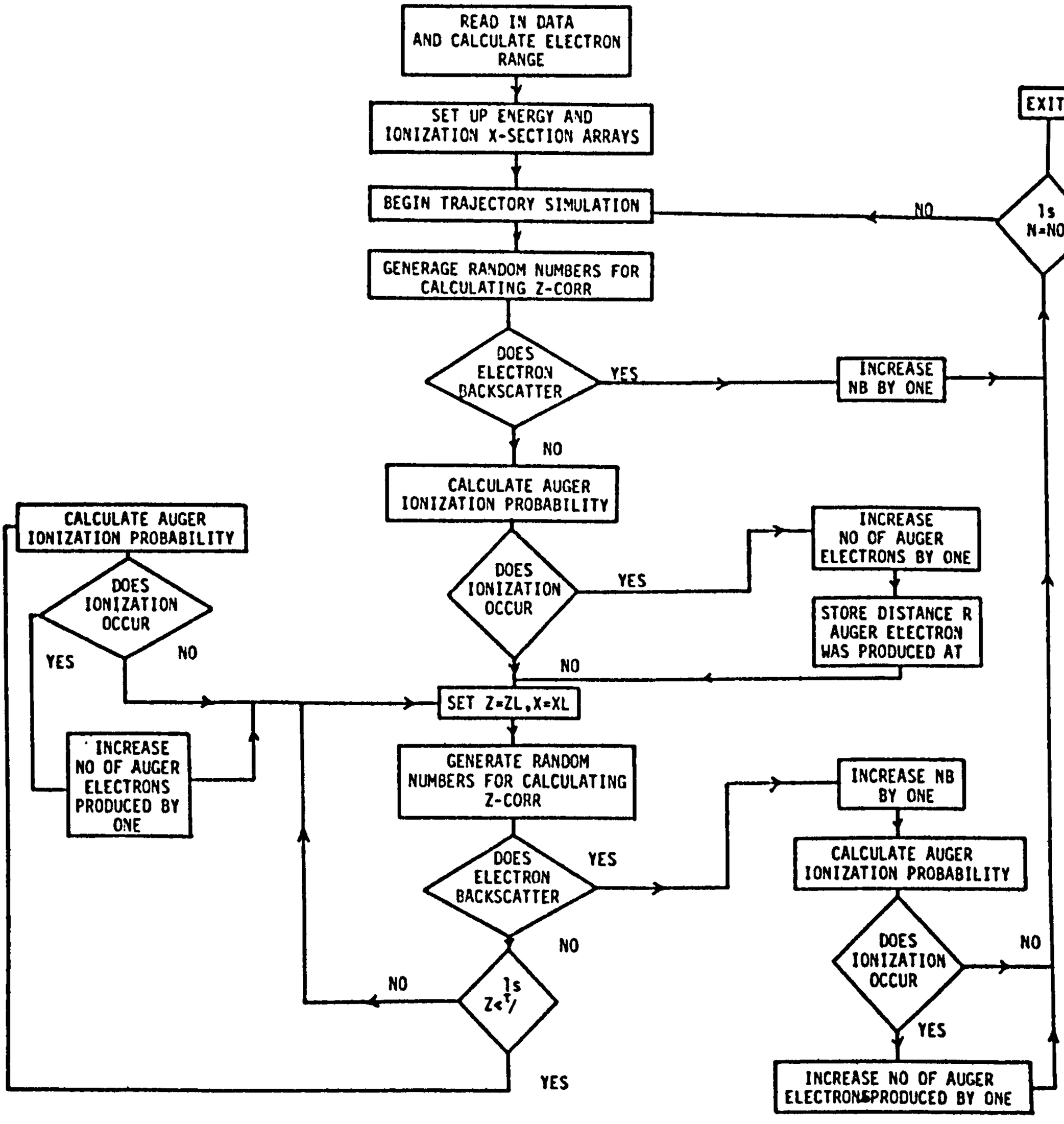

Figure A1 Flow chart showing main steps of the Monte Carlo program.

APPENDIX B

The spatial image function H(x,y) is calculated by performing a convolution operation of the following

a) a Gaussian incident beam of half width σ_1

$$S(x,y) = \frac{I_o}{2\pi\sigma_1^2} \exp - \frac{(x^2 + y^2)}{2\,\sigma_1^2} \qquad (B1)$$

b) Backscattered response function consisting of two parts, a sharp distribution at origin due to primaries and a broad one due to the backscattered and secondary electrons

$$R(x,y) = a\,S(x,y) + B(x,y) \qquad (B2)$$

where

$$B(x,y) = \frac{I_B}{2\pi\sigma_2^2} \exp - \frac{(x^2 + y^2)}{2\,\sigma_2^2}$$

c) C(x,y) be a step in the surface composition profile and is placed along y = o for a surface in the (x,y) plane. H(x,y) will then be given by

$$H(x,y) = S(x,y) * R(x,y) * C(x,y) \qquad (B3)$$

where * represents the convolution operation.

It is convenient to evaluate (B3) in parts, such that

$$H_1(x,y) = S(x,y) * R(x,y) \qquad (B4)$$

$$= \frac{a\,I_o}{2\pi\sigma_1^2} \exp \frac{-(x^2 + y^2)}{2\,\sigma_1^2} + H_B(x,y) \qquad (B5)$$

$$H_B(x,y) = \frac{I_B}{2\pi\sigma_3^2} \exp \frac{-(x^2 + y^2)}{2\sigma_3^2} \qquad (B6)$$

where

$$\sigma_3^2 = \sigma_1^2 + \sigma_2^2$$

Now assume the collected Auger current I_A to consist of two parts, due to primaries and backscattered electrons, then

$$I_A = a\, I_o(1 + \eta) \qquad (B7)$$

where η is backscattering contribution then $H_B(x,y)$ can be written as

$$H_B(x,y) = \frac{a\,\eta\, I_o}{2\pi\sigma_3^2} \exp \frac{-(x^2 + y^2)}{2\sigma_3^2} \qquad (B8)$$

and

$$H_1(x,y) = \frac{a\, I_o}{2\pi} \left\{ \frac{1}{\sigma_1^2} \exp \frac{-(x^2+y^2)}{2\sigma_1^2} + \frac{\eta}{\sigma_3^2} \exp \frac{-(x^2 + y^2)}{2\sigma_3^2} \right\} \qquad (B9)$$

Now for the concentration distribution, assume a square of constant concentration C and of side 2 b with its centre placed at the origin as shown in Fig. (B1)

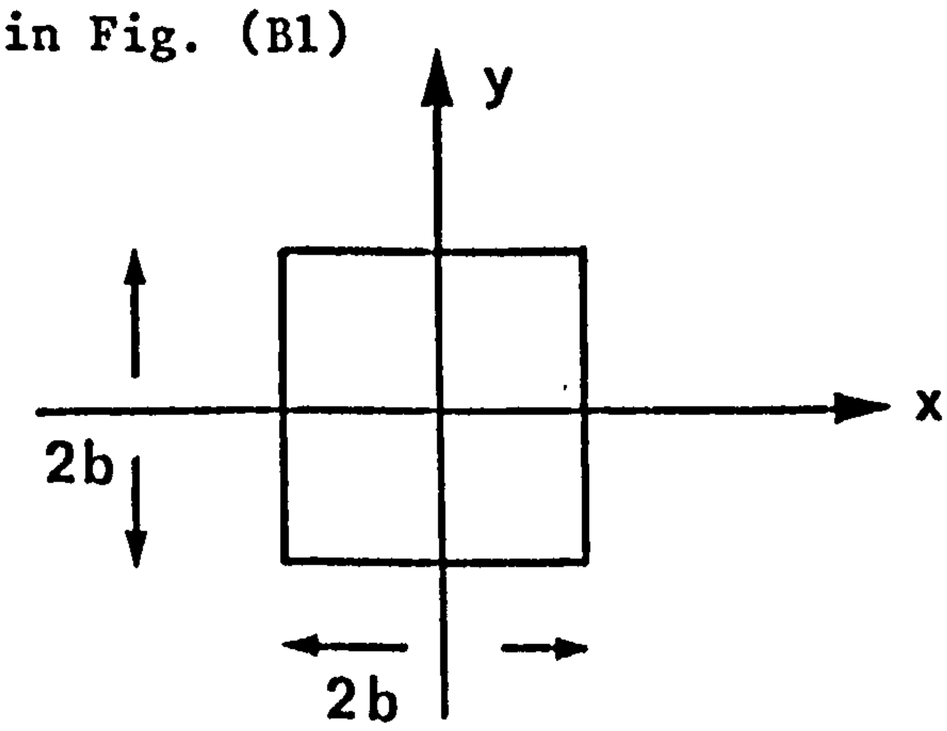

Fig. B1

then

$$H(x,y) = \frac{a\, I_o\, C}{2\pi} \left\{ \frac{1}{\sigma_1^2} \int_{-b}^{b} \int_{-b}^{b} \exp \frac{-(x-x')^2 + (y-y')^2}{2\sigma_1^2} \, dx' \, dy' \right.$$

$$+ \frac{\eta}{\sigma_3^2} \int_{-b}^{b} \int_{-b}^{b} \exp^{-\frac{(x-x')^2 + (y-y')^2}{2\sigma_3^2}} \, dx' \, dy' \Bigg\} \qquad \text{(B10)}$$

if substitute $x - x' = t$ and $y - y' = t$, expression (B10) then gives the following

$$H(x,y) = \frac{a I_o C}{4} \left\{ G(x) G(y) + \eta \; P(x) P(y) \right\} \qquad \text{(B11)}$$

where $G(x) = \text{erf} \; \frac{x - b}{\sqrt{2}\,\sigma_1} - \text{erf} \; \frac{x - b}{\sqrt{2}\,\sigma_1}$

$$P(x) = \text{erf} \; \frac{x + b}{\sqrt{2}\,\sigma_3} - \text{erf} \; \frac{x - b}{\sqrt{2}\,\sigma_3}$$

Along the x-axis, y = o then B(11) becomes

$$H(x) = \frac{K}{2r} \left\{ \text{erf} \; \frac{x}{\sqrt{2}\,\sigma_1} + (r - 1) \; \frac{x}{\sqrt{2}\,\sigma_2} \right\} \qquad \text{(B12)}$$

where $K = a I_o C$ and $r = 1 + \eta$. This is equal to equation (4.16) in the text.

"And the last to be said is that:

Praise be to Allah, the Lord of the Worlds! "